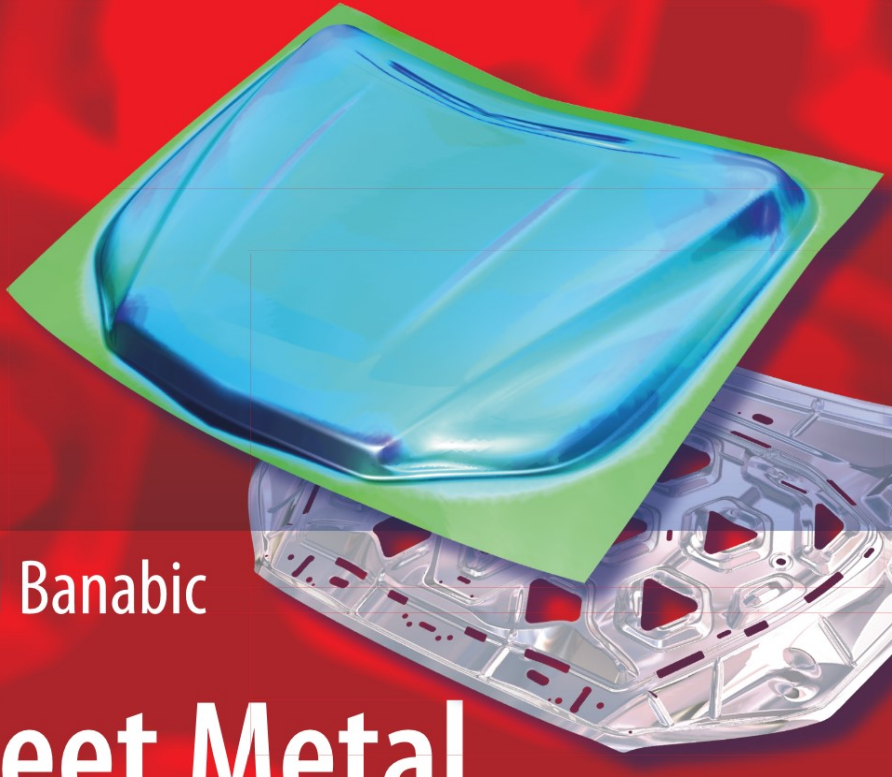

Dorel Banabic

Sheet Metal Forming Processes

Constitutive Modelling and Numerical Simulation

Springer

Sheet Metal Forming Processes

Dorel Banabic

Sheet Metal Forming Processes

Constitutive Modelling and Numerical Simulation

Springer

Prof. Dr. Ing. Dorel Banabic
Technical University of Cluj-Napoca
Research Centre on Sheet Metal
Forming – CERTETA
27 Memorandumului
400114 Cluj Napoca
Romania
banabic@tcm.utcluj.ro

ISBN 978-3-540-88112-4 e-ISBN 978-3-540-88113-1
DOI 10.1007/978-3-540-88113-1
Springer Heidelberg Dordrecht London New York

Library of Congress Control Number: 2010927076

Cover design: Frido Steinen

Printed on acid-free paper

Springer is part of Springer Science+Business Media (www.springer.com)

Preface

The concept of *virtual manufacturing* has been developed in order to increase the industrial performances, being one of the most efficient ways of reducing the manufacturing times and improving the quality of the products. *Numerical simulation* of metal forming processes, as a component of the virtual manufacturing process, has a very important contribution to the reduction of the lead time. The finite element method is currently the most widely used numerical procedure for simulating sheet metal forming processes. The accuracy of the simulation programs used in industry is influenced by the *constitutive models* and the *forming limit curves models* incorporated in their structure. From the above discussion, we can distinguish a very strong connection between *virtual manufacturing* as a general concept, *finite element method* as a numerical analysis instrument and *constitutive laws*, as well as *forming limit curves* as a specificity of the sheet metal forming processes. Consequently, the *material modeling* is strategic when models of reality have to be built.

The book gives a synthetic presentation of the research performed in the field of sheet metal forming simulation during more than 20 years by the members of three international teams: the Research Centre on Sheet Metal Forming—CERTETA (Technical University of Cluj-Napoca, Romania); AutoForm Company from Zürich, Switzerland and VOLVO automotive company from Sweden.

The first chapter presents an overview of different Finite Element (FE) formulations used for sheet metal forming simulation, now and in the past. The objective of this chapter is to give a general understanding of the advantages and disadvantages of the various methods in use. The first section is dedicated to some of the necessary ingredients of the fundamentals of continuum mechanics for large deformation problems. These are needed for a better understanding of the forthcoming FE-formulations.

A more extended chapter is devoted to the presentation of the phenomenological yield criteria. Due to the fact that this chapter is only a synthetic overview of the yield criteria, the reader interested in some particular formulation should also read the original paper listed in the reference section. We have tried to use the symbols adopted by the authors, especially in the mathematical relationships defining

the yield stresses and the coefficients of plastic anisotropy. This decision has been made in order to facilitate the reading of the original papers. Of course, under these circumstances, the coherency of the notations cannot be preserved. As one may see in the list of symbols, several identifiers have different meanings. The reader should take this aspect into account. This chapter gives a more detailed presentation of the yield criteria implemented in the commercial programs used for the finite element simulation (emphasizing the formulations proposed by the CERTETA team—BBC models—implemented in the AutoForm commercial code) or the yield criteria having a major impact on the research progress. To improve the springback prediction a novel approach to model the Bauschinger effect has been developed and implemented in the commercial code AutoForm. Consequently, an extended section of this chapter has been dedicated to the modeling of the Bauschinger effect, especially in the AutoForm model.

The sheet metal formability is discussed in a separate chapter. After presenting the methods used for the formability assessment, the discussion focuses on the Forming Limit Curves (FLC). Experimental methods used for limit strains determination and the main factors influencing the FLC are presented in detail. A section is dedicated to the use of Forming Limit Diagrams in industrial practice. Theoretical predictions of the FLCs are presented in an extended section. In this context, the authors emphasize their contributions to the mathematical modeling of FLCs. A special section has been devoted to present an original implicit formulation of the Hutchinson–Neale model, developed by the authors of this chapter, used for calculating the FLCs of thin sheet metals. The commercial programs (emphasizing the FORM CERT program) and the semi-empirical models for FLC prediction are presented in the last sections of the chapter.

The aspects related to the numerical simulation of the sheet metal forming processes are discussed in the last chapter of the book. The role of simulation in process planning, part feasibility and quality, process validation and robustness are presented based on the AutoForm solutions. The performances of the material models are proved by the numerical simulation of various sheet metal forming processes: bulge and stretch forming, deep-drawing and forming of the complex parts. A section has been devoted to the robust design of sheet metal forming processes. Springback is the major quality concern in the stamping field. Consequently, two sections of this chapter are focused on the springback analysis and Computer Aided Springback Compensation (CASP).

The authors wish to express their gratitude to Dr. Waldemar Kubli, founder and CEO, Dr. Mike Selig, CTO and Markus Thomma, CMD of AutoForm Company, for their support of the book project. They have created favorable conditions for the AutoForm team in order to make this book possible. The authors also wish to thank Dr. Alan Leacock from University of Ulster (UK) for his help in proofing the English of the manuscript. Prof. Banabic wishes to express his thanks to his former PhD students Dr. L. Paraianu, Dr. P. Jurco, Dr. M. Vos, Dr. G. Cosovici and his current PhD students G. Dragos and I. Bichis for their help in preparing and editing this book.

The book will be of interest to both the research and industrial communities. It is useful for the students, doctoral fellows, researchers and engineers who are mainly interested in the material modeling and numerical simulation of sheet metal forming processes.

Cluj-Napoca, Romania Dorel Banabic
December 2009

Contents

List of the Authors

Prof. Dorel Banabic
Professor at the Technical University of Cluj-Napoca
Director of the Research Centre in Sheet Metal Forming – CERTETA
27 Memorandumului, 400114 Cluj Napoca, Romania
e-mail: banabic@tcm.utcluj.ro
URL: www.certeta.utcluj.ro

Dr. Bart Carleer
AutoForm Engineering Deutschland GmbH
Emil-Figge-Str. 76-80, 44227 Dortmund, Germany
e-mail: bart.carleer@autoform.de
URL: www.autoform.com

Dr. Dan-Sorin Comsa
Reader at the Technical University of Cluj Napoca
15 C. Daicoviciu, 400020 Cluj Napoca, Romania
e-mail: dscomsa@tcm.utcluj.ro
URL: www.certeta.utcluj.ro

Eric Kam
AutoForm Engineering USA, Inc.
560 Kirts Blvd, Suite 113, Troy, Michigan 48084-4141, USA
e-mail: eric.kam@autoform.com
URL: www.autoform.com

Dr. Andriy Krasovskyy
Formerly AutoForm Development GmbH
Technoparkstrasse 1, CH-8005 Zurich, Switzerland
URL: www.autoform.com

Prof. Kjell Mattiasson
Chalmers University of Technology
SE-412 96 Goteborg, Sweden
e-mail: mailto:kjellm@chalmers.se
URL: www.chalmers.se

Volvo Cars Safety Centre
Dept. 91432/PV 22, SE-405 31 Goteborg, Sweden
e-mail: kmattias@volvocars.com
URL: www.volvocars.com

Dr. Matthias Sester
AutoForm Development GmbH
Technoparkstrasse 1, CH-8005 Zurich, Switzerland
e-mail: matthias.sester@autoform.ch
URL: www.autoform.com

Mats Sigvant PhD
Technical Expert, Sheet Metal Forming Simulation
Stamping CAE, Volvo Car Corporation
Dept. 81153/26HK3, Olofstrom, Sweden
e-mail: msigvan1@volvocars.com
URL: www.volvocars.com

Xiaojing Zhang PhD
AutoForm Engineering Deutschland GmbH
Emil-Figge-Str. 76-80, 44227 Dortmund, Germany
e-mail: xiaojing.zhang@autoform.de
URL: www.autoform.com

Contributions of the Authors

Dorel Banabic	Co-ordination of the book Sections 2.1–2.4, 2.7; Chapter 3
Bart Carleer	Section 4.4
Dan-Sorin Comsa	Sections 2.5, 2.6, 3.4.4
Eric Kam	Section 4.1
Andriy Krasovskyy	Section 2.8
Kjell Mattiasson	Chapter 1
Matthias Sester	Sections 4.2.1, 4.2.3
Mats Sigvant	Sections 4.2.2, 4.3
Xiaojing Zhang	Sections 4.5, 4.6

Chapter 1
FE-Models of the Sheet Metal Forming Processes

List of Special Symbols

[A]	matrix with constants describing the anisotropy of the material
$[B]$	strain matrix
$[B_{\mathrm{L}}]$	linear strain matrix
$[B_{\mathrm{NL}}]$	nonlinear strain matrix
c	speed of sound
$\mathbf{d}$	rate of deformation tensor
$\mathbf{d}^{\mathrm{p}}$	plastic rate of deformation
$\mathbf{D}$	elastic constitutive tensor
$[D]$	matrix of the elastic constitutive tensor
$[D_{\mathrm{T}}]$	matrix form of the constitutive tensor
ds	lengths of the vector d$\mathbf{x}$
dS	lengths of the vector d$\mathbf{X}$
dv	volume element in the current configuration
dV	volume element in the reference configuration
E	Young's modulus
E_1, E_2	principal values of Lagrangian strains
$\mathbf{E}$	Green's strain tensor
$\dot{\mathbf{E}}$	Green strain rate tensor
f	yield function
f	load
$\{f^{\mathrm{ext}}\}$	external force vector
$\{f^{\mathrm{int}}\}$	internal force vector
$\mathbf{F}$	deformation gradient tensor
$[K]$	linear stiffness matrix
$[K_{\mathrm{G}}]$	geometric stiffness matrix
$[K_{\mathrm{M}}]$	material stiffness matrix
$[K_{\mathrm{S}}]$	initial stress stiffness matrix
$[K_{\mathrm{T}}]$	tangent matrix
L	lenght
$\mathbf{L}$	velocity gradient tensor

D. Banabic, *Sheet Metal Forming Processes*, DOI 10.1007/978-3-540-88113-1_1,

$[M]$	consistent mass matrix
$\hat{\mathbf{n}}$	unit vector
$[\,N(\mathbf{x})\,]$	matrix with base functions
S	surface area
$\mathbf{S}$	second Piola-Kirchhhoff (PK2) stress
t	time
$\mathbf{t}$	traction or stress vector
$\{\tilde{u}\}$	vector with nodal displacements
$\dot{\mathbf{u}}$	velocity
$\ddot{\mathbf{u}}$	acceleration
V	volume
$\mathbf{W}$	spin tensor
$\mathbf{x}$	position vector
$\mathbf{X}$	position of the particle in the reference configuration
$\bar{\varepsilon}$	effective strain
$\bar{\varepsilon}^p$	effective plastic strain
$\dot{\bar{\varepsilon}}^p$	effective plastic strain rate
ξ	fraction of critical damping of the highest eigen-mode.
Λ_1, Λ_2	principal stretch values
$\dot{\lambda}$	scalar in the associated flow rule
ν	Poisson's ratio
ρ	mass densities in the current configuration
ρ_0	mass densities in the reference configuration
$\{\Psi\}$	residual vector
$\boldsymbol{\sigma}$	Cauchy stress
$\hat{\boldsymbol{\sigma}}$	Jaumann or co-rotational rate
$\boldsymbol{\sigma}^{\nabla}$	objective stress rate tensor
$\bar{\sigma}$	effective stress
$\boldsymbol{\tau}$	Kirchhoff stress
$\omega_{\max}$	maximum eigen-frequency

1.1 Introduction

In the current section an overview of different Finite Element (FE) formulations used for sheet metal forming simulation, now and in the past, will be given. The theories of FE-simulation of large deformation problems will be briefly touched upon herein, but for thorough presentations the reader is referred to the many existing text books on the subject, e.g. Belytschko et al. [1], Zienkiewicz and Taylor [2] and Crisfield [3]. The object is rather to give a general understanding of the advantages and disadvantages of the various methods in use. Review articles on sheet forming simulation and comparative studies of different FE-procedures are found in e.g. Honecker and Mattiasson [4], Oñate and Agelet de Saracibar [5], Oñate et al. [6], Mattiasson [7], Kawka et al. [8], Wenner [9], Wang et al. [10], Mattiasson [11],

Makinouchi [12] and Wenner [13]. State-of-the-art articles on the utilization of sheet forming simulation today, and outlooks against the future are given in Banabic and Tekkaya [14] and Roll and Weigand [15].

Finite Element Methods (FEM) have been developed and used for sheet forming simulations since the 1970s, when the continuum mechanics foundations for problems involving large displacements and large strains became well established. FE-procedures for sheet forming analysis can be classified into two main groups depending on if they are based on an *elastic-plastic* or a *rigid-plastic* material model. Large strain formulations may be based on either an *Eulerian* or a *Lagrangian description of motion*, leading to two basically different FE-procedures with nodal velocities and nodal incremental displacements, respectively, as primary unknowns.

1.2 Fundamentals of Continuum Mechanics

1.2.1 Introduction

In [16] and [17] an extended presentation of the fundamentals of continuum mechanics for large deformation problems and the theory of phenomenological plasticity are given. Here, some of the necessary ingredients for the forthcoming FE-formulations will be briefly presented.

When discussing the kinematics of continua it is important to make clear the meanings of the terms *point* and *particle.* The word *point* will be used to designate a certain location in space, while the word *particle* will denote a small part of a material continuum. There are basically two ways of describing the motion of such a continuum.

In the *material* or *Lagrangian* descrition the independent variables are the particle P and the time t. The motion may then be expressed by an equation of the form

$$\mathbf{x} = \mathbf{x}(P, t) \tag{1.1}$$

where $\mathbf{x}$ is the position vector of the particle P at time t. It is common to write this equation in terms of the position $\mathbf{X}$ of the particle P in the reference configuration, i.e.

$$\mathbf{x} = \mathbf{x}(\mathbf{X}, t) \tag{1.2}$$

In the *spatial* or *Eulerian* description attention is fixed to a given region in space (a point) instead of a certain particle of a continuum. Independent variables are the present time t and the present position $\mathbf{x}$ of the particle that occupied the point $\mathbf{X}$ at time t=0. The motion is thus expressed by

$$\mathbf{X} = \mathbf{X}(\mathbf{x}, t) \tag{1.3}$$

If Eqs. (1.2) and (1.3) represent one-to-one mappings with continuous partial derivatives, the two mappings are unique inverses of each other.

The Eulerian description is the description best suited for fluid mechanics problems, as it focuses attention on a certain region in space, which enables us to observe the flow in a point in a channel or a wind tunnel. The Lagrangian formulation has traditionally been used in solid and structural mechanics problems, in which there normally exist a natural reference configuration with known stresses and deformations. In a Finite Element context, the primary variables in the Lagrangian formulation are *displacements,* while in the Eulerian formulation they are *velocities.*

In some metal forming processes, especially bulk forming processes, the metal flow resembles that of a fluid, and the problems have consequently been solved by means of the Eulerian formulation. But even a problem like sheet metal forming has been analyzed by means of this approach as will be discussed in one of the coming sections.

In the following we will focus on the Lagrangian approach. To generalize a formulation for small deformations to large deformations adds a great deal of complexity. There are a number of different ways to formulate and solve the problem. Here we will only present a couple of possible alternatives. As mentioned in the introduction of this chapter, the reader is referred to one or more of the previously mentioned textbooks to get a more complete coverage of the subject.

The main challenge when formulating the basic equations in the Lagrangian formulation is to do it in such a way that they become independent of rigid-body rotations. This means that a rigid body rotation should not give rise to additional strains and stresses. We say that the formulation must be *objective* or *frame invariant*, which also implies that the strain and stress measures being a part of the formulation also must satisfy the objectivity requirement. There are a number of such strain and stress measures appearing in the literature, but we will here limit our discussion to only a few of them.

1.2.2 Strain Measures

We will first introduce a tensor called the *deformation gradient* tensor $\mathbf{F}$, defined by

$$\mathbf{F} = \frac{\partial \mathbf{x}}{\partial \mathbf{X}}; \qquad F_{iJ} = \frac{\partial x_i}{\partial X_J}. \tag{1.4}$$

This tensor is *not* objective, but plays an important role in the derivation of the above mentioned strain and stress tensors. The tensor relates a line segment in current and reference configurations, respectively, as

$$d\mathbf{x} = \mathbf{F} \cdot d\mathbf{X}; \qquad dx_i = F_{iJ}\, dX_J \tag{1.5}$$

To emphasize the distinction between the two sets of coordinates, we will use capital letters for indices on tensor components referred to the reference configuration and

lower case letters on those referred to the current configuration. The deformation gradient tensor is said to be a two-point tensor, since its components are referred to both the reference and the current configuration.

Let dS and ds denote the lengths of the vectors $d\mathbf{X}$ and $d\mathbf{x}$, respectively. The squares of these lengths may be written as

$$\begin{aligned} dS^2 &= |d\mathbf{X}|^2 = d\mathbf{X}\cdot d\mathbf{X} = dX_I\, dX_I \\ ds^2 &= |d\mathbf{x}|^2 = d\mathbf{x}\cdot d\mathbf{x} = dx_i\, dx_i \end{aligned} \tag{1.6}$$

Using Eq. (1.5), we can rewrite ds^2 as

$$\begin{aligned} ds^2 &= (\mathbf{F}\cdot d\mathbf{X})\cdot(\mathbf{F}\cdot d\mathbf{X}) = d\mathbf{X}\cdot(\mathbf{F}^T\cdot\mathbf{F})\cdot d\mathbf{X} \\ ds^2 &= (F_{kI}\, dX_I)(F_{kJ}\, dX_J) = F_{kI}F_{kJ}\, dX_I\, dX_J \end{aligned} \tag{1.7}$$

The difference ds^2–dS^2 for two neighboring particles of a continuum is used as a measure of deformation. This difference can be written

$$\begin{aligned} ds^2 - dS^2 &= d\mathbf{X}\cdot(\mathbf{F}^T\cdot\mathbf{F})\cdot d\mathbf{X} - d\mathbf{X}\cdot d\mathbf{X} = d\mathbf{X}\cdot(\mathbf{F}^T\cdot\mathbf{F}-\mathbf{I})\cdot d\mathbf{X} = \\ &= 2\, d\mathbf{X}\cdot\mathbf{E}\cdot d\mathbf{X} \\ ds^2 - dS^2 &= F_{kI}F_{kJ}\, dX_I\, dX_J - dX_I\, dX_I = (F_{kI}F_{kJ}-\delta_{IJ})\, dX_I\, dX_J = \\ &= 2\, E_{IJ}\, dX_I\, dX_J \end{aligned} \tag{1.8}$$

From Eq. (1.8) the definition of *Green's strain* tensor is found to be

$$\mathbf{E} = \frac{1}{2}(\mathbf{F}^T\cdot\mathbf{F}-\mathbf{I}); \qquad E_{IJ} = \frac{1}{2}(F_{kI}F_{kJ}-\delta_{IJ}) \tag{1.9}$$

In a rigid body rotation the difference ds^2–dS^2 is constant. This can only be accomplished if also the tensor $\mathbf{E}$ is constant, which proves that the tensor is invariant under a rigid body rotation and, thus, objective.

An especially useful form of the strain tensor is obtained when it is expressed in displacement gradients. Define the displacement $\mathbf{u}$ from the following relation:

$$\mathbf{x} = \mathbf{X} + \mathbf{u}; \qquad x_I = X_I + u_I \tag{1.10}$$

Introducing this expression into the equation for $\mathbf{F}$ in Eq. (1.4), we get

$$\mathbf{F} = \frac{\partial\mathbf{x}}{\partial\mathbf{X}} = \mathbf{I} + \frac{\partial\mathbf{u}}{\partial\mathbf{X}}; \qquad F_{iJ} = \frac{\partial x_i}{\partial X_J} = \delta_{iJ} + \frac{\partial u_i}{\partial X_J} \tag{1.11}$$

Green's strain tensor can then be rewritten as

$$\begin{aligned} \mathbf{E} &= \frac{1}{2}\left[\frac{\partial\mathbf{u}}{\partial\mathbf{X}} + \left(\frac{\partial\mathbf{u}}{\partial\mathbf{X}}\right)^T + \frac{\partial\mathbf{u}}{\partial\mathbf{X}}\cdot\left(\frac{\partial\mathbf{u}}{\partial\mathbf{X}}\right)^T\right] \\ E_{IJ} &= \frac{1}{2}\left[\frac{\partial u_I}{\partial X_J} + \frac{\partial u_J}{\partial X_I} + \frac{\partial u_K}{\partial X_J}\cdot\frac{\partial u_K}{\partial X_I}\right] \end{aligned} \tag{1.12}$$

Now, consider two neighboring particles with instantaneous positions $\mathbf{x}$ and $\mathbf{x}+d\mathbf{x}$, respectively. The difference in velocity between these two points point is

$$d\mathbf{v} = \frac{\partial \mathbf{v}}{\partial \mathbf{x}} d\mathbf{x}\,; \qquad dv_i = \frac{\partial v_i}{\partial x_j} dx_j \tag{1.13}$$

The gradient in the above equation is called the *velocity gradient* tensor and is, thus, defined by

$$\mathbf{L} = \frac{\partial \mathbf{v}}{\partial \mathbf{x}}\,; \qquad L_{ij} = \frac{\partial v_i}{\partial x_j} \tag{1.14}$$

The velocity gradient can be decomposed into a symmetric and a skew-symmetric part according to

$$\begin{aligned} \mathbf{L} &= \frac{1}{2}(\mathbf{L} + \mathbf{L}^T) + \frac{1}{2}(\mathbf{L} - \mathbf{L}^T); \\ L_{ij} &= \frac{1}{2}\left(\frac{\partial v_i}{\partial x_j} + \frac{\partial v_j}{\partial x_i}\right) + \frac{1}{2}\left(\frac{\partial v_i}{\partial x_j} - \frac{\partial v_j}{\partial x_i}\right) \end{aligned} \tag{1.15}$$

The symmetric part $\mathbf{d}$

$$\mathbf{d} = \frac{1}{2}(\mathbf{L} + \mathbf{L}^T)\,; \qquad d_{ij} = \frac{1}{2}\left(\frac{\partial v_i}{\partial x_j} + \frac{\partial v_j}{\partial x_i}\right) \tag{1.16}$$

is called *rate of deformation* tensor, while the skew-symmetric part $\mathbf{W}$

$$\mathbf{W} = \frac{1}{2}(\mathbf{L} - \mathbf{L}^T)\,; \qquad W_{ij} = \frac{1}{2}\left(\frac{\partial v_i}{\partial x_j} - \frac{\partial v_j}{\partial x_i}\right) \tag{1.17}$$

is called the *spin* tensor.

The physical interpretation of these tensors is now quite obvious. Rewriting Eq. (1.13), we get

$$d\mathbf{v} = (\mathbf{d} + \mathbf{W}) \cdot d\mathbf{x}\,; \qquad dv_i = (d_{ij} + W_{ij})\, dx_j \tag{1.18}$$

If all the components d_{ij} are equal to zero at a certain point P, the instantaneous motion in the neighbourhood of P is a rigid body motion. This is a consequence of the skew-symmetry of the tensor $\mathbf{W}$. We then realize that, if all components W_{ij} are zero, we have a pure deformation without any rigid body rotation. The rate of deformation tensor is, thus, an objective tensor. It should also be observed that for a *small deformation problem* the rate of deformation tensor is simply the time derivative of the strain tensor, i.e. $d_{ij} = \dot{\varepsilon}_{ij}$.

We shall now find the relationship between the rate of deformation tensor and the time derivative of Green's strain tensor. From the definition of Green's strain tensor in Eq. (1.8) we get

$$\frac{d}{dt}(s^2) \;=\; 2\,d\mathbf{X}\;\cdot\;\dot{\mathbf{E}}\;\cdot\;d\mathbf{X} \;=\; 2\,\dot{E}_{IJ}\,dX_I\,dX_J \tag{1.19}$$

The left hand side of the above equation can also be written

$$\begin{aligned}\tfrac{d}{dt}(s^2) \;&=\; 2\,d\mathbf{x}\cdot\tfrac{d}{dt}(d\mathbf{x}) \;=\; 2\,d\mathbf{x}\cdot d\mathbf{v} \;=\; 2\,d\mathbf{x}\cdot\tfrac{\partial\mathbf{v}}{\partial\mathbf{x}}\cdot d\mathbf{x} \;=\\ &=\; d\mathbf{x}\cdot(\mathbf{d}\;+\;\mathbf{W})\cdot d\mathbf{x} \;=\; dx_k\,(d_{km}\;+\;W_{km})\,dx_m\end{aligned} \tag{1.20}$$

Due to the skew-symmetry of the spin tensor $\mathbf{W}$, i.e. $\mathrm{W}_{ij} = -\mathrm{W}_{ji}$, it is easy to show that

$$d\mathbf{x}\;\cdot\;\mathbf{W}\;\cdot\;d\mathbf{x} \;=\; dx_k\,W_{km}\,dx_m \;=\; 0 \tag{1.21}$$

Eq. (1.20) can then be rewritten as

$$\frac{d}{dt}(s^2) \;=\; d\mathbf{x}\;\cdot\;\mathbf{d}\;\cdot\;d\mathbf{x} \;=\; dx_k\;d_{km}\;dx_m \tag{1.22}$$

Introducing the definition of the deformation gradient tensor $\mathbf{F}$ according to Eq. (1.5), we can rewrite the above equation as

$$\frac{d}{dt}(s^2) \;=\; (d\mathbf{X}\cdot\mathbf{F}^T)\;\cdot\;\mathbf{d}\;\cdot\;(\mathbf{F}\cdot d\mathbf{X}) \tag{1.23}$$

Comparing Eqs. (1.19) and (1.23), we find the following relation between Green's strain rate tensor and the rate of deformation tensor:

$$\dot{\mathbf{E}} \;=\; \mathbf{F}^T\;\cdot\;\mathbf{d}\;\cdot\;\mathbf{F}\,; \qquad\qquad \dot{E}_{IJ} \;=\; d_{km}\,F_{kI}F_{mJ} \tag{1.24}$$

From Eq. (1.24) we note that also the components of the tensor $\dot{\mathbf{E}}$ vanish when the neighborhood of the particle considered moves like a rigid body. That is, the Green strain rate tensor is objective.

It is much more convenient to express the Green strain rate in velocity gradients referred to the reference coordinates. Taking the time derivative of Eq. (1.12) we get

$$\begin{aligned}\dot{\mathbf{E}} \;&=\; \frac{1}{2}\left[\frac{\partial\dot{\mathbf{u}}}{\partial\mathbf{X}} \;+\; \left(\frac{\partial\dot{\mathbf{u}}}{\partial\mathbf{X}}\right)^T \;+\; \frac{\partial\dot{\mathbf{u}}}{\partial\mathbf{X}}\;\cdot\;\left(\frac{\partial\mathbf{u}}{\partial\mathbf{X}}\right)^T \;+\; \frac{\partial\mathbf{u}}{\partial\mathbf{X}}\;\cdot\;\left(\frac{\partial\dot{\mathbf{u}}}{\partial\mathbf{X}}\right)^T\right]\\ \dot{E}_{IJ} \;&=\; \frac{1}{2}\left[\frac{\partial\dot{u}_I}{\partial X_J} \;+\; \frac{\partial\dot{u}_J}{\partial X_I} \;+\; \frac{\partial\dot{u}_K}{\partial X_J}\frac{\partial u_K}{\partial X_I} \;+\; \frac{\partial u_K}{\partial X_J}\frac{\partial\dot{u}_K}{\partial X_I}\right]\end{aligned} \tag{1.25}$$

Finally, it should be mentioned (without proof) that the determinant of the deformation gradient tensor expresses the relation between a volume element in the current and the reference configuration, respectively, so that

$$dv \;=\; \det(\mathbf{F})\,dV \;=\; J\,dV \tag{1.26}$$

where dv is the volume element in the current configuration and, dV is the same element in the reference configuration.

1.2.3 Stress Measures

There are a number of different stress measures appearing in the continuum mechanics literature. Here we will only consider three of them: The *Cauchy* stress $\boldsymbol{\sigma}$, the *Kirchhoff* stress $\boldsymbol{\tau}$ and the *Second Piola-Kirchhhoff* (*PK*2) stress $\mathbf{S}$, together with rates of these tensors.

The *Cauchy stress* tensor $\boldsymbol{\sigma}$ is also known as the *true stress* tensor and measures the force per unit area in the current configuration. The *traction* or *stress vector* $\mathbf{t}$ at a boundary point is related to the Cauchy stress tensor through the relation

$$\mathbf{t} \;=\; \hat{n} \cdot \boldsymbol{\sigma}\,; \qquad\qquad t_i \;=\; \hat{n}_j\,\sigma_{ji} \tag{1.27}$$

where $\hat{\mathbf{n}}$ is an outward unit vector at the boundary point.

In a Lagrangian formulation equilibrium equations are often written in terms of variables referred to the reference configuration. To this purpose a variety of so called *pseudo stress* measures have been defined, of which two will be discussed here. The first one is the *Kirchhoff stress* tensor $\boldsymbol{\tau}$, which frequently has been used in constitutive equations in finite strain plasticity. It is related to the Cauchy stress tensor by

$$\boldsymbol{\tau} \;=\; \frac{\rho_0}{\rho}\,\boldsymbol{\sigma} \;=\; J\,\boldsymbol{\sigma}\,; \qquad\qquad \tau_{ij} \;=\; \frac{\rho_0}{\rho}\,\sigma_{ij} \;=\; J\,\sigma_{ij} \tag{1.28}$$

where ρ_0 and ρ are the mass densities in the reference and current configurations, respectively, and J is the determinant of the deformation gradient tensor. It should be noted that for an *incompressible* material the Cauchy and Kirchhoff stress tensors are equal.

The *Second Piola-Kirchhof f* stress tensor $\mathbf{S}$ is defined to be *energy conjugate* to the Green strain rate tensor. The work rate can then be written

$$\dot{W} \;=\; \int_v \boldsymbol{\sigma} \;:\; \mathbf{d}\; dv \;=\; \int_V \mathbf{S} \;:\; \dot{\mathbf{E}}\; dV \;=\; \int_v \frac{1}{J}\,\mathbf{S} \;:\; \dot{\mathbf{E}}\; dv \tag{1.29}$$

Introducing the relation between the rate of deformation tensor and Green's strain rate according to Eq. (1.24), we get

$$J\,\boldsymbol{\sigma} \;:\; \mathbf{d} \;=\; \mathbf{S} \;:\; \dot{\mathbf{E}} \;=\; \mathbf{S} \;:\; (\mathbf{F}^T \cdot \mathbf{d} \cdot \mathbf{F}) \tag{1.30}$$

After some tensor manipulations the following relation is obtained

$$\mathbf{S} \;=\; J\,\mathbf{F}^{-1} \cdot \boldsymbol{\sigma} \cdot \mathbf{F}^{-T}; \qquad\qquad S_{IJ} \;=\; J\,F^{-1}_{Ik}\,\sigma_{km}\,F^{-1}_{Jm} \tag{1.31}$$

It can be shown that the Cauchy stress tensor $\boldsymbol{\sigma}$ is symmetric and objective. As a consequence of Eq. (1.31) it can be understood that also the PK2 tensor $\mathbf{S}$ is symmetric and objective.

The constitutive equations for certain material types like *hypoelastic* and *elastic-plastic* ones are formulated in rate form. The rate of deformation tensor $\mathbf{d}$ is a suitable deformation measure in such material laws. The problem is to choose a proper stress rate measure. The material time derivative of the Cauchy stress tensor, $\dot{\boldsymbol{\sigma}}$, can be shown *not* to be objective. Hence, the material time derivative of the Cauchy stress tensor cannot serve as a proper stress rate measure. Of course this defect is valid for the Kirchhoff stress rate $\dot{\boldsymbol{\tau}}$ as well.

There do, however, exist a number of different objective rates of the Cauchy stress tensor. Here we will only mention one of them: The *Jaumann* or *co-rotational* rate, $\boldsymbol{\sigma}^{\nabla}$, defined by

$$\boldsymbol{\sigma}^{\nabla} = \dot{\boldsymbol{\sigma}} + \boldsymbol{\sigma} \cdot \mathbf{W} - \mathbf{W} \cdot \boldsymbol{\sigma}\,; \quad \sigma_{ij}^{\nabla} = \dot{\sigma}_{ij} + \sigma_{ik} W_{kj} - W_{ik} \sigma_{kj} \tag{1.32}$$

1.3 Material Models

In the following we will assume that the *yield condition* can be expressed in the form

$$f = \bar{\sigma} - H(\bar{\varepsilon}^p) = 0 \tag{1.33}$$

This relation implies that yielding occurs when the *effective stress* $\bar{\sigma}$, which is a scalar function of the state of stress, reaches a critical value H, which in turn is a function of the *effective plastic strain* $\bar{\varepsilon}^p$. The function $H(\bar{\varepsilon}^p)$ is usually obtained from a uniaxial stress-plastic strain curve.

The *rate of deformation tensor* $\mathbf{d}$, defined in Eq. (1.16), is used as a strain rate measure in elastic-plastic constitutive equations. We will in the following assume that the rate of deformation tensor can be additively divided into an elastic and a plastic part:

$$\mathbf{d} = \mathbf{d}^e + \mathbf{d}^p \tag{1.34}$$

The *normality condition* states that the plastic rate of deformation $\mathbf{d}^p$ is outward normal to the yield surface $f = 0$. This is expressed as

$$\mathbf{d}^p = \dot{\lambda} \frac{\partial f}{\partial \boldsymbol{\sigma}} \tag{1.35}$$

where $\dot{\lambda}$ is a scalar function that depends on the current state of stress and strain. The relationship (1.35) is called an *associated flow rule.*

During plastic loading the stress point remains on the yield surface. This implies that $\dot{f} = 0$, which is known as the *consistency condition*. In the present case we find

$$\dot{f} \;=\; \frac{\partial f}{\partial \boldsymbol{\sigma}} \;:\; \boldsymbol{\sigma}^{\nabla} \;-\; H' \,\dot{\bar{\varepsilon}}^{p} \;=\; \frac{\partial f}{\partial \sigma_{km}} \,\sigma_{km}^{\nabla} \;-\; H' \,\dot{\bar{\varepsilon}}^{p} \;=\; 0 \tag{1.36}$$

where $H' = d\,H/d\,\bar{\varepsilon}^{p}$ is the slope of the uniaxial stress-plastic strain curve, and $\boldsymbol{\sigma}^{\nabla}$ is an *objective stress rate* tensor.

The *effective plastic strain rate* $\dot{\bar{\varepsilon}}^{p}$ is defined by the rate of plastic work equation

$$\dot{W}^{p} \;=\; \bar{\sigma}\;\dot{\bar{\varepsilon}}^{p} \;=\; \boldsymbol{\sigma} \;:\; \mathbf{d}^{p} \tag{1.37}$$

Combining Eqs. (1.35) and (1.37), we note that

$$\dot{\lambda} \;=\; \dot{\bar{\varepsilon}}^{p} \tag{1.38}$$

Typical for an elastic-plastic law is that there exists a relation between *rates* (or increments) of stress and strain. This relation can be written

$$\boldsymbol{\sigma}^{\nabla} \;=\; \mathbf{D} \;:\; \mathbf{d}^{e} \;=\; \mathbf{D} \;:\; (\,\mathbf{d} \;-\; \mathbf{d}^{p}\,) \tag{1.39}$$

where $\mathbf{D}$ is the elastic constitutive tensor.

For simplicity, we will in the following gather the Cartesian components of the tensors $\boldsymbol{\sigma}$ and $\mathbf{d}^{\mathrm{p}}$ in two vectors (column matrices) $\{\sigma\}$ and $\{\mathrm{d}^{\mathrm{p}}\}$. For the case of *plane stress* these vectors will have the following appearances

$$\begin{aligned} \{\,\sigma\,\} \;&=\; \left[\,\sigma_x \quad \sigma_y \quad \tau_{xy}\,\right]^{T} \\ \left\{\,d^{p}\,\right\} \;&=\; \left[\,d_x^{p} \;\; d_x^{p} \;\; 2\,d_{xy}^{p}\,\right]^{T} \end{aligned} \tag{1.40}$$

For a quadratic yield condition, e.g. the von Mises or the Hill'48 condition, the effective stress can in matrix form be expressed as

$$\bar{\sigma} \;=\; \left(\{\sigma\}^{T}\,[\,A\,]\,\{\sigma\}\right)^{1/2} \tag{1.41}$$

where $[A]$ is a matrix with constants describing the anisotropy of the material.

The gradient to the yield surface can then be expressed as

$$\left\{\,\frac{\partial f}{\partial\,\sigma}\,\right\} \;=\; \frac{1}{\bar{\sigma}}\;\,[\,A\,]\,\{\,\sigma\,\} \tag{1.42}$$

and according to the normality condition the components of the plastic rate of deformation tensor are given by

$$\left\{\,d^{p}\,\right\} \;=\; \frac{\dot{\bar{\varepsilon}}^{p}}{\bar{\sigma}}\;\,[\,A\,]\,\{\,\sigma\,\} \tag{1.43}$$

To give an example of the appearance of the matrix $[A]$, let us consider a transversally anisotropic material obeying the Hill'48 yield condition. Eq. (1.43) can then be expressed in matrix form as

$$\begin{bmatrix} d_x^p \\ d_y^p \\ 2d_{xy}^p \end{bmatrix} = \frac{\dot{\bar{\varepsilon}}^p}{\bar{\sigma}} \begin{bmatrix} 1 & -\frac{R}{1+R} & 0 \\ -\frac{R}{1+R} & 1 & 0 \\ 0 & 0 & 2\frac{1+2R}{1+R} \end{bmatrix} \begin{bmatrix} \sigma_x \\ \sigma_y \\ \tau_{xy} \end{bmatrix} \tag{1.44}$$

Inverting Eq. (1.43), we get

$$\{\sigma\} = \frac{\bar{\sigma}}{\dot{\bar{\varepsilon}}^p} \; [A]^{-1} \left\{ d^p \right\} \tag{1.45}$$

Note that this equation expresses *total* stress in terms of *rate* of plastic strain. Note also that it is only for quadratic yield conditions that the normality condition can be inverted to this form.

If the *total* strain rates in Eq. (1.45) are replaced by *plastic* strain rates, i.e. the elastic part of the rate of deformation tensor is ignored, this equation will form the basis of the *rigid-plastic* theory. A couple of the earlier FE formulations for sheet forming simulation were based on this form of the constitutive equations. In matrix form this equation takes the form

$$\begin{bmatrix} \sigma_x \\ \sigma_y \\ \tau_{xy} \end{bmatrix} = \frac{\bar{\sigma}}{\dot{\bar{\varepsilon}}^p} \frac{1+R}{1+2R} \begin{bmatrix} 1+R & R & 0 \\ R & 1+R & 0 \\ 0 & 0 & \frac{1}{2} \end{bmatrix} \begin{bmatrix} d_x \\ d_y \\ 2d_{xy} \end{bmatrix} \tag{1.46}$$

Using the work Eq. (1.37), we can easily derive the following expression for the effective strain rate

$$\dot{\bar{\varepsilon}}^p = \left(\{d\}^T [A]^{-1} \{d\} \right)^{1/2} \tag{1.47}$$

1.4 FE-Equations for Small Deformations

The dynamic equilibrium conditions of a body are readily expressed by means of the principle of virtual velocities. In terms of variables referred to the current configuration the principle is stated

$$\int_V \boldsymbol{\sigma} : \delta \mathbf{d} \, dV + \int_V \rho \ddot{\mathbf{u}} : \delta \dot{\mathbf{u}} \, dV = \int_S \mathbf{t} : \delta \dot{\mathbf{u}} \, dS + \int_V \mathbf{f} : \delta \dot{\mathbf{u}} \, dV \tag{1.48}$$

where $\ddot{\mathbf{u}}$ is the *acceleration*, $\dot{\mathbf{u}}$ is the *velocity*, $\mathbf{t}$ is the *surface traction*, and $\mathbf{f}$ is the *body load.* Integration is performed over current volume V and surface area S.

Assume now for a moment that we are dealing with a *small deformation problem*. FE-approximations can be introduced as

$$\begin{array}{rcl} \{\, u(\mathbf{x})\} & = & [\, N(\mathbf{x})\,]\,\{\,\tilde{u}\,\} \\ \{\, \dot{u}(\mathbf{x})\} & = & [\, N(\mathbf{x})\,]\,\{\,\dot{\tilde{u}}\,\} \\ \{\, \delta\, \dot{u}(\mathbf{x})\} & = & [\, N(\mathbf{x})\,]\,\{\,\delta\, \dot{\tilde{u}}\,\} \end{array} \tag{1.49}$$

where $\{\,\tilde{u}\,\}$ is a vector with *nodal displacements* and $[\,N(\mathbf{x})\,]$ is a matrix with *base functions*.

Introducing the above FE-approximations into the equation for the strain rate, Eq. (1.16), we obtain the expressions for the strain rate and virtual strain rate, respectively, according to

$$\begin{array}{l} \{\,\dot{\varepsilon}\,\} \;=\; \{\,d\,\} \;=\; [\,B\,]\,\{\,\dot{\tilde{u}}\,\} \\ \{\,\delta\,\dot{\varepsilon}\,\} \;=\; \{\,\delta\, d\,\} \;=\; [\,B\,]\,\{\,\delta\,\dot{\tilde{u}}\,\} \end{array} \tag{1.50}$$

where the matrix $[B]$ is known as the *strain matrix.*

The discretized equilibrium equations will now take the form

$$\left\{ f^{\text{int}} \right\} \;+\; [\,M\,]\,\{\ddot{\tilde{u}}\} \;=\; \left\{ f^{\text{ext}} \right\} \tag{1.51}$$

where $[M]$ is the *consistent mass matrix,* defined by

$$[\,M\,] \;=\; \int_V \rho\; [\,N\,]^T\, [\,N\,]\; dV \tag{1.52}$$

The *external force vector* is given by

$$\left\{ f^{\text{ext}} \right\} \;=\; \int_V [\,N\,]^T\, \{\, b\,\}\; dV \;+\; \int_S [\,N\,]^T\, \{\, t\,\}\; dS \tag{1.53}$$

and, finally, the *internal force* or *stress force vector* is defined by

$$\left\{ f^{\text{int}} \right\} \;=\; \int_V [\,B\,]^T\, \{\, \sigma\,\}\; dV \tag{1.54}$$

In the case of *linear elasticity* the constitutive relation can be written in matrix form as

$$\{\, \sigma\,\} \;=\; [\,D\,]\,\{\,\varepsilon\}\tag{1.55}$$

where $[D]$ is the matrix form of the elastic constitutive tensor. The internal force vector can then be rewritten as

$$\left\{ f^{\text{int}} \right\} = \left(\int_V [B]^T [D][B] \, dV \right) \{ \tilde{u} \} = [K] \{ \tilde{u} \} \tag{1.56}$$

where $[K]$ is the *linear stiffness matrix.*

1.5 FE-Equations for Finite Deformations

The virtual velocity equation (1.48) is a correct representation of the dynamic equilibrium of a body, even if the deformations are of finite magnitudes, on the assumption that all quantities are measured in the *current* configuration. In a Lagrangian formulation it is, however, much more convenient to express equilibrium in variables referred to the *reference* configuration. The transformation of Eq. (1.48) can be shown to give

$$\int_{V_0} \mathbf{S} : \delta \dot{\mathbf{E}} \, dV_0 + \int_{V_0} \rho_0 \ddot{\mathbf{u}} : \delta \dot{\mathbf{u}} \, dV_0 = \int_{S_0} \mathbf{t}^0 : \delta \dot{\mathbf{u}} \, dS_0 + \int_{V_0} \mathbf{f}^0 : \delta \dot{\mathbf{u}} \, dV_0 \tag{1.57}$$

In Eq. (1.57) an index '0' has been assigned to variables measured in the reference configuration. The variables $\mathbf{t}^0$ and $\mathbf{f}^0$ are pseudo forces per unit area and volume, respectively, in the reference configuration. They are defined by

$$\mathbf{t}^0 \, dS_0 = \mathbf{t} \, dS; \qquad \mathbf{f}^0 \, dV_0 = \mathbf{f} \, dV \tag{1.58}$$

In accordance with the small deformation formulation in Eq. (1.50), the expressions for the strain rate and virtual strain rate in matrix notation now become

$$\begin{aligned} \{ \dot{E} \} &= \left[\hat{B} \right] \{ \dot{\tilde{u}} \} \\ \{ \delta \dot{E} \} &= \left[\hat{B} \right] \{ \delta \dot{\tilde{u}} \} \end{aligned} \tag{1.59}$$

The strain matrix $\left[\hat{B} \right]$ can formally be divided in two parts according to

$$\left[\hat{B} \right] = [B_{\text{L}}] + [B_{\text{NL}}] \tag{1.60}$$

Here $[B_{\text{L}}]$ is the ordinary linear strain matrix, equivalent with the matrix $[B]$ in the small deformation theory, while $[B_{\text{NL}}]$ is a nonlinear matrix, which arises as a consequence of the displacement dependent terms in the expression for the Green strain rate $\dot{\mathbf{E}}$ according to Eq. (1.25).

In accordance with the small deformation theory the discretized dynamic equilibrium equations can be expressed as

$$\left\{ f^{\text{int}} \right\} + [M] \{ \ddot{\tilde{u}} \} = \left\{ f^{\text{ext}} \right\} \tag{1.61}$$

with the *consistent mass matrix*

$$[M] = \int_{V_0} \rho_0 [N]^T [N] \, dV_0 \tag{1.62}$$

the *external force vector*

$$\left\{ f^{\text{ext}} \right\} = \int_{V_0} [N]^T \{ b_0 \} \, dV_0 + \int_{S_0} [N]^T \{ t_0 \} \, dS_0 \tag{1.63}$$

and the *internal force vector*

$$\left\{ f^{\text{int}} \right\} = \int_{V_0} \left[\hat{B} \right]^T \{ S \} \, dV_0 \tag{1.64}$$

We will henceforth assume that the problem is quasi-static, i.e. we neglect the inertia term in the equilibrium equations in Eq. (1.61). The simplified equations can then be written

$$\{ \Psi \} = \int_{V_0} \left[\hat{B} \right]^T \{ S \} \, dV_0 - \left\{ f^{\text{ext}} \right\} = 0 \tag{1.65}$$

where $\{ \Psi \}$ is a residual vector, whose elements should be zero when the equilibrium equations are satisfied.

In order to solve the resulting set of nonlinear equations, the Newton-Raphson iterative solution procedure, or related techniques, is commonly used. This requires a linearization of Eq. (1.65) around the last obtained solution. Taking the time derivative of the equilibrium equation in Eq. (1.65), we get

$$\{ \dot{\Psi} \} = \int_{V_0} \left(\left[\hat{B} \right]^T \{ \dot{S} \} + \left[\dot{\hat{B}} \right]^T \{ S \} \right) dV_0 - \{ \dot{f}^{\text{ext}} \} = 0 \tag{1.66}$$

Assuming that the constitutive equations can be transformed to a form such as

$$\{ \dot{S} \} = [D_T] \{ \dot{E} \} \tag{1.67}$$

where $[D_{\text{T}}]$ is a matrix form of the constitutive tensor. It can then be shown that Eq. (1.66) can be rewritten as

$$\{\dot{\Psi}\} = [K_T] \left\{ \dot{\dot{u}} \right\} - \{\dot{f}^{\text{ext}}\} = 0 \tag{1.68}$$

where the *tangent matrix* $[K_T]$ formally can be divided into three matrices:

$$[K_T] = [K_M] + [K_G] + [K_S] \tag{1.69}$$

The first of these matrices, $[K_M]$, is called the *material stiffness matrix* and is defined by

$$[K_M] = \int_{V_0} \{B_L\}^T [D_T] \{B_L\} dV_0 \tag{1.70}$$

This matrix is recognized as the ordinary *small deformation tangent stiffness matrix*. The second one, $[K_G]$, is known as the *geometric stiffness matrix*, and is a consequence of the nonlinear terms in the strain-displacement relation. Finally, the third matrix, $[K_S]$, is called the *initial stress stiffness matrix*, and is a function of the stress state in the current configuration.

Various FE-approaches, based on a Lagrangian description, can be constructed depending on the choice of reference configuration. The most well-known Lagrangian formulations are the *Total* (*TL*) and *Updated Lagrangian* (*UL*) formulations, respectively. In the TL-formulation the initial, stress free configuration is taken as reference configuration, while in the UL-formulation the last calculated configuration is taken as reference state. These two formulations are described below.

The *TL*-formulation follows basically the one described above. The reference coordinates should here be interpreted as the *initial* ones, and the displacements are the *total* ones. Integrations are, furthermore, performed over initial volume and surface area, respectively. The Green strain tensor components at time $t+\Delta t$ can either be calculated from the total displacements at time $t+\Delta t$, or by adding the strain increment during the time increment Δt to the strains at time t. This is justified by the fact that all tensors, even incremental ones, are referred to the same reference configuration.

One of the primary objects of the simulations is to determine the strain distribution in the blank. Principal logarithmic strains in the plane of the sheet are given by

$$\varepsilon_1 = \ln \Lambda_1 ; \qquad \varepsilon_2 = \ln \Lambda_2 \tag{1.71}$$

where Λ_1 and Λ_2 are principal *stretch* values. Stretch is a measure of extensional strain of a differential line element, defined by $\Lambda = ds/dS$. The principal stretch values can be shown to be related to the in-plane principal values of Lagrangian strain, E_1 and E_2, by

$$\Lambda_1 = \sqrt{2E_1 + 1}; \qquad \Lambda_2 = \sqrt{2E_2 + 1} \tag{1.72}$$

where

$$E_{1,2} = \frac{1}{2}(E_x + E_y) \pm \sqrt{\frac{1}{4}(E_x - E_y) + E_{xy}^2}; \tag{1.73}$$

The *UL* FE-formulation follows largely the same pattern as outlined for the TL-approach above. The main differences are as follow. All *coordinates* entering the formulation should be the *current* ones. Since the displacements are measured from the reference (current) configuration, all terms involving displacements in the general formulation will vanish. This implies that the matrices $[B_{\mathrm{NL}}]$ and $[K_{\mathrm{G}}]$ of the general formulation do not enter the UL-formulation. Furthermore, integrals are carried out over *current* volume and area.

The calculation of total strain is much more complicated in the UL-formulation than in the TL-formulation, since the Lagrangian strain increments in each time step is referred to different configurations. This implies that they cannot be added to total strains without complicated transformations.

For three-dimensional shell and membrane elements it is usually necessary to use a local coordinate system for each element, which is redefined (updated) in each step. This implies that a new transformation matrix has to be established in each step, and that a number of transformations of displacement and load vectors between local and global systems have to be performed.

1.6 The 'Flow Approach'—Eulerian FE-Formulations for Rigid-Plastic Sheet Metal Analysis

The rigid-plastic constitutive relations in Sect. 1.3 have the form of the constitutive relations for a *non-Newtonian viscous fluid*. In steady-state metal forming problems, such as extrusion and rolling, the velocities at a given point in space remain constant in time. The material behavior in this type of problems is similar to that of a fluid, and an Eulerian FE-approach is a natural choice. The FE mesh in such problems is fixed (Eulerian).

The Eulerian formulation has, however, also been used for the solution of rigid-plastic, *transient* problems, such as stretch forming and deep-drawing of metal sheets, although the material behavior in such problems bears small resemblance with a fluid flow. In such transient problems the control volume is identified with the sheet geometry in each deforming step. The element mesh has, thus, to be 'updated' in each step (Lagrangian).

The use of the flow approach in sheet metal forming problems has been advocated particularly by Prof. O.C. Zienkiewicz and co-workers in Swansea, and by Prof. E. Oñate in Barcelona [5, 6, 18–21]. A review of the flow approach in application to various steady-state and transient forming problems is given in Zienkiewicz [22].

In Sect. 1.3 the constitutive relations of a *rigid-plasti c* model were derived by neglecting the elastic part of an elastic-plastic model (Eqs. 1.45, 1.46, 1.47). Some writers have derived the constitutive relations for a rigid-plastic material starting from the general form of a *viscoplastic* material as suggested by Perzyna [23]. If the time dependent effects in the viscoplastic model are neglected, the equations of the rigid-plastic model are recovered. It is interesting to note the analogy between the equations of rigid-plastic or viscoplastic flow, and those of small strain, linear elasticity. It is easily shown that completely analogous stress-strain relations are obtained, if the velocity and rate of deformation variables of the flow equations are interchanged by displacement and strain of the linear elasticity equations. Take for instance Hooke's generalized law in the case of plane stress and replace Poisson's ratio ν by $R/(1+R)$. Hooke's law then takes the form

$$\begin{bmatrix} \varepsilon_x \\ \varepsilon_y \\ 2\varepsilon_{xy} \end{bmatrix} = \frac{1}{E} \begin{bmatrix} 1 & -\frac{R}{1+R} & 0 \\ -\frac{R}{1+R} & 1 & 0 \\ 0 & 0 & 2\frac{1+2R}{1+R} \end{bmatrix} \begin{bmatrix} \sigma_x \\ \sigma_y \\ \tau_{xy} \end{bmatrix} \tag{1.74}$$

The analogy between these equations and the corresponding plastic flow equations in Eq. (1.44) is immediately seen. It is noted that the modulus of elasticity E in the elasticity relations plays the role of the 'viscosity' $\bar{\sigma}/\dot{\bar{\varepsilon}}$ in the flow relations.

The above discussed analogy makes it possible to use a standard FE-program for linear elastic analysis in large strain viscoplastic analysis with only minor modifications of the program. Basically, the same FE-equations outlined in Sect. 1.4 for linear elasticity are also applicable in the current flow approach, but with nodal displacements replaced by nodal velocities, and the constitutive relationship modified as described above. In the solution process a steady-state flow situation is assumed at every deformation level. Due to the nonlinear 'viscosity', $\bar{\sigma}/\dot{\bar{\varepsilon}}$, an iterative solution scheme has to be employed at every step to ensure equilibrium.

The FE-equations are thus established in a standard fashion. We assume that a local Catresian coordinate system is defined for each element and is updated in each step. Components referred to these local axes are in the following marked by a super-scribed star. Briefly, the major steps of the discretization process are the following:

Velocity assumptions:

$$\{\dot{u}^*\} = [N^*]\,\{\dot{\tilde{u}}^*\} \tag{1.75}$$

Rate of deformation-velocity relations:

$$\begin{aligned} d^*_{\alpha\beta} &= \frac{1}{2}(\dot{u}^*_{\alpha,\beta} + \dot{u}^*_{\alpha}) \\ \{d^*\} &= [N^*]\,\{\dot{\tilde{u}}^*\} \end{aligned} \tag{1.76}$$

Local equilibrium equations:

$$\begin{aligned} &\left[K^*\right]\left\{\dot{\tilde{u}}^*\right\} = \{f^*\} \\ &\left[K^*\right] = \int_V \left[B^*\right]^T [C]\left[B^*\right] dV \\ &[C] = \frac{\bar{\sigma}}{\dot{\bar{\varepsilon}}}\,[G]^{-1} \end{aligned} \tag{1.77}$$

Transformations between local and global system:

$$\begin{aligned} &\{f^*\} = [A]\left\{f^{\text{ext}}\right\}; \qquad \left\{\dot{\tilde{u}}^*\right\} = [A]\left\{\dot{\tilde{u}}\right\}; \quad [A]^T[A] = [I] \\ &[K] = [A]^T\left[K^*\right][A] \end{aligned} \tag{1.78}$$

Global equilibrium equations:

$$[K]\left\{\dot{\tilde{u}}\right\} = \left\{f^{\text{ext}}\right\} \tag{1.79}$$

When convergence is achieved, the geometry is updated by $\dot{\tilde{u}}\,\Delta t$. The effective strain at time $t+\Delta t$ is obtained as ${}^{t+\Delta t}\bar{\varepsilon} = {}^{t}\bar{\varepsilon} + \dot{\bar{\varepsilon}}\,\Delta t$. A new value of the effective stress is obtained from the hardening curve as ${}^{t+\Delta t}\bar{\sigma} = H({}^{t+\Delta t}\bar{\varepsilon})$.

In rigid or nearly rigid zones of the material the value of $\dot{\bar{\varepsilon}}$ tends to zero and, thus, the 'viscosity' $\bar{\sigma}/\dot{\bar{\varepsilon}}$ tends to infinity. To avoid numerical difficulties due to this fact, the use of a large but finite cut off value of the 'viscosity' is recommended in the references above. Such a cut off value makes it possible to compute stresses even in zones, where the stress state is below the yield stress.

Osakada et al. [24] have pointed out the importance of satisfying the equilibrium conditions at the end of the increment, at time $t+\Delta t$, in certain large strain transient problems, such as sheet metal forming problems. Such a procedure incorporates the effects of shape change and work hardening during the incremental step, and yields for certain problems more accurate results than the simple extrapolation scheme previously described. In the method proposed in [24] the *nodal velocities* are assumed *constant* during the time increment Δt. In the equilibrium relations the matrix $[B]$ and the integration domains are functions of the unknown nodal coordinates at the end of the increment. Furthermore, the effective stress $\bar{\sigma}$ is a function of the unknown effective strain $\bar{\varepsilon}$

Concerning the strain calculation in the flow approach, the same comments can be made as for the UL-formulation in Sect. 1.5.

1.7 The Dynamic, Explicit Method

In a mathematical sense there are basically two methods for solving the discretized, dynamic equilibrium equations outlined in Eqs. (1.57), (1.58), (1.59), (1.60), (1.61),

(1.62), (1.63) and (1.64). These are the *implicit* and *explicit* methods, respectively. The *implicit* method is the most common one. The problem can be formulated in the following way: From a known solution at time step n, we like to compute the solution at time step $n+1$. In the implicit method the time derivatives of displacements at time step $n+1$ is part of the solution. This necessitates the solution of a system of nonlinear equations in every time step. The implicit time integration methods can be proved to be *unconditionally stable* (at least for linear problems). One of the most well-known integration schemes of this kind is the *Newmark beta* scheme.

Explicit time integration methods are mainly used for transient dynamic problems of very short duration, such as for structures submitted to blast and impact loads. Such problems do normally have durations of the order of 1–100 ms. In an *explicit* method the solution at time step $n+1$ is only based on known quantities at time step n. This implies that no system of equations has to be solved in every time step. Explicit time integration methods can be proved to be only *conditionally stable*, i.e. there exist a critical time step size, which cannot be exceeded in order to get a stable solution. The critical time step size is usually of the order of a fraction of a microsecond. The most common explicit time integration method is the *Central difference* method, whose basic equations are the following:

$$ {}^{n+\frac{1}{2}}\left\{ \dot{\tilde{u}} \right\} = \frac{1}{\Delta t}\left({}^{n+1}\{ \tilde{u} \} - {}^{n}\{ \tilde{u} \} \right) \tag{1.80} $$

$$ {}^{n}\left\{ \ddot{\tilde{u}} \right\} = \frac{1}{\Delta t}\left({}^{n+\frac{1}{2}}\left\{ \dot{\tilde{u}} \right\} - {}^{n-\frac{1}{2}}\left\{ \dot{\tilde{u}} \right\} \right) = \frac{1}{\Delta t^2}\left({}^{n+1}\{ \tilde{u} \} - 2\,{}^{n}\{ \tilde{u} \} + {}^{n-1}\{ \tilde{u} \} \right) \tag{1.81} $$

Typical for the Central difference method is that displacements $\{\tilde{u}\}$ and accelerations $\left\{ \ddot{\tilde{u}} \right\}$ are evaluated at whole time steps ${}^{n-1}t$, ${}^{n}t$, ${}^{n+1}t$, and so on, while velocities $\left\{ \dot{\tilde{u}} \right\}$ are evaluated at the midpoints of the time intervals, i.e. at ${}^{n-\frac{1}{2}}t$ and ${}^{n+\frac{1}{2}}t$.

To advance one step in the explicit calculation scheme, we start from known velocities ${}^{n-\frac{1}{2}}\left\{ \dot{\tilde{u}} \right\}$ and displacements ${}^{n}\{\tilde{u}\}$, and would like to calculate ${}^{n+\frac{1}{2}}\left\{ \dot{\tilde{u}} \right\}$ and ${}^{n+1}\{\tilde{u}\}$. The dynamic equilibrium equations at time ${}^{n}t$ can be written

$$ [M]\,{}^{n}\{ \ddot{\tilde{u}} \} + [C]\,{}^{n}\{ \dot{\tilde{u}} \} = {}^{n}\left\{ f^{ext} \right\} - {}^{n}\left\{ f^{\text{int}} \right\} \tag{1.82} $$

Here a damping term has been included for the sake of completeness. Since the velocity is not known at time ${}^{n}t$, the following approximation is introduced:

$$ [C]\,{}^{n}\{ \dot{\tilde{u}} \} \approx [C]\,{}^{n-\frac{1}{2}}\{ \dot{\tilde{u}} \} \tag{1.83} $$

In order to fully employ the benefits of the explicit method, the mass matrix will in the following be assumed to be a diagonal matrix, thus avoiding a time consuming inversion of the matrix. The explicit calculations are now performed according to the following scheme:

$$ {}^{n}\{\ddot{\tilde{u}}\} = [M]^{-1}\left(-[C]\,{}^{n-\frac{1}{2}}\{\dot{\tilde{u}}\} + {}^{n}\left\{f^{\text{ext}}\right\} - {}^{n}\left\{f^{\text{int}}\right\}\right) \tag{1.84} $$

$$ {}^{n+\frac{1}{2}}\{\dot{\tilde{u}}\} = {}^{n-\frac{1}{2}}\{\dot{\tilde{u}}\} + {}^{n}\{\ddot{\tilde{u}}\}\,\Delta t \tag{1.85} $$

$$ {}^{n+1}\{\tilde{u}\} = {}^{n}\{\tilde{u}\} + {}^{n+\frac{1}{2}}\{\dot{\tilde{u}}\}\,\Delta t \tag{1.86} $$

In the above equations no time step index has been assigned to the time increment Δt. It should, however, be understood that Δt has to be continuously updated as the analyzed structure deforms.

For a damped system the critical time step can be shown to be (Belytschko et al. [1])

$$ \Delta t_{cr} = \frac{2}{\omega_{\max}}\left(\sqrt{1+\xi^2} - \xi\right) \tag{1.87} $$

where $\omega_{\max}$ is the maximum eigen-frequency of the system, and ξ is the fraction of critical damping of the highest eigen-mode. From Eq. (1.87) we see that the critical time step has its biggest value for $\xi=0$, i.e. for an undamped system. It can also be noted that a critically damped system, i.e. for $\xi=1$, has a critical time step, which is about 60% of that of an undamped system.

The critical time step according to Eq. (1.87) is only valid for linear systems. In practice, therefore, a smaller time step should be used. Belytschko et al. [1] make the following recommendation:

$$ \Delta t = \alpha\,\Delta t_{cr}\,; \qquad 0.8 \le \alpha \le 0.98 \tag{1.88} $$

The maximum eigen-frequency of a discretized structure is determined by the smallest element in the FE-mesh. Let c denote the speed of sound in the structure. Then, according to the so-called Courant condition

$$ \Delta t \le \frac{l}{c} \tag{1.89} $$

where l is a characteristic length of the smallest element. The interpretation of the above equation is that the time step should be so small that information does not propagate across more than one element during a single time step. This observation is only true for constant strain elements. The speed of sound for two common structural elements are

$$ \text{Bar}: \quad c = \sqrt{\frac{E}{\rho}}\,; \qquad \text{Shell}: \quad c = \sqrt{\frac{E}{\rho\,(1-\nu^2)}}\,; \tag{1.90} $$

The special characteristics of the dynamic, explicit method can now be summarized as follow:

- In explicit codes the *Central difference* time integration method is usually employed.
- The explicit method is *conditionally* stable, i.e. there exists a critical time step , which must not be exceeded in order to get a stable solution.
- The critical time step is approximately equal to the time for a compression or a bending wave to travel through the smallest element in the mesh.
- The number of time steps in a typical explicit analysis is tens of thousands.
- A typical critical step size is of the order of a fraction of a microsecond.
- When a diagonal mass matrix, e.g. a lumped matrix, is used, no system of equations has to be solved, and the method is truly explicit.
- For a given FE-mesh the computing time is directly proportional to the duration of the studied event.
- An explicit method is very robust. The frequently occurring convergence problems in implicit simulations are completely avoided in explicit analyses, since no iterations are performed on a global level.
- The finite elements used in explicit codes are usually simple, linear displacement based elements. They are often under-integrated, which is why *hourglass control* is an important issue.
- Since the time steps are very small, the incremental deformations during a step are also very small. This implies that the complex equations of the Lagrangian description of motion can be ignored, and simplified, linear geometric relations can be used instead. Also the contact conditions can be strongly simplified.
- Since no material tangent stiffness matrices have to be established, the implementation of new material laws is considerable simplified (compared to an implicit method).
- Since no matrices are stored during an explicit simulation, the data storage requirements are much smaller than for an implicit method.
- The explicit method is well adapted for parallelization.

1.8 A Historical Review of Sheet Forming Simulation

The possibility to perform simulations of sheet forming processes was for a long time an unattainable desire in the sheet forming industry. The process engineers liked to be able to reveal any possible forming defects at an early stage, and to minimize the need for expensive modifications of the tools in a trial-and-error process. From a theoretical perspective the forming problem was, however, considered to be a very complicated problem in the early days of FEM in the 1960s and early 1970s. Modelling sheet metal forming problems requires accurate characterisation of effects like nonlinear material behavior, large deformations, and complicated contact conditions between the tools and the blank. The simulation of a real, industrial forming operation with the computing power of the time considered to be an extremely computationally demanding task.

Not until 1970 the first theoretically correct FE-formulation of the large deformation problem was presented by Hibbitt et al. [25]. These equations were

written in a TL-frame (see Sect. 1.5). Later in 1975 McMeeking and Rice [26] and Bathe et al. [27] presented correct UL-formulations of the problem. The attempts to solve forming problems at that period of time were usually based on plane strain or axi-symmetric formulations, and from a theoretically point of view they were often not fully consistent.

The first theoretically correct, 3D formulation of the sheet forming problem was presented by Wang and Budiansky [28] in 1978. The presented method was a TL-formulation and involved triangular, constant strain membrane elements. The material model was an elastic-plastic one. The solution was advanced with a simple forward Euler, incremental scheme. Methods based on such a solution scheme are sometimes denoted *static-explicit* methods.

The following decade saw a high activity in the field. The development took place along several different paths. Methods based on 2D as well as 3D formulations were developed. Depending on the choice of description of motion, type of constitutive relations, and solution procedures, the methods were described as the *solid* approach, the *static-implicit* approach, the *static-explicit* approach, the *rigid-plastic* approach and the *flow* approach.

The *solid* approach and the *static-implicit* approach are two different names of the same procedure. The basic equations of this method are the same as those presented in Sect. 1.5, with the difference that the problem is considered as a quasistatic one, and the inertia term is therefore neglected. This method is based on a *Lagrangian* description of motion and an *elastic-plastic* constitutive relation. The solution is advanced incrementally, and in every increment the equilibrium equations are solved iteratively with some Newton-Raphson-like procedure. The typical number of incremental steps in such a simulation is of the order of hundreds..

The previous approach is *implicit* in the sense that an iterative procedure is employed in each step in order to fulfill the static equilibrium conditions. However, some authors have used an alternative technique, called the *static-explicit* approach, in which no iterations at all are performed. The updating of the geometry is just based on the tangent moduli in the previous step. This implies that equilibrium is never satisfied. In order to reduce the errors involved, very small steps have to be taken. Several thousand steps are common for an ordinary simulation. The advantage of this approach is that it is quite robust, since there are no iterative processes that have to converge. Even instability phenomena like wrinkling have been simulated by means of this procedure.

The *flow approach* was previously described in Sect. 1.6. It uses a kind of *Updated Eulerian* formulation and a *rigid-plastic* material law. Nodal velocities are primary unknowns. The geometry is fixed in each time step, while the equilibrium is iteratively solved for. The geometry is then updated based on the calculated velocities. One of the main advantages of the flow approach is, thus, that the governing equations get a very simple appearance. An obvious disadvantage is of course that no phenomena related to elasticity, such as springback, can be simulated.

The *rigid-plastic approach* is based on the same rigid-plastic constitutive relations as the flow approach (the two methods are sometimes mixed-up). However, some writers have preferred to rewrite these relations in terms of *increments*

of strain. This leads naturally to a *Langrangian* FE-formulation with nodal displacements as primary unknowns. The disadvantages of such an approach are of course the same as those of the flow approach. However, the present formulation do also lack the simplicity of the flow formulation, since the kinematic relations in a Lagrangian formulation are much more complicated than those in an Eulerian one.

During this period of time (the 1980s) the *flow* and *rigid-plastic* approaches were more popular than the *static-implicit* one, mainly because they were more stable, and considerably larger time-steps could be employed. In spite of a lot of promising development, the practical application of sheet forming simulation was, however, for many years hampered by too unstable numerical procedures and excessive computing times, even for very small problems. As an example of state-of-the art at that time, Tang et al. [29] published results from practical applications of a code, developed at Ford, to the simulation of the stamping of real 3D automotive parts. This code was based on 3D shell theory and a *static-implicit* approach. Models with up to 400 higher order shell elements were analyzed, and the reported computing time was about 20 h on a super-computer.

In 1989 Honecker and Mattiasson [4] presented results from a study, in which the *dynamic-explicit* approach was evaluated in application to sheet metal stamping. The results from this study were very promising. Problems with up to 10,000 shell elements could be solved within 1.5 h on a super computer. Also the robustness of this approach was found to be widely superior to that of any other method.

Since sheet forming processes usually have much longer durations than what the dynamic, explicit method normally is intended for, the prerequisites for the problem have to be modified in some way, in order to fully utilize the benefits of the method. This can be done in two different ways. Either the virtual velocity in the simulation is substantially increased in comparison to the physical one, in order to reduce the virtual process time, or the density of the sheet metal is increased, in order to increase the critical time step size, and thereby reducing the total number of time steps. Both these methods lead to an increase of the virtual inertia forces. It is, thus, of utmost importance to have a strict control of these forces so that they have only a marginal influence on the solution. Experience has shown that the physical velocity can be increased by a factor 10–50 without inertia forces having any influence. Some guidelines for the choice of virtual quantities are given in e.g. Chung et al. [30]. A comprehensive overview of the use of the dynamic, explicit method in sheet metal forming simulations is given in Nielsen [31].

From the beginning of the 1990s there was an explosive increase of the practical utilization of sheet forming simulations within the industry, and from the middle of this decade most companies within the automotive industry were performing sheet stamping simulations on a regular basis. Dynamic, explicit codes were dominating the software market. General purpose codes like LS-DYNA and ABAQUS/Explicit, and specialized codes such as PAM-STAMP and OPTRIS are examples of codes in use. In Japan also a couple of codes based on the *static-explicit* approach found some industrial usage; see Kawka et al. [8] and Makinouchi [12]. A few *static-implicit* codes like INDEED in the German automotive industry and MTLFORM at

Ford Motor Company were still in use. The *static-implicit* method was at that time, and is still today, frequently used in academic circles.

The highly specialized code for stamping simulations, AutoForm emerged from a research project at ETH in Zurich in the early 1990s. The code is based on the *static-implicit* approach, but uses some innovative algorithms to enhance stability and computational efficiency. Characteristic for the code in its original form was the use of bending-enhanced membrane elements, and an iterative linear equation solver. In course of time the code has developed and includes now also conventional shell elements. For stamping applications the code is competitive with, or even superior to the dynamic, explicit codes with regard to efficiency and robustness. The code will be treated more in detail in Sect. 4.1 of this book.

Today (2009), AutoForm is probably the most commonly used code in the industry for sheet stamping simulations. Beside this code the software market is still dominated by various dynamic, explicit codes like LS-DYNA, ABAQUS/Explicit, PAM-STAMP 2G and STAMPACK. The use of other types of codes is now only marginal.

References

1. Belytschko T, Liu WK, Moran B (2000) Nonlinear finite elements for continua and structures. John Wiley & Sons, Chichester
2. Zienkiewicz OC, Taylor RL (2000) The finite element method, 5th edn, Vol 2. Solid mechanics. Butterworth-Heinemann, Oxford
3. Crisfield MA (1991) Non-linear finite element analysis of solids and structures, Vol 1. John Wiley & Sons, Hoboken, NJ
4. Honecker A, Mattiasson K (1989) Finite element procedures for 3D sheet forming simulation. In: Thompson EG, Wood RD, Zienkiewicz OC, Samuelsson A (eds) NUMIFORM'89, AA Balkema, Fort Collins
5. Oñate E, Agelet de Saracibar C (1992) Alternatives for finite element analysis of sheet metal forming problems. In: Chenot JL, Wood RD, Zienkiewicz OC (eds) NUMIFORM'92, AA Balkema, Sophia Antipolis
6. Oñate E, Garcia Garino C et al. (1993) NUMISTAMP: A research project for assessment of finite element models for stamping processes. In: Makinouchi A, Nakamachi E, Oñate E, Wagoner RH (eds) NUMISHEET'93, Isehara, Japan
7. Mattiasson K (1996) Computational strategies for sheet forming problems. ECCOMAS'96, John Wiley & Sons, Paris
8. Kawka M, Makinouchi A, Wang SP, Nakamachi E (1997) Advances and trends in sheet metal forming simulation in Japanese automotive industry. SAE Technical Paper 970432
9. Wenner M (1997) State-of-the-art of mathematical modeling of sheet metal forming of automotive body panels. SAE Technical Paper 970431
10. Wang SP, Choudhry S, Wertheimer TB (1998) Comparison between the static implicit and dynamic explicit methods for FEM simulation of sheet forming processes. In: Huétink J, Baaijens FPT (eds) NUMIFORM'98, AA Balkema, Twente
11. Mattiasson K (2000) On Finite Element simulation of sheet metal forming processes in industry. ECCOMAS 2000, Barcelona
12. Makinouchi A (2001) Recent developments in sheet metal forming simulation. In: Mori K (ed) NUMIFORM 2001, AA Balkema, Toyohashi, Japan
13. Wenner M (2005) Overview – Simulation of sheet metal forming. In: Smith LM, Pourboghrat F, Yoon JW, Stoughton TB (eds) NUMISHEET 2005, Detroit, AIP 0-7354-0265-5

14. Banabic D, Tekkaya E (2006) Forming simulation – Numerical simulation and material models of aluminium sheet forming. In: Hirsch J (ed) Virtual fabrication of aluminum products. Microstructural modeling in industrial aluminum production. Wiley-VCH Verlag, Weinheim, 275–302
15. Roll K, Weigand K (2009) Tendencies and new requirements in the simulation of sheet metal forming processes. Computer Methods in Materials Science 9:12–24
16. Malvern LE (1969) Introduction to the mechanics of a continuous medium. Prentice-Hall, Englewood Cliffs, NJ
17. Gurtin ME (1981) An introduction to continuum mechanics. Academic Press, London
18. Zienkiewicz OC, Jain PC, Oñate E (1978) Flow of solids during forming and extrusion: Some aspects of numerical solutions. International Journal of Solids and Structures 14:15–38
19. Baynham JMW, Zienkiewicz OC (1982) Developments in the finite element analysis of thin sheet drawing and direct redrawing processes, using a rigid/plastic approach. In: Pittman JFT et al. (eds) Numerical methods in industrial forming processes. Pineridge Press, Swansea
20. Oñate E, Zienkiewicz OC (1983) A viscous shell formulation for the analysis of thin sheet metal forming. International Journal of Mechanical Sciences 25:305–335
21. Wood RD, Mattiasson K, Honnor ME, Zienkiewicz OC (1985) Viscous flow and solid mechanics approaches to the analysis of thin sheet forming. In: Wang N-M, Tang SC (ed) Proceedings of the Symposium on computer modeling of the sheet forming process – Theory, verification and applications, Ann Arbor. The Metallurgical Society, Warrendale, PA
22. Zienkiewicz OC (1984) Flow formulation for the numerical solution of forming processes. In: Pittman JFT et al. (eds) Numerical analysis of forming processes. Wiley-InterScience, New York, NY
23. Perzyna P (1966) Fundamental problems in viscoplasticity. Recent advances in applied mechanics. Academic Press, New York, NY
24. Osakada K, Nakano J, Mori K (1982) Finite element method for rigid-plastic analysis of metal forming – Formulation for finite deformation. International Journal of Mechanical Sciences 24:459–468
25. Belytschko T, liu wk, Moran B (2000) Nonlinear Finite Elements for continua and Structures. John Wiley & Sons Ltd, Chichester
26. Hibbitt HD, Marcal PV, Rice JR (1970) A finite element formulation for problems of large strain and large displacement. International Journal of Solids and Structures 6:1069–1086
27. McMeeking RM, Rice JR (1975) Finite element formulations for problems of large elastic-plastic deformations. International Journal of Solids and Structures 11:601–616
28. Bathe KJ, Ramm E, Wilson EL (1975) Finite element formulations for large deformation dynamic analysis. International Journal for Numerical Methods in Engineering 9:353–386
29. Wang N-M, Budiansky B (1978) Analysis of sheet metal stamping by finite element method. Journal of Applied Mechanics, Transaction ASME 45:73–82
30. Tang SC, Ilankamban R, Ling P (1988) A finite element modeling of the stretch-draw forming process. SAE Paper 880527
31. Chung WJ, Cho JW, Belytschko T (1998) On the dynamic effects of explicit FEM in sheet metal forming analysis. Engineering Computations 15:750–776
32. Nielsen KB (2000) Sheet metal forming simulation using explicit finite element methods, PhD thesis, Third edition. Department of Production, Aalborg University, Denmark

Chapter 2
Plastic Behaviour of Sheet Metal

List of Special Symbols

a	exponent in the Hershey and Hosford yield criteria
a, b	coefficients in the Hill 1990 yield criterion
a, b, c, f, g, h	material parameters in the Barlat 1991 yield criterion
a, b, c, h, p	coefficients in the Barlat 1989 yield criterion
a, b, m, n, p, q	parameters describing the planar anisotropy of the material in the Ferron yield criterion
a, b, c, d, e, f, g	coefficients in the BBC 2000 yield criterion
$a_{1\ldots}\, a_4$	coefficients in the Cazacu–Barlat yield criteria
$a_{1\ldots}\, a_{25}$	coefficients in the Soare yield criteria
$A_0, \ldots, A_9$	coefficients in the Gotoh yield criterion
$b_1 \ldots b_{11}$	coefficients in the Cazacu–Barlat yield criteria
c	weighting coefficient in the Karafillis–Boyce yield criterion
c, p, q	coefficients in the Hill 1993 yield criterion
c_1, c_2, c_3	material coefficients describing the material anisotropy in the Barlat 1994 yield criterion
$c_{12}, c_{13} \ldots c_{66}$	coefficients in the linear transformation in Barlat 2000 yield criterion
$\boldsymbol{C}$	elasticity tensor
$\boldsymbol{C}', \boldsymbol{C}''$	linear transformations in Barlat 2000 yield criterion
C_D	material constant in the Drucker yield criterion
$\boldsymbol{D}$	strain-rate tensor
E	elastic modulus
f, F, φ	yield function
f, g, h, a, b, c	coefficients in the Hill 1979 yield criterion
F, G, H, L, M, N	coefficients in the Hill 1948 yield criterion
F_1, F_2	functions in the expresion of the uniaxial yield stress (Barlat 1989 yield criterion)
F_b	function used to define the biaxial yield stress and the biaxial anisotropy coefficient

D. Banabic, *Sheet Metal Forming Processes*, DOI 10.1007/978-3-540-88113-1_2,

F_θ	function used to define the uniaxial yield stress and the anisotropy coefficient
$g(\alpha)$	function used to define the Budiansky yield criterion
$g(\theta, \alpha)$	function used to define the Ferron yield criterion
h	scalar parameter which defines the plastic deformation accumulated in the material
h_{ij}	anisotropy coefficients in the von Mises 1928 yield criterion
I_2, I_3	second and third invariants of the stress tensor
J_2, J_3	second and third invariants of the stress tensor
k	exponent in the the Karafillis–Boyce and BBC yield criteria
k_1, k_2	invariants of the stress tensor
l	final gage length
l_0	initial gage length
$\boldsymbol{L}$	linear transformation tensor in the Karafillis–Boyce yield criterion
L, M, N	function in the Comsa yield criterion
M	integer exponent used by the yield criteria
M, N, P, Q, R, S, T	coefficients in the BBC yield criteria
m, n	exponents used by the yield criteria
p	exponent in the generalized Drucker yield criterion
p	accumulated equivalent plastic strain
$p_1 \ldots p_8$	coefficients in the Comsa yield criterion
R	material parameter in the Lin–Ding yield criterion
R	isotropic hardening variable
R, S, T	shear yield stresses in the principal anisotropic directions (Hill 1948)
r, R	normal anisotropy coefficient
r_b	biaxial anisotropy coefficient
r_θ	anisotropy coefficient associated to the direction θ
r_0, r_{45}, r_{90}	anisotropy coefficients at 0, 45 and 90° from the rolling direction
s	exponent in the Lin–Ding yield criterion
$\boldsymbol{s}$	deviatoric stress tensor in Barlat 2000 yield criterion
$\boldsymbol{S}$	IPE stress tensor used by the Karafillis–Boyce yield criterion
$\boldsymbol{S}$	stress deviatoric tensor
S_1, S_2, S_3	principal deviatoric stresses
$S_{11}, S_{22}, S_{33}, S_{12}, S_{23}, S_{31}$	components of the IPE stress tensor used by the Karafillis–Boyce yield criterion
t_0, t	initial and final thickness of the specimen
t_1, t_2	functions in the expresion of the uniaxial anisotropy coefficient (Barlat 1989 yield criterion)
$\boldsymbol{T}$	transformation matrix in Barlat 2000 yield criterion

w	final width of the specimen
w_0	initial width of the specimen
W_f	energy of distortion
W_p	elastic potential energy
W_v	volumetric change energy
$\boldsymbol{X}$	linear transformation stress tensor in Barlat 2000 yield criterion
X, Y, Z	tensile yield stresses in principal anisotropic directions (Hill 1948)
Y	yield stress
Y_θ	uniaxial yield stress in a sample inclined by θ with respect to the rolling direction
Y_b	theoretical biaxial yield stress
α	angle between principal stress σ_1 and rolling direction
α, β, γ	coefficients in the Wang yield criterion
$\alpha = \sigma_2/\sigma_1$	ratio of the principal stresses
$\boldsymbol{\alpha}$	back-stress tensor
$\alpha_1, \alpha_2, \alpha_3$	coefficients in the Barlat 1994 yield criterion
$\alpha_1, \ldots \alpha_8$	coefficients in the Barlat 2000 yield criterion
$\alpha_1, \alpha_2, \gamma_1, \gamma_2, \gamma_3, C$	parameters defining the anisotropy of the material in the Karafillis-Boyce yield criterion
$\alpha_x, \alpha_y, \alpha_z$	coefficients in the Barlat 1994 yield criterion
$\beta, \varphi, \delta, \gamma$	accuracy index of the yield criteria
$\beta_1, \beta_2, \beta_3$	auxiliary coefficients used to define the linear transformation tensor in the Karafillis–Boyce yield criterion
Δr	variation of anisotropy coefficients
ε_e	equivalent (effective) strain
$\varepsilon_1, \varepsilon_2, \varepsilon_3$	principal (logarithmic) strains
$\boldsymbol{\varepsilon}, \boldsymbol{\varepsilon}_\mathrm{e}, \boldsymbol{\varepsilon}_\mathrm{p}$	tensors of total, elastic and plastic strain respectively
Φ	plastic potential
ϕ	invariant homogeneous function
Γ, Ψ, Λ	function in the BBC yield criteria angle between the specimen longitudinal axis and the rolling direction
λ	parameter of the Bézier function used in Vegter's yield criterion
λ	plastic multiplier in the flow rule
μ	Poisson's ratio
$\boldsymbol{\sigma}$	stress tensor
$\sigma_0, \sigma_{45}, \sigma_{90}$	uniaxial yield stress at 0, 45 and 90° from the rolling direction
σ_0	initial yield stress
$\sigma_1, \sigma_2, \sigma_3$	principal stresses
σ_b	equibiaxial yield stress
σ_e	equivalent (effective) stress
σ_k	hardening stress

σ_u	uniaxial yield stress
$\sigma_{11}, \sigma_{22}, \sigma_{33},$ $\sigma_{12}, \sigma_{23}, \sigma_{31}$	components of the actual stress tensor
τ	shear yield stress

In the Sect. 2.8 the summation convention over repeated indices is used. Let $\mathbf{A}$ denote second-order tensor and $\mathbf{B}$ a forth-order tensor. One can define the double contracted tensor product as $\mathbf{A} : \mathbf{A} = A_{ij}A_{ij}$ and $(\mathbf{B} : \mathbf{A})_{ij} = B_{ijkl}A_{kl}$. The norm of $\mathbf{A}$ is $\|\mathbf{A}\| = \sqrt{\mathbf{A} : \mathbf{A}}$ and its direction is $\mathbf{n} = \mathbf{A}/\|\mathbf{A}\|$. The time derivative is $\dot{\mathrm{A}} = d\mathbf{A}/dt$.

2.1 Anisotropy of Sheet Metals

2.1.1 Uniaxial Anisotropy Coefficients

Due to their crystallographic structure and the characteristics of the rolling process, sheet metals generally exhibit a significant anisotropy of mechanical properties. In fact, the rolling process induces a particular anisotropy characterised by the symmetry of the mechanical properties with respect to three orthogonal planes. Such a mechanical behaviour is called orthotropy. The intersection lines of the symmetry planes are the orthotropy axes. In the case of the rolled sheet metals, their orientation is as follows (see Fig. 2.1): rolling direction (RD); transverse direction (TD); normal direction (ND).

The variation of their plastic behavior with direction is assessed by a quantity called Lankford parameter or anisotropy coefficient [1]. This coefficient is determined by uniaxial tensile tests on sheet specimens in the form of a strip. The anisotropy coefficient r is defined by

$$r = \frac{\varepsilon_{22}}{\varepsilon_{33}} \tag{2.1}$$

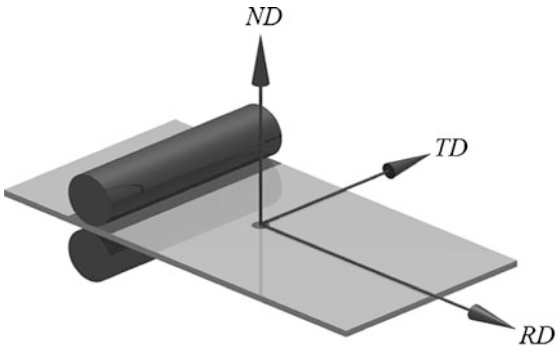

Fig. 2.1 Orthotropy axes of the rolled sheet metals: LD—longitudinal direction; TD—transversal direction; ND—normal direction

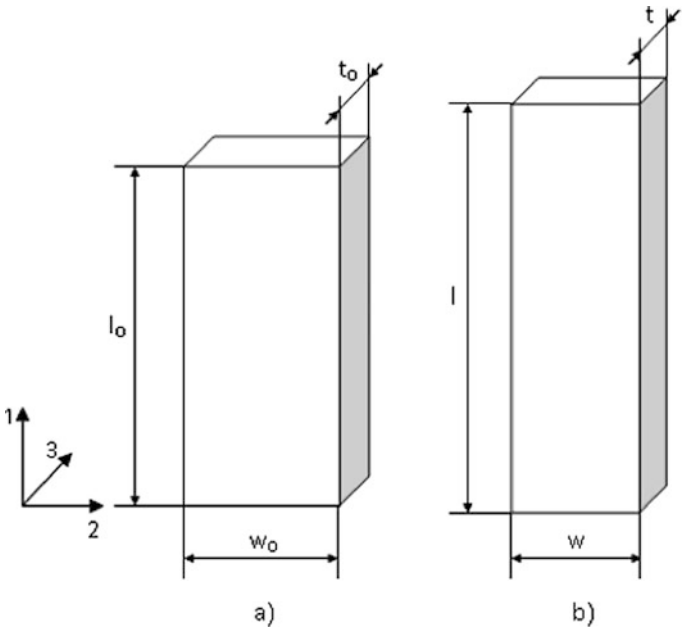

Fig. 2.2 Geometry of the specimen: (**a**) before and (**b**) after deformation

where, $\varepsilon_{22}, \varepsilon_{33}$ are the strains in the width and thickness directions, respectively. In the case of an isotropic material, the coefficient is one and the width and thickness strains have the same value. If the coefficient is greater than one, the width strains will be dominant (the 'thinning resistance' is more pronounced). On the other hand, for the materials having a coefficient less than one, the thickness strains will dominate.

Using the notations from Fig. 2.2, Eq. (2.1) can be written in the form

$$r = \frac{\ln \frac{w}{w_0}}{\ln \frac{t}{t_0}} \tag{2.2}$$

where w_0 and w are the initial and final width, while t_0 and t are the initial and final thickness of the specimen, respectively.

As the thickness of the specimen is very small compared to its width (usually by at least one order), the relative errors of measurement of the two strains will be quite different. Therefore the above relationships are replaced by one implying quantities having the same order of magnitude: length and width of the specimen. Taking into account the condition of volume constancy

$$\varepsilon_{11} + \varepsilon_{22} + \varepsilon_{33} = 0 \tag{2.3}$$

the following form of Eq. (2.1) is obtained

$$r = -\frac{\varepsilon_{22}}{\varepsilon_{11} + \varepsilon_{22}} \tag{2.4}$$

and Eq. (2.2) becomes

$$r = \frac{-\ln \frac{w}{w_0}}{\ln \frac{l}{l_0} + \ln \frac{w}{w_0}} \tag{2.5}$$

where l_0 and l are the initial and final gage length. The length l_0 is specified by standards, see [2]. Equation (2.5) can be rearranged as follows:

$$r = \frac{\ln \frac{w}{w_0}}{\ln \frac{l_0 \cdot w_0}{l \cdot w}}. \tag{2.6}$$

This relationship is used in practice for evaluating the anisotropy coefficient.

Experiments show that r depends on the in-plane direction. If the tensile specimen is cut having its longitudinal axis inclined with the angle θ to the rolling direction, the coefficient r_θ is obtained (see Fig. 2.3). The subscript specifies the angle between the axis of the specimen and the rolling direction.

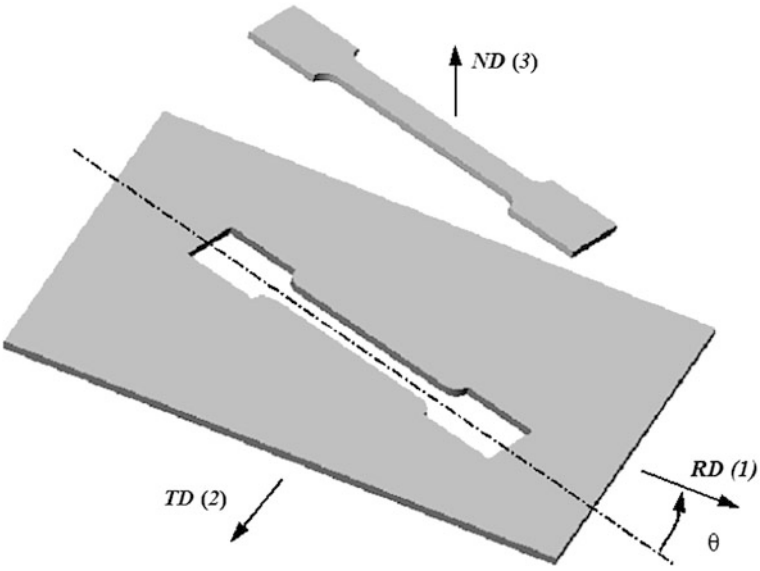

Fig. 2.3 Tensile specimen prelevated at the angle θ (measured from the rolling direction)

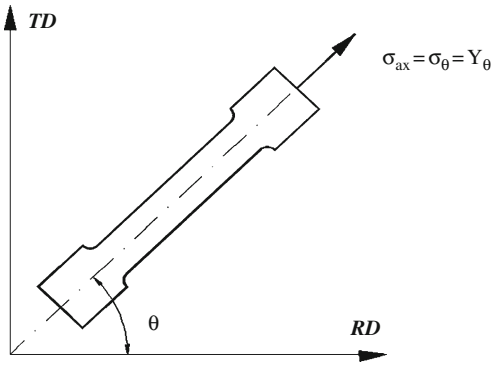

Fig. 2.4 Uniaxial yield stress corresponding to a direction in the plane of the sheet metal

Another important element characterising the performances of a yield criterion is the capability to predict the variations of the uniaxial yield stress and coefficient of plastic anisotropy in the plane of the sheet metal.

In order to assess this capability, we shall establish the relationships defining the dependence of the parameters mentioned above on the angle θ measured from the rolling direction (Fig. 2.4).

Let us denote by Y_θ the uniaxial yield stress corresponding to the direction inclined at the angle θ with respect to the rolling direction. In the case of a uniaxial load, the components of the stress tensor can be expressed as follows:

$$\begin{aligned} \sigma_{11} &= Y_\theta \cos^2\theta; \\ \sigma_{22} &= Y_\theta \sin^2\theta; \\ \sigma_{21} &= \sigma_{12} = Y_\theta \sin\theta\cos\theta \end{aligned} \tag{2.7}$$

By replacing Eq. (2.7) in the relationship defining the equivalent stress and taking into account its homogeneity, we obtain:

$$\sigma = Y_\theta \cdot F_\theta, \tag{2.8}$$

where F_θ is a function depending on the angle θ. Of course, F_θ is defined according to the specific formulation of the equivalent stress. If we combine Eq. (2.8) with the coherence condition,

$$\Phi(\sigma, Y) := \sigma - Y(h) = 0, \tag{2.9}$$

where $\Phi(\sigma, Y)$ is the yield function associated to the yield criterion, Y—yield stress, h—scalar parameter defining the plastic strain accumulated by the material, we get:

$$Y_\theta = \frac{Y(h)}{F_\theta}. \tag{2.10}$$

Equation (2.10) defines the uniaxial yield stress corresponding to the planar direction identified by the angle θ. If the reference yield stress is selected to be the one corresponding to the rolling direction ($Y(h) = Y_0$), we obtain the following relationship:

$$Y_\theta = \frac{Y_0}{F_\theta}. \tag{2.11}$$

In this case, the yield stress corresponding to some planar direction will depend only on the yield stress associated to the rolling direction and the function F_θ (which is related to the yield criterion adopted in the model). The determination of the function F_θ will be presented in the next subchapters, for each type of yield criterion.

In a similar way, we can establish the relationship defining the variation of the coefficient of plastic anisotropy in the plane of the sheet metal. Let us consider the specimen inclined at the angle θ with respect to the rolling direction (Fig. 2.4). According to Eq. (2.1), the instantaneous coefficient of plastic anisotropy r_θ is defined as the ratio of the plastic strain rates associated to the width (inclined at the angle θ+90° with respect to the rolling direction), $\dot{\varepsilon}_{\theta+90}$, and thickness, $\dot{\varepsilon}_{33}$:

$$r_\theta = \frac{\dot{\varepsilon}_{\theta+90}}{\dot{\varepsilon}_{33}} \tag{2.12}$$

Taking into account the incompressibility restraint (see Eq. 2.3), as well as the expressions of the strain rate components along the principal directions,

$$\begin{aligned} &\dot{\varepsilon}_\theta = \dot{\varepsilon}_{11}\cos^2\theta + \dot{\varepsilon}_{22}\sin^2\theta + \dot{\varepsilon}_{12}\sin\theta\cos\theta, \\ &\dot{\varepsilon}_{33} = -(\dot{\varepsilon}_{11} - \dot{\varepsilon}_{22}). \end{aligned} \tag{2.13}$$

we obtain the relationship defining the coefficient of plastic anisotropy associated to the direction θ:

$$r_\theta = \frac{\dot{\varepsilon}_{11}\cos^2\theta + \dot{\varepsilon}_{22}\sin^2\theta + \dot{\varepsilon}_{12}\sin\theta\cos\theta}{\dot{\varepsilon}_{11} + \dot{\varepsilon}_{22}} - 1. \tag{2.14}$$

Equation (2.14) can be rewritten in terms of the stress components if the associated flow rule is used:

$$r_\theta = \frac{\sigma_{11}\dfrac{\partial\sigma}{\partial\sigma_{11}} + \sigma_{22}\dfrac{\partial\sigma}{\partial\sigma_{22}} + \sigma_{12}\dfrac{\partial\sigma}{\partial\sigma_{12}}}{\sigma_{11}\dfrac{\partial\sigma}{\partial\sigma_{11}} + \sigma_{22}\dfrac{\partial\sigma}{\partial\sigma_{22}}} - 1. \tag{2.15}$$

By coupling Eq. (2.15) with Euler's identity, we obtain:

$$r_\theta = \frac{\sigma}{Y_\theta\left(\dfrac{\partial\sigma}{\partial\sigma_{11}} + \dfrac{\partial\sigma}{\partial\sigma_{22}}\right)} - 1. \tag{2.16}$$

Finally, after replacing Eq. (2.8) in the last relationship, we get:

$$r_\theta = \frac{F_\theta}{\frac{\partial \sigma}{\partial \sigma_{11}} + \frac{\partial \sigma}{\partial \sigma_{22}}} - 1. \tag{2.17}$$

This formula defines the coefficient of plastic anisotropy as a dependence of the specimen inclination. In order to make use of it, we need the expression of the equivalent stress and the function F_θ, both of them being specific to the yield criterion adopted in the plasticity model. The planar distribution of the coefficient of plastic anisotropy will be determined in the next subchapters, for different yield criteria.

The average of the *r*-values obtained for different directions in the plane of the sheet metal represents the so-called coefficient of normal anisotropy r_n. Having determined the values of *r* at specimens cut along three directions in the plane of the sheet metal (0°, 45°, 90°, respectively), the coefficient of normal anisotropy is determined by:

$$r_n = \frac{r_0 + 2r_{45} + r_{90}}{4}. \tag{2.18}$$

A measure of the variation of normal anisotropy with the angle to the rolling direction is given by the quantity:

$$\Delta r = \frac{r_0 + r_{90} - 2r_{45}}{2}, \tag{2.19}$$

known as planar anisotropy.

This quantity is related to the earring amplitude of the deep-drawn cups. More precisely, if the value of the anisotropy coefficient is the same along all the directions in the plane of the sheet metal, the earring phenomenon will not be observed. In order to get a more intuitive image of the planar anisotropy of sheet metals, a polar coordinate representation is frequently used. The diagram in Fig. 2.5 [3] gives such a representation for an aluminium alloy (AA5182-0). The polar diagrams are preferred due to their capability to offer direct information on the tendency of the sheet metal to form ears. One may notice the symmetry of the curve with respect to the coordinate axes. This fact is a proof of the orthotropic behaviour of the sheet metal.

By convention the *r*-values usually are determined at 20% elongation for the purpose of comparison. Modern tensile testing machines perform instantaneous measurement of the quantities required for evaluating the anisotropy coefficient and calculate it during the test. Values of *r* at 20% elongation as well as its variation with strain can be determined.

Figure 2.6 [4] shows the planar variation of the anisotropy coefficient for DDQ mild steel at different straining degrees. One may notice a significant variation of the r_{45} coefficient with respect to the straining degree.

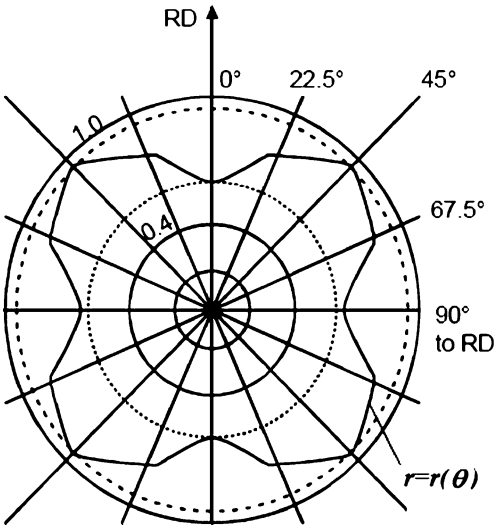

Fig. 2.5 Variation of the anisotropy coefficient in the plane of the sheet metal [3]

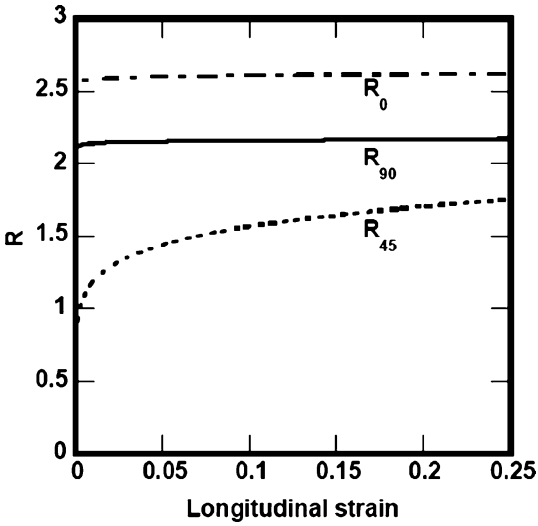

Fig. 2.6 Variation of the anisotropy coefficients with respect to the straining degree [4]

2.1.2 Biaxial Anisotropy Coefficient

The experimental research has proved that the yield surfaces are not symmetric in the biaxial region [5, 6]. This fact is also a consequence of the plastic anisotropy. In order to give a quantitative description of such a behaviour, the so-called coefficient of biaxial anisotropy has been defined independently by Barlat et al. [5] and Poehlandt et al. [7]. Barlat and his co-workers [5] have proposed the use of

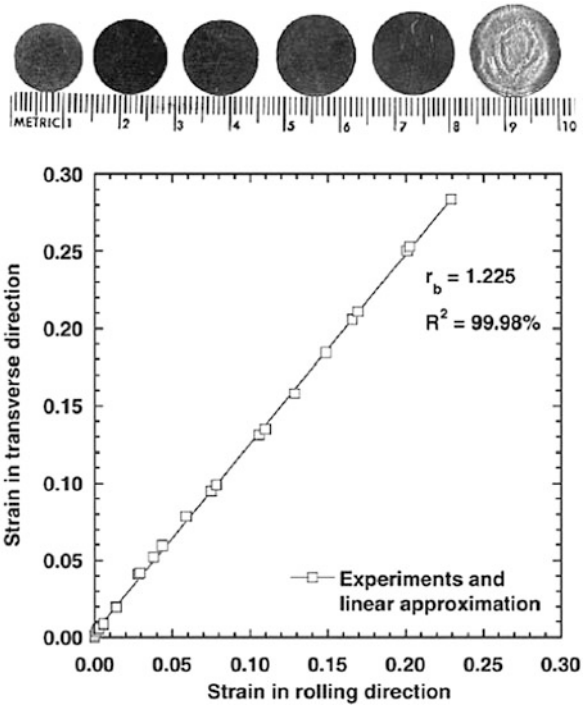

Fig. 2.7 Strains measured on the specimen during the disk compression test [5]

a compression test for the experimental determination of this mechanical parameter. A set of circular specimens are subjected to a normal pressure. Due to the plastic anisotropy, the discs become elliptic during the compression. The phenomenon can be observed in Fig. 2.7 [5], showing the results of a compression test for an AA6111-T4 aluminium alloy. By measuring the major and minor axes of the elliptic specimen, the corresponding principal strains can be evaluated.

As in the case of the uniaxial tension, the ratio of the principal strains will define the coefficient of biaxial anisotropy:

$$r_b = \frac{\varepsilon_{22}}{\varepsilon_{11}} \tag{2.20}$$

If the material is isotropic, the coefficient will be one. The more pronounced is the anisotropy, the farther is the coefficient from unity. This parameter is a direct measure of the slope of the yield locus at the balanced biaxial stress state. Pöhlandt et al. [7] have proposed to use the biaxial tensile testing machine to determine the coefficient.

Figure 2.8 shows the method used for the determination of the principal strains on a biaxial testing machine. This experimental procedure is limited by the fact that the straining degree is rather small (less than 5%).

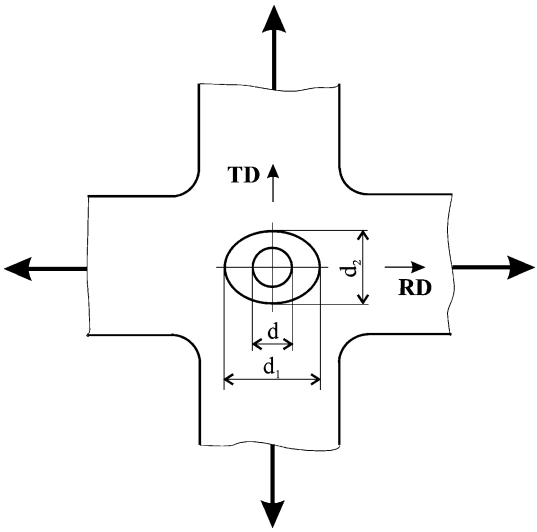

Fig. 2.8 Strains measured on the cross specimen during the biaxial tensile test [7]

As for the uniaxial coefficient of plastic anisotropy, we shall define a general relationship defining the biaxial coefficient. The relationship will be usable for any yield criterion.

In the case of biaxial tension along the rolling and transverse directions, Eqs. (2.7) will get the following particular forms:

$$\begin{aligned} \sigma_{11} &= \sigma_{22} = Y_b; \\ \sigma_{21} &= \sigma_{12} = 0. \end{aligned} \tag{2.21}$$

where, Y_b is the theoretical biaxial yield stress.

Consequently, Eq. (2.8) becomes:

$$\sigma_b = Y_b \cdot F_b, \tag{2.22}$$

Here, σ_b stands for the experimental biaxial yield stress, while F_b is a constant quantity depending on the yield criterion adopted in the plasticity model.

Equation (2.22) provides the theoretical biaxial yield stress as a dependence of the the experimental biaxial yield stress and the parameter F_b:

$$Y_b = \frac{\sigma_b}{F_b}. \tag{2.23}$$

In a very close analogy with the case of the uniaxial coefficient of plastic anisotropy (see Eqs. 2.12, 2.13, 2.14, 2.15, 2.16, and 2.17), one may deduce the relationship defining the coefficient of biaxial plastic anisotropy:

$$r_b = \frac{F_b}{\frac{\partial \sigma}{\partial \sigma_{11}}} - 1. \tag{2.24}$$

This relationship involves only the parameter F_b and the expression of the equivalent stress, both of them being specific to the yield criterion adopted in the plasticity model. The determination of the biaxial coefficient of anisotropy will be presented in the next subchapters, for different yield criteria.

2.2 Yield Criteria for Isotropic Materials

In this section the focus is on the conditions under which a material passes from the elastic to the plastic state and on the associated flow rules. In order to describe the plastic behavior of a material in a general stress state, three elements are needed:

a) a yield criterion expressing a relationship between the stress components at the moment when plastic 'yielding' occurs
b) an associated flow rule expressing the relationship between the components of the strain-rate and stress
c) a hardening rule describing the evolution of the initial yield stress during the forming process.

The transition from the elastic to the plastic state occurs when the stress reaches the yield point of the material. The yield point in uniaxial tension is established using the stress-strain curve of the material whereby a convention is necessary in order to define it, or by temperature measurement.

In case of a multiaxial stress state it is more difficult to define a criterion for the transition from the elastic to the plastic state. A relationship between the principal stresses is needed specifying the conditions under which plastic flow occurs. Such a relationship is usually defined in the form of an implicit function (known as the 'yield function'):

$$F(\sigma_1, \sigma_2, \sigma_3, Y) = 0 \tag{2.25}$$

where σ_1, σ_2, σ_3 are the principal stresses and Y is the yield stress obtained from a simple test (tension, compression or shearing).

Equation (2.25) can be interpreted as the mathematical description of a surface in the three dimensional space of the principal stresses usually called the 'yield surface'. It must be *closed, smooth* and *convex*. For incompressible materials it is a cylinder the cross section of which depends on the material (only for the von Mises criterion—see below—it is a *circular* cylinder as shown in Fig. 2.9).

All the points located in the inside of the surface ($F < 0$) are related to an elastic state of the material. The points belonging to the surface ($F = 0$) are related to a plastic state. The points located outside the surface ($F > 0$) have no physical meaning.

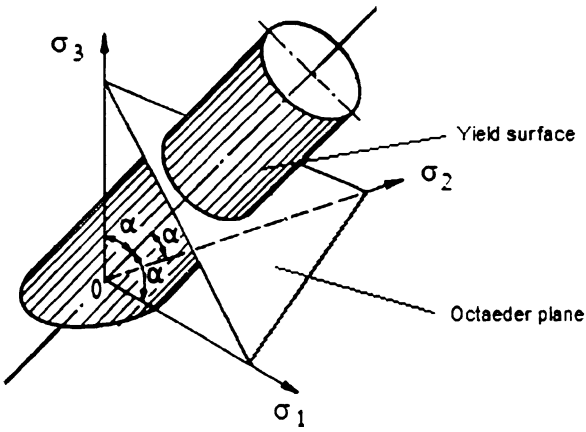

Fig. 2.9 von Mises yield surface in the stress space

In the case of plane stress (e.g. $\sigma_3 = 0$) the yield surface reduces to a curve in the plane of the principal stresses σ_1 and σ_2.

The expression of the yield function is established on the basis of some phenomenological considerations concerning the transition from the elastic to the plastic state.

The most widely used yield criteria for isotropic materials have been proposed by Tresca (the 'maximum shear stress criterion') and Huber–von Mises (the 'strain energy criterion') [8].

Basically the yield function may be defined in two different ways [9]: either by assuming that plastic yield begins when some physical quantity (energy, stress, etc.) attains a critical value or by approximating experimental data by an analytical function.

The latter class of yield functions are *not* obtained from a calculus based on the crystallographic structure of the material; they are purely phenomenological functions. The advantages of using such phenomenological yield functions instead of those based on the crystallographic texture are [10]:

- they usually have a simpler mathematical form
- they are easy to understand and manipulate ('user-friendly')
- they may be easily implemented in finite element codes
- they may be generalized to describe the anisotropic behavior of the materials
- they may also be easily adapted to describe the behavior of fcc instead of bcc materials (for example, by simply changing the exponent of the Hershey family yield criteria).

The main disadvantage of the phenomenological approach is the poor accuracy under multi-axial and non-proportional loading conditions.

2.2.1 Tresca Yield Criterion

The oldest yield criterion was proposed by Tresca in 1864 [11] on the basis of his observation that plastic strains appear by crystallographic gliding under acting shear stresses.

According to this criterion the material passes from an elastic to a plastic state when the maximum shear stress τ_{max} reaches a critical value.

In the general case, the criterion may be written as follows:

$$\max\left\{|\sigma_1 - \sigma_2|, |\sigma_2 - \sigma_3|, |\sigma_3 - \sigma_1|\right\} = \sigma_0 \tag{2.26}$$

where σ_1, σ_2 and σ_3 are principal stresses.

Under plane stress condition ($\sigma_3 = 0$), Eq. (2.26) becomes

$$\sigma_1 - \sigma_2 = \sigma_0 = 2K; \quad \sigma_1 > \sigma_2 \tag{2.27}$$

$$\sigma_2 - \sigma_1 = \sigma_0 = 2K; \quad \sigma_1 < \sigma_2 \tag{2.28}$$

Equations (2.27) and (2.28) can be unified:

$$\sigma_1 - \sigma_2 = \pm\sigma_0 = \pm 2K; \tag{2.29}$$

Equation (2.29) represents a polygon in the plane of the principal stresses σ_1 and σ_2 and a hexagonal prism in the space, see Fig. 2.10.

By squaring Eq. (2.29) it is obtained

$$(\sigma_1 - \sigma_2)^2 = \sigma_0^2 \tag{2.30}$$

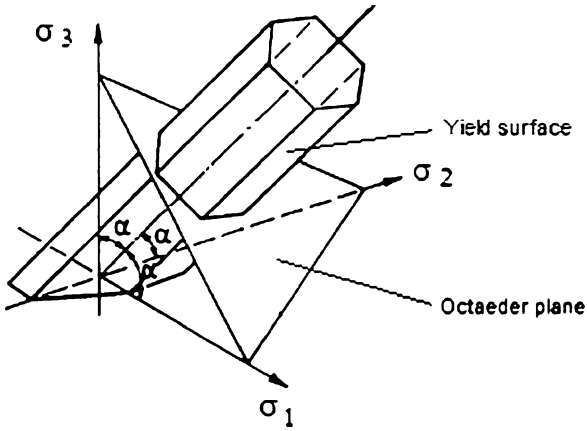

Fig. 2.10 Tresca yield surface in the stress space

In the case when the stress components σ_{11} and σ_{22} do not coincide with the principal stresses, the latter takes the following form:

$$(\sigma_{11} - \sigma_{22})^2 + 4\sigma_{12}^2 = \sigma_0^2 \tag{2.31}$$

2.2.2 Huber–Mises–Hencky Yield Criterion

This criterion was proposed independently by Huber [12] and von Mises [13] and further developed by Hencky [14]. It is based on the observation that a hydrostatic pressure cannot cause plastic yielding of the material. Thus, the conclusion that only the elastic energy of distortion influences the transition from an elastic to a plastic state comes naturally. This idea has been proposed first by Maxwell in a letter to Thomson [15] but it was not published at the time. For simplicity, in the following text the criterion will often be referred to as the Mises criterion.

This criterion can be formulated as follows: the material passes from an elastic to a plastic state when the elastic energy of distortion reaches a critical value that is independent of the type of the stress state.

The elastic potential energy, W_p, has two components: the volumetric change energy W_v and the energy of distortion, W_f.

$$W_p = W_v + W_f \tag{2.32}$$

Thus W_f can be written in the form

$$W_f = W_p - W_v \tag{2.33}$$

After replacing the expressions of the elastic potential energy and energy of distortion in Eq. (2.33), it is obtained

$$W_f = \frac{1+\mu}{6E} \cdot \left[(\sigma_1 - \sigma_2)^2 + (\sigma_2 - \sigma_3)^2 + (\sigma_3 - \sigma_1)^2\right] \tag{2.34}$$

In the case of uniaxial tension ($\sigma_2 = \sigma_3 = 0$) yielding of the material occurs if $\sigma_1 = \sigma_0$, where σ_0 is the uniaxial yield stress in direction 1. Thus, the critical value of the elastic energy of distortion at which the material passes from an elastic to the plastic state is:

$$W_f = \frac{1+\mu}{6E} 2\sigma_0^2 \tag{2.35}$$

Then the Mises criterion may be written in the form:

$$\frac{1+\mu}{6E} 2\sigma_0^2 = \frac{1+\mu}{6E}\left[(\sigma_1 - \sigma_2)^2 + (\sigma_2 - \sigma_3)^2 + (\sigma_3 - \sigma_1)^2\right], \tag{2.36}$$

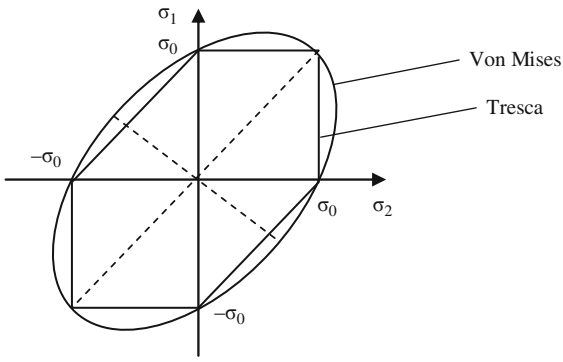

Fig. 2.11 Graphical representation of the Tresca and von Mises yield criteria

or

$$(\sigma_1 - \sigma_2)^2 + (\sigma_2 - \sigma_3)^2 + (\sigma_3 - \sigma_1)^2 = 2\sigma_0^2 \tag{2.37}$$

For plane stress ($\sigma_3 = 0$) Eq. (2.37) becomes

$$(\sigma_1 - \sigma_2)^2 + \sigma_1^2 + \sigma_2^2 = 2\sigma_0^2 \tag{2.38}$$

rewritten in the form

$$\sigma_1^2 + \sigma_2^2 - \sigma_1 \cdot \sigma_2 = \sigma_0^2 \tag{2.39}$$

Another equivalent of the Mises criterion is

$$3\left(\frac{\sigma_1 - \sigma_2}{\sigma_0}\right)^2 + \left(\frac{\sigma_1 + \sigma_2}{\sigma_0}\right)^2 = 4 \tag{2.40}$$

Equations (2.39) and (2.40) represent an ellipse in the plane of the principal stresses σ_1–σ_2 which is circumscribed to the polygon given by Tresca criterion, see Fig. 2.11.

2.2.3 Drucker Yield Criterion

In order to represent the experimental data located between the Tresca and Mises yield surfaces, Drucker [16] proposed the following criterion:

$$J_2^3 - C_D J_3^2 = F \tag{2.41}$$

where J_2 and J_3 are the second and third invariants of the stress tensor, respectively, and C_D is a constant.

Equation (2.41) may be generalized in the form

$$J_2^{3p} - C_D J_3^{2p} = F \tag{2.42}$$

p being an integer.

2.2.4 Hershey Yield Criterion

Based on the Norton [17] and Bailey [18] laws used for non-linear creep, Hershey introduced a non-quadratic formulation of the yield criterion [19]

$$(\sigma_1 - \sigma_2)^a + (\sigma_2 - \sigma_3)^a + (\sigma_3 - \sigma_1)^a = 2Y^a \tag{2.43}$$

Here Y is the uniaxial yield stress and a is an exponent determined based on the crystallographic structure of the material. For $a = 2$, Eq. (2.43) reduces to the Mises yield condition, whereas for $a = 1$ and in the limit case $a \to \infty$ it leads to the Tresca yield condition. For $2 < a < 4$, the corresponding surface lies outside the Mises circular cylinder, whereas for $1 < a < 2$ and for $a > 4$, it lies between Mises and Tresca. The Hershey formulation has been used later (1972) by Hosford [20].

The Hershey's formulation has been generalized by Karafillis and Boyce [21] in the following form

$$\Phi = (1 - c)\,\Phi_1 - c\Phi_2, \tag{2.44}$$

where

$$\Phi_1 = |S_1 - S_2|^{2k} + |S_2 - S_3|^{2k} + |S_3 - S_1|^{2k} = 2\sigma_e^{2k} \tag{2.45}$$

and

$$\Phi_2 = |S_1|^{2k} + |S_2|^{2k} + |S_3|^{2k} = \frac{2^{2k} + 2}{3^{2k}}\sigma_e^{2k} \tag{2.46}$$

Here S_1, S_2, and S_3 are the principal deviatoric stresses, c is a weighting coefficient, and $2k$ is an exponent having the same significance as the exponent a in Hosford's criterion.

For $k = 1$ the Eqs. (2.45) and (2.46) take the form given by von Mises, however, for $k = \infty$ Eq. (2.45) becomes the Tresca function and (2.46) gives an upper limit of the yield surface.

The value of the coefficient c is in the range [0, 1]. It determines the weight of the functions Φ_1 and Φ_2 in the yield function Φ. As a consequence, there are two parameters k and c that may be used in order to 'adjust' the shape of the yield locus whereas the other criteria use only one parameter (exponent a or m) for this purpose. Therefore the new criterion is very flexible.

More examples of isotropic yield functions are reviewed by Życzkowski [9] and Yu [22].

2.3 Classical Yield Criteria for Anisotropic Materials

The first yield criterion for anisotropic materials was proposed by von Mises in the form of a quadratic function [23]. Though it was initially used for describing the plastic behavior of an anisotropic single crystal, later it was also used for polycrystals.

This criterion is given by

$$\begin{aligned}\Phi = {} & h_{11}\sigma_{11}^2 + h_{22}\sigma_{22}^2 + h_{33}\sigma_{33}^2 + h_{44}\sigma_{12}^2 + h_{55}\sigma_{23}^2 + h_{66}\sigma_{31}^2 + 2h_{12}\sigma_{11}\sigma_{22} + \\ & 2h_{13}\sigma_{11}\sigma_{33} + 2h_{14}\sigma_{11}\sigma_{12} + 2h_{15}\sigma_{11}\sigma_{23} + 2h_{16}\sigma_{11}\sigma_{31} + 2h_{23}\sigma_{22}\sigma_{33} + \\ & 2h_{24}\sigma_{22}\sigma_{12} + 2h_{25}\sigma_{22}\sigma_{23} + 2h_{26}\sigma_{22}\sigma_{31} + 2h_{34}\sigma_{33}\sigma_{12} + 2h_{35}\sigma_{33}\sigma_{23} + \\ & 2h_{36}\sigma_{33}\sigma_{31} + 2h_{45}\sigma_{12}\sigma_{12} + 2h_{46}\sigma_{12}\sigma_{31} + 2h_{56}\sigma_{23}\sigma_{31}\end{aligned} \tag{2.47}$$

where h_{ij} ($i, j = 1, 2, \ldots, 6$) are coefficients of anisotropy which can be identified by mechanical tests. Equation (2.47) gives a quadratic function containing products implying both normal and shear stresses.

Olszak [24] gave a generalization of this function for non-homogeneous anisotropic materials. In the case of an orthotropic material, it can be reduced to a quadratic function having only six terms and coefficients of anisotropy. This is the same as the function proposed by Hill in 1948 [25].

2.3.1 Hill's Familly Yield Criteria

2.3.1.1 Hill 1948 Yield Criterion

In 1948 Hill [25] proposed an anisotropic yield criterion as a generalization of the Huber-Mises-Hencky criterion. The material is supposed to have an anisotropy with three orthogonal symmetry planes.

The yield criterion is expressed by a quadratic function of the following type:

$$\begin{aligned}2f\left(\sigma_{ij}\right) \equiv {} & F\left(\sigma_{22} - \sigma_{33}\right)^2 + G\left(\sigma_{33} - \sigma_{11}\right)^2 + H\left(\sigma_{11} - \sigma_{22}\right)^2 \\ & + 2L\sigma_{23}^2 + 2M\sigma_{31}^2 + 2N\sigma_{12}^2 = 1,\end{aligned} \tag{2.48}$$

Here f is the yield function; F, G, H, L, M and N are constants specific to the anisotropy state of the material, and x, y, z are the principal anisotropic axes.

In the case of sheet metals, axis 1 is usually parallel to the rolling direction, 2 is parallel to the transverse direction and 3 is collinear with the normal direction.

If the tensile yield stresses in the principal anisotropy directions are denoted by X, Y and Z it can easily be shown that

$$\frac{1}{X^2} = G + H; \quad \frac{1}{Y^2} = H + F; \quad \frac{1}{Z^2} = F + G \tag{2.49}$$

From this equation, by some simple mathematical calculations the coefficients F, G and H are obtained as functions of the uniaxial yield stresses:

$$2F = \frac{1}{Y^2} + \frac{1}{Z^2} - \frac{1}{X^2}; \quad 2G = \frac{1}{Z^2} + \frac{1}{X^2} - \frac{1}{Y^2}; \quad 2H = \frac{1}{X^2} + \frac{1}{Y^2} - \frac{1}{Z^2}. \tag{2.50}$$

If *R, S* and *T* are the shear yield stresses associated to the same directions, then

$$2L = \frac{1}{R^2}, 2M = \frac{1}{S^2}, 2N = \frac{1}{T^2}. \tag{2.51}$$

Only one of the parameters *F, G, H* can be negative. This situation rarely occurs in practice (it would cause great differences between the stresses); $F > G$ if and only if $X > Y$, etc. *L, M* and *N* are always positive.

As a consequence, in order to give a complete description of the anisotropy of the material, six independent yield stresses (*X, Y, Z, R, S* and *T*) have to be known as well as the orientation of the principal anisotropy axes.

The yield criterion may be interpreted as a surface in a six-dimensional space of the stress components. The points located at the interior of the surface represent the elastic states of the material, while points belonging to the surface correspond to the plastic state.

For plane stress ($\sigma_{33} = \sigma_{31} = \sigma_{23} = 0; \sigma_{11} \neq 0; \sigma_{22} \neq 0; \sigma_{12} \neq 0$), the yield criterion becomes

$$2f\left(\sigma_{ij}\right) \equiv (G+H)\,\sigma_{11}^2 - 2H\sigma_{11}\sigma_{22} + (H+F)\,\sigma_{22}^2 + 2N\sigma_{12}^2 = 1. \tag{2.52}$$

After introducing the yield stress *X, Y, Z* and *T*, Eq. (2.52) may be rewritten as

$$\frac{1}{X^2}\sigma_{11}^2 - \left(\frac{1}{X^2} + \frac{1}{Y^2} - \frac{1}{Z^2}\right)\sigma_{11}\sigma_{22} + \frac{1}{Y^2}\sigma_{22}^2 + \frac{1}{T^2}\sigma_{12}^2 = 1, \tag{2.53}$$

When the principal directions of the stress tensor coincide with the principal anisotropic axes, the Hill 1948 yield criterion has the form

$$\frac{1}{X^2}\sigma_1^2 - \left(\frac{1}{X^2} + \frac{1}{Y^2} - \frac{1}{Z^2}\right)\sigma_1\sigma_2 + \frac{1}{Y^2}\sigma_2^2 = 1, \tag{2.54}$$

where σ_1, σ_2 are the non-zero principal stresses.

When simulating sheet metal forming processes, the anisotropy coefficients are denoted (r_0, r_{45}, r_{90}) and the yield stresses in the directions of the principal anisotropic axes are denoted as follows: $X = \sigma_0$, $Y = \sigma_{90}$. The relations between the anisotropy coefficients and the coefficients *F, G, H*,... may be easily obtained from the flow rule associated to the yield function:

$$r_0 = \frac{H}{G}; \quad r_{90} = \frac{H}{F}; \quad r_{45} = \frac{N}{F+G} - \frac{1}{2}. \tag{2.55}$$

It can be shown that the following relation between the yield stresses and the anisotropy coefficients applies:

$$\frac{\sigma_0}{\sigma_{90}} = \sqrt{\frac{r_0\,(1+r_{90})}{r_{90}\,(1+r_0)}} \tag{2.56}$$

This equation implies that from $r_0 > r_{90}$ it follows $\sigma_0 > \sigma_{90}$ and the reciprocal, however, some materials do not satisfy this condition.

The last of the three Eqs. (2.55) leads to

$$N = (F+G)\left(r_{45} + \frac{1}{2}\right) \tag{2.57}$$

or, according to Eq. (2.57),

$$2N = \frac{1}{Z^2}\frac{2r_{45}+1}{2} = \frac{1}{\sigma_0^2}\frac{r_0 + r_{90}}{r_{90}\,(1+r_0)}\,(2r_{45}+1)\,. \tag{2.58}$$

Finally it is obtained

$$\begin{aligned}\frac{1}{\sigma_0^2}\sigma_{11}^2 - \left(\frac{1}{\sigma_0^2} + \frac{1}{\sigma_{90}^2} - \frac{1}{\sigma_0^2}\frac{r_0+r_{90}}{r_{90}\,(1+r_0)}\right)\sigma_{11}\sigma_{22} + \frac{1}{r_{90}^2}\sigma_{22}^2 + \\ + \frac{1}{\sigma_0^2}\frac{r_0+r_{90}}{r_{90}\,(1+r_0)}\,(2r_{45}+1)\,\sigma_{12}^2 = 1\end{aligned} \tag{2.59}$$

As σ_0 and σ_{90} are not independent, but related by (2.57), Eq. (2.59) may also be written as

$$\sigma_{11}^2 - \frac{2r_0}{1+r_0}\sigma_{11}\sigma_{22} + \frac{r_0(1+r_{90})}{r_{90}\,(1+r_0)}\sigma_{22}^2 + \frac{r_0+r_{90}}{r_{90}\,(1+r_0)}\,(2r_{45}+1)\,\sigma_{12}^2 = \sigma_0^2 \tag{2.60}$$

In case that the principal directions of the stress tensor are coincident with the anisotropic axes ($\sigma_{11} = \sigma_1$, $\sigma_{22} = \sigma_2$, $\sigma_{12} = 0$), the Hill 1948 yield criterion can be written as a dependence of the principal stress in the form

$$\sigma_1^2 - \frac{2r_0}{1+r_0}\sigma_1\sigma_2 + \frac{r_0(1+r_{90})}{r_{90}\,(1+r_0)}\sigma_2^2 = \sigma_0^2 \tag{2.61}$$

or, taking into account Eq. (2.56)

$$\sigma_1^2 - \frac{2r_0}{1+r_0}\sigma_1\sigma_2 + \frac{r_0(1+r_{90})}{r_{90}\,(1+r_0)}\sigma_2^2 = \frac{r_0(1+r_{90})}{r_{90}\,(1+r_0)}\sigma_{90}^2. \tag{2.62}$$

From Eqs. (2.61) and (2.62) it follows that in order to define the yield under plane stress condition, three mechanical parameters, namely the coefficients r_0 and r_{90} and one of the uniaxial yield stresses σ_0 and σ_{90} are needed.

Equations (2.61) or (2.62) geometrically represent families of ellipses depending on the parameters r_0 and r_{90}. The influence of these parameters upon the yield loci is demonstrated in Figs. 2.12 and 2.13.

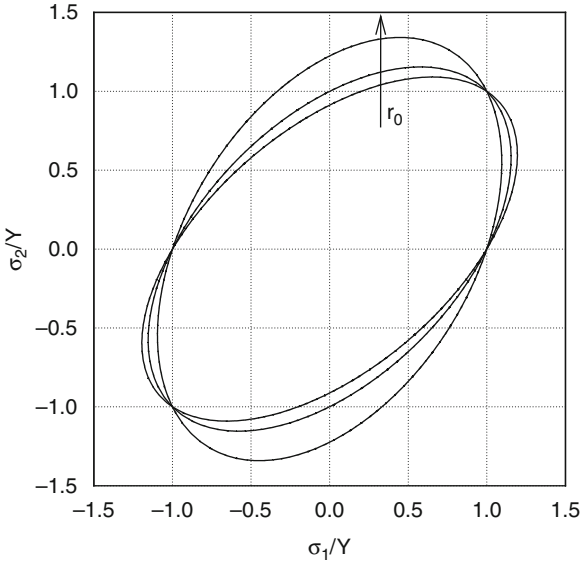

Fig. 2.12 Influence of the r_0 anisotropy coefficient upon the shape of the yield locus defined by the Hill 1948 criterion

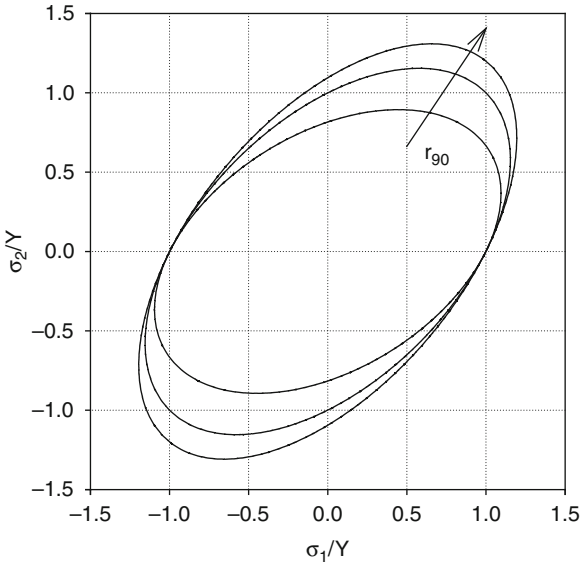

Fig. 2.13 Influence of the r_{90} anisotropy coefficient upon the shape of the yield locus defined by the Hill 1948 criterion

In case of a material exhibiting only normal anisotropy ($r_0 = r_{90} = r$) Eq. (2.56) imposes that $\sigma_0 = \sigma_{90}$ and Eqs. (2.61) and (2.62) take the same form:

$$\sigma_1^2 - \frac{2r}{1+r}\sigma_1\sigma_2 + \sigma_2^2 = \sigma_u^2 \tag{2.63}$$

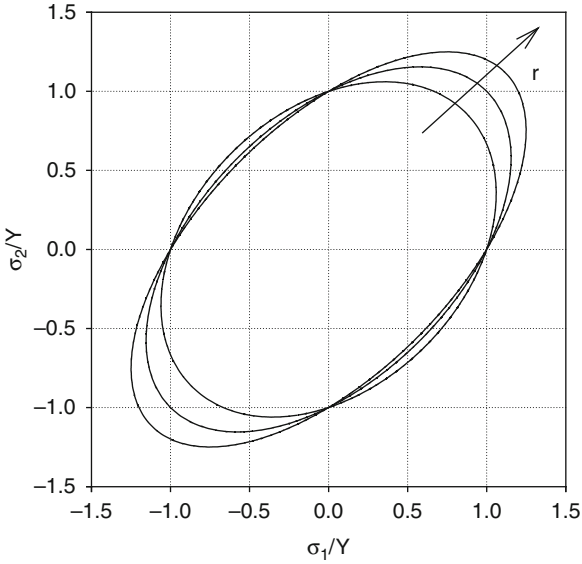

Fig 2.14 Influence of the normal anisotropic coefficient on the shape of the yield locus defined by the Hill 1948 criterion

where σ_u is the uniaxial yield stress.

The influence of the parameters r and σ_u upon the shape of the yield locus is shown in Figs. 2.14 and 2.15.

It can be seen that if $r < 1$, the yield locus predicted by the Hill 1948 criterion is located inside the one given by von Mises; if $r > 1$ the Hill 1948 yield locus is outside the von Mises yield locus. Woodthrope and Pearce [26] and Pearce [27] noticed that some materials (in particular aluminum alloys) have the yield locus outside the von Mises surface though their r-coefficient was less than one.

This behavior cannot be properly described by the Hill 1948 yield criterion and materials exhibiting it are called 'anomalous'.

Indeed, by rewriting Eq. (2.63) for the case of the equibiaxial tension ($\sigma_1 = \sigma_2 = \sigma_b$) one obtains

$$\sigma_b = \sigma_u \sqrt{\frac{1+r}{2}}, \tag{2.64}$$

where σ_b is the equibiaxial yield stress.

It follows that if $r > 1$, then $\sigma_b > \sigma_u$ and if $r < 1$ then $\sigma_b < \sigma_u$. This problem will be considered again below.

It can be seen from Fig. 2.15 that if the uniaxial yield stress increases, the yield surface expands uniformly. This is called isotropic hardening.

Equation (2.63) may be rewritten in the form

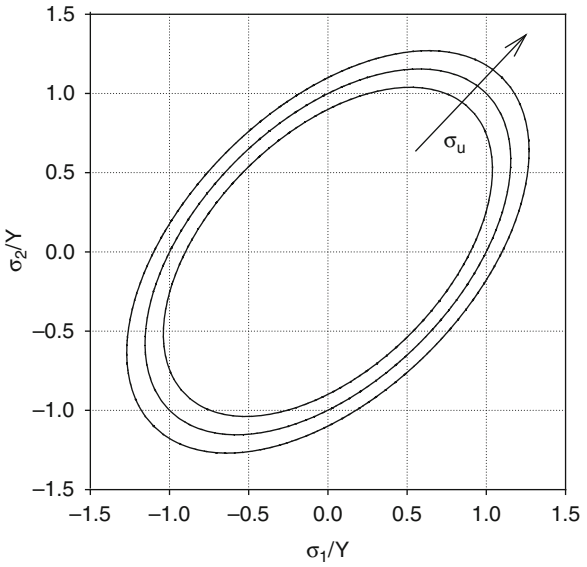

Fig 2.15 Influence of the uniaxial yield stress on the shape of the yield locus defined by the Hill 1948 criterion

$$(1+2r)\left(\frac{\sigma_1-\sigma_2}{\sigma_u}\right)^2+\left(\frac{\sigma_1+\sigma_2}{\sigma_u}\right)^2=2\,(1+r) \tag{2.65}$$

In case of an isotropic material ($r=1$), Eqs. (2.63) and (2.65) reduce to the von Mises relationships (2.38) and (2.39), respectively.

In the above equations, the yielding condition is expressed by relations between components of the stress tensor. This defines the shape of the yield surface. Its extension in the space of the stress components is given by the equivalent or effective stress σ_e. This is the stress associated to a simple mechanical test that causes the transition of the material from an elastic state to a plastic state. Yield criteria are frequently expressed using this parameter.

If we take into account Eqs. (2.52) and (2.7), the equivalent stress can be expressed as

$$\sigma = Y_\theta[G\cos^2\theta + F\sin^2\theta + H(\cos^2\theta-\sin^2\theta)+2N\sin^2\theta\cos^2\theta]^{\frac{1}{2}} \tag{2.66}$$

Consequently, F_θ will be defined by the relationship

$$F_\theta = [G\cos^2\theta + F\sin^2\theta + H(\cos^2\theta-\sin^2\theta)+2N\sin^2\theta\cos^2\theta]^{\frac{1}{2}} \tag{2.67}$$

In the case of the Hill'48 yield criterion, the uniaxial yield stress corresponding to a direction inclined at the angle θ with respect to the rolling direction is

$$Y_\theta = \frac{Y(h)}{[G\cos^2\theta + F\sin^2\theta + H(\cos^2\theta - \sin^2\theta) + 2N\sin^2\theta\cos^2\theta]^{\frac{1}{2}}} \tag{2.68}$$

If the yield parameter $Y(h)$ is set equal to the uniaxial yield stress σ_u, the uniaxial yield stress predicted by this criterion is

$$Y_0 = \frac{\sigma_u}{\sqrt{G+H}}. \tag{2.69}$$

The expression of the uniaxial anisotropy predicted by the Hill'48 yield criterion is obtained by replacing Eq. (2.67) in Eq. (2.17):

$$r_\theta = \frac{G\cos^4\theta + F\sin^4\theta + H\cos^2 2\theta + \frac{1}{2}N\sin^2 2\theta}{G\cos^2\theta + F\sin^2\theta} - 1. \tag{2.70}$$

Equations (2.69) and (2.70) are used for predicting the uniaxial yield stress and coefficient of plastic anisotropy, in the case when the parameters *F, G, H* and *N* of the Hill 1948 yield criterion are related to the experimental yield stress σ_u and the experimental coefficients of plastic anisotropy r_0, r_{45} and r_{90}. The identification of the yield criterion can be also performed by using three experimental values of the yield stress and one experimental value of the coefficient of plastic anisotropy.

2.3.1.2 Comments on the Hill'48 Yield Criterion

When describing the anisotropy of metals, the Hill 1948 yield criterion has the advantage that its basic assumptions are easy to understand. The parameters included in the yield functions have a direct physical meaning. This explains its wide use in practice. In addition, the model has a simple formulation for the 3D case. The criterion needs a small number of mechanical parameters for determining the yield function. Under plane stress conditions, four parameters are sufficient, namely, r_0, r_{45}, r_{90} and σ_0 or r_0, r_{45}, r_{90} and σ_{90} because the parameters r_0, r_{90}, σ_0 and σ_{90} are related by Eq. (2.56). In practice, the values of the anisotropy coefficients and an average of the uniaxial yield stress (σ_u) are used.

Besides its advantages, the criterion also has some drawbacks:

1. It cannot represent the 'anomalous' behavior observed by Woodthrope and Pearce [26]: $r < 1$ and $\sigma_b > \sigma_u$ (or the reciprocal) because the criterion predicts (see Eq. 2.64)

$$\sigma_b = \sigma_u\sqrt{\frac{1+r}{2}} \tag{2.71}$$

2. It cannot represent the 'second order anomalous' behaviour (this new concept has been introduced in the literature by the author in the paper [28]): $\frac{r_0}{r_{90}} > 1$ and $\frac{\sigma_0}{\sigma_{90}} < 1$ (or vice-versa) because the criterion predicts

$$\frac{\sigma_0}{\sigma_{90}} = \sqrt{\frac{r_0\,(1 + r_{90})}{r_{90}\,(1 + r_0)}} \tag{2.72}$$

3. It can only be applied to materials forming four 'ears' in axisymmetric deep-drawing processes whereas in practice also different numbers of ears are observed.
4. The curves equivalent stress σ_e vs. equivalent strain ε_e for different materials depend on the loading path, although they should be unique and intrinsic for a given material.
5. In uniaxial tensile tests, the dependence of the yield stress on direction is poorly predicted by the theory, although the variation of the r-coefficient is properly determinate. There is also the possibility to perform the identification of the Hill 1948 model by using only yield stresses and not coefficients of plastic anisotropy. Of course, in such a case, the accuracy of the predictions related to the variability of the anisotropy coefficients is poorer. The model cannot use the same number of yield stresses and anisotropy coefficients in the identification procedure. This characteristic is an important drawback, especially in the case of materials exhibiting significant variations of the mechanical parameters mentioned above [28].

2.3.1.3 Hill 1979 Yield Criterion

As mentioned above the quadratic yield criteria cannot describe the plastic behavior of some materials such as aluminum alloys. According to Woodthrope and Pearce [26, 27], these metals, though having anisotropy coefficients less than unity, have an experimental yield surface located outside the surface predicted by the von Mises yield criterion ($\sigma_b > \sigma_u$). Since the Hill 1948 yield criterion cannot describe such a situation, the above authors improperly called this behavior 'anomalous' (see also the comments to Eq. 2.64).

Starting from this experimental observation, in the 1970s several researchers concluded independently from each other that only non-quadratic functions are suitable. In the next sections various criteria of this kind are presented in order to describe the so-called 'anomalous' behavior of some materials.

Whereas the quadratic criterion by Hill can be applied both to sheet metal and to round bars, the non-quadratic yield criteria described below generally can only be applied to sheet metal.

This function was expressed in its general form as well as in four special cases [29]. If the directions of the principal stresses coincide with the axes of anisotropy the criterion is written as

$$f\,|\sigma_2-\sigma_3|^m + g\,|\sigma_3-\sigma_1|^m + h\,|\sigma_1-\sigma_2|^m + a\,|2\sigma_1-\sigma_2-\sigma_3|^m + \\ +b\,|2\sigma_2-\sigma_1-\sigma_3|^m + c\,|\sigma_3-\sigma_1-\sigma_2|^m = \sigma_e^m \tag{2.73}$$

Here *f, g, h, a, b* and *c* are anisotropy coefficients; the exponent *m* can be calculated from the non-linear relationship obtained from Eq. (2.73) written for equibiaxial tension ($\sigma_1 = \sigma_2 = \sigma_b\,;\ \sigma_3 = 0$) [29]:

$$\left(\frac{\sigma_b}{\sigma_m}\right)^m = \frac{1}{2}\,(1+r)\cdot\left(1+\frac{\left(2^{m-1}-2\right)\cdot(a-c)}{a+2^{m-1}\cdot c+f}\right), \tag{2.74}$$

This equation can be solved numerically.

If $m \neq 2$, there are seven parameters taking different values (according to the convexity conditions), ensuring an improved flexibility as compared to the Hill 1948 yield criterion.

For plane stress ($\sigma_3 = 0$) Eq. (2.73) can be written in four particular forms given by Hill [29]. The most frequently used formulation is the so-called Case 4, according to Hill's paper [29]. As a consequence, we shall describe only this model.

Case 4 is defined by the following constraint acting on the parameters: $a = b = f = g = 0$. Equation (2.73) reads now

$$c\,|\sigma_1+\sigma_2|^m + h\,|\sigma_1-\sigma_2|^m = \sigma_e^m \tag{2.75}$$

Lian, Zhou and Baudelet [30] proved that the four forms of the Hill 1979 yield criterion can be expressed as functions of only two coefficients depending on the parameters *r* and *m*. The coefficients in Eq. (2.75) is given by

$$c = \frac{r}{2\,(1+r)} \quad , \quad h = \frac{1+2\cdot r}{2\,(1+r)} \tag{2.76}$$

These particular forms of the Hill'79 are based on the assumption of planar isotropy whereby the axes 1 and 2 can be arbitrarily oriented in the plane of the sheet metal and the terms associated to shear stress are not necessary.

However, it is possible to generalize the Hill 1979 criterion for taking into account planar anisotropy [31–33].

For planar isotropy, the most widely used expression of the Hill 1979 yield criterion is in the form (2.75). This expression shall be considered more thoroughly. It can be rewritten in the form

$$|\sigma_1+\sigma_2|^m + (1+2\cdot r)\,|\sigma_1-\sigma_2|^m = 2\,(1+r)\,\sigma_u^m \tag{2.77}$$

The convexity condition requires that m be greater than unity. In this particular case Eq. (2.74) has the form

$$\left(\frac{\sigma_b}{\sigma_u}\right)^m = \frac{1+r}{2^{m-1}} \tag{2.78}$$

By solving Eq. (2.78), usually non-integer values of m are obtained.

For the aluminum alloy DIN-AlMgSi1 having $\sigma_u = 138$ MPa, $\sigma_b = 156$ MPa, $r = 0.50$ it follows $m = 1.358$ [34]. For $m = 2$ the criterion is reduced to Eq. (2.63) associated to the Hill 1948 yield criterion.

In 1977 Bassani published a paper [35] where he proved independently of Hill that a family of yield functions depending on four parameters may be constructed in order to approximate a relatively broad category of transversally isotropic yield surfaces predicted by the Bishop–Hill theory [36].

He proposed the yield function:

$$f = \left|\frac{\sigma_1 + \sigma_2}{2\sigma_b}\right|^n + \left|\frac{\sigma_1 - \sigma_2}{2\tau}\right|^m - 1 \tag{2.79}$$

where τ is the yield stress in pure shearing, while n and m are two constants greater than unity.

One may notice that this function is a generalised expression of Case 4 proposed by Hill in 1979 (for $n = m$, Eq. (2.79) reduces to Eq. (2.75)). The difference consists in the way of defining the coefficients.

Bassani concluded that the proposed family of yield functions, for arbitrarily chosen values of m or n approximates the yield surfaces predicted by the Bishop-Hill theory.

Extensions of the Hill 1979 model for stress states with a planar shearing component have been proposed by Chu [32], Zhou [33], [37] and Monteillet [38].

Advantages of the Hill 1979 yield criterion are [30]:

- it can describe the Woodthrope-Pearce 'anomalous' behavior of materials
- it has a relatively simple form
- it leads to of an analytical expression of the associated flow rule and equivalent strain.

Disadvantages are:

- it cannot describe the behavior of the materials having $\frac{r_0}{r_{90}} \neq 1$ and $\frac{\sigma_0}{\sigma_{90}} \neq 1$
- due to the non-integer value of the exponent m, it requires numerical procedures even for the solution of quite simple cases
- although it allows the description of the 'anomalous' behavior, the predicted yield surfaces are sometimes far from the experimental surfaces predicted by the Bishop-Hill theory [36].

2.3.1.4 Hill 1990 Yield Criterion

As mentioned above, the yield criterion proposed by Hill in 1979 can only be used when the directions of the principal stresses are coincident with the orthotropic axes.

This causes severe limitations of application. The generalisation of the criterion by expressing it in a general coordinate system was realised by Hill in 1990 [39]:

$$\varphi = |\sigma_{11} + \sigma_{22}|^m + \left(\sigma_b^m / \tau^m\right) \left|(\sigma_{11} - \sigma_{22})^2 + 4\sigma_{12}^2\right|^{m/2} + \left|\sigma_{11}^2 + \sigma_{22}^2 + 2\sigma_{12}^2\right|^{(m/2)-1} \cdot$$
$$\cdot \left\{-2a\left(\sigma_{11}^2 - \sigma_{22}^2\right) + b\left(\sigma_{11} - \sigma_{22}\right)^2\right\} = (2\sigma_b)^m \tag{2.80}$$

Here σ_b is the yield stress in equibiaxial tension, τ is the yield stress in pure shear deformation ($\sigma_1 = -\sigma_2$), a and b are material constants.

The m exponent is obtain by solving the following equation

$$\left(\frac{2 \cdot \sigma_b}{\sigma_{45}}\right)^m = 2 \cdot (1 + r_{45}) \tag{2.81}$$

The value of the m exponent is

$$m = \frac{\ln\left[2\left(r_{45} + 1\right)\right]}{\ln \dfrac{2\sigma_b}{\sigma_{45}}} \tag{2.82}$$

The constants a and b are determined from the equations

$$a = \frac{1}{4}\left|\left(\frac{2\sigma_b}{\sigma_{90}}\right)^m - \left(\frac{2\sigma_b}{\sigma_0}\right)^m\right|;$$
$$b = \frac{1}{2}\left[\left(\frac{2\sigma_b}{\sigma_0}\right)^m + \left(\frac{2\sigma_b}{\sigma_{90}}\right)^m\right] - \left(\frac{2\sigma_b}{\sigma_{45}}\right)^m. \tag{2.83}$$

The ratio σ_b/τ may be also expressed as a function of coefficient r_{45} (see Eq. 2.57):

$$\left(\frac{\sigma_b}{\tau}\right)^m = 1 + 2 \cdot r_{45} \tag{2.84}$$

It can be shown that the parameters a and b can also be determined as functions of the anisotropy coefficients r_0, r_{45} and r_{90}:

$$a = \frac{(r_0 - r_{90})\left[1 - \left((m-2)/2\right) \cdot r_{45}\right]}{(r_0 + r_{90}) - (m-2) \cdot r_0 \cdot r_{90}};$$
$$b = \frac{m \cdot [2 \cdot r_0 \cdot r_{90} - r_{45} \cdot (r_0 + r_{90})]}{(r_0 + r_{90}) - (m-2) \cdot r_0 \cdot r_{90}}. \tag{2.85}$$

$$a = \frac{F-G}{F+G}; \quad b = \frac{F+G+4H-2N}{F+G} \tag{2.86}$$

or as functions of the coefficients in Eqs. (2.50) and (2.51).

By using the methodology described in Sect. 2.1.1, the equivalent stress associated to the Hill 1990 yield criterion can be expressed as follows:

$$\sigma = Y_\theta \frac{1}{2}[1 + \left(\frac{\sigma_b}{\tau}\right)^m - 2a\cos 2\theta + b\cos^2 2\theta]^{\frac{1}{m}} \tag{2.87}$$

The corresponding function F_θ is

$$F_\theta = \frac{1}{2}[1 + \left(\frac{\sigma_b}{\tau}\right)^m - 2a\cos 2\theta + b\cos^2 2\theta]^{\frac{1}{m}} \tag{2.88}$$

In the case of Hill 1990 model, the yield parameter $Y(h)$ is set equal to the biaxial yield stress ($Y(h)$=Y_b). In order to preserve the original notations, we shall use the symbol σ_b for the biaxial yield stress. According to Eq. (2.10), the uniaxial yield stress is defined as follows:

$$Y_\theta = \frac{4\sigma_b}{[1 + \left(\frac{\sigma_b}{\tau}\right)^m - 2a\cos 2\theta + b\cos^2 2\theta]^{\frac{1}{m}}} \tag{2.89}$$

The planar distribution of the uniaxial anisotropy coefficient is predicted by the formula

$$r_\theta = \frac{\left(\frac{\sigma_b}{\tau}\right)^m - 1 + \frac{2}{m}b\cos^2 2\theta}{2 - 2a\cos 2\theta + \frac{m-2}{m}b\cos^2 2\theta} - 1 \tag{2.90}$$

Equations (2.89) and (2.90) allow the determination of the planar distribution of the uniaxial yield stress and coefficient of plastic anisotropy.

A detailed discussion of the computational methodology of the parameters in Hill's 1990 yield function is presented in [40] and [41]. By comparing the yield loci computed with Eq. (2.80) using the coefficients a and b evaluated on the basis of the yield stresses (Eq. 2.83) as well as on the basis of the anisotropy coefficients (Eq. 2.85), with the yield loci given by the Taylor theory, Lin and Ding [40] concluded that the identification procedure using stresses ensured a better approximation.

Using Mohr's circle, the yield function (2.80) can be expressed in principal stresses:

$$\begin{aligned} &\varphi = |\sigma_1 + \sigma_2|^m + \left(\frac{\sigma_b^m}{\tau^m}\right)|\sigma_1 - \sigma_2|^m + \left|\sigma_1^2 + \sigma_2^2\right|^{(m/2)-1} \cdot \\ &\cdot \left[-2a\left(\sigma_1^2 - \sigma_2^2\right) + b\left(\sigma_1 - \sigma_2\right)^2 \cos 2\theta\right] \cos 2\theta = (2\sigma_b)^m \end{aligned} \tag{2.91}$$

Here θ is the angle between the direction of σ_1 and the rolling direction. If $a = b$ or $\theta = \pi/4$, Eqs. (2.80) and (2.91) reduce to Case 4° of the Hill 1979 yield criterion (Eq. 2.75).

The flow rule associated to this yield criterion is presented in [41]. The Hill 1990 yield criterion preserves all the advantages of the Hill 1979 criterion. In addition, it includes all the planar components of the stress tensor (σ_{11}, σ_{22} and σ_{12}). As a consequence it is possible to evaluate the distribution of the uniaxial yield stress and anisotropy coefficient in the plane of the sheet metal. From Eqs. (2.81) to (2.83) it can be seen that five parameters are needed for defining the yield function: σ_0, σ_{45}, σ_{90}, σ_b and r_{45}.

If Eqs. (2.84) and (2.85) are used for calculating the coefficients a and b, the mechanical parameters necessary for defining the yield function are σ_{45}, σ_b, r_0, r_{45} and r_{90} and again three uniaxial tensile tests and a biaxial tensile test are required.

In their analysis of Hill's 1990 yield criterion, Lin and Ding [40] proposed a more general expression:

$$\begin{aligned} &\varphi = |\sigma_1 + \sigma_2|^m + (1 + 2R)\,|\sigma_1 - \sigma_2|^m + \left|\sigma_1^2 + \sigma_2^2\right|^{m-\frac{1}{2}} \cdot \\ &\cdot \{-2a\,(|\sigma_1|^s - |\sigma_2|^s) + b\,|\sigma_1 - \sigma_2|^s \cos 2\theta\} \cos 2\theta = (2\sigma_b)^m \end{aligned} \tag{2.92}$$

where R and s are material parameters. For $\theta = \pi/4$ and $s = 2$ Eq. (2.92) is simplified to Eq. (2.75) i.e. Hill's 1979 criterion (Case 4°). The new characteristic of this criterion is that the additional terms are not quadratic. The exponent s is calculated from the equation

$$s = -\frac{mr_0\left\{2\,(r_{90} - R) + r_{90}\left[\left(\frac{2\sigma_b}{\sigma_{90}}\right)^m - 2\,(1 + R)\right]\right\}}{(1 + R)\,(r_0 - r_{90}) - \frac{1}{2}\,(r_0 + r_{90} + 2r_0 r_{90})\left[\left(\frac{2\sigma_b}{\sigma_{90}}\right)^m - 2\,(1 + R)\right]} \tag{2.93}$$

where R is determined from

$$R = \frac{1}{2}\left[\left(\frac{2\sigma_b}{\sigma_{45}}\right)^m - 1\right]. \tag{2.94}$$

If the identification of the parameters a and b is made using stresses then

$$\begin{aligned} a &= \frac{1}{4}\left[\left(\frac{2\sigma_b}{\sigma_{90}}\right)^m - \left(\frac{2\sigma_b}{\sigma_0}\right)^m\right]; \\ b &= \frac{1}{2}\left[\left(\frac{2\sigma_b}{\sigma_0}\right)^m + \left(\frac{2\sigma_b}{\sigma_{90}}\right)^m\right] - 2\,(1 + R)\,. \end{aligned} \tag{2.95}$$

where by s is calculated from

$$s = \frac{m\,[(b - 2a)\,r_0 + 2\,(r_0 - r_{45})]}{(1 + r_0)\,b} \tag{2.96}$$

The above equations show that the determination of the proposed yield function demands six parameters (σ_0, σ_{90}, σ_b, r_0, r_{45} and r_{90}) in the first identification procedure, or σ_{45}, σ_b, r_0, r_{45} and r_{90} in the second one. In order to establish these parameters, three uniaxial tensile tests and a biaxial tensile test have to be carried out. The paper by Lin and Ding [40] also gives a comparison of the yield surfaces computed with coefficients *a, b, s* and *R* identified in the two manners described above with the yield surfaces predicted by the Taylor theory. The identification of the coefficients *a* and *b* could be made on the basis of the anisotropy coefficients [40]. In this case a better approximation of the yield surfaces predicted by the Taylor theory would be obtained (contrary to the situation occurring when the original Hill 1990 yield criterion is used). This is due to the non-quadratic terms added to the yield function.

Leacock [42] extended the formulation proposed by Hill in 1990 [39] by defining the following yield criterion:

$$\begin{aligned}&|\sigma_1+\sigma_2|^m + A^m\,|\sigma_1-\sigma_2|^m + \left|\sigma_1^2+\sigma_2^2\right|^{(m/2)-2}\left[\left(\sigma_1^2-\sigma_2^2\right)\right.\\&\left\{H(\sigma_1^2+\sigma_2^2)+I(\sigma_1^2-\sigma_2^2)\cos 2\theta\right\}+(\sigma_1-\sigma_2)^2\\&\left.\left\{J(\sigma_1^2+\sigma_2^2)+K(\sigma_1^2-\sigma_2^2)\cos 2\theta\right\}\cos 2\theta\ \right]=(2\sigma_b)^m.\end{aligned} \tag{2.97}$$

The evaluation of the constants *A, H, I, J, K* and *m* is based on 6 mechanical parameters, namely σ_0, σ_{45}, σ_{90}, σ_b, r_0, r_{45} and $r_{90.}$

Equation (2.97) can be reduced to the formulation proposed by Hill in 1990 (Eq. 2.80).

The uniaxial yield stress is defined by the relationship

$$\sigma_\theta = 2\sigma_b\left(1+A^m+(H+I\cos 2\theta)+(J+K\cos 2\theta)\cos^2 2\theta\right)^{-1/m}. \tag{2.98}$$

while the coefficient of uniaxial anisotropy is expressed as

$$r_\theta = \frac{A^m+0.5(H+I(\cos 2\theta)\cos 2\theta+\left[(m+2)/(2m)\right]/(J+K\cos 2\theta)\cos^2 2\theta}{2\left\{1+0.5(H+I(\cos 2\theta)\cos 2\theta+\left[(m-2)/(2m)\right]/(J+K\cos 2\theta)\cos^2 2\theta\right\}}-1/2. \tag{2.99}$$

Due to the use of seven mechanical parameters in the identification procedure, Leacock's model gives better predictions than Hill 1990 and Lin 1996 models both for the yield surfaces and the planar distributions of the uniaxial yield stresses and coefficient of plastic anisotropy.

Advantages of the Hill 1990 yield criterion are the following:

- it allows to describe both the 'first order anomalous behavior' ($r < 1$, $\sigma_b < \sigma_u$) and the 'second order anomalous behavior' ($r_0 < r_{90}$, $\sigma_0 > \sigma_{90}$ and vice-versa)
- it is able to describe very well the variation of the anisotropy coefficient and of the uniaxial yield stress in the plane of the sheet

- it has a great flexibility due to the high number of the mechanical parameters incorporated
- Leacock's modification [42] is shown to explicitly deal with the second order anomalous behaviour.

However, there are also some *disadvantages*:

- the formulation is not user-friendly
- due to the trigonometric functions incorporated in their formulation, both Lin and Ding [40] and Leacock [42] extensions of the Hill 1990 model need larger CPU times when used in the numerical simulation of sheet metal forming processes.

2.3.1.5 Hill 1993 Yield Criterion

In 1993 Hill [43] improved the model of plastic behavior of textured sheet metals, namely those observed when complex loads are applied along the planar orthotropic axes.

There are some situations that cannot be dealt with completely by any of the criteria described above. A comprehensive analysis of these problems is given in [43] where Hill showed that for all the criteria described above the condition $\sigma_0 = \sigma_{90}$ enforces $r_0 = r_{90}$ and the reciprocal.

However, it has been observed experimentally that some materials, especially aluminum alloys and brass have almost equal yield stresses but different anisotropy coefficients in rolling and transverse direction. This applies to the results reported in [44] for a brass 70-30 sheet ($\sigma_0 = 126$ MPa, $\sigma_{90} = 125$ MPa, $r_0 = 1.51$, $r_{90} = 0.37$) and in [34] for AlMgSi1 sheet ($\sigma_0 = 143$ MPa, $\sigma_{90} = 133$ MPa, $r_0 = 0.48$, $r_{90} = 0.61$).

For this phenomenon the term 'anomalous behavior of second order' should be used [28], in order to distinguish it from the 'anomalous behavior' of the aluminum alloy described in [26, 27] whereby $r < 1$ though the equibiaxial yield stress is higher than the uniaxial one: $\sigma_b/\sigma_u > 1$.

For this reason Hill [43] proposed a new yield criterion that should preserve the generality of the one proposed in 1979, that is, the capability of modelling both the 'anomalous behavior' and the 'anomalous behavior of second order'.

These constraints are satisfied by the following polynomial function, valid for stress states in the first quadrant (biaxial tension) which is most relevant for thin sheet metals:

$$\frac{\sigma_1^2}{\sigma_0^2} - \frac{c\sigma_1\sigma_2}{\sigma_0\sigma_{90}}\sigma_1\sigma_2 + \frac{\sigma_2^2}{\sigma_{90}^2} + \left\{(p+q) - \frac{(p\sigma_1 + q\sigma_2)}{\sigma_b}\right\}\frac{\sigma_1\sigma_2}{\sigma_0\sigma_{90}} = \sigma_u^2 \tag{2.100}$$

where

$$\frac{c}{\sigma_0\sigma_{90}} = \frac{1}{\sigma_0^2} + \frac{1}{\sigma_{90}^2} - \frac{1}{\sigma_b^2} \tag{2.101}$$

while p and q are calculated with the normality condition of the strain rate tensor to the yield surface applied to function (2.100) at the intersection with the coordinate axes:

$$p = \left[\frac{2r_0 \left(\sigma_b - \sigma_{90}\right)}{\left(1 + r_0\right) \sigma_0^2} - \frac{2r_{90}\sigma_b}{\left(1 + r_{90}\right) \sigma_{90}^2} + \frac{c}{\sigma_0} \right] \frac{1}{\frac{1}{\sigma_0} + \frac{1}{\sigma_{90}} - \frac{1}{\sigma_b}}; \tag{2.102}$$

$$q = \left[\frac{2r_{90} \left(\sigma_b - \sigma_{90}\right)}{\left(1 + r_{90}\right) \sigma_{90}^2} - \frac{2r_0\sigma_b}{\left(1 + r_0\right) \sigma_0^2} + \frac{c}{\sigma_{90}} \right] \frac{1}{\frac{1}{\sigma_0} + \frac{1}{\sigma_{90}} - \frac{1}{\sigma_b}}; \tag{2.103}$$

From Eqs. (2.100) to (2.103) it follows that in order to define the yield function, five mechanical parameters are required (r_0, r_{90}, σ_0, σ_{90} and σ_b). These parameters can be determined by two uniaxial tensile tests and an equibiaxial tensile test.

By expressing the modulus of the principal stress σ_1 and σ_2 from the third order term of Eq. (2.100) the criterion can be extrapolated to the other quadrants of the plane (σ_1, σ_2). This leads to some discontinuity of the yield locus which, however, can be tolerated if the discontinuity errors are within the limits of the experimental errors.

Equation (2.100) show that the proposed yield function is nonhomogeneous with respect to σ_1 and σ_2. Consequently it is not possible to get an explicit expression of the strain increment from the normality condition.

Advantages of the Hill 1993 yield criterion are the following:

- it allows to describe both the 'first order anomalous behavior' ($r < 1$, $\sigma_b < \sigma_u$) and the 'second order anomalous behavior' ($r_0 < r_{90}$, $\sigma_0 > \sigma_{90}$ and vice versa)
- it has a relatively simple and user-friendly expression; it has a great flexibility due to the five mechanical parameters incorporated.

However, there are also some *disadvantages*:

- the yield function is non-homogenous with respect to σ_1 and σ_2 and hence does not allow to obtain explicit expressions of the strain increments
- it can be used only if the directions of the principal stresses are coincident with the orthotropic axes
- it does not allow to describe the variation of the anisotropy coefficient and of the uniaxial yield stress in the plane of the sheet
- the yield surface predicted by this function is far from that obtained from polycrystal theories (Taylor or Bishop-Hill).

Due to the disadvantages mentioned above, the applicability of this yield criterion is limited.

2.3.2 Yield Function Based on Crystal Plasticity (Hershey's Familly)

Besides the family of Hill yield criteria presented in the previous subchapter, we have to mention another class of models based on the isotropic formulation proposed by Hershey [19]. Hosford 'rediscovered' Hershey's model in 1972 [20] and used it for the development of an anisotropic yield criterion. Barlat et al. [5] and Banabic et al. [51] as well as some other researchers proposed further extensions of the model.

2.3.2.1 Hosford Yield Criterion

Independently of Hill, Hosford proposed a yield criterion in the form [31]

$$F\,|\sigma_{22}-\sigma_{33}|^a + G\,|\sigma_{33}-\sigma_{11}|^a + H\,|\sigma_{11}-\sigma_{22}|^a = \sigma^a \tag{2.104}$$

This is a generalization of his own isotropic criterion [20].

One may consider this criterion as a particular expression ($a = b = c = 0$ and $f = g$) of Case 4° of Hill's 1979 yield criterion (see Eq. 2.75).

The essential difference between the approaches by Hosford and Hill consists in the different way of determining the exponent a. Hosford related a to the crystallographic structure of the material [45–48]. He concluded that the best approximation was given by $a = 6$ for BCC materials and $a = 8$ for FCC materials, see also [45].

For plane stress Eq. (2.104) reduces to

$$r_{90}\,|\sigma_{11}|^a + r_0\,|\sigma_{22}|^a + r_0 r_{90}\,|\sigma_{11}-\sigma_{22}|^a = r_{90}\,(r_0+1)\,\sigma_0^a \tag{2.105}$$

The main advantage of the Hosford 1979 yield criterion is that by fitting the value of the exponent a it ensures a good approximation of the yield locus computed through the Bishop-Hill theory [36] as well as from experimental data.

An important drawback of this criterion is caused by the lack of shear stress: it cannot predict the variation of the coefficient r with direction (planar anisotropy).

2.3.2.2 Barlat 1989 Yield Criterion

Barlat and Richmond [49] proposed a more general form of Hosford's criterion for *isotropic* materials [20] by expressing it in an *x, y, z* coordinate system, not necessarily coincident with the principal directions (the so-called 'tricomponent plane stress yield surface'):

$$f = |k_1 + k_2|^M + |k_1 - k_2|^M + |2k_2|^M = 2\sigma_e^M \tag{2.106}$$

Here k_1 and k_2 are invariants of the stress tensor while M is an integer exponent having the same significance as the exponent a used by Hosford; k_1 and k_2 are obtained from

$$k_1 = \frac{\sigma_{11} + \sigma_{22}}{2}$$
$$k_2 = \sqrt{\left(\frac{\sigma_{11} - \sigma_{22}}{2}\right)^2 + \sigma_{12}^2} \tag{2.107}$$

For $\sigma_{12} = 0$ it follows $\sigma_{11} \to \sigma_1$ and $\sigma_{22} \to \sigma_2$ and Eq. (2.106) is reduced to the isotropic Hosford criterion which now includes the shear stresses (incorporated in the invariant k_2).

The yield function given by Eq. (2.106) was also extended to the case of *normal anisotropy* in the form:

$$f = a\,|k_1 + k_2|^M + b\,|k_1 - k_2|^M + c\,|2k_2|^M = 2\sigma_e^M \tag{2.108}$$

where *a, b* and *c* depend on the anisotropy coefficients while k_1 and k_2 are calculated from the equation

$$a = b = 2 - c = \frac{2}{1 + r} \tag{2.109}$$

In 1989, Barlat and Lian [50] published a generalisation of Eq. (2.106) for materials exhibiting *planar anisotropy* by introducing the following yield function:

$$f = a\,|k_1 + k_2|^M + a\,|k_1 - k_2|^M + c\,|2k_2|^M = 2\sigma_e^M \tag{2.110}$$

The coefficients k_1 and k_2 are given by

$$k_1 = \frac{\sigma_{11} + h\sigma_{22}}{2}; \quad k_2 = \left[\left(\frac{\sigma_{11} - h\sigma_{22}}{2}\right)^2 + p^2\sigma_{12}^2\right]^{1/2} \tag{2.111}$$

and *a, c, h* and *p* are material parameters identified by

$$a = 2 - c = \frac{2\left(\frac{\sigma_e}{\tau_{s2}}\right)^M - 2\left(1 + \frac{\sigma_e}{\sigma_{90}}\right)^M}{1 + \left(\frac{\sigma_e}{\sigma_{90}}\right)^M - \left(1 + \frac{\sigma_e}{\sigma_{90}}\right)^M}$$
$$h = \frac{\sigma_e}{\sigma_{90}} \tag{2.112}$$
$$p = \frac{\sigma_e}{\tau_{s1}}\left(\frac{2}{2a + 2^M c}\right)^{\frac{1}{M}}$$

Here τ_{s1} and τ_{s2} are yield stresses for two different types of shear tests: $\sigma_{12} = \tau_{s1}$ for $\sigma_{11} = \sigma_{22} = 0$ and $\sigma_{12} = 0$ for $\sigma_{22} = -\sigma_{11} = \tau_{s2}$.

Using another identification procedure based on the coefficients r_0 and r_{90} it is obtained

$$a = 2 - c = 2 - 2\sqrt{\frac{r_0}{1+r_0} \cdot \frac{r_{90}}{1+r_{90}}};$$
$$h = \sqrt{\frac{r_0}{1+r_0} \cdot \frac{1+r_{90}}{r_{90}}}. \tag{2.113}$$

The coefficient p has to be calculated by a numerical procedure or by using Eq. (2.112) instead. For $\sigma_{12} = 0$, Eqs. (2.110) and (2.111) are practically reduced to the Hosford yield criterion in principal stresses (except of the constant h, see Eq. 2.105).

In order to establish the expression of the uniaxial yield stress, Eq. (2.7) will be replaced in Eqs. (2.110) and (2.111). We get the relationship

$$Y_\theta = \frac{Y_0}{[a(F_1+F_2)^M + a(F_1-F_2)^M + (1-a)(2F_2)^M]^{\frac{1}{M}}}, \tag{2.114}$$

where

$$F_1 = \frac{h\sin^2\theta + \cos^2\theta}{2}; \quad F_2 = \left[\left(\frac{h\sin^2\theta - \cos^2\theta}{2}\right)^2 + p^2\sin^2\theta\cos^2\theta\right]. \tag{2.115}$$

The function F_θ is obtained from Eq. (2.114):

$$F_\theta = [a(F_1+F_2)^M + a(F_1-F_2)^M + (1-a)(2F_2)^M]^{\frac{1}{M}} \tag{2.116}$$

The yield parameter $Y(h)$ in Eq. (2.114) has been set equal to the uniaxial yield stress corresponding to the rolling direction ($Y(h) = Y_0$).

By replacing in Eq. (2.17) the F_θ expression given by Eq. (2.116) and performing some computations, we get the relationship defining the coefficient of plastic anisotropy:

$$r_\theta = \frac{[a(F_1+F_2)^M + a(F_1-F_2)^M + (1-a)(2F_2)^M]^{\frac{1}{M}}}{a(K_1+K_2)^{M-1}(t_1+t_2) + a(K_1-K_2)^{M-1}(t_1-t_2) + 2(a-1)(2K_2)^{M-1}t_2} - 1 \tag{2.117}$$

where

$$K_1 = \frac{h\sin^2\theta + \cos^2\theta}{2}\,Y_\theta; \quad K_2 = \left[\frac{h\sin^2\theta - \cos^2\theta}{2} + p^2\sin^2\theta\cos^2\theta\right]. \tag{2.118}$$

and t_1 and t_2 are

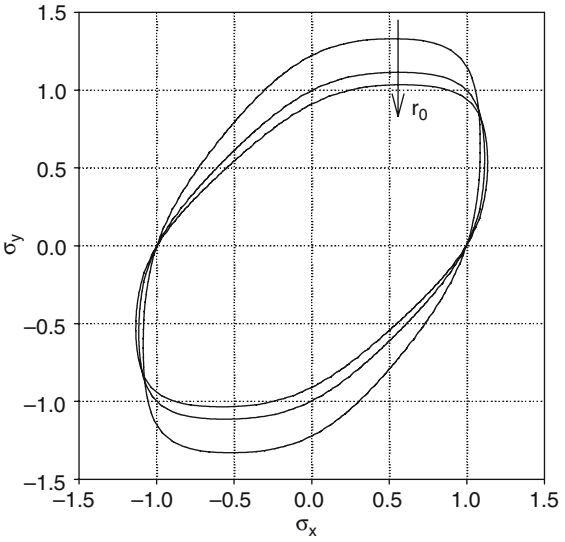

Fig. 2.16 Influence of r_0 anisotropy coefficient on the Barlat 1989 yield locus

$$t_1 = \frac{a(K_1 + K_2)^{M-1} + a(K_1 - K_2)^{M-1}}{\sigma^{M-1}};$$
$$t_2 = \frac{a(K_1 + K_2)^{M-1} - a(K_1 - K_2)^{M-1} + 2(a-1)(2K_2)^{M-1}}{\sigma^{M-1}}. \tag{2.119}$$

where σ represents the equivalent stress corresponding to the Barlat 1989 yield criterion.

Equations (2.114) and (2.117) allow the calculation of the uniaxial yield stress and the coefficient of plastic anisotropy corresponding to different directions in the plane of the sheet metal.

Figures 2.16 and 2.17 shows that the anisotropy coefficient r_0 and r_{90} act in a different manner on the yield locus. In case of the 'tricomponent plane stress' the influence of the exponent M extends to the region of biaxial tension (Fig. 2.18). The figures demonstrates that the yield criterion by Barlat 1989 has a great flexibility. This is due to the large number of parameters (four material parameters and M chosen in accordance with the crystallographic structure of the material).

The advantages of the Barlat 1989 yield criterion are:

- the reduced number of the mechanical parameters (four parameters) used in the identification
- relatively easy identification (except for the coefficient p)
- a relativ good prediction of the yield locus for aluminium alloys without high anisotropy;
- by correctly choosing the exponent M a very good correlation with the yield locus predicted by the Bishop-Hill theory is obtained.

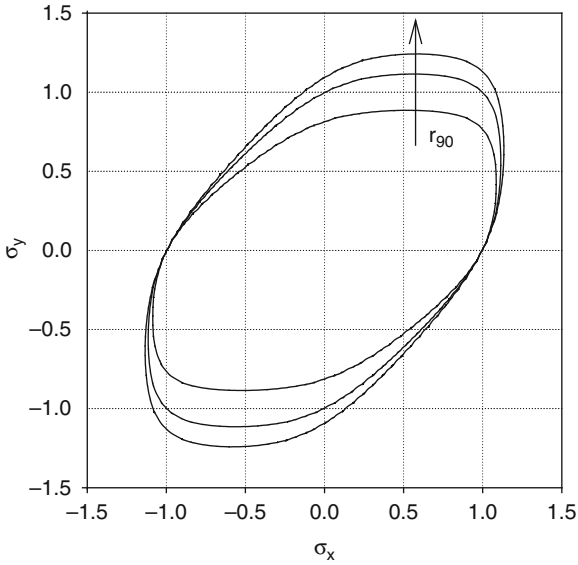

Fig. 2.17 Influence of r_{90} anisotropy coefficient on the Barlat 1989 yield locus

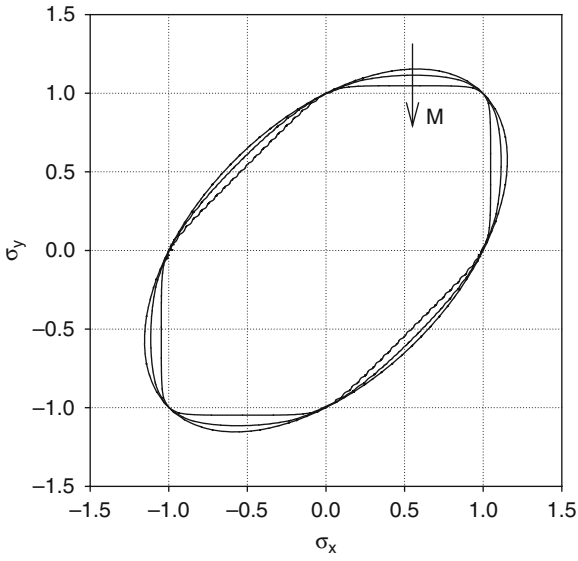

Fig. 2.18 Influence of parameter M on the Barlat 1989 yield locus

The most important disadvantages are as follows:

- the coefficients of the yield function have not a direct and intuitive physical significance.
- the evaluation of the parameter p can be performed only numerically, by solving a non-linear equation.

- the model does not give accurate predictions of the biaxial yield stress, especially in the case of aluminium alloys exhibiting a pronounced anisotropy
- the model cannot capture simultaneously the planar variation of the uniaxial yield stress and uniaxial coefficient of plastic anisotropy
- the model does not give accurate predictions of the biaxial coefficient of plastic anisotropy in case of highly-anisotropic materials.

Despite its limitations, the Barlat 1989 yield criterion is still frequently used in the numerical simulation of sheet metal forming processes.

In 1991, Barlat proposed a 3D extension of his yield criterion [10] (see the next section). Banabic et al. [51–53] also proposed extensions of the Barlat 1989 yield criterion (with seven and eight coefficients), aiming to remove the disadvantages mentioned above (a detailed description of these formulations can be found in Sect. 2.4.2).

2.3.2.3 Barlat 1991 Yield Criterion

Barlat [10] proposed a general six-component yield criterion (σ_{11}, σ_{22}, σ_{33}, σ_{12}, σ_{23}, σ_{31}) that could be adopted with no restrictions to any stress state. With this aim in view, the isotropic Hershey criterion [19] is rewritten in a form containing the deviator principal stresses S_1, S_2 and S_3:

$$\Phi = |S_1 - S_2|^m + |S_2 - S_3|^m + |S_3 - S_1|^m = 2 \cdot \sigma_e^m, \tag{2.120}$$

After a complex number transformation and the Bishop-Hill notation (see [10]),

$$A = \sigma_{22} - \sigma_{33}, B = \sigma_{33} - \sigma_{11}, C = \sigma_{11} - \sigma_{22}, F = \sigma_{12}, G = \sigma_{31}, H = \sigma_{12}, \tag{2.121}$$

Barlat obtained the following expression of the isotropic Hershey yield criterion:

$$\begin{aligned} \Phi = (3I_2)^{\frac{m}{2}} \left\{ \left| 2\cos\left(\frac{2\theta + \pi}{6}\right)\right|^m + \left| 2\cos\left(\frac{2\theta + 3\pi}{6}\right)\right|^m + \right. \\ \left. + \left| -2\cos\left(\frac{2\theta + 5\pi}{6}\right)\right|^m \right\} = 2\sigma_e^m, \end{aligned} \tag{2.122}$$

where

$$\theta = \arccos\left(\frac{I_3}{I_2^{3/2}}\right), \tag{2.123}$$

where I_2 and I_3 are the second and third invariant of the stress determinant, respectively:

$$I_2 = \frac{F^2 + G^2 + H^2}{3} + \frac{(A - C)^2 + (C - B)^2 + (B - A)^2}{54}, \tag{2.124}$$

$$I_3 = \frac{(C-B)\cdot(A-C)\cdot(B-A)}{54} + F\cdot G\cdot H - \\ - \frac{(C-B)\cdot F^2 + (A-C)\cdot G^2 + (B-A)\cdot H^2}{6} \tag{2.125}$$

The yield function defined above was generalised to the anisotropic case by using weighting coefficients (*a, b, c, f, g, h*), multiplying the stress components given by Eq. (2.121). After this modification, the expressions of the yield function ϕ (Eq. 2.122) and angle θ (Eq. 2.123) remain the same. The expression of the invariants I_2 and I_3 become:

$$I_2 = \frac{(fF)^2 + (gG)^2 + (hH)^2}{3} + \frac{(aA-cC)^2 + (cC-bB)^2 + (bB-aA)^2}{54} \tag{2.126}$$

$$I_3 = \frac{(cC-bB)\cdot(aA-cC)\cdot(bB-aA)}{54} + (fF)\cdot(gG)\cdot(hH) - \\ - \frac{(cC-bB)\cdot(fF)^2 + (aA-cC)\cdot(gG)^2 + (bB-aA)\cdot(hH)^2}{6} \tag{2.127}$$

The weight factors *a, b, c, f, g, h* describe the anisotropy of the material. They are identified by three uniaxial tensile tests in the directions of the orthotropic axes (*a, b, c*) and three pure shearing tests (*f, g, h*).

For the case of plane stress, the number of coefficients diminishes to four (*a, b, c* and *h*). They may be established by three uniaxial tensile tests (at 0°, 45° and 90° with the rolling directions) and a uniaxial compressive test through the thickness.

Alternatively, the identification of the coefficients may be performed using the uniaxial yield stresses (σ_0, σ_{45}, σ_{90}) and the equibiaxial yield stress (σ_b). By introducing these values in the expression of the yield function given by Eq. (2.120), one gets a set of four non-linear equations that can be solved numerically. Another identification method makes use of the anisotropy coefficients r_0, r_{45} and r_{90}. In this case, the value of one coefficient is assumed as being known. The rest of three is obtained by numerically solving a set of non-linear equations.

The exponent m is above unity and is chosen in the same manner as in the case of Hershey's yield criterion. For $a = b = c = f = g = h = 1$ the criterion given by Eq. (2.122) reduces to the isotropic Hershey expression (Eq. 2.120).

The methodology used for obtaining the associative flow rules is rather difficult. It is fully detailed in [41] and [54].

More recently, Choi et al. [54] used the transformation proposed by Karafillis and Boyce [21] for his criterion. As will be shown below, the Barlat 1991 yield criterion may be considered as a special case of the Karafillis-Boyce yield criterion ($c = 0$).

The Barlat 1991 criterion has the advantage of being general and flexible (like the Hill 1948 criterion it has six stress components); it predicts yield surfaces in good agreement with those calculated from polycristal theories (Taylor and Bishop-Hill);

it is easy to implement in finite-element codes; it gives a realistic estimation of the distribution of the uniaxial yield stress and coefficient r in the plane of the sheet.

The main disadvantage of the yield criterion is the complicated flow rule which is not user-friendly.

A similar methodology was used by Lian and Chen [55] for generalising the Hill 1979 criterion in the case of the three-dimensional stress state. They established the following six-component expression of the Hill 1979 criterion:

$$2^m J_2^{m/2}\Big\{f\,|\sin(\varphi/3)|^m + g\,|\cos(\varphi/3+\pi/6)|^m + h\,|\cos(\varphi/3-\pi/6)|^m + \\ + 3^{m/2}\left[a\,|\cos(\varphi/3)|^m + b\,|\cos(\varphi/3-\pi/3)|^m + c\,|\cos(\varphi/3+\pi/3)|^m\right]\Big\} = \sigma_e^m \tag{2.128}$$

where φ depends on the second and third invariant of the deviatoric stress tensor. The *a, b, c, f, g* and *h* are the material coefficients, like in the Barlat model.

The methodology proposed by Lian and Chen is very general and can be applied to any yield criterion written by using principal stresses in order to obtain a six-component expression.

2.3.2.4 Yield Criteria by Barlat 1994 and 1996

Experimental studies showed that aluminum alloys have a plastic behavior that is very difficult to model with the criteria above. At the beginning of 1990 several researchers have focused their interest on this problem.

In [56] Barlat and co-workers proposed a more general expression of the yield function introduced by himself in 1991. The generalization consisted in giving weight factors to the terms of Eq. (2.120):

$$\Phi = \alpha_x \left|S_y - S_z\right|^m + \alpha_y \left|S_z - S_x\right|^m + \alpha_z \left|S_x - S_y\right|^m = 2\sigma_e^m \tag{2.129}$$

The weight factors α_x, α_y and α_z are related to the anisotropy of the materials; S_x, S_y, and S_z are normal component of the stress tensor modified with the linear transformation like in the Karafillis-Boyce proposal [21]; *m* has not the same significance as in case of the Barlat 1991 criterion.

Assuming the shear stresses to be zero, the linear-transformation operator from Karafillis-Boyce proposal (see [21]) becomes

$$\mathrm{L} = \begin{bmatrix} \dfrac{c_2+c_3}{3} & -\dfrac{c_3}{3} & -\dfrac{c_2}{3} \\ -\dfrac{c_3}{3} & \dfrac{c_3+c_1}{3} & -\dfrac{c_1}{3} \\ -\dfrac{c_2}{3} & \dfrac{c_2+c_3}{3} & \dfrac{c_1+c_2}{3} \end{bmatrix} \tag{2.130}$$

where c_1, c_2 and c_3 are material coefficients describing the anisotropy of the material.

The generalization of this function in order to include the shear stresses (six-component formulation) as obtained by rewriting Eq. (2.130) in the principal stresses:

$$\Phi = \alpha_1 |S_2 - S_2|^m + \alpha_2 |S_3 - S_1|^m + \alpha_3 |S_1 - S_2|^m = 2\sigma_e^m \tag{2.131}$$

where the coefficients α_1, α_2 and α_3 are computed from α_x, α_y and α_z by the transformation:

$$\alpha_k = \alpha_x p_{1\,k}^2 + \alpha_y p_{2\,k}^2 + \alpha_z p_{3\,k}^2, \tag{2.132}$$

The coefficients $p_{1\,k}$, $p_{2\,k}$, $p_{3\,k}$ are components of a rotation matrix relating the anisotropy axes to the principal directions of the stress tensor $\boldsymbol{S}$.

In the case of plane stress six independent coefficients must be determined. As a consequence, four mechanical tests have to be made (three uniaxial tensile tests for establishing $\sigma_0, \sigma_{45}, \sigma_{90}, r_0$ and r_{90} and one biaxial tensile test for establishing σ_b).

The yield surfaces predicted by this criterion are good approximations of those calculated by the Bishop-Hill theory and of experimental data. However, finite-element simulations based on this criterion [57] revealed some inaccuracies in predicting blank earing in deep-drawing.

In order to improve the performance of his criterion, Barlat and co-workers [58] proposed a generalisation of the 1994 criterion whereby α_x, α_y and α_z are not constant anymore. They depend on the angles $\beta_1, \beta_2, \beta_3$ between the principal directions of the stress tensor and the anisotropic axes:

$$\begin{aligned}
\alpha_x &= \alpha_{x0} \cos^2 2\beta_1 + \alpha_{x1} \cos^2 2\beta_1; \\
\alpha_y &= \alpha_{y0} \cos^2 2\beta_2 + \alpha_{y1} \cos^2 2\beta_2; \\
\alpha_z &= \alpha_{z0} \cos^2 2\beta_3 + \alpha_{z1} \cos^2 2\beta_3.
\end{aligned} \tag{2.133}$$

where

$$\begin{aligned}
\alpha_{i0} &= \alpha_i \text{ for } \beta_i = 0; \\
\alpha_{i1} &= \alpha_i \, for \, \beta_i = \pi/2.
\end{aligned} \tag{2.134}$$

and

$$\begin{aligned}
\cos^2 2\beta_1 &= \begin{cases} y \cdot 1 \; if \;\; |S_1| \geq |S_3| \;\; or \\ y \cdot 3 \; if \;\; |S_1| < |S_3| \, ; \end{cases} \\
\cos^2 2\beta_2 &= \begin{cases} z \cdot 1 \; if \;\; |S_1| \geq |S_3| \;\; or \\ z \cdot 3 \; if \;\; |S_1| < |S_3| \, ; \end{cases} \\
\cos^2 2\beta_3 &= \begin{cases} x \cdot 1 \; if \;\; |S_1| \geq |S_3| \;\; or \\ x \cdot 3 \; if \;\; |S_1| < |S_3| \, . \end{cases}
\end{aligned} \tag{2.135}$$

For plane stress, after applying the linear transformation introduced by Karafillis and Boyce (see [21]) the components of the **IPE** (isotropic plastic equivalent) stress tensor are written

$$\begin{aligned} S_{11} &= \frac{c_3\,(\sigma_{11}-\sigma_{22})+c_2\sigma_{11}}{3};\\ S_{22} &= \frac{c_1\sigma_{22}+c_3\,(\sigma_{11}-\sigma_{22})}{3};\\ S_{33} &= \frac{-c_2\sigma_{11}-c_1\sigma_{22}}{3};\\ S_{12} &= c_6\sigma_{12}. \end{aligned} \tag{2.136}$$

where c_1, c_2, c_3 and c_6 are material coefficients defining the anisotropy. The principal deviatoric stresses are computed as follows:

$$\begin{aligned} S_{1,2} &= \frac{S_{11}+S_{22}}{2} \pm \sqrt{\left(\frac{S_{11}+S_{22}}{2}\right)^2 + S_{12}^2},\\ S_3 &= -S_1 - S_2 = -S_{11} - S_{22}. \end{aligned} \tag{2.137}$$

In this case the coefficients α_1, α_2 and α_3 are

$$\begin{aligned} \alpha_1 &= \alpha_x \cos^2 2\theta + \alpha_x \cos^2 2\theta;\\ \alpha_2 &= \alpha_y \cos^2 2\theta + \alpha_y \cos^2 2\theta;\\ \alpha_3 &= \alpha_{z0} \cos^2 2\theta + \alpha_{z1} \cos^2 2\theta. \end{aligned} \tag{2.138}$$

whereby $\alpha_{z0} = 1$ and

$$\theta = \tan^{-1}\left(\frac{S_{11}-S_{22}}{S_{12}}\right). \tag{2.139}$$

The orthotropic axes 1, 2 and 3 are oriented along the rolling, transverse and normal direction, respectively. The methodology used for establishing the yield function is the same as that used by Karafillis and Boyce (see [21]).

Equations (2.136) and (2.138) show that in order to determine the yield function eight parameters are necessary: c_1, c_2, c_3, c_6, α_x, α_y and α_0 and the exponent set in accordance with the crystallographic structure of the material. The great number of parameters ensures a good flexibility of the criterion but implies a large number of mechanical tests.

Simulations of deep-drawing of cylindrical cups using the new criterion [59] revealed a very good agreement of the predicted earing with experimental data. The computed yield surfaces are also in good agreement with those predicted by the Bishop-Hill theory and experiments. A very good agreement between theory and experiment has also been found for the distribution of the uniaxial yield stresses and anisotropy coefficients in the plane of sheet.

The most important disadvantages of these models are as follows:

- the convexity of the yield functions is not guaranteed
- the derivatives of the equivalent stress are difficult to obtain analytically and, consequently, the usability of the models in the numerical simulation codes is reduced.

- the application for full stress states leads to numerical problems due to the complexity of the yield functions
- the CPU time is considerably larger than in the case of simpler models. This is a major drawback in the numerical simulation of sheet metal forming processes.

2.3.2.5 Karafillis–Boyce Yield Criterion

As mentioned in Sect. 2.2.4 Karafillis and Boyce [21] proposed a very general yield criterion. Its originality is given by the expression of the yield function (a weighted combination between the von Mises and Tresca expression) as well as the use of a linear transformation in order to pass from the isotropic to the anisotropic case.

The proposed isotropic yield function is presented in the Sect. 2.2.4. In order to adopt the yield criterion for anisotropic materials, Karafillis and Boyce proposed an original method based on the linear transformation:

$$\tilde{\boldsymbol{S}} = \tilde{\boldsymbol{L}} \cdot \tilde{\boldsymbol{\sigma}}, \tag{2.140}$$

where $\tilde{\boldsymbol{S}}$ is a deviatoric stress tensor associated to an 'isotropic plastic equivalent' (IPE) state, $\tilde{\boldsymbol{\sigma}}$ is the actual anisotropic stress tensor; $\tilde{\boldsymbol{L}}$ is a linear operator depending on the material which is defined as follows:

$$\tilde{\boldsymbol{L}} = \mathrm{C} \begin{bmatrix} 1 & \beta_1 & \beta_2 & 0 & 0 & 0 \\ \beta_1 & \alpha_1 & \beta_3 & 0 & 0 & 0 \\ \beta_2 & \beta_3 & \alpha_2 & 0 & 0 & 0 \\ 0 & 0 & 0 & \gamma_1 & 0 & 0 \\ 0 & 0 & 0 & 0 & \gamma_2 & 0 \\ 0 & 0 & 0 & 0 & 0 & \gamma_3 \end{bmatrix} \tag{2.141}$$

where

$$\begin{aligned} \beta_1 &= \frac{\alpha_2 - \alpha_1 - 1}{2}, \\ \beta_2 &= \frac{\alpha_1 - \alpha_2 - 1}{2}, \\ \beta_3 &= \frac{1 - \alpha_1 - \alpha_2}{2}, \end{aligned} \tag{2.142}$$

and α_1, α_2, γ_1, γ_2, γ_3 and C are parameters defining the anisotropy of the metallic material.

Thus the Karafillis-Boyce yield function is defined be eight coefficients (α_1, α_2, γ_1, γ_2, γ_3, c, C and k).

In case of an isotropic material the parameters have the values

$$c = \frac{2}{3}, \alpha_1 = \alpha_2 = 1, \gamma_1 = \gamma_2 = \gamma_3 = \frac{3}{2} \tag{2.143}$$

For loading with negligible non-planar shear stresses ($\sigma_{32} = \sigma_{13} \approx 0$) it is obtained $\gamma_2 = \gamma_3 = 3/2$.

Equation (2.140) may be written in the form

$$\begin{bmatrix} S^i_{11} \\ S^i_{22} \\ S^i_{33} \\ S^i_{23} \\ S^i_{31} \\ S^i_{12} \end{bmatrix} = C \cdot \begin{bmatrix} 1 & \beta_1 & \beta_2 & 0 & 0 & 0 \\ \beta_1 & \alpha_1 & \beta_3 & 0 & 0 & 0 \\ \beta_2 & \beta_3 & \alpha_2 & 0 & 0 & 0 \\ 0 & 0 & 0 & \gamma_1 & 0 & 0 \\ 0 & 0 & 0 & 0 & \gamma_2 & 0 \\ 0 & 0 & 0 & 0 & 0 & \gamma_3 \end{bmatrix} \cdot \begin{bmatrix} \sigma^a_{11} \\ \sigma^a_{22} \\ \sigma^a_{33} \\ \sigma^a_{23} \\ \sigma^a_{31} \\ \sigma^a_{12} \end{bmatrix} \tag{2.144}$$

The 'i' and 'a' superscripts specify the 'isotropic' and 'anisotropic' state, respectively. In case of a plane-stress state, Eq. (2.144) becomes:

$$\begin{bmatrix} S^i_{11} \\ S^i_{22} \\ S^i_{12} \end{bmatrix} = C \cdot \begin{bmatrix} 1 & \frac{\alpha_2-\alpha_1-1}{2} & 0 \\ \frac{\alpha_2-\alpha_1-1}{2} & \alpha_1 & 0 \\ 0 & 0 & \gamma_3 \end{bmatrix} \cdot \begin{bmatrix} \sigma^a_{11} \\ \sigma^a_{22} \\ \sigma^a_{12} \end{bmatrix} \tag{2.145}$$

and only six parameters needed for defining the yield surface (α_1, α_2, γ_3, c, C and k), one more than for the Barlat 1991 criterion. Therefore the Karafillis-Boyce criterion is more flexible than Barlat 1991.

The linear transformation of an anisotropic stress state $\tilde{\boldsymbol{S}}^{\mathrm{a}}$ to an equivalent isotropic one, $\tilde{\boldsymbol{S}}^{\mathrm{i}}$, has been called by Karafillis and Boyce as 'Isotropic Plasticity Equivalent' (IPE). A similar transformation, although not in the same form, was used by Barlat in 1991 [10] in order to change the isotropic Hosford criterion into a six-component anisotropic one.

The methodology used to establish the Karafillis-Boyce yield function for plane stress is as follows:

1° Let σ_{11}, σ_{22} and σ_{12} be the planar components of the anisotropic stress tensor

2° By using the linear transformation (2.145) the components of the **IPE** deviatoric stress tensor are obtained:

$$\begin{aligned} S_{11} &= C\left(\sigma_{11} + \tfrac{\alpha_2-\alpha_1-1}{2}\sigma_{22}\right); \\ S_{22} &= C\left(\tfrac{\alpha_2-\alpha_1-1}{2}\sigma_{11} + \alpha_1\sigma_{22}\right); \\ S_{12} &= \gamma_3 \cdot \sigma_{12}. \end{aligned} \tag{2.146}$$

3° The principal deviatoric stresses are calculated:

$$\begin{aligned} S_1 &= \tfrac{S_{11}+S_{22}}{2} + \sqrt{\left(\tfrac{S_{11}-S_{22}}{2}\right)^2 + S_{12}^2}; \\ S_2 &= \tfrac{S_{11}+S_{22}}{2} - \sqrt{\left(\tfrac{S_{11}-S_{22}}{2}\right)^2 + S_{12}^2}; \\ S_3 &= -\left(S_1 + S_2\right). \end{aligned} \tag{2.147}$$

4° Using Eqs. (2.146) the principal deviatoric stress tensor σ is obtained. By inserting into Eq. (2.44), an expression of the yield function in terms of the components of the anisotropic stress tensor and the coefficients $\alpha_1, \alpha_2, \gamma_3, c, C$ and k is obtained:

$$\Phi = \Phi\left(\sigma_{11}, \sigma_{22}, \sigma_{12}, c, C, \alpha_1, \alpha_2, \gamma_3, k, \sigma_e\right) \tag{2.148}$$

This methodology is used in order to establish the yield function for the Barlat 1994 and 1996 yield criteria (presented above).

Karafillis and Boyce applied the inverse transformation

$$\tilde{\boldsymbol{D}}^{\mathrm{a}} = \tilde{\boldsymbol{L}} \cdot \tilde{\boldsymbol{D}}^{\mathrm{i}} \tag{2.149}$$

in order to determinate the associated flow rules in the anisotropic state as functions to the isotropic ones. Here $\tilde{\boldsymbol{D}}^{\mathrm{a}}$ is the anisotropic strain-rate tensor (for the beginning of plastic yielding) while $\tilde{\boldsymbol{D}}^{\mathrm{i}}$ is the same tensor associated to the **IPE** material. $\tilde{\boldsymbol{D}}^{\mathrm{i}}$ may be calculated from the associated flow rule assuming the yield function Φ (Eq. 2.44):

$$\tilde{\boldsymbol{D}}^{\mathrm{i}} = \lambda \frac{\partial \Phi}{\partial \boldsymbol{S}} \tag{2.150}$$

The transformation (2.145) is used for identifying the anisotropy coefficients r_0, r_{45} and r_{90}. The numerical procedure used for the inverse determination of these coefficients in the operator L (Eq. 2.141) is presented in [21] as a flowchart.

Bron and Besson [60] have proposed a very general model that extends both Barlat 1991 [10] and Karafillis–Boyce [21] formulations.

The equivalent stress of the new yield function is defined in the folowing form:

$$\sigma = \left(\sum_{k=1}^{K} \alpha^k (\sigma^k)^a \right)^{1/a} \tag{2.151}$$

where the K functions σ^k are convex, positive and homogeneous of degree 1 and α^k are positive coefficients (the sum of which is 1).

In their original paper [60], Bron and Besson use only two functions ($K = 2$). In this case, the general formulation of the criterion (2.151) reduces to

$$\sigma^k = (\psi^k)^{1/b^k} \tag{2.152}$$

$$\Psi^1 = \frac{1}{2}\left(\left| S_2^1 - S_3^1 \right|^{b^1} + \left| S_3^1 - S_1^1 \right|^{b^1} + \left| S_1^1 - S_2^1 \right|^{b^1} \right) \tag{2.153}$$

$$\Psi^2 = \frac{3^{b^2}}{2^{b^2} + 2}\left(\left| S_1^2 \right|^{b^2} + \left| S_2^2 \right|^{b^2} + \left| S_3^2 \right|^{b^2} \right) \tag{2.154}$$

where $S^k{}_{i=1-3}$ are the principal values of the stress deviator $\boldsymbol{S^k}$. The stress deviator is determined by a linear transformation $\boldsymbol{L}^k$ defined in the paper [60].

In the formulation proposed by Bron and Besson, a total number of 16 parameters are involved. Due to this fact, the model is very flexible. The convexity of the yield function has been proved.

A similar model with the Karafillis and Boyce one has been developed for anisotropic modelling of the polimeric foams by Wang and Pan [61]. An extra parameter is used to model the different yield behaviours under tension and compression.

The yield surfaces predicted by Karafillis-Boyce criterion are in very good agreement with experimental data as well as with the predictions of the Bishop-Hill theory [21]. The same agreement is also obtained when comparing the variation of the uniaxial yield stress and anisotropy coefficients in the plane of the sheet with experimental data [21]. Another advantage of the criterion is that it uses only uniaxial tensile tests for identifying the material parameters. From a mathematical point of view the method proposed by Karafillis and Boyce is both elegant and rigorous.

A disadvantage of the criterion is that the identification procedure of the tensor operator is complex and requires a numerical solution. But this is not a major difficulty when implementing the yield criterion into an FE code.

2.3.3 Yield Criteria Expressed in Polar Coordinates

2.3.3.1 Budiansky Yield Criterion

Budiansky proposed a general yield criterion [62] in a form that seems to be attractive for applications, especially when using it together with appropriate planar constitutive equations. Planar isotropy allows that any two-dimensional yield criterion is expressed as a function of the stress points $(\sigma_2 + \sigma_1)$ and $(\sigma_2 - \sigma_1)$. Budiansky's criterion can be written in the form

$$\begin{aligned} x &= \frac{\sigma_1 + \sigma_2}{2\sigma_b} = g(\alpha)\cos\alpha; \\ y &\equiv \frac{\sigma_2 - \sigma_1}{2\sigma_s} = g\,(\alpha)\sin\alpha. \end{aligned} \tag{2.155}$$

where $g\,(\alpha) > 0$ is the radial coordinate of a point located on the yield surface, α is the associated polar angle, σ_s is the yield stress in pure shear, and σ_b is the yield stress in equibiaxial tension.

The problem that arises is to establish the function $g(\alpha)$. By using the ratios $X = \sigma_b/\sigma_u$ and $Y = \sigma_b/\sigma_s$ as non-dimensional parameters characteristic of the material Eq. (2.155) can be rewritten in the form:

$$\begin{aligned} \frac{\sigma_2 + \sigma_1}{2\sigma_u} &= Xg\,(\alpha)\cos\alpha \\ \frac{\sigma_2 - \sigma_1}{2\sigma_u} &= \frac{Xg\,(\alpha)\sin\alpha}{Y} \end{aligned} \tag{2.156}$$

Hence,

$$\alpha = \tan^{-1}\left[\frac{Y(\sigma_2 - \sigma_1)}{\sigma_2 + \sigma_1}\right] \tag{2.157}$$

The associated flow rule is fully detailed in [62].

Ferron [63] proposed a yield criterion more general that by Budiansky [62] since it allows to include the case of planar anisotropy due to the dependence of g on two parameters θ and α. The function $g(\theta, \alpha)$ must satisfy the symmetry and convexity conditions imposed to the function $g(\alpha)$ in Budiansky's criterion and is determined starting from the isotropic criterion by Drucker [16].

Ferron [63] yield criterion is defined as follows:

$$(1-k)^{m/6}\, g(\theta,\alpha)^{-m} = \begin{bmatrix} F(\theta)^{m/6} + 2a\sin\theta\cos^{2n-1}\theta\cos 2\alpha + \\ +6\sin^{2p}\theta\cos^{2q}2\alpha \end{bmatrix} \tag{2.158}$$

Here a, m, n, p and q are material parameters. The identification of these parameters is made by uniaxial tensile and shearing tests.

Among the parameters in Ferron's yield function five are independent. This ensures a great flexibility of the criterion.

The obtained yield surfaces are in good agreement with experiments. The yield criterion can also model accurately the distribution of the uniaxial yield stress and coefficient r in the plane of the sheet [63].

2.3.4 Other Yield Criteria

In addition to the criteria described in the previous sections, several other non-quadratic yield criteria have been developed. With respect to their restrained use they are only described briefly.

2.3.4.1 Gotoh Yield Criterion

In order to overcome the disadvantages of the Hill 1948 criterion, Gotoh proposed in 1977 [64] a polynomial yield function of fourth degree (instead of the quadratic one) for orthotropic rolled sheet metals by writing the yield function in the form given by Hill in 1950 [65].

$$f = \sum_{i,j,k} A_{ijk}\sigma_{11}^{i}\sigma_{22}^{j}\sigma_{12}^{2k} \tag{2.159}$$

where i, j, $2k \leq 4$, x, y are the orthotropic axes, and A_{ijk} are constant coefficients.

The conditions of orthotropy and wrinkling of the blank in axisymetric deep-drawing necessitate to write for the function f

$$f = A_0 (\sigma_{11} + \sigma_{22})^2 + \left[A_1\sigma_{11}^4 + A_2\sigma_{11}^3\sigma_{22} + A_3\sigma_{11}^2\sigma_{22}^2 + A_4\sigma_{11}\sigma_{22}^3 + A_5\sigma_{22}^4 + \left(A_6\sigma_{11}^2 + A_7\sigma_{11}\sigma_{22} + A_8\sigma_{22}^2\right)\sigma_{12}^2 + A_9\sigma_{12}^4\right] \tag{2.160}$$

The first term may be considered as a function of the mean normal pressure and thus, assuming an incompressible material, A_0 is obtained. The condition to avoid wrinkling leads to the equations [64]

$$\begin{aligned} &\cos\alpha \sin\alpha F(c) = 0 \\ &c = \cos^2\alpha \\ &F(c) = 4Ac^3 + 3Bc^2 + 2Cc + D \end{aligned} \tag{2.161}$$

$A \ldots D$ are coefficients depending on $A_1 \ldots A_9$:

$$\begin{aligned} A &= (A_1 + A_3 + A_5 + A_7 + A_9) - (A_2 + A_4 + A_6 + A_8) \\ B &= (A_2 + 3A_4 + A_6 + 3A_8) - 2(A_3 + 2A_5 + A_7 + A_9) \\ C &= (A_3 + 6A_5 + A_7 + A_9) - 3(A_4 + A_8) \\ D &= A_4 + A_8 - 4A_5 \end{aligned} \tag{2.162}$$

Since the identification of the coefficients A_1–A_9 is made by means of an equibiaxial tensile test, this criterion can model the 'anomalous behavior' observed by Woodthrope and Pearce. This criterion is presented in detail in [64].

The large number of coefficients will generally allow a high flexibility of the yield criterion. The model captures the planar variation of both the uniaxial yield stress and uniaxial coefficient of plastic anisotropy. The advantages previously mentioned above explain why the model is frequently used, especially by the Japanese researchers.

A disadvantage of the criterion is its complicated form and the large number of mechanical tests needed for identifying the coefficients.

2.4 Advanced Anisotropic Yield Criteria

During the last years, the competition in the automotive and aeronautical industry has become more intense. This fact has lead to the development of new steel alloys (Bake Hardenable, Dual Phase, Complex Phase, Transformation Induced Plasticity-TRIP, Martensitic Steels, Hot-stamping boron-alloyed steels), aluminium alloys having better performances and increased interest on the use of magnesium and superplastic alloys. Since 2000, the modelling of the anisotropic behaviour of these materials has encouraged the research activities focused on the development of yield criteria. Several new models have been proposed during the last years. These models allow a very good description of the anisotropic behaviour both of steel alloys (BCC crystallographic structure), aluminium alloys (FCC structure) and magnesium alloys (HCP structure). The new yield criteria incorporate a large number of coefficients (usually, at least 8 coefficients). Due to this fact, they are able to

give an accurate description of the yield surface and follow closely the planar variations of the uniaxial yield stress and the coefficient of plastic anisotropy. Even more, some of the recently developed models can also capture the non-symmetric response in tension/compression specific to the HCP alloys. Due to the significant impact of these advanced yield criteria, they will be described in a separate subchapter entitled 'Advanced Anisotropic Yield Criteria'.

2.4.1 Barlat Yield Criteria

In order to remove the disadvantages of the Barlat 1994 and Barlat 1996 yield criteria (see Sect. 2.3.2), but aiming to preserve their flexibility, Barlat proposed in 2000 [5, 66] a new model particularized for plane stress (2D).

Let us consider a liniear transformation defined as follows:

$$\mathbf{X} = \mathbf{C} \cdot \mathbf{s} \tag{2.163}$$

where **s** is the deviatoric stress tensor and **X** the linearly transformed stress tensor. This gives 9 independent coefficients for the general case and 7 for plane stress. However, applied to plane stress conditions, only one coefficient is available to account for σ_{45} and r_{45}. As pointed out in Barlat et al. [5] additional coefficients in the context of linear transformations can be obtained by using two transformations associated to two different isotropic yield functions, respectively.

As a consequence, Barlat et al. [5] proposed a yield function expressed by the relationship

$$\Phi = \Phi' + \Phi'' = 2\sigma^a, \tag{2.164}$$

where

$$\Phi' = |\mathrm{S}_1 - \mathrm{S}_2|^a \tag{2.165}$$

$$\Phi'' = |2S_2 + S_1|^a + |2S_2 + S_2|^a \tag{2.166}$$

S_1, and S_2 are the principal deviatoric stresses and 'a' is an exponent determined based on the crystallographic structure of the material.

By applying a linear transformation to each of the isotropic functions defined by Eqs. (2.165) and (2.166), we obtain the yield function

$$\Phi = \Phi'\left(X'\right) + \Phi''\left(X''\right) = 2\sigma^a \tag{2.167}$$

where σ is the effective stress, 'a' is a material coefficient and

$$\Phi' = \left|X_1' + X_2'\right|^a \tag{2.168}$$

$$\Phi'' = \left|2X_2'' + X_1''\right|^a + \left|2X_1'' + X_2''\right|^a \tag{2.169}$$

and

$$\begin{aligned} \mathbf{X}' &= C'.s = C'.\mathbf{T}.\boldsymbol{\sigma} = L'.\boldsymbol{\sigma} \\ \mathbf{X}'' &= \mathbf{C}''.\mathbf{s} = \mathbf{C}''.\mathbf{T}.\boldsymbol{\sigma} = L''.\boldsymbol{\sigma} \end{aligned} \tag{2.170}$$

T is a matrix that transforms the Cauchy stress tensor **σ** to its deviator **s**:

$$\mathbf{T} = \begin{bmatrix} 2/3 & -1/3 & 0 \\ -1/3 & 2/3 & 0 \\ 0 & 0 & 1 \end{bmatrix} \tag{2.171}$$

C′ and C′ being the linear transformations.

In the reference frame associated with the material symmetry,

$$\begin{bmatrix} X'_{11} \\ X'_{22} \\ X'_{12} \end{bmatrix} = \begin{bmatrix} C'_{11} & C'_{12} & 0 \\ C'_{21} & C'_{22} & 0 \\ 0 & 0 & C'_{66} \end{bmatrix} \begin{bmatrix} s_{11} \\ s_{22} \\ s_{12} \end{bmatrix} \tag{2.172}$$

and

$$\begin{bmatrix} X''_{11} \\ X''_{22} \\ X''_{12} \end{bmatrix} = \begin{bmatrix} C''_{11} & C''_{12} & 0 \\ C''_{21} & C''_{22} & 0 \\ 0 & 0 & C''_{66} \end{bmatrix} \begin{bmatrix} s_{11} \\ s_{22} \\ s_{12} \end{bmatrix} \tag{2.173}$$

Because Φ' depends on $X'_1 - X'_2$, only three coefficients remain independent in C′ (see more details in [5]). In C″ are five independent coefficients. Totally, in both transformations, are 8 independent coefficients.

The principal values X_1 and X_2 of there $\mathbf{X}''$ and $\mathbf{X}''$ are the follows:

$$X_1 = \frac{1}{2}\left(X_{11} + X_{22} + \sqrt{(X_{11} - X_{22})^2 + 4X_{12}^2}\right), \tag{2.174}$$

$$X_2 = \frac{1}{2}\left(X_{11} + X_{22} - \sqrt{(X_{11} - X_{22})^2 + 4X_{12}^2}\right). \tag{2.175}$$

The coefficients of $\mathbf{L}'$ and $\mathbf{L}''$ are expressed as follows

$$\begin{bmatrix} L'_{11} \\ L'_{12} \\ L'_{21} \\ L'_{22} \\ L'_{66} \end{bmatrix} = \begin{bmatrix} 2/3 & 0 & 0 \\ -1/3 & 0 & 0 \\ 0 & -1/3 & 0 \\ 0 & 2/3 & 0 \\ 0 & 0 & 1 \end{bmatrix} \begin{bmatrix} \alpha_1 \\ \alpha_2 \\ \alpha_7 \end{bmatrix} \tag{2.176}$$

$$\begin{bmatrix} L''_{11} \\ L''_{12} \\ L''_{21} \\ L''_{22} \\ L''_{66} \end{bmatrix} = \frac{1}{9} \begin{bmatrix} -2 & 2 & 8 & -2 & 0 \\ 1 & -4 & -4 & 4 & 0 \\ 4 & -4 & -4 & 1 & 0 \\ -2 & 8 & 2 & -2 & 0 \\ 0 & 0 & 0 & 0 & 1 \end{bmatrix} \begin{bmatrix} \alpha_3 \\ \alpha_4 \\ \alpha_5 \\ \alpha_6 \\ \alpha_8 \end{bmatrix} \tag{2.177}$$

Due to the fact that 8 coefficients are incorporated in the linear transformations, we need 8 material characteristics for evaluating them. The uniaxial tension test along the rolling, diagonal and transversal directions, together with the biaxial tension test can provide only 7 characteristics (3 uniaxial yield stresses, 3 coefficients of uniaxial anisotropy and the biaxial yield stress). Barlat adopted the coefficient of biaxial anisotropy r_b as the eighth characteristic in the identification procedure. The experimental procedure used for the determination of this mechanical parameter is described in Sect. 2.1.2.

By using the same methodology as the one described above, Aretz and Barlat [67] and Barlat et al. [68] proposed a 3D yield criterion called Barlat 2004-18p:

$$\begin{aligned} \Phi = &\left|s'_1 - s''_1\right|^a + \left|s'_1 - s''_2\right|^a + \left|s'_1 - s''_3\right|^a + \left|s'_2 - s''_1\right|^a + \left|s'_2 - s''_2\right|^a + \\ &+ \left|s'_2 - s''_3\right|^a + \left|s'_3 - s''_1\right|^a + \left|s'_3 - s''_2\right|^a + \left|s'_3 - s''_3\right|^a = 4\sigma^a, \end{aligned} \tag{2.178}$$

where, σ represent the uniaxial yield stress (any other yield stress may be use as reference yield stress) and a is an exponent determined based on the crystallographic structure of the material.

The associated linear transformation on the stress deviator is defined:

$$\mathbf{C} = \begin{bmatrix} 0 & -c_{12} & -c_{13} & 0 & 0 & 0 \\ -c_{21} & 0 & -c_{23} & 0 & 0 & 0 \\ -c_{31} & -c_{32} & 0 & 0 & 0 & 0 \\ 0 & 0 & 0 & c_{44} & 0 & 0 \\ 0 & 0 & 0 & 0 & c_{55} & 0 \\ 0 & 0 & 0 & 0 & 0 & c_{66} \end{bmatrix} 0 \tag{2.179}$$

and $\mathbf{C}'$ and $\mathbf{C}''$ are obtained by adding prime and double prime symbols.

Each transformation provides 9 coefficients and totally both transformations give 18 coefficients. In order to determine all this coefficients an the minimization of the error function method is used (see [51]). If only one linear transformation is assumed the Barlat 2004-18p formulation reduce to Barlat 1991 yield criterion.

The uniaxial yield stresses and anisotropy coefficients in seven directions in the plane of the sheets (0, 15, 30, 45, 60, 75 and 90 degree to the rolling direction), the biaxial yield stress, the biaxial anisotropy coefficient and four additional data characterizing out-of-plane properties (two tensile and two simple shear yield stresses) are used in the identification of all the coeficients. For determination of the out-of-plane parameters the crystal plasticity models are nedded (see [68]).

If we adopt a yield function defined by the relationship

$$\Phi = \left|s'_1 - s''_2\right|^a + \left|s'_2 - s''_3\right|^a + \left|s'_3 - s''_1\right|^a - \{\left|s'_1\right|^a + \left|s'_2\right|^a + \left|s'_3\right|^a\} + \left|s''_1\right|^a + \left|s''_2\right|^a + \left|s''_3\right|^a = 4\sigma^a, \tag{2.180}$$

the number of coefficients incorporated in the linear transformations will reduce to 13:

$$\mathbf{C}' = \begin{bmatrix} 0 & -1 & -c'_{13} & 0 & 0 & 0 \\ -c'_{21} & 0 & -c'_{23} & 0 & 0 & 0 \\ -1 & -1 & 0 & 0 & 0 & 0 \\ 0 & 0 & 0 & c'_{44} & 0 & 0 \\ 0 & 0 & 0 & 0 & c'_{55} & 0 \\ 0 & 0 & 0 & 0 & 0 & c'_{66} \end{bmatrix} \tag{2.181}$$

$$\mathbf{C}'' = \begin{bmatrix} 0 & -c''_{12} & -c''_{13} & 0 & 0 & 0 \\ -c''_{21} & 0 & -c''_{23} & 0 & 0 & 0 \\ -1 & -1 & 0 & 0 & 0 & 0 \\ 0 & 0 & 0 & c''_{44} & 0 & 0 \\ 0 & 0 & 0 & 0 & c''_{55} & 0 \\ 0 & 0 & 0 & 0 & 0 & c''_{66} \end{bmatrix} \tag{2.182}$$

For the plane stress case the number of the coefficients are reduced from 13 to 9.

The yield function has been tested for different aluminium alloys exhibiting a pronounced anisotropy. The model has proved its capability to provide an accurate prediction of the planar variations of the uniaxial yield stress and coefficient of plastic anisotropy.

The implementation of the Barlat 2004-18p model in finite-element codes [69] proved its capability to predict the occurrence of six and eight ears in the process of cup drawing. Barlat 2004-18p is one of the phenomenological model being able to capture more than 4 ears. This is the most important advantage of the yield criterion. Of course, it is possible to develop models incorporating more and more linear transformations and thus having a larger number of coefficients. The practical difficulty related to the use of such yield criteria consists in the experimental determination of the mechanical parameters needed for the evaluation of the coefficients.

The disadvantages of the models presented above are:

- due to the complexity of the formulation, they are not user-friendly
- they need crystal plasticity models for the evaluation of some parameters.

The Barlat 2004-18p is implemented in the LS Dyna commercial code.

2.4.2 Banabic–Balan–Comsa (BBC) Yield Criteria

In 2000 the members of the CERTETA[1] team started a research programme having as principal objective the development of a model able to provide an accurate description of the yield surfaces predicted by texture computations. The new formulation was developed on the basis of the isotropic formulation proposed by Hershey. By adding weight coefficients to that model, the researchers succeeded in developing a flexible yield criterion. The last version incorporates a number of 8 coefficients and, consequently, its identification procedure uses 8 mechanical parameters (3 uniaxial yield stresses, 3 uniaxial coefficients of anisotropy, the biaxial yield stress and the biaxial coefficient of plastic anisotropy).

The first formulation of the yield criterion was proposed by Banabic et al. [51] in the form

$$\overline{\sigma} = \left[a\left(b\Gamma + c\Psi\right)^{2k} + a\left(b\Gamma - c\Psi\right)^{2k} + (1-a)\left(2c\Psi\right)^{2k}\right]^{\frac{1}{2k}} \tag{2.183}$$

where *a, b, c,* and k are material parameters, while Γ and Ψ are functions of the second and third invariants of a transformed stress tensor $\boldsymbol{s\prime} = \boldsymbol{L}\sigma$, where $\boldsymbol{L}$ is a 4th order tensor. In this formulation anisotropy is described by means of the tensor $\boldsymbol{L}$, which satisfies: (i) the symmetry conditions $L_{ijkl} = L_{jikl} = L_{jilk} = L_{klij}$ ($i, j, k, l = 1\ldots3$), (ii) the requirement of invariance with respect to the symmetry group of the material, and (iii) the three conditions $L_{1k} + L_{2k} + L_{3k} = 0$ (for $k = 1$, 2, and 3), which ensures that $\boldsymbol{s}'$ is traceless (see Karafillis–Boyce [21]). Hence, in the reference system associated with the directions of orthotropy, the tensor $\boldsymbol{L}$ has 6 non-zero components for 3D conditions and 4 components for plane stress state.

Let define (1, 2, 3), the reference frame associated with orthotropy. For a rolled sheet, 1, 2, and 3 represent the rolling direction, the long transverse direction, and the short transverse direction, respectively. In the reference system (1, 2, 3):

$$\begin{aligned} s'_{11} &= d\sigma_{11} + e\sigma_{22} \\ s'_{22} &= e\sigma_{11} + f\sigma_{22} \\ s'_{33} &= -\left(d+e\right)\sigma_{11} - \left(e+f\right)\sigma_{22} \\ s'_{12} &= g\sigma_{12} \\ s'_{13} &= s'_{23} = 0 \end{aligned} \tag{2.184}$$

where *d, e, f,* and *g* are the four independent components of the tensor $\boldsymbol{L}$.

The expressions of Γ and Ψ in terms of the stress components are

$$\begin{aligned} \Gamma &= M\sigma_{11} + N\sigma_{22} \\ \Psi &= \sqrt{\left(P\sigma_{11} + Q\sigma_{22}\right)^2 + R\sigma_{12}^2} \end{aligned} \tag{2.185}$$

[1] Research Centre in Sheet Metal Forming Technology belong the Technical University of Cluj Napoca, Romania (http://www.certeta.utcluj.ro).

where

$$\begin{aligned} M &= d + e \\ N &= e + f \\ P &= \frac{d - e}{2} \\ Q &= \frac{e - f}{2} \\ R &= g^2 \end{aligned} \tag{2.186}$$

(for more details see Banabic et al. [52]).

The convexity of the yield surface described by (2.183) is ensured if $a \in [0, 1]$ and k is a strictly positive integer number.

The yield stress in uniaxial tension along an axis at orientation θ to the rolling direction ***x,*** the equibiaxial yield stress and the coefficient of plastic anisotropy associated to a direction inclined at an angle $\theta \in [0, 90°]$ with the rolling direction are presented in the paper [70]. Further details related to the evaluation of the coefficients as well as to the experimental validation of the BBC2000 yield criterion can be found in the paper [70].

The shape of the yield surface is defined by the material parameters *a, b, c, d, e, f, g,* and *k*. Among these parameters, *k* has a distinct status. More precisely, its value is set in accordance with the crystallographic structure of the material [45]: $k = 3$ for BCC alloys, and $k = 4$ for FCC alloys. The other 7 parameters are determined such that the model reproduces as well as possible the following experimental characteristics of the orthotropic sheet metal: ${\sigma_0}^{exp}$, ${\sigma_{90}}^{exp}$, ${\sigma_{45}}^{exp}$, ${\sigma_b}^{exp}$, ${r_0}^{exp}$, ${r_{90}}^{exp}$ and ${r_{45}}^{exp}$. It is possible to obtain their values by solving a set of seven non-linear equations.

An improvement of this criterion was proposed by Banabic et al. [53] in order to account for an additional mechanical parameter, namely, the biaxial anisotropy coefficient. The new formulation is given by:

$$\sigma = \left[a\,(\Gamma + \Psi)^{2k} + a\,(\Gamma - \Psi)^{2k} + (1 - a)\,(2\Lambda)^{2k} \right]^{\frac{1}{2k}} \tag{2.187}$$

where $k \in \mathbf{N} \geq 1$ and $0 \leq a \leq 1$are material parameters, while Γ, Ψ and Λ are functions depending on the planar components of the stress tensor:

$$\begin{aligned} \Gamma &= \frac{\sigma_{11} + M\,\sigma_{22}}{2} \\ \Psi &= \sqrt{\left(\frac{N\sigma_{11} - P\,\sigma_{22}}{2} \right)^2 + Q^2 \sigma_{12}\sigma_{21}} \\ \Lambda &= \sqrt{\left(\frac{R\,\sigma_{11} - S\,\sigma_{22}}{2} \right)^2 + T^2 \sigma_{12}\sigma_{21}} \end{aligned} \tag{2.188}$$

where the quantities *M, N, P, Q, R, S* and *T* are also material parameters.

More details converning the uniaxial yield stress and anisotropy coefficients variations are presented in the paper [53]. Further details related to the evaluation of the quantities mentioned above as well as to the convergence of

Table 2.1 Different strategies to identify the coefficients in the BBC2003 yield function

Mechanical parameters	BBC2003-8	BBC2003-7	BBC2003-6	BBC2003-5	BBC2003-4	BBC2003-2
σ_0	■	■	■	■	■	■
σ_{45}	■	■	■			
σ_{90}	■	■	■			
σ_b	■	■		■		
r_0	■	■	■	■	■	■
r_{45}	■	■	■	■	■	
r_{90}	■	■	■	■	■	
r_b	■					

the identification procedure of the BBC2003 yield criterion can be found in the paper [71].

The other eight parameters are determined such that the model reproduces the experimental characteristics of the orthotropic sheet metal as well as possible, namely, σ_0, σ_{45}, σ_{90}, σ_b, r_0, r_{45}, r_{90} and r_b. It is possible to obtain the value of these parameters by solving a set of eight non-linear equations. However, this set of equations has multiple solutions. A more effective strategy of identification is to impose the minimization of the following error function:

$$\mathcal{F}(\mathrm{a,M,N,P,Q,R,S,T}) = \left(\frac{\mathrm{r_0^p}}{\mathrm{r_0}} - 1\right)^2 + \left(\frac{\mathrm{r_{45}^p}}{\mathrm{r_{45}}} - 1\right)^2 + \left(\frac{\mathrm{r_{90}^p}}{\mathrm{r_{90}}} - 1\right)^2 + \left(\frac{\mathrm{r_b^p}}{\mathrm{r_b}} - 1\right)^2 + \left(\frac{\sigma_0^{\mathrm{p}}}{\sigma_0} - 1\right)^2 + \left(\frac{\sigma_{45}^{\mathrm{p}}}{\sigma_{45}} - 1\right)^2 + \left(\frac{\sigma_{90}^{\mathrm{p}}}{\sigma_{90}} - 1\right)^2 + \left(\frac{\sigma_{\mathrm{b}}^{\mathrm{p}}}{\sigma_{\mathrm{b}}} - 1\right)^2 \tag{2.189}$$

where the superscript $(.)^p$ denotes the values predicted by the constitutive equation.

For the numerical minimization, the downhill simplex method proposed by Nelder and Mead [72] has been adopted because it does not need the evaluation of the gradients. The identification procedure can also use a reduced number of mechanical parameters (2, 4, 5, 6 or 7), as shown in Table 2.1. The particular set of mechanical parameters used by each identification strategy is specified in the table. The author have also developed identification procedures based on uniaxial and plane-strain experimental data [71].

A version of the BBC 2003 yield criterion has been improved by Aretz [73].

The BBC2003 yield criterion is reducible both to Hill 1948 and Barlat 1989 formulations (see more details in Sect. 2.3).

Barlat et al. [74] showed that the BBC 2003 and Barlat 2000 are the same. But one should notice that the development procedures adopted by the authors where different: the BBC models emerged in a classical manner by adding coefficients to Hershey's formulation, while Barlat 2000 used two linear transformations.

The most important advantages of these models are:

- the yield functions have simple expressions
- they are able to describe accurately the yield surface and also give good predictions of the planar distribution of the uniaxial yield stress and uniaxial coefficient of plastic anisotropy

- the predicted shape of the yield surface closely follows the results of the texture models
- the CPU time needed for the simulation of complex sheet metal forming processes is not considerably increased
- the models can be used also in the cases when less then 8 mechanical parameters are available (e.g., 2, 4, 5, 6 or 7 parameters)
- the models are reducible to classical formulations such as Hill 1948 or Barlat 1989.

The following disadvantages can be mentioned:

- the formulation of the yield criterion is not very user-friendly
- the coefficients of the yield function do not have a direct physical meaning
- the development of 3D extensions is difficult.

A modified version of this criterion (BBC 2005) has been implemented in the AutoForm 4.1 commercial Finite Element program (issued May 2007).

2.4.3 Cazacu–Barlat Yield Criteria

To introduce orthotropy in the expression of an isotropic criterion, Cazacu and Barlat [75] proposed an alternative method based of the theory of the representation of tensor functions. They developed a method of generalizations of the invariants of the stress deviator J_2 and J_3. Based on this method, an anisotropic yield criterion is obtained by substituting the expression of the stress deviator invariants in the isotropic criterion by their respective anisotropic forms.

The generalized forms of the invariants, J_3^0 and J_2^0, respectively, are:

$$\begin{aligned} J_3^o = & \frac{1}{27}(b_1 + b_2)\,\sigma_{11}^3 + \frac{1}{27}(b_3 + b_4)\,\sigma_{22}^3 + \frac{1}{27}\,[2\,(b_1 + b_4) - b_2 - b_3]\,\sigma_{33}^3 \\ & - \frac{1}{9}\,(b_1\sigma_{22} + b_2\,\sigma_{33})\,\sigma_{11}^2 - \frac{1}{9}\,(b_3\,\sigma_{33} + b_4\,\sigma_{11})\,\sigma_{22}^2 \\ & - \frac{1}{9}\,[(b_1 - b_2 + b_4)\,\sigma_{11} + (b_1 - b_3 + b_4)\,\sigma_{22}]\,\sigma_{33}^2 \\ & + \frac{2}{9}\,(b_1 + b_4)\,\sigma_{11}\,\sigma_{22}\sigma_{33} - \frac{\sigma_{xz}^2}{3}\,[2\,b_9\,\sigma_{22} - b_8\,\sigma_{33} - (2\,b_9 - b_8)\,\sigma_{11}] \\ & - \frac{\sigma_{12}^2}{3}\,[2\,b_{10}\,\sigma_{33} - b_5\,\sigma_{22} - (2\,b_{10} - b_5)\,\sigma_{11}\,] \\ & - \frac{\sigma_{23}^2}{3}\,[(b_6 + b_7)\,\sigma_{11} - b_6\sigma_{22} - b_7\sigma_{33}\,] + 2\,b_{11}\sigma_{12}\sigma_{13}\sigma_{23}\,. \end{aligned} \tag{2.190}$$

where the coefficients b_k ($k = 1 \ldots 11$) describe the anisotropy and they reduce to unity for isotropic conditions.

$$J_2^o = \frac{a_1}{6}(\sigma_{11} - \sigma_{22})^2 + \frac{a_2}{6}(\sigma_{22} - \sigma_{33})^2 + \frac{a_3}{6}(\sigma_{11} - \sigma_{33})^2 + a_4\sigma_{12}^2 + a_5\sigma_{13}^2 + a_6\sigma_{23}^2 \tag{2.191}$$

where the coefficients a_k ($k = 1 \ldots 6$) describe the anisotropy and they reduce to unity in the isotropic case. Note that J_2^0 is Hill's [25] quadratic yield function.

In Cazacu and Barlat [75], this approach was used to extend Drucker's [16] isotropic yield criterion to an orthotropic one. For this case the expression of the proposed orthotropic criterion is:

$$f^O = \left(J_2^o\right)^3 - c\left(J_3^o\right)^2 = k^2. \tag{2.192}$$

where c is a constant,

$$k^2 = 18\left(\frac{Y}{3}\right)^6 \tag{2.193}$$

and Y is the uniaxial limit stress.

For the in-plane case the yield function may be writen in the form:

$$f_2^O \equiv \left[\tfrac{1}{6}(a_1 + a_3)\,\sigma_{11}^2 - \tfrac{a_1}{3}\sigma_{11}\sigma_{22} + \tfrac{1}{6}(a_1 + a_2)\,\sigma_{22}^2 + a_4\sigma_{12}^2\right]^3 - c\left\{\begin{array}{l}\frac{1}{27}(b_1 + b_2)\,\sigma_{11}^3 + \frac{1}{27}(b_3 + b_4)\,\sigma_{22}^3 \\ -\frac{1}{9}(b_1\sigma_{11} + b_4\sigma_{22})\,\sigma_{11}\sigma_{22} \\ -\frac{1}{3}\sigma_{12}^2[(b_5 - 2b_{10})\,\sigma_{11} - b_5\sigma_{22}]\end{array}\right\}^2 = k^2. \tag{2.194}$$

where $a_1 - a_4$ and $b_1 - b_5$ and b_{10} are coefficients describing the anisotropy, c is a constant and k is expressed by Eq. (2.193).

As one may see, the yield function incorporates 10 anisotropy coefficients and an extra constant c. The 10 anisotropy coefficients and the value of c can be determined from the measured uniaxial yield stresses σ_θ and strain ratios r_θ in 5 different orientations and σ_b, the value of the equibiaxial tensile stress. In the 3D case, the model incorporates 18 coefficients.

The yield stress in uniaxial tension along an axis at orientation θ to the rolling direction is predicted by:

$$\sigma_\theta = k^{\frac{1}{3}}\left\{\left[\tfrac{1}{6}(a_1 + a_3)\cos^4\theta + (a_4 - a_1/3)\cos^2\theta\sin^2\theta + \tfrac{1}{6}(a_1 + a_2)\sin^4\theta\right]^3 - c\left[\begin{array}{l}\frac{1}{27}(b_1 + b_2)\cos^6\theta + \frac{1}{27}(b_3 + b_4)\sin^6\theta \\ -\frac{1}{9}\left[\begin{array}{l}(b_1 + 3b_5 - 6b_{10})\cos^2\theta + \\ +(b_4 - 3b_5)\sin^2\theta\end{array}\right]\sin^2\theta\cos^2\theta\end{array}\right]^2\right\}^{-1/6} \tag{2.195}$$

and the biaxial yield stress by:

$$\sigma_b \;=\; k^{\frac{1}{3}}\left[\left(\frac{a_2 \;+\; a_3}{6}\right)^3 \;-\; c\;\left(\frac{-2\;b_1 \;+\; b_2 \;+\; b_3 \;-2b_4}{27}\right)^2\right]^{-\frac{1}{6}} \tag{2.196}$$

Yielding under pure shear parallel to the orthotropic axes occurs when σ_{xy} is equal to

$$\tau \;=\; k^{\frac{1}{3}}\,(a_4)^{-\frac{1}{2}} \tag{2.197}$$

In order to predict the distribution of the anisotropy coefficient r_θ, the function f_2^0 defined by Eq. (2.194) should be replaced in the relationship

$$r_\theta \;=\; -\;\frac{\sin^2\theta\;\frac{\partial f^o}{\partial\sigma_x} \;-\sin 2\theta\;\frac{\partial f^o}{\partial\,\sigma_{xy}} \;+\; \cos^2\;\theta\;\frac{\partial f^o}{\partial\,\sigma_y}}{\frac{\partial f^o}{\partial\sigma_x} \;+\; \frac{\partial f^o}{\partial\sigma_y}} \tag{2.198}$$

Cazacu and Barlat [76] also applied the representation theorems for transverse isotropy and cubic symmetries. The general expressions of the invariants of the stress deviators in these conditions are presented in detail in [75]. The method is applied for the extension of Drucker's isotropic yield criterion to transverse isotropy and cubic symmetries.

Aiming to develop models of the asymmetrical tension/compression behaviour specific to the alloys having a Hexagonal Closed Packed-HCP structure, Cazacu and Barlat have successfully used the representation theory of tensor functions. They have proposed an isotropic yield function in the form [77]:

$$f = (\mathrm{J}_2)^{3/2} - cJ_3 = \tau_Y^3 \tag{2.199}$$

where τ_Y is the yield stress in pure shear and c a constant. This constant can be expressed in the terms of the uniaxial yield stresses in tension σ_T and compression σ_C, respectively, as follow:

$$c = \frac{3\sqrt{3}(\sigma_T^3 - \sigma_C^3)}{2(\sigma_T^2 + \sigma_C^2)}. \tag{2.200}$$

Anisotropy was introduced in the formulation using the same method presented above.

For plane stress conditions, the yield locus is:

$$\left[\frac{1}{3}\left(\sigma_1^2 - \sigma_1\sigma_2 + \sigma_2^2\right)\right]^{3/2} - \frac{c}{27}[2\sigma_1^3 + \sigma_2^3 - 3(\sigma_1 + \sigma_2)\sigma_1\sigma_2] = \tau_Y^3, \tag{2.201}$$

where σ_1 and σ_2 are the principal stresses.

The expressions of the anisotropic yield function and of the uniaxial yield stresses in tension and compression along an axis at orientation θ to the rolling direction direction are presented in [77]. The predictions of the biaxial yield stresses corresponding to the tension and compression, as well as the planar distribution of the anisotropy coefficient are also presented.

The yield function defined by Eq. (2.190) is a third-order expression. The experimental researches [78] have shown that for some HCP alloys (e.g., titanium based alloys) the yield surface is better described by fourth order functions. As a consequence, in order to describe such a behaviour, Cazacu et al. [79] proposed an isotropic yield function for which the degree of homogeneity a is not fixed:

$$\Phi = \left||S_1| - kS_1\right|^a + \left||S_2| - kS_2\right|^a + \left||S_3| - kS_3\right|^a, \tag{2.202}$$

where, S_1, S_2, S_3 are the principal values of the stress deviator, a—an positive integer and k—the strength differential parameter.

In order to extend the isotropic criterion defined by Eq. (2.202) to an anisotropic formulation, the principal values of the deviatoric stress (S_1, S_2, S_3) are replaced by the principal values of the transformed tensor (Σ_1, Σ_2, Σ_3), obtained after applying a linear transformation. In this way, the new anisotropic yield criterion (CPB05) can be written as

$$\Phi = \left||\Sigma_1| - k\Sigma_1\right|^a + \left||\Sigma_2| - k\Sigma_2\right|^a + \left||\Sigma_3| - k\Sigma_3\right|^a. \tag{2.203}$$

The paper [79] gives a detailed presentation of the relationships used to predict the uniaxial yield stresses and the coefficients of plastic anisotropy both for tension and compression states. Additional linear transformations can be incorporated into the CPB 2005 criterion for an improved representation of the anisotropy.

The most important advantage of this yield criterion consists in its capability to provide an accurate description of the tension/compression behaviour specific to the magnesium and titanium alloys.

2.4.4 Vegter Yield Criterion

Using points of the yield locus which had been determined directly by experiments, Vegter [80, 81] obtained the yield locus in the first quadrant by applying a Bezier interpolation. The Vegter criterion requires the determination of three parameters for each reference point (two principal stresses σ_1 and σ_2 and the strain vector $\rho = d\varepsilon_2/d\varepsilon_1$). In order to describe planar anisotropy Vegter's criterion needs as many as 17 parameters.

The analytical expression of the criterion is

$$\begin{pmatrix}\sigma_1\\ \sigma_2\end{pmatrix} = (1-\lambda)^2 \begin{pmatrix}\sigma_1\\ \sigma_2\end{pmatrix}_i^r + 2\lambda\,(1-\lambda) \begin{pmatrix}\sigma_1\\ \sigma_2\end{pmatrix}_i^h + \lambda^2 \begin{pmatrix}\sigma_1\\ \sigma_2\end{pmatrix}_{i+1}^r \tag{2.204}$$

for σ_e and angle φ where

$$\begin{pmatrix} \sigma_1 \\ \sigma_2 \end{pmatrix}^{r}_{i+1} = \sum_{j=0}^{m\cos} \begin{pmatrix} a_1^j \\ a_2^j \end{pmatrix}^{r}_{i} \cos(2j\varphi) \tag{2.205}$$

is a trigonometric expansion associated to the reference point;

$$R(\varphi) = \sum_{j=0}^{m\cos} b^j \cos(2j\varphi) \tag{2.206}$$

is cosine interpolation of the function $R(\varphi)$; φ is the angle between the principal directions and the orthotropic axes; λ is a parameter of the Bézier function; r is a superscript denoting the reference point; h is a superscript denoting the breaking point; $\begin{pmatrix} a_1^j \\ a_2^j \end{pmatrix}^{r}_{i}$ are parameters of the trigonometric interpolation to be determined at the reference points; b^j are parameters of the trigonometric interpolation of the R-function.

The most important advantage of the criterion is the flexibility ensured by the large number of parameters. Disadvantages are the unfriendly form of the yield function making it improper for analytical computation; the large number of experiments required (uniaxial tension, biaxial tension, plane strain and pure shearing) and the necessity of mathematical abilities of the user.

The Vegter's model has been implemented in the PAMSTAMP FE commercial program.

Mollica and Srinivasa [82] proposed a method for generating the yield locus similar to the one presented above. A simple way to obtain a closed convex surface is to consider the intersection of a sufficient number of elementary convex surfaces. Each elementary surface is defined by an equation having the form $f_i = 0$. In order to avoid the sharp corners and edges a special regularization procedure is proposed. The method is illustrated in [82] for Hill 1948 [25] and Hosford [31] criteria.

2.4.5 Polynomial Yield Criteria

Hill [65] proposed in 1950 a general formulation of a plane-stress anisotropic yield criterion having the polynomial expression defined by Eq. (2.159). Gotoh [64] succeeded to apply that idea in the 1970s by developing a polynomial yield function of fourth degree (see Sect. 2.3.4).

During the last years, a new family of polynomial yield criteria has been created on the basis of Hill's idea.

2.4.5.1 Hu Yield Criteria

Hu [83] proposed a yield criterion in the form

$$f(\sigma_{ij}) = \frac{1}{\sigma_0^4}\sigma_{11}^4 - \frac{4R_0}{(1+R_0)\sigma_0^4}\sigma_{11}^3\sigma_{22} + [\frac{1}{\sigma_b^4} - \frac{1}{\sigma_0^4} - \frac{1}{\sigma_{90}^4} + \frac{4R_{90}}{(1+R_{90})\sigma_{90}^4} + \\ + \frac{4R_0}{(1+R_0)\sigma_0^4}]\sigma_{11}^2\sigma_{22}^2 - \frac{4R_{90}}{(1+R_{90})\sigma_{90}^4}\sigma_{11}\sigma_{22}^3 + \frac{1}{\sigma_{90}^4}\sigma_{22}^4 + \\ + [\frac{16}{(1+R_{45})\sigma_{45}^4} - \frac{2}{\sigma_b^4}](\sigma_{11}^2 + \sigma_{22}^2 - \sigma_{11}\sigma_{22})\sigma_{12}^2 + [\frac{1}{\sigma_b^4} + \frac{16R_{45}}{(1+R_{45})\sigma_{45}^4}]\sigma_{12}^4 = 1. \tag{2.207}$$

The planar distributions of the uniaxial yield stress and of the anisotropy coefficient are presented in [83]. Hu also succeeded to develop a 3D extension of his criterion [84]. A quadratic formulation of the yield function has been presented by Hu in [85].

2.4.5.2 Wang Yield Criterion

Wang (2005, Constitutive Modeling of Orthotropic Plasticity in Sheet Metals, private communication) proposed a 2D polynomial formulation of the yield function as:

$$\sigma_{11}^{m+1} - F\sigma_{11}^m\sigma_{22} - G\frac{\beta}{\alpha}\sigma_{11}\sigma_{22}^{m+1} + \frac{\beta}{\alpha}\sigma_{22}^{m+1} + \frac{\gamma}{\alpha}\sigma_{12}^{m+1} = \sigma_Y^{m+1} \tag{2.208}$$

where m is an odd integer 3, 5 or 7 (depending on the crystallographic structure), F, G, β/α and γ/α are anisotropic coefficients and σ_Y is the uniaxial yield stress in the rolling direction.

2.4.5.3 Comsa Yield Criterion

Comsa also developed in his PhD thesis [86] a polynomial criterion of sixth order:

$$\Phi = \left[\begin{matrix} p_1(L+M)(cL+M)(L+cM)+ \\ +p_2(L+N)(cL+N)(L+cN) \end{matrix}\right]^{1/6} - Y, \tag{2.209}$$

where,

$$\begin{aligned} L &= (p_3\sigma_{11} - p_4\sigma_{22})^2 + \sigma_{12}\sigma_{21}, \\ M &= (p_5\sigma_{11} - p_6\sigma_{22})^2 + \sigma_{12}\sigma_{21}, \\ N &= (p_7\sigma_{11} - p_8\sigma_{22})^2. \end{aligned} \tag{2.210}$$

and $c = (2+\sqrt{3})^2$, p_1 –p_8 (p_1 –$p_8 > 0$) are the material parameters and Y is the yield parameter. As one may see in the above relationship, the yield function incorporates

8 coefficients. These coefficients can be evaluated by using three uniaxial tensile tests and a biaxial tensile experiment.

The convexity of the yield surface is proved in [86]. The relationships used to evaluate the uniaxial/biaxial yield stress and the uniaxial/biaxial coefficients of plastic anisotropy are also presented.

The predictions of the model have been tested by comparison with experimental data for several types of materials (steel and aluminium alloys). The yield criterion has been also implemented by the author in the LS-DYNA programme and used for the numerical simulation of various sheet metal forming processes (deep-drawing and bending) [87].

2.4.5.4 Soare Yield Criteria

Soare [88] proposed three yield criteria expressed by polynomial functions of 4th, 6th and 8th order, respectively (Poly 4, 6 and 8).

The yield function is defined as

$$f(\sigma_{11},\, \sigma_{22},\, \sigma_{12}) := [P_n(\sigma_{11},\, \sigma_{22},\, \sigma_{12})]^{1/n}, \tag{2.211}$$

where, P_n is the polynomial function and n—the order of the polynomial function.

The form of the orthotropic fourth order polynomial (Poly 4) is:

$$\begin{aligned} P_4 = {} & a_1\sigma_{11}^4 + a_2\sigma_{11}^3\sigma_{22} + a_3\sigma_{11}^2\sigma_{22}^2 + a_4\sigma_{11}\sigma_{22}^3 + a_5\sigma_{22}^4 + \\ & + (a_6\sigma_{11}^2 + a_7\sigma_{11}\sigma_{22} + a_8\sigma_{22}^2)\sigma_{12}^2 + a_9\sigma_{12}^4 \end{aligned} \tag{2.212}$$

where $a_1 - a_9$ are coefficents describing the anisotropy.

The formulation proposed by Soare for the fourth order yield function differs from Gotoh's model [64] only in one aspect: elimination of the first term in Eq. (2.160). Soare has paid a special attention to the convexity analysis. He has proposed an original identification strategy which is able to remove the large overall error affecting Gotoh's procedure.

The 6th and 8th order polynomial functions developed by Soare are

$$\begin{aligned} P_6 = {} & a_1\sigma_{11}^6 + a_2\sigma_{11}^5\sigma_{22} + a_3\sigma_{11}^4\sigma_{22}^2 + a_4\sigma_{11}^3\sigma_{22}^3 + a_5\sigma_{11}^2\sigma_{22}^4 + a_6\sigma_{11}\sigma_{22}^5 + a_7\sigma_{22}^6 + \\ & + (a_8\sigma_{11}^4 + a_9\sigma_{11}^3\sigma_{22} + a_{10}\sigma_{11}^2\sigma_{22}^2 + a_{11}\sigma_{11}\sigma_{22}^3 + a_{12}\sigma_{22}^4)\sigma_{12}^2 + \\ & + (a_{13}\sigma_{11}^2 + a_{14}\sigma_{11}\sigma_{22} + a_{15}\sigma_{22}^2)\sigma_{12}^4 + a_{16}\sigma_{12}^2, \end{aligned} \tag{2.213}$$

respectively,

$$\begin{aligned} P_8 = {} & a_1\sigma_{11}^8 + a_2\sigma_{11}^7\sigma_{22} + a_3\sigma_{11}^6\sigma_{22}^2 + a_4\sigma_{11}^5\sigma_{22}^3 + a_5\sigma_{11}^4\sigma_{22}^4 + a_6\sigma_{11}^3\sigma_{22}^5 + a_7\sigma_{11}^2\sigma_{22}^6 + \\ & + a_8\sigma_{11}\sigma_{22}^7 + a_9\sigma_{22}^8 + (a_{10}\sigma_{11}^6 + a_{11}\sigma_{11}^5\sigma_{22} + a_{12}\sigma_{11}^4\sigma_{22}^2 + a_{13}\sigma_{11}^3\sigma_{22}^3 + a_{14}\sigma_{11}^2\sigma_{22}^4 + \\ & + a_{15}\sigma_{11}\sigma_{22}^5 + a_{16}\sigma_{22}^6)\sigma_{12}^2 + (a_{17}\sigma_{11}^4 + a_{18}\sigma_{11}^3\sigma_{22} + a_{19}\sigma_{11}^2\sigma_{22}^2 + a_{20}\sigma_{11}\sigma_{22}^3 + \\ & + a_{21}\sigma_{22}^4)\sigma_{12}^4 + (a_{22}\sigma_{11}^2 + a_{23}\sigma_{11}\sigma_{22} + a_{24}\sigma_{22}^2)\sigma_{12}^6 + a_{25}\sigma_{12}^2. \end{aligned} \tag{2.214}$$

As one may notice, Poly 6 and 8 have 16 and 25 coefficients. The procedure used for evaluating them is based on the minimisation of an error-function. Due to the large number of coefficients, Poly 6 and 8 allow a better description of the plastic behaviour, even in the case of materials exhibiting a pronounced variation of the anisotropy characteristics. By implementing them in finite-element codes, the author has proved the ability of the new models to capture the occurrence of 6 or 8 ears in the deep-drawing process of cylindrical cups. The strength-differential effect into the yield surface has been also introduced in these formulations [89].

The most important advantages of these yield criteria are as follows:

- Simplicity of the formulation
- Direct formulation (use of the actual stress components)
- Flexibility ensured by the large number of coefficients (Poly 6 and 8)
- Easy extension to 3D stress states (see [88]).

The are also some disadvantages that should be mentioned:

- Not all the formulations are convex. Due to this fact, the variation range of some coefficients must be bounded
- The identification procedure is quite complex, especially for the Poly 6 and 8 models.

A quadratic yield model to describe the ortotropic behaviour of the sheet metals has been proposed by Oller et al. [90]. It deals with the case in which the yield stress in simple tension is different from the one in compression.

2.5 BBC 2005 Yield Criterion

2.5.1 Equation of the Yield Surface

The sheet metal is assumed to behave as a plastically orthotropic membrane under plane stress conditions. By making this assumption, we can use the following description of the yield surface:

$$\Phi\left(\sigma_{\alpha\beta}, Y\right) \; := \; \overline{\sigma}\left(\sigma_{\alpha\beta}\right) \; - \; Y \; = \; 0 \tag{2.215}$$

where $\overline{\sigma}\left(\sigma_{\alpha\beta}\right) > 0$ is the BBC 2005 equivalent stress (see Sect. 2.5.3), $Y > 0$ is a yield parameter, and $\sigma_{\alpha\beta} = \sigma_{\beta\alpha}$ $(\alpha, \beta = 1, 2)$ are planar components of the stress tensor expressed in an orthonormal basis superimposed to the axes of plastic orthotropy: (1) rolling direction (RD), (2) transverse direction (TD), (3) normal direction (ND). The other components are subjected to the restriction

$$\sigma_{3i} = \sigma_{i3} = 0, \; (i = 1, 2, 3) \tag{2.216}$$

arising from the plane stress hypothesis. Whenever not clearly specified, we shall use the following convention: Greek indices take the values 1 and 2, while the Latin ones take the values 1, 2 and 3.

The BBC 2005 yield criterion does not enforce some special constraints on the choice of the yield parameter (Y). In fact, any quantity representing a yield stress can act as Y. For example, Y may be the uniaxial yield stress Y_θ associated to a direction defined by the angle θ measured from RD, an average of several uniaxial yield stresses, or the biaxial yield stress Y_b associated to RD and TD.

2.5.2 Flow Rule Associated to the Yield Surface

The flow rule associated to the yield surface described by Eq. (2.215) is

$$\sigma_{3i} = \sigma_{i3} = 0, \ (i = 1, 2, 3) \tag{2.216}$$

$$\dot{\varepsilon}^p_{\alpha\beta} = \dot{\lambda}\frac{\partial \Phi}{\partial \sigma_{\alpha\beta}}, \quad \alpha, \beta = 1, 2 \tag{2.217}$$

where $\dot{\varepsilon}^p_{\alpha\beta} = \dot{\varepsilon}^p_{\alpha\beta}$ $(\alpha, \beta = 1, 2)$ are planar components of the plastic strain-rate tensor (expressed in the same basis as the corresponding components of the stress tensor), and $\dot{\lambda} \geq 0$ is a scalar multiplier (its significance is not essential for our discussion). The out of plane components of the plastic strain-rate tensor are subjected to the restrictions

$$\dot{\varepsilon}^p_{3\alpha} = \dot{\varepsilon}^p_{\alpha 3} = 0, \quad \alpha = 1, 2 \tag{2.218}$$

$$\dot{\varepsilon}^p_{33} = -\dot{\varepsilon}^p_{11} - \dot{\varepsilon}^p_{22} \tag{2.219}$$

arising from the plane stress hypothesis and the isochoric character of the plastic deformation.

When using Eq. (2.217) we need the partial derivatives of the function Φ with respect to the planar components of the stress tensor. Equation (2.215) allows us to calculate them as partial derivatives of the equivalent stress:

$$\frac{\partial \Phi}{\partial \sigma_{\alpha\beta}} = \frac{\partial \overline{\sigma}}{\partial \sigma_{\alpha\beta}}, \quad \alpha, \beta = 1, 2 \tag{2.220}$$

2.5.3 BBC 2005 Equivalent Stress

The equivalent stress used in Eq. (2.215) is defined by the following formula:

$$\overline{\sigma} = \left[a\,(\Lambda + \Gamma)^{2k} + a\,(\Lambda - \Gamma)^{2k} + b\,(\Lambda + \Psi)^{2k} + b\,(\Lambda - \Psi)^{2k}\right]^{\frac{1}{2k}} \tag{2.221}$$

where $k \in \mathbf{N} \geq 1$ and $a, b > 0$ are material parameters, while Γ, $\Lambda$and Ψ are functions depending on the planar components of the stress tensor:

$$\begin{aligned} \Gamma &= L\sigma_{11} + M\sigma_{22} \\ \Lambda &= \sqrt{(N\sigma_{11} - P\sigma_{22})^2 + \sigma_{12}\sigma_{21}} \\ \Psi &= \sqrt{(Q\sigma_{11} - R\sigma_{22})^2 + \sigma_{12}\sigma_{21}} \end{aligned} \tag{2.222}$$

The coefficients L, M, N, P, Q, and R involved in Eqs. (2.222) are also material parameters.

Despite the fact that Eqs. (2.221) and (2.222) do not enforce any constraint on the sign of the coefficients L, M, N, P, Q, and R, the numerical tests performed by the authors have shown that positive values of these parameters lead to better predictions of the BBC 2005 yield criterion.

The conditions $k \in \mathbf{N} \geq 1$ and $a, b > 0$ ensure the convexity of the yield surface defined by Eqs. (2.215), (2.221) and (2.222). The parameters L, M, N, P, Q, and R are not subjected to any constraint from this point of view.

Nine material parameters are involved in the expression of the BBC 2005 equivalent stress: k, a, b, L, M, N, P, Q, and R (see Eqs. 2.221 and 2.222). The integer exponent k has a special status, due to the fact that its value is fixed from the very beginning in accordance with the crystallographic structure of the material: $k = 3$ for BCC materials, $k = 4$ for FCC materials.

The identification procedure calculates the other parameters (a, b, L, M, N, P, Q, and R) by forcing the constitutive equations associated to the BBC 2005 yield criterion to reproduce the following experimental data:

- The uniaxial yield stresses associated to the directions defined by 0°, 45° and 90° angles measured from RD (denoted as Y_0, Y_{45} and Y_{90})
- The coefficients of uniaxial plastic anisotropy associated to the directions defined by 0°, 45° and 90° angles measured from RD (denoted as r_0, r_{45} and r_{90})
- The biaxial yield stress associated to RD and TD (denoted as Y_b)
- The coefficient of biaxial plastic anisotropy associated to RD and TD (denoted as r_b).

There are 8 constraints acting on 8 material parameters. The identification procedure has enough data to generate a set of equations having a, b, L, M, N, P, Q, and R as unknowns. The structure of this set of equations, as well as the solution strategy will be presented in Sect. 2.5.4.

When using the flow rule given by Eq. (2.217), we need the partial derivatives of the function ϕ with respect to the planar components of the stress tensor. Equations (2.220), (2.221) and (2.222) lead to the following formula:

$$\frac{\partial \Phi}{\partial \sigma_{\alpha\beta}} = \frac{\partial \overline{\sigma}}{\partial \Gamma}\frac{\partial \Gamma}{\partial \sigma_{\alpha\beta}} + \frac{\partial \overline{\sigma}}{\partial \Lambda}\frac{\partial \Lambda}{\partial \sigma_{\alpha\beta}} + \frac{\partial \overline{\sigma}}{\partial \Psi}\frac{\partial \Psi}{\partial \sigma_{\alpha\beta}}, \quad \alpha, \beta = 1, 2 \tag{2.223}$$

where

$$\begin{aligned}
\frac{\partial\overline{\sigma}}{\partial\Gamma} &= \frac{a}{\bar{\sigma}^{2k-1}}\left[(\Lambda+\Gamma)^{2k-1}-(\Lambda-\Gamma)^{2k-1}\right]\\
\frac{\partial\overline{\sigma}}{\partial\Lambda} &= \frac{1}{\bar{\sigma}^{2k-1}}\left\{a\left[(\Lambda+\Gamma)^{2k-1}+(\Lambda-\Gamma)^{2k-1}\right]+b\left[(\Lambda+\Psi)^{2k-1}+(\Lambda-\Psi)^{2k-1}\right]\right\}\\
\frac{\partial\overline{\sigma}}{\partial\Psi} &= \frac{b}{\bar{\sigma}^{2k-1}}\left[(\Lambda+\Psi)^{2k-1}-(\Lambda-\Psi)^{2k-1}\right]
\end{aligned} \tag{2.224}$$

and

$$\begin{aligned}
&\frac{\partial\Gamma}{\partial\sigma_{11}} = L, \quad \frac{\partial\Gamma}{\partial\sigma_{22}} = M, \quad \frac{\partial\Gamma}{\partial\sigma_{12}} = 0, \quad \frac{\partial\Gamma}{\partial\sigma_{21}} = 0,\\
&\frac{\partial\Lambda}{\partial\sigma_{11}} = \frac{N\left(N\sigma_{11}-P\sigma_{22}\right)}{\Lambda}, \quad \frac{\partial\Lambda}{\partial\sigma_{22}} = -\frac{P\left(N\sigma_{11}-P\sigma_{22}\right)}{\Lambda},\\
&\frac{\partial\Lambda}{\partial\sigma_{12}} = \frac{\sigma_{21}}{2\Lambda}, \quad \frac{\partial\Lambda}{\partial\sigma_{21}} = \frac{\sigma_{12}}{2\Lambda},\\
&\frac{\partial\Psi}{\partial\sigma_{11}} = \frac{Q\left(Q\sigma_{11}-R\sigma_{22}\right)}{\Psi}, \quad \frac{\partial\Psi}{\partial\sigma_{22}} = -\frac{R\left(Q\sigma_{11}-R\sigma_{22}\right)}{\Psi},\\
&\frac{\partial\Psi}{\partial\sigma_{12}} = \frac{\sigma_{21}}{2\Psi}, \quad \frac{\partial\Psi}{\partial\sigma_{21}} = \frac{\sigma_{12}}{2\Psi},
\end{aligned} \tag{2.225}$$

Equations (2.221), (2.222), (2.223), (2.224) and (2.225) allow us to express the flow rule given by Eq. (2.217) as a dependency of the stress components $\sigma_{\alpha\beta}$ $(\alpha,\beta=1,2)$.

2.5.4 Identification Procedure

As mentioned in Sect. 2.5.3, the parameters a, b, L, M, N, P, Q, and R are obtained by constraining the constitutive equations associated to the BBC 2005 yield criterion to reproduce the following experimental data: Y_0, Y_{45}, Y_{90}, r_0, r_{45}, r_{90}, Y_b, and r_b. In fact, the identification procedure will solve the following set of 8 equations considering a, b, L, M, N, P, Q, and R as unknowns:

$$\begin{aligned}
&\tilde{Y}_0 = Y_0, \tilde{Y}_{45} = Y_{45}, \tilde{Y}_{90} = Y_{90}\\
&\tilde{r}_0 = r_0, \tilde{r}_{45} = r_{45}, \tilde{r}_{90} = r_{90}\\
&\tilde{Y}_b = Y_b, \tilde{r}_b = r_b
\end{aligned} \tag{2.226}$$

where:

- $\tilde{Y}_0$, $\tilde{Y}_{45}$ and $\tilde{Y}_{90}$ are the theoretical yield stresses corresponding to pure tension along the directions defined by 0°, 45° and 90° angles measured from RD
- $\tilde{r}_0$, $\tilde{r}_{45}$ and $\tilde{r}_{90}$ are the theoretical coefficients of uniaxial plastic anisotropy associated to the directions mentioned above

- $\tilde{Y}_b$ is the theoretical yield stress corresponding to biaxial tension along RD and TD
- $\tilde{r}_b$ is the theoretical coefficient of biaxial plastic anisotropy associated to RD and TD.

It is obvious that the identification procedure needs formulas for evaluating $\tilde{Y}_0$, $\tilde{Y}_{45}$, $\tilde{Y}_{90}$, $\tilde{r}_0$, $\tilde{r}_{45}$, $\tilde{r}_{90}$, $\tilde{Y}_b$, and $\tilde{r}_b$. These formulas will be presented below.

2.5.4.1 Theoretical Yield Stress in Pure Tension

Let $\tilde{Y}_\theta$ be the theoretical yield stress corresponding to pure tension along a direction defined by the angle θ measured from RD. The planar components of the stress tensor are

$$\sigma_{11} = \tilde{Y}_\theta \cos^2\theta, \quad \sigma_{22} = \tilde{Y}_\theta \sin^2\theta, \quad \sigma_{12} = \sigma_{21} = \tilde{Y}_\theta \sin\,\theta\,\cos\,\theta \tag{2.227}$$

The quantities Γ, Λ and Ψdefined by Eqs. (2.222) become

$$\Gamma = \tilde{Y}_\theta \Gamma_\theta, \quad \Lambda = \tilde{Y}_\theta \Lambda_\theta, \quad \Psi = \tilde{Y}_\theta \Psi_\theta \tag{2.228}$$

where

$$\begin{aligned} \Gamma_\theta &= L\cos^2\theta + M\sin^2\theta \\ \Lambda_\theta &= \sqrt{\left(N\cos^2\theta - P\sin^2\theta\right)^2 + \sin^2\theta\cos^2\theta} \\ \Psi_\theta &= \sqrt{\left(Q\cos^2\theta - R\sin^2\theta\right)^2 + \sin^2\theta\cos^2\theta} \end{aligned} \tag{2.229}$$

Equations (2.221) and (2.228) lead to the following expression of the equivalent stress when pure tension is applied along the θ direction:

$$\bar{\sigma}|_\theta = \tilde{Y}_\theta \cdot F(\theta) \tag{2.230}$$

where

$$F(\theta) = \left[a\left(\Lambda_\theta + \Gamma_\theta\right)^{2k} + a\left(\Lambda_\theta - \Gamma_\theta\right)^{2k} + b\left(\Lambda_\theta + \Psi_\theta\right)^{2k} + b\left(\Lambda_\theta - \Psi_\theta\right)^{2k}\right]^{\frac{1}{2k}} \tag{2.231}$$

$\bar{\sigma}|_\theta$ given by Eq. (2.230) should be replaced in Eq. (2.215). We thus obtain the desired formula of the theoretical yield stress $\tilde{Y}_\theta$:

$$\tilde{Y}_\theta = \frac{Y}{F(\theta)} \tag{2.232}$$

$\tilde{Y}_0$, $\tilde{Y}_{45}$ and $\tilde{Y}_{90}$ can be calculated from Eqs. (2.232) and (2.231) using θ =0°, 45° and 90°, respectively.

2.5.4.2 Theoretical Coefficient of Uniaxial Plastic Anisotropy

The theoretical coefficient of uniaxial plastic anisotropy associated to a direction inclined at the angle θ measured from RD is defined as follows:

$$\tilde{r}_\theta = \frac{\dot{\varepsilon}^p_{\theta+90^\circ}}{\dot{\varepsilon}^p_{DN}} \tag{2.233}$$

where: $\dot{\varepsilon}^p_{\theta+90^\circ}$ is the plastic strain-rate component associated to the direction defined by the angle $\theta + 90^\circ$, and $\dot{\varepsilon}^p_{DN}$ is the component of the same tensor associated to ND. After using the condition of plastic incompressibility

$$\dot{\varepsilon}^p_\theta + \dot{\varepsilon}^p_{\theta+90^\circ} + \dot{\varepsilon}^p_{DN} = 0 \tag{2.234}$$

Equation (2.233) becomes

$$\tilde{r}_\theta = -\frac{\dot{\varepsilon}^p_\theta}{\dot{\varepsilon}^p_{DN}} - 1 \tag{2.235}$$

The symbol $\dot{\varepsilon}^p_\theta$ denotes the plastic strain-rate component associated to the θ direction. $\dot{\varepsilon}^p_\theta$ and $\dot{\varepsilon}^p_{DN}$ may be rewritten using the components of the plastic strain-rate tensor expressed in the orthotropy basis:

$$\begin{aligned} \dot{\varepsilon}^p_\theta &= \dot{\varepsilon}^p_{11}\cos^2\theta + \dot{\varepsilon}^p_{22}\sin^2\theta + \left(\dot{\varepsilon}^p_{12} + \dot{\varepsilon}^p_{21}\right)\sin\theta\cos\theta \\ \dot{\varepsilon}^p_{DN} &= \dot{\varepsilon}^p_{33} = -\dot{\varepsilon}^p_{11} - \dot{\varepsilon}^p_{22} \end{aligned} \tag{2.236}$$

We can replace now $\dot{\varepsilon}^p_\theta$ and $\dot{\varepsilon}^p_{DN}$ given by Eqs. (2.236) into Eq. (2.235):

$$\tilde{r}_\theta = \frac{\dot{\varepsilon}^p_{11}\cos^2\theta + \dot{\varepsilon}^p_{22}\sin^2\theta + \left(\dot{\varepsilon}^p_{12} + \dot{\varepsilon}^p_{21}\right)\sin\theta\cos\theta}{\dot{\varepsilon}^p_{11} + \dot{\varepsilon}^p_{22}} - 1 \tag{2.237}$$

The right-hand side of Eq. (2.237) should be expressed in terms of the planar stress components. This transformation is achieved using the flow rule (see Eqs. 2.217 and 2.220), as well as Eqs. (2.227) (they are valid because $\tilde{r}_\theta$ is defined for a uniaxial stress state):

$$\tilde{r}_\theta = \frac{1}{\tilde{Y}_\theta}\frac{\left(\sigma_{\alpha\beta}\frac{\partial\bar{\sigma}}{\partial\sigma_{\alpha\beta}}\right)\Big|_\theta}{\left(\frac{\partial\bar{\sigma}}{\partial\sigma_{11}} + \frac{\partial\bar{\sigma}}{\partial\sigma_{22}}\right)\Big|_\theta} - 1 \tag{2.238}$$

The notation $(\cdot)|_\theta$ means that the expression enclosed by parentheses should be calculated for pure tension along the θ direction. The summation rule for tensor components has been used in Eq. (2.238).

The equivalent stress defined by Eqs. (2.221) and (2.222) is a homogeneous function of the stress components $\sigma_{\alpha\beta}$ $(\alpha, \beta = 1, 2)$, its degree of homogeneity being one. Thus we can use Euler's theorem:

$$\bar{\sigma} \;=\; \sigma_{\alpha\beta}\,\frac{\partial\bar{\sigma}}{\partial\sigma_{\alpha\beta}} \tag{2.239}$$

Equations (2.238), (2.239) and (2.230) lead to the following formula for $\tilde{r}_\theta$:

$$\tilde{r}_\theta \;=\; \frac{F\,(\theta)}{\left(\frac{\partial\bar{\sigma}}{\partial\sigma_{11}}+\frac{\partial\bar{\sigma}}{\partial\sigma_{22}}\right)\Big|_\theta} \;-\; 1 \tag{2.240}$$

We shall express now $\left(\frac{\partial\bar{\sigma}}{\partial\sigma_{11}}+\frac{\partial\bar{\sigma}}{\partial\sigma_{22}}\right)\Big|_\theta$ as a dependency of the θ angle. We start by rewriting Eq. (2.223) both for $\alpha=\beta=1$ and $\alpha=\beta=2$, assuming a uniaxial stress state along the θ direction. We have two relationships that can be added, thus obtaining

$$\begin{aligned}\left(\frac{\partial\bar{\sigma}}{\partial\sigma_{11}}+\frac{\partial\bar{\sigma}}{\partial\sigma_{22}}\right)\Big|_\theta &= \frac{\partial\bar{\sigma}}{\partial\Gamma}\Big|_\theta\left(\frac{\partial\Gamma}{\partial\sigma_{11}}+\frac{\partial\Gamma}{\partial\sigma_{22}}\right)\Big|_\theta + \\ &+ \frac{\partial\bar{\sigma}}{\partial\Lambda}\Big|_\theta\left(\frac{\partial\Lambda}{\partial\sigma_{11}}+\frac{\partial\Lambda}{\partial\sigma_{22}}\right)\Big|_\theta + \frac{\partial\bar{\sigma}}{\partial\Psi}\Big|_\theta\left(\frac{\partial\Psi}{\partial\sigma_{11}}+\frac{\partial\Psi}{\partial\sigma_{22}}\right)\Big|_\theta\end{aligned} \tag{2.241}$$

Equations (2.224), (2.228) and (2.230) allows us to express the derivatives $\frac{\partial\bar{\sigma}}{\partial\Gamma}\big|_\theta$, $\frac{\partial\bar{\sigma}}{\partial\Lambda}\big|_\theta$ and $\frac{\partial\bar{\sigma}}{\partial\Psi}\big|_\theta$ as functions of the θ angle:

$$\begin{aligned}\frac{\partial\bar{\sigma}}{\partial\Gamma}\Big|_\theta &= \frac{a}{[F(\theta)]^{2k-1}}\left[(\Lambda_\theta+\Gamma_\theta)^{2k-1} - \;(\Lambda_\theta-\Gamma_\theta)^{2k-1}\right] \\ \frac{\partial\bar{\sigma}}{\partial\Lambda}\Big|_\theta &= \frac{1}{[F(\theta)]^{2k-1}}\left\{a\left[(\Lambda_\theta+\Gamma_\theta)^{2k-1} + \;(\Lambda_\theta-\Gamma_\theta)^{2k-1}\right] + b\left[(\Lambda_\theta+\Psi_\theta)^{2k-1}\right.\right. \\ &\quad \left.\left. + \;(\Lambda_\theta-\Psi_\theta)^{2k-1}\right]\right\} \\ \frac{\partial\bar{\sigma}}{\partial\Psi}\Big|_\theta &= \frac{b}{[F(\theta)]^{2k-1}}\left[(\Lambda_\theta+\Psi_\theta)^{2k-1} - \;(\Lambda_\theta-\Psi_\theta)^{2k-1}\right]\end{aligned} \tag{2.242}$$

where Γ_θ, Λ_θ and Ψ_θ are defined by Eqs. (2.229). The other derivatives appearing in the right-hand side of Eq. (2.241) can be also expressed as functions of the θ angle (see Eqs. 2.225, 2.227, and 2.228):

$$\begin{aligned}\left(\frac{\partial\Gamma}{\partial\sigma_{11}}+\frac{\partial\Gamma}{\partial\sigma_{22}}\right)\Big|_\theta &= L \;+\; M, \\ \left(\frac{\partial\Lambda}{\partial\sigma_{11}}+\frac{\partial\Lambda}{\partial\sigma_{22}}\right)\Big|_\theta &= \frac{(N-P)\left(N\,\cos^2\theta - P\,\sin^2\theta\right)}{\Lambda_\theta}, \\ \left(\frac{\partial\Psi}{\partial\sigma_{11}}+\frac{\partial\Psi}{\partial\sigma_{22}}\right)\Big|_\theta &= \frac{(Q-R)\left(Q\,\cos^2\theta - R\,\sin^2\theta\right)}{\Psi_\theta}\end{aligned} \tag{2.243}$$

After replacing the quantities given by Eqs. (2.242) and (2.243) into Eq. (2.241) and making some rearrangements, we get the following relationship for $\left(\frac{\partial\bar{\sigma}}{\partial\sigma_{11}}+\frac{\partial\bar{\sigma}}{\partial\sigma_{22}}\right)\Big|_\theta$:

$$\left(\frac{\partial\bar{\sigma}}{\partial\sigma_{11}}+\frac{\partial\bar{\sigma}}{\partial\sigma_{22}}\right)\Bigg|_{\theta}=\frac{G(\theta)}{[F(\theta)]^{2k-1}} \tag{2.244}$$

where

$$\begin{aligned}
G(\theta)=\,& a\left[\frac{(N-P)\left(N\cos^2\theta-P\sin^2\theta\right)}{\Lambda_\theta}+L+M\right](\Lambda_\theta+\Gamma_\theta)^{2k-1}+\\
& a\left[\frac{(N-P)\left(N\cos^2\theta-P\sin^2\theta\right)}{\Lambda_\theta}-L-M\right](\Lambda_\theta-\Gamma_\theta)^{2k-1}+\\
& b\left[\frac{(N-P)\left(N\cos^2\theta-P\sin^2\theta\right)}{\Lambda_\theta}+\frac{(Q-R)\left(Q\cos^2\theta-R\sin^2\theta\right)}{\Psi_\theta}\right](\Lambda_\theta+\Psi_\theta)^{2k-1}+\\
& b\left[\frac{(N-P)\left(N\cos^2\theta-P\sin^2\theta\right)}{\Lambda_\theta}-\frac{(Q-R)\left(Q\cos^2\theta-R\sin^2\theta\right)}{\Psi_\theta}\right](\Lambda_\theta-\Psi_\theta)^{2k-1}
\end{aligned} \tag{2.245}$$

We can now combine Eqs. (2.240) and (2.244) to obtain a formula for evaluating the coefficient of uniaxial plastic anisotropy:

$$\tilde{r}_\theta=\frac{[F(\theta)]^{2k}}{G(\theta)}-1 \tag{2.246}$$

$\tilde{r}_0$, $\tilde{r}_{45}$ and $\tilde{r}_{90}$ can be calculated from Eqs. (2.246), (2.245) and (2.231) using $\theta=0°$, 45° and 90°, respectively.

2.5.4.3 Theoretical Yield Stress in Biaxial Tension Along RD and TD

Let $\tilde{Y}_b$ be the theoretical yield stress corresponding to biaxial tension along RD and TD. The planar components of the stress tensor are

$$\sigma_{11}=\tilde{Y}_b,\quad \sigma_{22}=\tilde{Y}_b,\quad \sigma_{12}=\sigma_{21}=0 \tag{2.247}$$

The quantities Γ, Ψ and Λ defined by Eqs. (2.222) become

$$\Gamma=\tilde{Y}_b\Gamma_b,\quad \Lambda=\tilde{Y}_b\Lambda_b,\quad \Psi=\tilde{Y}_b\Psi_b \tag{2.248}$$

where

$$\begin{aligned}
\Gamma_b &= L+M\,,\\
\Lambda_b &= \sqrt{(N-P)^2}=|N-P|\,,\\
\Psi_b &= \sqrt{(Q-R)^2}=|Q-R|
\end{aligned} \tag{2.249}$$

Equations (2.221) and (2.248) lead to the following expression of the equivalent stress when biaxial tension is applied along RD and TD:

$$\bar{\sigma}|_b = \tilde{Y}_b \cdot F_b \tag{2.250}$$

where

$$F_b = \left[a\,(\Lambda_b + \Gamma_b)^{2k} + a\,(\Lambda_b - \Gamma_b)^{2k} + b\,(\Lambda_b + \Psi_b)^{2k} + b\,(\Lambda_b - \Psi_b)^{2k}\right]^{\frac{1}{2k}} \tag{2.251}$$

$\bar{\sigma}|_b$ given by Eq. (2.250) should be replaced in Eq. (2.215). We thus obtain the desired formula of the theoretical yield stress $\tilde{Y}_b$:

$$\tilde{Y}_b = \frac{Y}{F_b} \tag{2.252}$$

$\tilde{Y}_b$ can be calculated from Eqs. (2.252) and (2.251).

2.5.4.4 Theoretical Coefficient of Biaxial Plastic Anisotropy

The theoretical coefficient of biaxial plastic anisotropy associated to RD and TD is defined as follows:

$$\tilde{r}_b = \frac{\dot{\varepsilon}^p_{TD}}{\dot{\varepsilon}^p_{RD}} \tag{2.253}$$

where $\dot{\varepsilon}^p_{RD}$ and $\dot{\varepsilon}^p_{TD}$ are the components of the plastic strain-rate tensor corresponding to RD and TD, respectively. The choice of the orthonormal basis allows us to write the equalities

$$\dot{\varepsilon}^p_{RD} = \dot{\varepsilon}^p_{11}, \quad \dot{\varepsilon}^p_{TD} = \dot{\varepsilon}^p_{22} \tag{2.254}$$

We can replace now $\dot{\varepsilon}^p_{RD}$ and $\dot{\varepsilon}^p_{TD}$ given by Eqs. (2.254) into Eq. (2.253):

$$\tilde{r}_b = \frac{\dot{\varepsilon}^p_{22}}{\dot{\varepsilon}^p_{11}} = \frac{\dot{\varepsilon}^p_{11} + \dot{\varepsilon}^p_{22}}{\dot{\varepsilon}^p_{11}} - 1 \tag{2.255}$$

The right-hand side of Eq. (2.255) should be expressed in terms of the planar stress components. This transformation is achieved using the flow rule (see Eqs. 2.217 and 2.220), as well as Eqs. (2.247) (they are valid because $\tilde{r}_b$ is defined for a biaxial stress state):

$$\tilde{r}_b = \frac{1}{\tilde{Y}_b} \frac{\left(\sigma_{\alpha\beta} \dfrac{\partial \bar{\sigma}}{\partial \sigma_{\alpha\beta}}\right)\Big|_b}{\left(\dfrac{\partial \bar{\sigma}}{\partial \sigma_{11}}\right)\Big|_b} - 1 \tag{2.256}$$

The notation $(\cdot)|_b$ means that the expression enclosed by parentheses should be calculated for biaxial tension along RD and TD. Eqs. (2.256), (2.239) and (2.250) lead to the following formula for $\tilde{r}_b$:

$$\tilde{r}_b = \frac{F_b}{\left(\dfrac{\partial\bar{\sigma}}{\partial\sigma_{11}}\right)\Big|_b} - 1 \tag{2.257}$$

We shall find now the expression of the denominator $\left(\frac{\partial\bar{\sigma}}{\partial\sigma_{11}}\right)\Big|_b$. We start by rewriting Eq. (2.223) for $\alpha = \beta = 1$, assuming a biaxial stress state along RD and TD:

$$\left(\frac{\partial\bar{\sigma}}{\partial\sigma_{11}}\right)\Big|_b = \frac{\partial\bar{\sigma}}{\partial\Gamma}\Big|_b \frac{\partial\Gamma}{\partial\sigma_{11}}\Big|_b + \frac{\partial\bar{\sigma}}{\partial\Lambda}\Big|_b \frac{\partial\Lambda}{\partial\sigma_{11}}\Big|_b + \frac{\partial\bar{\sigma}}{\partial\Psi}\Big|_b \frac{\partial\Psi}{\partial\sigma_{11}}\Big|_b \tag{2.258}$$

Equations (2.224), (2.248) and (2.250) allows us to express the derivatives $\frac{\partial\bar{\sigma}}{\partial\Gamma}\big|_b$, $\frac{\partial\bar{\sigma}}{\partial\Lambda}\big|_b$ and $\frac{\partial\bar{\sigma}}{\partial\Psi}\big|_b$:

$$\begin{aligned}
\frac{\partial\overline{\sigma}}{\partial\Gamma}\Big|_b &= \frac{a}{F_b^{2k-1}}\left[(\Lambda_b+\Gamma_b)^{2k-1} - (\Lambda_b-\Gamma_b)^{2k-1}\right] \\
\frac{\partial\overline{\sigma}}{\partial\Lambda}\Big|_b &= \frac{1}{F_b^{2k-1}}\left\{a\left[(\Lambda_b+\Gamma_b)^{2k-1} + (\Lambda_b-\Gamma_b)^{2k-1}\right] + b\left[(\Lambda_b+\Psi_b)^{2k-1}\right.\right. \\
&\qquad \left.\left. + (\Lambda_b-\Psi_b)^{2k-1}\right]\right\} \\
\frac{\partial\overline{\sigma}}{\partial\Psi}\Big|_b &= \frac{b}{F_b^{2k-1}}\left[(\Lambda_b+\Psi_b)^{2k-1} - (\Lambda_b-\Psi_b)^{2k-1}\right]
\end{aligned} \tag{2.259}$$

where Γ_b, Λ_b and Ψ_b are defined by Eqs. (2.249). The other derivatives appearing in the right-hand side of Eq. (2.258) can be also expressed from Eqs. (2.225), (2.247) and (2.248):

$$\frac{\partial\Gamma}{\partial\sigma_{11}}\Big|_b = L, \quad \frac{\partial\Lambda}{\partial\sigma_{11}}\Big|_b = \frac{N(N-P)}{\Lambda_b}, \quad \frac{\partial\Psi}{\partial\sigma_{11}}\Big|_b = \frac{Q(Q-R)}{\Psi_b} \tag{2.260}$$

After replacing the quantities given by Eqs. (2.259) and (2.260) into Eq. (2.258), we get the following relationship for $\left(\frac{\partial\bar{\sigma}}{\partial\sigma_{11}}\right)\Big|_b$ (see also Eqs. 2.249):

$$\left(\frac{\partial\bar{\sigma}}{\partial\sigma_{11}}\right)\Big|_b = \frac{G_b}{F_b^{2k-1}} \tag{2.261}$$

where

$$G_b = a\left[\frac{N(N-P)}{\Lambda_b} + L\right](\Lambda_b + \Gamma_b)^{2k-1} + a\left[\frac{N(N-P)}{\Lambda_b} - L\right](\Lambda_b - \Gamma_b)^{2k-1} +$$
$$b\left[\frac{N(N-P)}{\Lambda_b} + \frac{Q(Q-R)}{\Psi_b}\right](\Lambda_b + \Psi_b)^{2k-1} + b\left[\frac{N(N-P)}{\Lambda_b} - \frac{Q(Q-R)}{\Psi_b}\right](\Lambda_b - \Psi_b)^{2k-1} \tag{2.262}$$

We can combine Eqs. (2.257) and (2.261) to obtain a formula for evaluating the coefficient of biaxial plastic anisotropy:

$$\tilde{r}_b = \frac{F_b^{2k}}{G_b} - 1 \tag{2.263}$$

Now we have all the quantities needed to construct the identification conditions (see Eqs. 2.226). At first, we shall refer to Eqs. (2.226.1), (2.226.2), (2.226.3) and (2.226.7) (the constraints associated to the yield stresses). Equations (2.232) and (2.252) allow us to rewrite Eqs. (2.226.1), (2.226.2), (2.226.3) and (2.226.7) in a more convenient form:

$$\begin{aligned} &[F(0°)]^{2k} = y_0^{2k}, \quad [F(45°)]^{2k} = y_{45}^{2k}, \\ &[F(90°)]^{2k} = y_{90}^{2k}, \quad F_b^{2k} = y_b^{2k}. \end{aligned} \tag{2.264}$$

where

$$y_0 = \frac{Y}{Y_0}, \quad y_{45} = \frac{Y}{Y_{45}}, \quad y_{90} = \frac{Y}{Y_{90}}, \quad y_b = \frac{Y}{Y_b} \tag{2.265}$$

are normalized values of the experimental yield stresses.

In a similar way, Eqs. (2.244), (2.263) and (2.264) lead to the following expressions of Eqs. (2.226.4), (2.226.5), (2.226.6) and (2.226.8) (the constraints associated to the coefficients of plastic anisotropy):

$$\begin{aligned} &G(0°) = \frac{1}{r_0 + 1} y_0^{2k}, \quad G(45°) = \frac{1}{r_{45} + 1} y_{45}^{2k}, \\ &G(90°) = \frac{1}{r_{90} + 1} y_{90}^{2k}, \quad G_b = \frac{1}{r_b + 1} y_b^{2k}. \end{aligned} \tag{2.266}$$

Finally, we use Eqs. (2.231), (2.229), (2.251), (2.249), (2.245) and (2.262) to put into evidence the unknown material parameters a, b, L, M, N, P, Q, and R in the left-hand side of Eqs. (2.264) and (2.266):

$$
\begin{aligned}
&a\,(N+L)^{2k}+a\,(N-L)^{2k}+b\,(N+Q)^{2k}+b\,(N-Q)^{2k} = y_0^{2k}\\
&a\left[\sqrt{(N-P)^2+1}+L+M\right]^{2k}+a\left[\sqrt{(N-P)^2+1}-L-M\right]^{2k}+\\
&\qquad b\left[\sqrt{(N-P)^2+1}+\sqrt{(Q-R)^2+1}\right]^{2k}+\\
&\qquad b\left[\sqrt{(N-P)^2+1}-\sqrt{(Q-R)^2+1}\right]^{2k} = (2\,y_{45})^{2k}\\
&a\,(P+M)^{2k}+a\,(P-M)^{2k}+b\,(P+R)^{2k}+b\,(P-R)^{2k} = y_{90}^{2k}\\
&a\,(N-P+L+M)^{2k}+a\,(N-P-L-M)^{2k}+\\
&\qquad b\,(N-P+Q-R)^{2k}+b\,(N-P-Q+R)^{2k} = y_b^{2k}\\
&a\,(P-M)\,(N+L)^{2k-1}+a\,(P+M)\,(N-L)^{2k-1}+\\
&\qquad b\,(P+R)\,(N+Q)^{2k-1}+b\,(P-R)\,(N-Q)^{2k-1} = \tfrac{r_0}{r_0+1}y_0^{2k}\\
&a\sqrt{(Q-R)^2+1}\left\{\left[\sqrt{(N-P)^2+1}+L+M\right]^{2k-1}+\right.\\
&\qquad \left.\left[\sqrt{(N-P)^2+1}-L-M\right]^{2k-1}\right\}+\\
&\qquad b\left\{\left[\sqrt{(N-P)^2+1}+\sqrt{(Q-R)^2+1}\right]^{2k}-\right.\\
&\qquad \left.\left[\sqrt{(N-P)^2+1}-\sqrt{(Q-R)^2+1}\right]^{2k}\right\} =\\
&\qquad \sqrt{(N-P)^2+1}\sqrt{(Q-R)^2+1}\,\frac{r_{45}+1/2}{r_{45}+1}\,(2\,y_{45})^{2k}\\
&a\,(N-L)\,(P+M)^{2k-1}+a\,(N+L)\,(P-M)^{2k-1}+\\
&\qquad b\,(N+Q)\,(P+R)^{2k-1}+b\,(N-Q)\,(P-R)^{2k-1} = \tfrac{r_{90}}{r_{90}+1}y_{90}^{2k}\\
&a\,(N+L)\,(N-P+L+M)^{2k-1}+a\,(N-L)\,(N-P-L-M)^{2k-1}+\\
&\qquad b\,(N+Q)\,(N-P+Q-R)^{2k-1}+\\
&\qquad b\,(N-Q)\,(N-P-Q+R)^{2k-1} = \tfrac{1}{r_b+1}y_b^{2k}
\end{aligned}
\tag{2.267}
$$

Equations (2.267) form together a set of 8 non-linear equations. The identification procedure uses Newton's method to obtain its numerical solution.

From now on we shall manipulate Eqs. (2.267) in a generic form:

$$
f_i\,(a,\,b,\,L,\,M,\,N,\,P,\,Q,\,R) = 0, \quad i = 1,\,2,\ldots,\,8 \tag{2.268}
$$

where

$$
\begin{aligned}
1.\quad & f_1 = a\,(N\ +\ L)^{2k} + a\,(N\ -\ L)^{2k} + b\,(N\ +\ Q)^{2k} + b\,(N\ -\ Q)^{2k} - y_0^{2k} \\
2.\quad & f_2 = a\left[\sqrt{(N\ -\ P)^2+1} + L + M\right]^{2k} + a\left[\sqrt{(N\ -\ P)^2+1} - L - M\right]^{2k} + \\
& \quad b\left[\sqrt{(N\ -\ P)^2+1} + \sqrt{(Q\ -\ R)^2+1}\right]^{2k} + \\
& \quad b\left[\sqrt{(N\ -\ P)^2+1} - \sqrt{(Q\ -\ R)^2+1}\right]^{2k} - (2\,y_{45})^{2k} \\
3.\quad & f_3 = a\,(P+M)^{2k} + a\,(P-M)^{2k} + b\,(P+R)^{2k} + b\,(P-R)^{2k} - y_{90}^{2k} \\
4.\quad & f_4 = a\,(N-P+L+M)^{2k} + a\,(N-P-L-M)^{2k} + \\
& \quad b\,(N-P+Q-R)^{2k} + b\,(N-P-Q+R)^{2k} - y_b^{2k} \\
5.\quad & f_5 = a\,(P-M)\,(N+L)^{2k-1} + a\,(P+M)\,(N-L)^{2k-1} + \\
& \quad b\,(P+R)\,(N+Q)^{2k-1} + b\,(P-R)\,(N-Q)^{2k-1} - \tfrac{r_0}{r_0+1} y_0^{2k} \\
6.\quad & f_6 = a\sqrt{(Q-R)^2+1}\left\{\left[\sqrt{(N-P)^2+1} + L + M\right]^{2k-1} + \right. \\
& \quad \left.\left[\sqrt{(N-P)^2+1} - L - M\right]^{2k-1}\right\} + \\
& \quad b\left\{\left[\sqrt{(N-P)^2+1} + \sqrt{(Q-R)^2+1}\right]^{2k} - \right. \\
& \quad \left.\left[\sqrt{(N-P)^2+1}\ - \sqrt{(Q-R)^2+1}\right]^{2k}\right\}\ - \\
& \quad \sqrt{(N-P)^2+1}\sqrt{(Q-R)^2+1}\,\tfrac{r_{45}+1/2}{r_{45}+1}\,(2\,y_{45})^{2k} \\
7.\quad & f_7 = a\,(N-L)\,(P+M)^{2k-1} + a\,(N+L)\,(P-M)^{2k-1} + \\
& \quad b\,(N+Q)\,(P+R)^{2k-1} +\ b\,(N-Q)\,(P-R)^{2k-1} - \tfrac{r_{90}}{r_{90}+1} y_{90}^{2k} \\
8.\quad & f_8 = a\,(N+L)\,(N-P+L+M)^{2k-1} + a\,(N-L)\,(N-P-L-M)^{2k-1} + \\
& \quad b\,(N+Q)\,(N-P+Q-R)^{2k-1} + \\
& \quad b\,(N-Q)\,(N-P-Q+R)^{2k-1} - \tfrac{1}{r_b+1} y_b^{2k}
\end{aligned}
\tag{2.269}
$$

As mentioned in Sect. 2.5.3, the parameters involved in the expression of the equivalent stress are subjected to constraints: $a > 0, b > 0, L > 0, M > 0, N > 0, P > 0, Q > 0,$ and $R > 0$. Aiming to ensure a natural treatment of these restrictions, the identification procedure replaces the parameters a, b, L, M, N, P, Q, and R with the following substitutes:

$$
\begin{aligned}
&a = \left(a'\right)^2, \quad b = \left(b'\right)^2, \quad L = \left(L'\right)^2, \quad M = \left(M'\right)^2, \\
&N = \left(N'\right)^2, \quad P = \left(P'\right)^2, \quad Q = \left(Q'\right)^2, \quad R = \left(R'\right)^2, \\
&a',\ b',\ L',\ M',\ N',\ P',\ Q',\ R' \in \mathbb{R}
\end{aligned}
\tag{2.270}
$$

In this way, $f_1, f_2, \ldots, f_8$ will become functions of the variables a', b', L', M', N', P', Q', and R'. As a consequence, Eqs. (2.268) should be rewritten in the form

$$
\begin{aligned}
&f_i\left[a\left(a'\right),\ b\left(b'\right),\ L\left(L'\right),\ M\left(M'\right),\ N\left(N'\right),\ P\left(P'\right),\ Q\left(Q'\right),\ R\left(R'\right)\right] = 0, \\
&i = 1, 2, \ldots, 8
\end{aligned}
\tag{2.271}
$$

The identification procedure will solve Eqs. (2.271) considering a', b', L', M', N', P', Q', and R' as unknowns. After finding the numerical solution, the values of the actual parameters a, b, L, M, N, P, Q, and R can be obtained from Eqs. (2.270).

Let a'_k, b'_k, L'_k, M'_k, N'_k, P'_k, Q'_k, and R'_k be the approximations of the numerical solution corresponding to the k-th Newton iteration. Eqs. (2.271) are linearised in the vicinity of this approximation using a truncated Taylor expansion:

$$
\begin{aligned}
&\left.\frac{\partial f_i}{\partial a}\right|_k \left.\frac{\partial a}{\partial a'}\right|_k \left(\Delta a'_k\right) + \left.\frac{\partial f_i}{\partial b}\right|_k \left.\frac{\partial b}{\partial b'}\right|_k \left(\Delta b'_k\right) + \\
&\left.\frac{\partial f_i}{\partial L}\right|_k \left.\frac{\partial L}{\partial L'}\right|_k \left(\Delta L'_k\right) + \left.\frac{\partial f_i}{\partial M}\right|_k \left.\frac{\partial M}{\partial M'}\right|_k \left(\Delta M'_k\right) + \\
&\left.\frac{\partial f_i}{\partial N}\right|_k \left.\frac{\partial N}{\partial N'}\right|_k \left(\Delta N'_k\right) + \left.\frac{\partial f_i}{\partial P}\right|_k \left.\frac{\partial P}{\partial P'}\right|_k \left(\Delta P'_k\right) + \\
&\left.\frac{\partial f_i}{\partial Q}\right|_k \left.\frac{\partial Q}{\partial Q'}\right|_k \left(\Delta Q'_k\right) + \left.\frac{\partial f_i}{\partial R}\right|_k \left.\frac{\partial R}{\partial R'}\right|_k \left(\Delta R'_k\right) = - f_i|_k , \\
&i = 1, 2, \ldots, 8
\end{aligned}
\tag{2.272}
$$

The symbol $\cdot|_k$ means that the associated expression should be evaluated considering

$a' = a'_k, b' = b'_k, L' = L'_k, M' = M'_k, N' = N'_k, P' = P'_k, Q' = Q'_k$, and $R' = R'_k$.

The unknowns of the linearised set (see Eqs. 2.271 and 2.270) are the corrections $\Delta a'_k$, $\Delta b'_k$, $\Delta L'_k$,$\Delta M'_k$, $\Delta N'_k$, $\Delta P'_k$, $\Delta Q'_k$, and $\Delta R'_k$. After adding them to a'_k, b'_k, L'_k, M'_k, N'_k, P'_k, Q'_k, and R'_k, respectively, we obtain a new approximation of the numerical solution that should be used in the next iteration:

$$\begin{aligned}
a'_{k+1} &= a'_k + \Delta a'_k \\
b'_{k+1} &= b'_k + \Delta b'_k \\
L'_{k+1} &= L'_k + \Delta L'_k \\
M'_{k+1} &= M'_k + \Delta M'_k \\
N'_{k+1} &= N'_k + \Delta N'_k \\
P'_{k+1} &= P'_k + \Delta P'_k \\
Q'_{k+1} &= Q'_k + \Delta Q'_k \\
R'_{k+1} &= R'_k + \Delta R'_k
\end{aligned} \tag{2.273}$$

Two convergence criteria are used to stop the iterations:

$$\begin{aligned}
&\sqrt{\frac{(\Delta a'_k)^2+(\Delta b'_k)^2+(\Delta L'_k)^2+(\Delta M'_k)^2+(\Delta N'_k)^2+(\Delta P'_k)^2+(\Delta Q'_k)^2+(\Delta R'_k)^2}{\left(a'_{k+1}\right)^2+\left(b'_{k+1}\right)^2+\left(L'_{k+1}\right)^2+\left(M'_{k+1}\right)^2+\left(N'_{k+1}\right)^2+\left(P'_{k+1}\right)^2+\left(Q'_{k+1}\right)^2+\left(R'_{k+1}\right)^2}} < 10^{-7} \\
&\sqrt{\sum_{i=1}^{8}\left(f_i|_k\right)^2} < 10^{-5}
\end{aligned} \tag{2.274}$$

The convergence of the Newton iterations is strongly influenced by the initial guess.

2.5.5 Particular Formulations of the BBC 2005 Yield Criterion

We can reduce BBC 2005 to Hill 1948 yield criterion if we choose the material parameters as follows:

$$\begin{aligned}
Y &= Y_0 \\
k &= 1 \\
a &= \frac{\sqrt{\frac{1+r_0}{r_0}\frac{1+r_{90}}{r_{90}}}-1}{\sqrt{\frac{1+r_0}{r_0}\frac{1+r_{90}}{r_{90}}}+1}\,\frac{1}{1+r_0}\left(1+\frac{r_0}{r_{90}}\right)\left(r_{45}+\frac{1}{2}\right) \\
b &= \frac{a}{\sqrt{\frac{1+r_0}{r_0}\frac{1+r_{90}}{r_{90}}}-1} \\
L &= N = Q = \frac{1}{2\sqrt{a+b}} \\
M &= P = R = \frac{1}{2}\sqrt{\frac{\frac{r_0}{1+r_0}\,\frac{1+r_{90}}{r_{90}}}{a+b}}
\end{aligned} \tag{2.275}$$

In this case, the identification procedure needs only r_0, r_{45} and r_{90} as input data.

The yield criterion proposed by Barlat and Lian in 1989 can be also obtained by enforcing the following constraints on the material parameters:

$$Y = Y_0,\ k = 3\ or\ 4,\ L = N = Q,\ M = P = R \tag{2.276}$$

As above, the identification procedure needs only r_0, r_{45} and r_{90} as input data.

Another situation of practical interest is the so-called normal anisotropy ($r_0 = r_{45} = r_{90} = r$; $Y_0 = Y_{45} = Y_{90} = Y$). In this case, BBC 2005 also reduces to the Hill 1948 or Barlat 1989 yield criteria (depending on the value of the exponent k):

$$\begin{array}{l} k = 1 \text{ (Hill 1948)},\ k = 3\ or\ 4 \text{ (Barlat 1989)}, \\ a = \frac{1}{1+r},\ b = \frac{r}{1+r},\ L = N = Q = M = P = R = \frac{1}{2} \end{array} \tag{2.277}$$

There are many situations when the coefficient of biaxial plastic anisotropy (r_b) is not available as input data. The most convenient strategy for handling such cases consists in replacing Eq. (2.267.8) with the following constraint:

$$N = P \tag{2.278}$$

In this way, the number of identification equations is preserved. As a consequence, the solution procedure discussed in Sect. 2.5.4 will remain usable. The numerical tests performed for several sorts of sheet metals have shown that the above constraint leads to well-shaped yield loci (i.e. the predicted value of r_b is not far from 1).

The situations when the biaxial yield stress (Y_b) and the coefficient of biaxial plastic anisotropy (r_b) are not available can be handled by replacing Eqs. (2.267.4) and (2.267.8) with the following constraints:

$$L + M = 2N, \quad N = P \tag{2.279}$$

This strategy has the same advantages as those mentioned above.

The situations when the uniaxial yield stresses Y_{45} and Y_{90}, as well as the coefficient of biaxial plastic anisotropy r_b are not available can be handled by replacing Eqs. (2.267.2), (2.267.3) and (2.267.8) with the following constraints:

$$M = R,\ L + M = 2N, \quad N = P \tag{2.280}$$

2.6 BBC 2008 Yield Criterion

In order to enhance the flexibility of the BBC 2005 yield criterion, a new version of this model has been developed [91]. The model is expressed as a finite series that can be expanded to retain more or less terms, depending on the volume of experimental

data. Different identification strategies (using 8, 16, 24, etc. input values) could be used in order to determine the coefficients of the yield function.

2.6.1 Equation of the Yield Surface

The sheet metal is assumed to behave as a plastically orthotropic membrane under plane-stress conditions. We use the following description of the yield surface:

$$\bar{\sigma}(\sigma_{\alpha\beta}) - Y = 0 \tag{2.281}$$

where $\bar{\sigma}(\sigma_{\alpha\beta}) \geq 0$ is the equivalent stress defined in Sect. 2.6.2, $Y > 0$ is the yield parameter, and $\sigma_{\alpha\beta} = \sigma_{\beta\alpha}$ $(\alpha, \beta = 1, 2)$ are planar components of the stress tensor expressed in an orthonormal basis superimposed to the axes of plastic orthotropy: (1) rolling direction (RD), (2) transverse direction (TD), (3) normal direction (ND). The other components are subjected to the constraint

$$\sigma_{3i} = \sigma_{i3} = 0, \quad i = 1, 2, 3 \tag{2.282}$$

arising from the plane-stress hypothesis. Whenever not specified, the following convention will be adopted: Latin subscripts take the values 1, 2 and 3, while the Greek ones take only the values 1 and 2.

The equivalent stress defined in Sect. 2.6.2 does not enforce constraints on the choice of the parameter Y. In fact, any quantity representing a yield stress can act as Y. For example, Y may be the uniaxial yield stress Y_θ associated to a planar direction defined by the angle θ measured from RD, an average of several uniaxial yield stresses, or the biaxial yield stress corresponding to the tension along RD and TD.

The flow rule associated to the yield surface described by Eq. (2.281) is

$$\dot{\varepsilon}^{(p)}_{\alpha\beta} = \dot{\lambda} \frac{\partial \bar{\sigma}}{\partial \sigma_{\alpha\beta}} \tag{2.283}$$

where $\dot{\varepsilon}^{(p)}_{\alpha\beta} = \dot{\varepsilon}^{(p)}_{\beta\alpha}$ are planar components of the plastic strain-rate tensor (expressed in the same basis as the corresponding components of the stress tensor), and $\dot{\lambda} \geq 0$ is a scalar multiplier (its significance is not essential for our discussion). The out of plane components of the plastic strain-rate are subjected to the constraints

$$\dot{\varepsilon}^{(p)}_{3\alpha} = \dot{\varepsilon}^{(p)}_{\alpha 3} = 0, \quad \dot{\varepsilon}^{(p)}_{33} = -\dot{\varepsilon}^{(p)}_{11} - \dot{\varepsilon}^{(p)}_{22} \tag{2.284}$$

arising from the plane-stress hypothesis and the isochoric character of the plastic deformation [29].

2.6.2 BBC 2008 Equivalent Stress

The equivalent stress used in Eq. (2.281) is defined as follows:

$$\begin{aligned}
&\frac{\bar{\sigma}^{2k}}{w-1} = \sum_{i=1}^{s} \left\{ w^{i-1} \left\{ \left[L^{(i)} + M^{(i)}\right]^{2k} + \left[L^{(i)} - M^{(i)}\right]^{2k} \right\} + \right. \\
&\left. w^{s-i} \left\{ \left[M^{(i)} + N^{(i)}\right]^{2k} + \left[M^{(i)} - N^{(i)}\right]^{2k} \right\} \right\} \\
&k, s \in \mathbf{N}^* \; w = \left(3/2\right)^{1/s} > 1 \\
&L^{(i)} = \ell_1^{(i)} \sigma_{11} + \ell_2^{(i)} \sigma_{22} \\
&M^{(i)} = \sqrt{\left[m_1^{(i)} \sigma_{11} - m_2^{(i)} \sigma_{22}\right]^2 + \left[m_3^{(i)} (\sigma_{12} + \sigma_{21})\right]^2} \\
&N^{(i)} = \sqrt{\left[n_1^{(i)} \sigma_{11} - n_2^{(i)} \sigma_{22}\right]^2 + \left[n_3^{(i)} (\sigma_{12} + \sigma_{21})\right]^2} \\
&\ell_1^{(i)}, \ell_2^{(i)}, m_1^{(i)}, m_2^{(i)}, m_3^{(i)}, n_1^{(i)}, n_2^{(i)}, n_3^{(i)} \in \mathbf{R}.
\end{aligned} \tag{2.285}$$

The quantities denoted k, $\ell_1^{(i)}, \ell_2^{(i)}, m_1^{(i)}, m_2^{(i)}, m_3^{(i)}, n_1^{(i)}, n_2^{(i)}, n_3^{(i)}$ $(i = 1, \ldots, s)$ are material parameters. One may prove that $k \in \mathbf{N}^*$ is a sufficient condition for the convexity of the yield surface defined by Eqs. (2.281) and (2.285). From this point of view, there is no constraint acting on the admissible values of the other material parameters.

It is easily noticeable that Eq. (2.285) reduces to the isotropic formulation proposed by Barlat and Richmond [49] if

$$\ell_1^{(i)} = \ell_2^{(i)} = m_1^{(i)} = m_2^{(i)} = m_3^{(i)} = n_1^{(i)} = n_2^{(i)} = n_3^{(i)} = 1/2, \quad i = 1, \ldots, s \tag{2.286}$$

Under these circumstances, the exponent k may be chosen as in Barlat and Richmond's model, i.e. according to the crystallographic structure of the sheet metal: $k = 3$ for BCC materials ($2k = 6$), and $k = 4$ for FCC materials ($2k = 8$).

The other parameters involved in Eq. (2.285) result from an identification procedure (see 2.6.3). Their number (n_p) is defined by the summation limit s:

$$n_p = 8s \tag{2.287}$$

Let n_e be the number of experimental values describing the plastic anisotropy. The summation limit should be chosen according to the following constraint:

$$n_p = 8s \leq n_e \tag{2.288}$$

i.e.

$$s \leq n_e/8, \quad s \in N^* \tag{2.289}$$

Apparently, Eq. (2.285) is usable only when $n_e \geq 8$. In fact, it also works with less experimental values. When such a situation occurs, the summation limit should be $s = 1$, and the $n_e < 8$ identification constraints arisen from experiments should be accompanied by at least $8 - n_e$ artificial conditions involving the material parameters. For example, if $n_e = 6$, we may enforce the equalities $m_1^{(1)} = n_1^{(1)}$ and $m_2^{(1)} = n_2^{(1)}$.

2.6.3 Identification Procedure

Due to the expandable structure of the yield criterion, many identification strategies can be devised. We shall restrict our discussion to a procedure that uses only normalized yield stresses and r-coefficients obtained from uniaxial and biaxial tensile tests.

Let Y_θ be the yield stress predicted by the yield criterion in the case of a uniaxial traction along the direction defined by the angle θ measured from RD. The planar components of the stress tensor are in this case

$$\begin{aligned} &\sigma_{11}|_\theta = Y_\theta \cos^2\theta, \quad \sigma_{22}|_\theta = Y_\theta \sin^2\theta, \\ &\sigma_{12}|_\theta = \sigma_{21}|_\theta = Y_\theta \sin\theta\cos\theta \end{aligned} \tag{2.290}$$

After replacing them in Eq. (2.285), we get the associated equivalent stress

$$\bar{\sigma}|_\theta = Y_\theta F_\theta \tag{2.291}$$

where F_θ is defined by the relationships

$$\begin{aligned} \frac{F_\theta^{2k}}{w-1} &= \sum_{i=1}^{s} \left\{ w^{i-1} \left\{ \left[L_\theta^{(i)} + M_\theta^{(i)}\right]^{2k} + \left[L_\theta^{(i)} - M_\theta^{(i)}\right]^{2k} \right\} + \right. \\ &\qquad \left. w^{s-i} \left\{ \left[M_\theta^{(i)} + N_\theta^{(i)}\right]^{2k} + \left[M_\theta^{(i)} - N_\theta^{(i)}\right]^{2k} \right\} \right\} \\ L_\theta^{(i)} &= \ell_1^{(i)} \cos^2\theta + \ell_2^{(i)} \sin^2\theta \\ M_\theta^{(i)} &= \sqrt{\left[m_1^{(i)} \cos^2\theta - m_2^{(i)} \sin^2\theta\right]^2 + \left[m_3^{(i)} \sin 2\theta\right]^2} \\ N_\theta^{(i)} &= \sqrt{\left[n_1^{(i)} \cos^2\theta - n_2^{(i)} \sin^2\theta\right]^2 + \left[n_3^{(i)} \sin 2\theta\right]^2} \end{aligned} \tag{2.292}$$

Equations (2.281) and (2.291) lead to the following expression of the normalized uniaxial yield stress:

$$y_\theta = \frac{Y_\theta}{Y} = \frac{1}{F_\theta} \tag{2.293}$$

The r-coefficient corresponding to the uniaxial traction along a direction inclined at the angle θ measured from RD is defined by the formula

$$r_\theta = \frac{\dot{\varepsilon}^{(p)}_{\theta+90^\circ}}{\dot{\varepsilon}^{(p)}_{ND}} \tag{2.294}$$

where $\dot{\varepsilon}^{(p)}_{\theta+90^\circ}$ is the plastic strain-rate component associated to the $\theta + 90^\circ$ planar direction, and $\dot{\varepsilon}^{(p)}_{ND}$ is the through-thickness component of the same tensor. After some simple mathematical manipulations, Eq. (2.294) becomes

$$r_\theta = \frac{F_\theta}{G_\theta} - 1 \tag{2.295}$$

where G_θ is defined by the relationships

$$\begin{aligned}
&\frac{F_\theta^{2k-1} G_\theta}{w-1} = \sum_{i=1}^{s} \left\{ w^{i-1} \left[\hat{L}_\theta^{(i)} + \hat{M}_\theta^{(i)} \right] \left[L_\theta^{(i)} + M_\theta^{(i)} \right]^{2k-1} + \right. \\
&w^{i-1} \left[\hat{L}_\theta^{(i)} - \hat{M}_\theta^{(i)} \right] \left[L_\theta^{(i)} - M_\theta^{(i)} \right]^{2k-1} + w^{s-i} \left[\hat{M}_\theta^{(i)} + \hat{N}_\theta^{(i)} \right] \left[M_\theta^{(i)} + N_\theta^{(i)} \right]^{2k-1} + \\
&\left. w^{s-i} \left[\hat{M}_\theta^{(i)} - \hat{N}_\theta^{(i)} \right] \left[M_\theta^{(i)} - N_\theta^{(i)} \right]^{2k-1} \right\} \\
&\hat{L}_\theta^{(i)} = \ell_1^{(i)} + \ell_2^{(i)} \\
&\hat{M}_\theta^{(i)} = \left[m_1^{(i)} - m_2^{(i)} \right] \left[m_1^{(i)} \cos^2 \theta - m_2^{(i)} \sin^2 \theta \right] \Big/ M_\theta^{(i)} \\
&\hat{N}_\theta^{(i)} = \left[n_1^{(i)} - n_2^{(i)} \right] \left[n_1^{(i)} \cos^2 \theta - n_2^{(i)} \sin^2 \theta \right] \Big/ N_\theta^{(i)}
\end{aligned} \tag{2.296}$$

together with Eq. (2.292).

Let us denote by Y_b the yield stress predicted in the case of a biaxial traction along RD and TD. The corresponding planar components of the stress tensor are

$$\sigma_{11}|_b = Y_b, \quad \sigma_{22}|_b = Y_b, \quad \sigma_{12}|_b = \sigma_{21}|_b = 0 \tag{2.297}$$

After replacing them in Eq. (2.285), we get the associated equivalent stress

$$\bar{\sigma}|_b = Y_b F_b \tag{2.298}$$

where F_b is defined by the relationships

$$\begin{aligned}
\frac{F_b^{2k}}{w-1} &= \sum_{i=1}^{s} \left\{ w^{i-1} \left\{ \left[L_b^{(i)} + M_b^{(i)} \right]^{2k} + \left[L_b^{(i)} - M_b^{(i)} \right]^{2k} \right\} + \right. \\
&\left. w^{s-i} \left\{ \left[M_b^{(i)} + N_b^{(i)} \right]^{2k} + \left[M_b^{(i)} - N_b^{(i)} \right]^{2k} \right\} \right\} \\
L_b^{(i)} &= \ell_1^{(i)} + \ell_2^{(i)},\ M_b^{(i)} = m_1^{(i)} - m_2^{(i)},\ N_b^{(i)} = n_1^{(i)} - n_2^{(i)}
\end{aligned} \tag{2.299}$$

Equations (2.281) and (2.298) lead to the following expression of the normalized biaxial yield stress:

$$y_b = \frac{Y_b}{Y} = \frac{1}{F_b} \tag{2.300}$$

The r-coefficient corresponding to the biaxial traction along RD and TD is defined by the formula

$$r_b = \frac{\dot{\varepsilon}_{TD}^{(p)}}{\dot{\varepsilon}_{RD}^{(p)}} \tag{2.301}$$

where $\dot{\varepsilon}_{RD}^{(p)}$ and $\dot{\varepsilon}_{TD}^{(p)}$ are the plastic strain-rate components associated to the rolling and transverse directions, respectively. After some simple mathematical manipulations, Eq. (2.301) becomes

$$r_b = \frac{F_b}{G_b} - 1 \tag{2.302}$$

where G_b is defined by the relationships

$$\begin{aligned}
\frac{F_b^{2k-1} G_b}{w-1} &= \sum_{i=1}^{s} \left\{ w^{i-1} \left[\hat{L}_b^{(i)} + \hat{M}_b^{(i)} \right] \left[L_b^{(i)} + M_b^{(i)} \right]^{2k-1} + \right. \\
&w^{i-1} \left[\hat{L}_b^{(i)} - \hat{M}_b^{(i)} \right] \left[L_b^{(i)} - M_b^{(i)} \right]^{2k-1} + w^{s-i} \left[\hat{M}_b^{(i)} + \hat{N}_b^{(i)} \right] \left[M_b^{(i)} + N_b^{(i)} \right]^{2k-1} + \\
&\left. w^{s-i} \left[\hat{M}_b^{(i)} - \hat{N}_b^{(i)} \right] \left[M_b^{(i)} - N_b^{(i)} \right]^{2k-1} \right\} \\
\hat{L}_b^{(i)} &= \ell_1^{(i)}, \quad \hat{M}_b^{(i)} = m_1^{(i)}, \quad \hat{N}_b^{(i)} = n_1^{(i)}
\end{aligned} \tag{2.303}$$

together with Eq. (2.299).

An identification procedure that strictly enforces a large number of experimental constraints on the yield criterion would be inefficient in practical applications. The failure probability of such a strategy increases when the external restrictions become stronger. Taking into account this aspect, the authors have developed an identification procedure based on the minimization of the following error-function:

$$E\left[\ell_1^{(i)},\ell_2^{(i)},m_1^{(i)},m_2^{(i)},m_3^{(i)},n_1^{(i)},n_2^{(i)},n_3^{(i)}\,\middle|\, i=1,\ldots,s\right]=$$

$$\sum_{\theta_j}\left[\frac{y_{\theta_j}^{(\exp)}}{y_{\theta_j}}-1\right]^2+\sum_{\theta_j}\left[r_{\theta_j}^{(\exp)}-r_{\theta_j}\right]^2+\left[\frac{y_b^{(\exp)}}{y_b}-1\right]^2+\left[r_b^{(\exp)}-r_b\right]^2 \tag{2.304}$$

where θ_j represents an individual element from a finite set of angles defining the orientation of the specimens used in the uniaxial tensile tests. One may notice that Eq. (2.304) describes a square-distance between the experimental and predicted values of the anisotropy characteristics.

Two versions of the BBC 2008 yield criterion have been evaluated from the point of view of their performances (see [91]). They include 8 and 16 material coefficients, respectively, and correspond to the smallest values of the summation limit ($s = 1$ and $s = 2$). The identification of the BBC 2008 (16 parameters) model has been performed using the following mechanical parameters: $y_{0^\circ}^{(\exp)}$, $y_{15^\circ}^{(\exp)}$, $y_{30^\circ}^{(\exp)}$, $y_{45^\circ}^{(\exp)}$, $y_{60^\circ}^{(\exp)}$, $y_{75^\circ}^{(\exp)}$, $y_{90^\circ}^{(\exp)}$, $y_b^{(\exp)}$, $r_{0^\circ}^{(\exp)}$, $r_{15^\circ}^{(\exp)}$, $r_{30^\circ}^{(\exp)}$, $r_{45^\circ}^{(\exp)}$, $r_{60^\circ}^{(\exp)}$, $r_{75^\circ}^{(\exp)}$, $r_{90^\circ}^{(\exp)}$ and $r_b^{(\exp)}$. In the case of BBC 2008 (8 parameters), the input data has been restricted to the values $y_{0^\circ}^{(\exp)}$, $y_{45^\circ}^{(\exp)}$, $y_{90^\circ}^{(\exp)}$, $y_b^{(\exp)}$, $r_{0^\circ}^{(\exp)}$, $r_{45^\circ}^{(\exp)}$, $r_{90^\circ}^{(\exp)}$ and $r_b^{(\exp)}$.

The predictions of the BBC 2008 model with 16 parameters are superior to those given by the 8-parameters version. The improvement is noticeable especially in the case of the r-coefficients. This capability of the 16-parameter version is relevant for the accurate prediction of the thickness when simulating sheet metal forming processes. For the materials exhibiting a distribution of the anisotropy characteristics that would lead to the occurrence of 8 ears in a cylindrical deep-drawing process [69] the planar distribution of the *r*-coefficient predicted by the BBC 2008 yield criterion with 8 parameters is very inaccurate (see [91]). This model would not be able to predict the occurrence of more than 4 ears at the top edge of a cup deep-drawn from a circular blank. In contrast, the variation of the r-coefficient described by BBC 2008 with 16 parameters closely follows the reference data. In conclusion, this model would predict the occurrence of 8 ears as reported by Yoon et al. [69].

As compared with other formulations described in the literature, the new model does not use linear transformations of the stress tensor. Due to this fact, its computational efficiency should be superior in the simulation of sheet metal forming processes.

2.7 Recommendations on the Choice of the Yield Criterion

As concerns the modelling of the anisotropic plasticity, the present state-of-the-art is somewhat confusing since most of the above-described yield criteria are still being used. The most important factors that must be taken into account when choosing the yield criterion are as follows:

- Accuracy of the prediction both of the yield locus and the uniaxial yield stress and uniaxial coefficient of plastic anisotropy
- Computational efficiency and ease of implementation in numerical simulation codes
- Flexibility of the yield criterion
- Degree of generality
- Number of mechanical parameters needed by the identification procedure
- Robustness of the identification procedure
- Experimental difficulties caused by the determination of the mechanical parameters involved in the identification procedure
- User-friendliness of the yield criterion
- Acceptance of the yield criterion in the scientific/industrial community.

We shall now analyse some of these factors.

2.7.1 Comparison of the Yield Criteria

At present, the most frequently used yield criteria are Hill 1948, Hill 1990 and Barlat 1989. Due to this fact, they have been chosen as reference models for comparison with one of the advanced yield criteria, namely BBC 2000. The comparison is focused on the following performance aspects: prediction of the yield locus geometry and description of the planar distribution both for uniaxial yield stress and uniaxial coefficient of plastic anisotropy. The aluminium alloy AA3103-0 has been chosen as a test material.

Figure 2.19 shows the normalised yield loci predicted by Hill 1948, Hill 1990, Barlat 1989 and BBC 2000 yield criteria together with experimental data [6, 70]. One may notice that the best predictions are provided by the BBC 2000 and Hill 1990 models, while the performances of the Hill 1948 and Barlat 1989 models are unsatisfactory, especially in the biaxial tension region.

The planar distribution of the uniaxial yield stresses predicted by the models is shown in Fig. 2.20. As one may notice, BBC 2000 and Hill 1990 have better performances. The predictions of the Hill 1948 and Barlat 1989 are in poorer agreement with the experimental data, due to the fact that only the uniaxial yield stress corresponding to the rolling direction is used by their identification procedure.

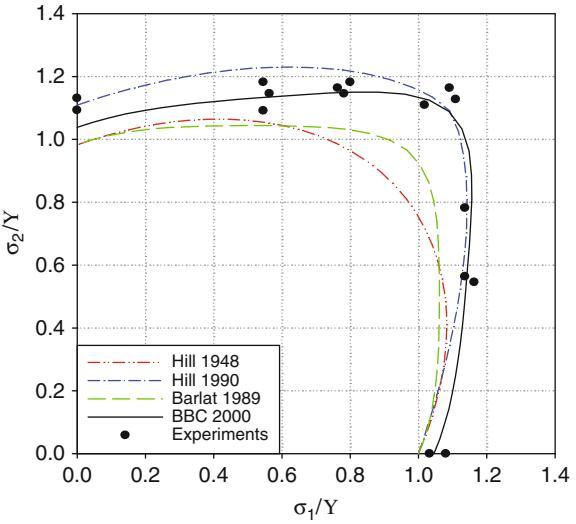

Fig. 2.19 Yield loci predicted by the Hill 1948, Hill 1990, Barlat 1989 and BBC 2000 criteria versus experimental one for the AA3103-0 aluminium alloy

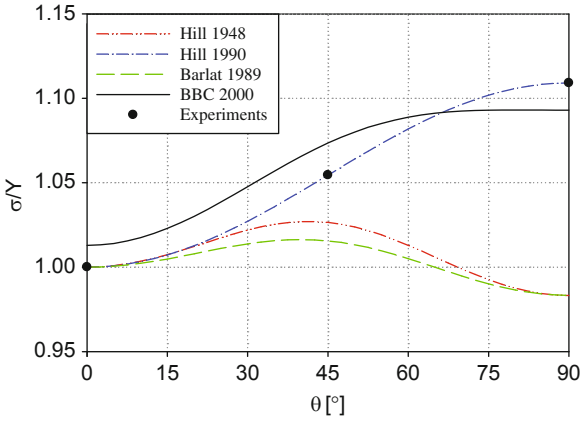

Fig. 2.20 Uniaxial yield stresses predicted by the Hill 1948, Hill 1990, Barlat 1989 and BBC 2000 yield criteria versus experimental one for the AA3103-0 aluminium alloy

As concerns the prediction of the uniaxial coefficient of plastic anisotropy (Fig. 2.21), the BBC 2000, Hill 1948 and Barlat 1989 have the best performances. Due to the fact that only the coefficient corresponding to the diagonal direction is used in its identification procedure, Hill 1990 cannot provide good predictions.

We can conclude that the best quality of the predictions will be ensured by the yield criteria having an identification procedure based both on uniaxial and biaxial tension experimental data. As concerns the experimental data obtained by uniaxial tension tests, the identification should use at least the yield stresses and the coefficients of plastic anisotropy corresponding to three planar directions (0, 45 and 90°). Under such circumstances, the yield criterion will have to fit a minimum number of seven mechanical parameters.

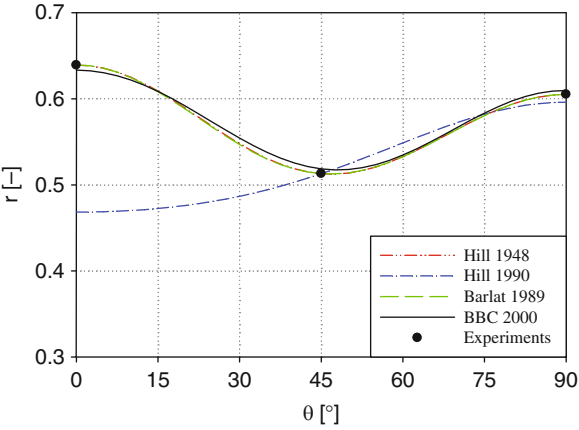

Fig. 2.21 Anisotropy coefficients predicted by the Hill 1948, Hill 1990, Barlat 1989 and BBC 2000 yield criteria versus experimental one for the AA3103-0 aluminium alloy

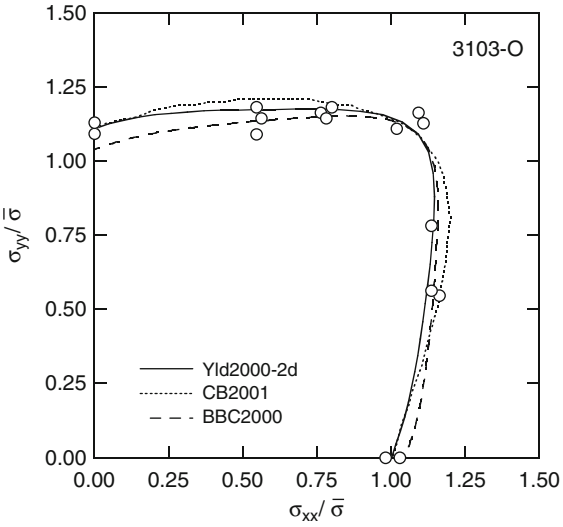

Fig. 2.22 Yield loci for 3103-0 alloy sheet predicted with the Yld2000-2d, CB 2001 and BBC 2000 yield functions

The yield criteria using at least seven mechanical parameters in the identification procedure provide almost the same predictions of the anisotropic behaviour for usual materials. This fact can be noticed by comparing three of the most recently developed models, namely Barlat 2000 (Yld2000-2d) [5], Cazacu–Barlat 2001 (CB 2001) [75] and BBC 2000 [51]. The AA3103-0 aluminium alloy has been used in order to evaluate the accuracy of the predictions (see [92, 93]). Figure 2.22 shows the yield locus for this material measured in the first quadrant using biaxial tensile testing of cruciform specimens [92] and predicted with the Yld2000-2d [5], CB 2001 [75] and BBC 2000 [51] yield functions.

Figure 2.23 shows the experimental normalized yield stress and r value as a function of the tensile direction for a 3103-0 aluminium alloy sheet sample. The three

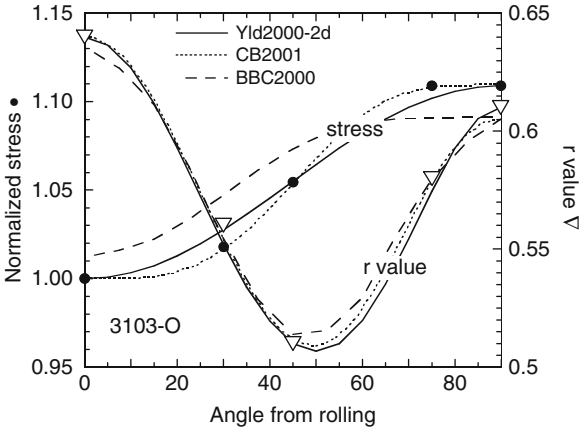

Fig. 2.23 Tensile anisotropy for 3103-0 alloy sheet

models are able to capture tensile anisotropy and the yield locus shape of this alloy very well.

The yield criteria that use a larger number of mechanical parameters in the identification (13 or even more—Barlat 2004, Soare 2007, BBC 2008 etc.) are able to provide highly accurate descriptions of the anisotropic behaviour. It is especially notable their capability to capture the occurrence of six or eight ears in the case of deep-drawing of cylindrical cups (see [69, 89]).

2.7.2 Evaluating the Performances of the Yield Criteria

As emphasized in the previous section, the performances of the yield criteria must be evaluated by thorough comparisons with experimental data. These comparisons should not be limited to the analysis of the yield locus shape. They should also envisage the planar distributions of the uniaxial yield stress and uniaxial coefficient of plastic anisotropy. In order to have a comprehensive evaluation tool, the members of the CERTETA research team have developed a global accuracy index defined as follows [70, 71, 94]:

$$\beta = \varphi + \delta + \gamma \, [\%] \tag{2.305}$$

where: ϕ is an accuracy index associated to the prediction of the yield locus shape in the plane of the principal stresses; δ is the accuracy index associated to the prediction of the planar distribution of the uniaxial yield stress; γ is the accuracy index associated to the prediction of the planar distribution of the uniaxial coefficient of plastic anisotropy.

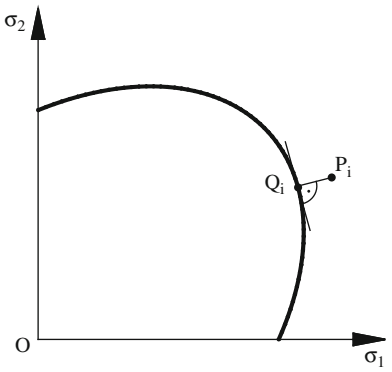

Fig. 2.24 Projection Q_i of an experimental point P_i onto the yield locus predicted by a yield criterion

φ is computed by using the formula

$$\varphi = \frac{\sqrt{\sum_{i=1}^{n} d^2\,(P_i, Q_i)}}{Y} 100\,[\%] \tag{2.306}$$

where Y is the reference yield stress, $d^2(P_i, Q_i)$ is the squared distance from an experimental point P_i and its projection Q_i onto the yield locus predicted by the yield criterion under testing (see Fig. 2.24), and n is the total number of the available experimental points.

δ is computed by using the formula

$$\delta = \sqrt{\sum_{i=1}^{n} \left(\frac{\sigma_{\theta_i}^{\exp} - \sigma_{\theta_i}^{t}}{\sigma_{\theta_i}^{\exp}} \right)} 100\ [\%] \tag{2.307}$$

where; $\sigma_{\theta_i}^{\exp}$ is the experimental uniaxial yield stress corresponding to the direction defined by the angle θ_i (measured from the rolling direction); $\sigma_{\theta_i}^{t}$ is the predicted uniaxial yield stress associated to the same direction; n is the total number of experimental points.

γ is computed by using the formula

$$\gamma = \sqrt{\sum_{i=1}^{n} \left(\frac{r_{\theta_i}^{\exp} - r_{\theta_i}^{t}}{r_{\theta_i}^{\exp}} \right)} 100\ [\%] \tag{2.308}$$

where: $r_{\theta_i}^{\exp}$ is the experimental anisotropy coefficient corresponding to the direction defined by the angle θ_i (measured from the rolling direction); $r_{\theta_i}^{t}$ is the predicted anisotropy coefficient corresponding to the same direction; n is the total number of experimental points.

The practical use of the global accuracy index is exemplified by comparing four yield criteria: Hill 1948, Hill 1990, Barlat 1989 and BBC 2000. The identification procedure of the BBC 2000 model is based on the minimisation of an

Table 2.2 Quality index for different yield criteria

Material	Quality index	Hill 1948	Hill 1990	Barlat 1989	BBC 2000
AA3103-0	φ [%]	42.64	18.8	30.64	13.41
	δ [%]	11.65	0	11.92	2.64
	γ [%]	0	36.05	0	1.60
	β [%]	54.29	56.03	42.56	17.65
AA5182-0	φ [%]	30.33	20.26	21.14	12.95
	δ [%]	8.58	0	8.54	1.96
	γ [%]	0	48.51	0	0.39
	β [%]	38.91	68.77	29.68	15.3
AA6111-T4	φ [%]	12.84	0	7.47	2.57
	δ [%]	16.76	1.95	12.47	6.69
	γ [%]	8.69	54.20	6.98	8.38
	β [%]	38.29	56.15	26.62	17.64

error-function. The comparison has been performed in the case of three aluminium alloys: AA3103-0, AA5182-0 and AA6111-T4. The values of the individual accuracy indices are listed in Table 2.2. The best overall performance corresponds to the lowest value of the global index β. Table 2.2 shows that BBC 2000 has better performances as compared to the other yield criteria (the corresponding overall index is three times smaller than in the case of the Hill 1948 yield criterion).

2.7.3 Mechanical Parameters Used by the Identification Procedure of the Yield Criteria

Table 2.3 shows the mechanical parameters needed for the identification of several yield criteria. On the basis of this list, we can estimate the amount of experimental tests and the costs required for identification of various yield criteria. The main question of interest is whether a biaxial yield stress and biaxial anisotropy coefficient have to be determined since this requires a special apparatus: either for cross tensile tests, hydraulic bulge tests or for disk compression, respectively.

Table 2.3 makes reference only to plane-stress models (2D). The following notations have been used in the table: 3D signifies the fact that the model is extendable to spatial stress states; A1 shows that the yield criterion is able to describe 'the first order anomalous behaviour' (see [26]); A2 shows that the yield criterion is able to describe 'the second order anomalous behaviour' (see [28]). The yield criteria belonging to Hershey family use an exponent chosen in accordance with the crystallographic structure of the material.

2.7.4 Implementation of the Yield Criteria in Numerical Simulation Programmes

The main criteria for selecting the yield function for implementation in Finite Element code are the prediction precision of the anisotropic behaviour and the CPU

Table 2.3 The mechanical parameters needed for the identification of several yield criteria

Author, year	σ_0	σ_{30}	σ_{45}	σ_{75}	σ_{90}	σ_b	r_0	r_{30}	r_{45}	r_{75}	r_{90}	r_b	3D	A1	A2
Hill's family															
Hill 1948	x						x		x		x		x		
Hill 1979	x					x	x						x	x	
Hill 1990	x		x		x	x			x					x	
Hill 1993	x				x	x	x				x			x	x
Lin, Ding 1996	x				x	x	x		x		x			x	x
Hu 2005					x	x	x		x		x		x	x	x
Leacock 2006					x	x	x		x		x			x	x
Hershey's family															
Hosford 1979	x						x				x		x	x	
Barlat 1989	x						x				x			x	
Barlat 1991	x		x		x	x							x	x	
Karafillis Boyce 1993	x		x		x		x		x		x		x	x	x
Barlat 1997	x		x		x	x	x		x		x		x	x	x
BBC 2000	x		x		x	x	x		x		x		x	x	x
Barlat 2000	x		x		x	x	x		x		x			x	x
Bron, Besson 2003	x		x		x	x	x		x		x	x	x	x	x
Barlat 2004	x		x		x	x	x		x		x	x	x	x	x
BBC 2005	x		x		x	x	x		x		x	x	x	x	x
Drucker's family															
Cazacu–Barlat 2001	x	x	x	x	x	x	x	x	x	x	x		x	x	x
Cazacu–Barlat 2003	x	x	x	x	x	x	x	x	x	x	x		x	x	x
C-P – B 2006	x	x	x	x	x	x	x	x	x	x	x		x	x	x
Polinomial criteria															
Comsa 2006	x		x		x	x	x		x		x	x	x	x	x
Soare 2007 (Poly 4)	x	x	x		x	x	x		x		x	x	x	x	x

time efficiency of the program. Table 2.4 presents the main commercial FE software and the anisotropic yield criteria implemented in them. The Barlat 2000, Vegter and BBC 2005 models have been implemented by various users in the material subroutines of ABAQUS and LS-DYNA.

Table 2.4 Various yield criteria implemented in some commercial codes

Software	Hill 1948	Hill 1990	Barlat 1989	Barlat 2000	Vegter	BBC 2005
ABAQUS	X	X	X			
AUTOFORM	X	X	X			X
LS-DYNA	X	X	X	X		
OPTRIS	X		X			
PAM STAMP	X	X			X	
STAM PACK	X	X				

2.7.5 Overview of the Anisotropic Yield Criteria Developing

The yield criterion proposed by Hill in 1948 [25] is still very used in industrial applications. Its general acceptance is due to the mathematical simplicity and the direct significance of the coefficients. The identification procedure of this yield criterion uses only four mechanical parameters. As a consequence, it cannot accurately describe the planar distribution of both the uniaxial yield stress and the uniaxial coefficient of plastic anisotropy. In addition, it cannot capture the biaxial yield stress.

The discussion in the previous sections of the chapter has shown the stages followed by the development of the anisotropic yield criteria:

Methods used for transforming isotropic formulations into anisotropic ones:

- inclusion of new coefficients into isotropic models: Hill 1948 [25], Hill 1979 [29], Hosford 1979 [31]
- use of linear transformations: Barlat 1991 [10], Karafillis-Boyce [21]
- representation functions: Cazacu–Barlat 2001 [75]
- geometrical methods: Vegter [80], Mollica [82]
- extension of the yield criteria outside the orthotropy axes by using coordinate transformations: Barlat 1989 [50], Hill 1990 [39].

Identification strategies:

- analytical solutions: Hill 1948 [25], Hill 1990 [39]
- numerical procedures:
  - Newton–Raphson: Barlat 1989 [50], Barlat 2000 [5], BBC 2005 [53], BBC 2008 [91] etc.
  - minimization of an error-function: BBC 2000 [51], BBC 2008 [91]
  - genetic algorithms: Chaparro et al. [95].

Further information referring to the most recent anisotropic yield criteria can be found in the synthesis papers/monographs [96–101].

2.7.6 Perspectives

As it can be seen from the previous sub-chapters, advanced yield criteria allow accurate prediction of the anisotropic behaviour of materials. On the one hand, it is possible to simultaneously describe both the uniaxial yield stress variation and the anisotropic coefficient in the sheet. On the other hand, it is also possible to model both „first and second order anisotropic behaviour anomalies'. As well as this, the yield criteria have been extended to 3D. The asymmetry of the yield loci can be accurately predicted, thus allowing modeling the strength differential effect specific to materials with hexagonal close packed structure.

In the future the research in this field of study will be oriented towards developing new models which include special properties (superplastic materials, shape memory materials etc.). By including the evolution of the coefficients in yield functions it will be possible to predict the yield loci for nonlinear loading. Stochastic modeling will be used for a more robust prediction of the yield loci (taking into account the variability of the mechanical parameters). Coupling of the phenomenological models with the ones based on crystal plasticity will allow better simulation of the parameters evolution in technological processes (these include temperature, strain rate, strain path, structural evolution).

Therefore, the virtual process chain will be described more accurately, allowing it to be used in real fabrication processes.

2.8 Modeling of the Bauschinger Effect

2.8.1 Reversal Loading in Sheet Metal Forming Processes

In a typical sheet metal forming process a considerable amount of material undergoes non-proportional loading. Such as during passing over a tool radius or through a draw bead material is subjected to the multiple bending-unbending, which means reverse tension-compression loading over the sheet thickness. Figure 2.25 shows the stress distribution for these two cases, calculated with the commercial FE-code ABAQUS [102].

It is well known that the mechanical response of metals depends not only on the current state but also on the previous deformation history. One of the phenomena related to the change of mechanical properties during a non-proportional loading is the Bauschinger effect. It is usually associated with conditions where the yield strength of a metal decreases when the direction of strain is changed. Figure 2.26a illustrates the Bauschinger effect for the uniaxial tension-compression

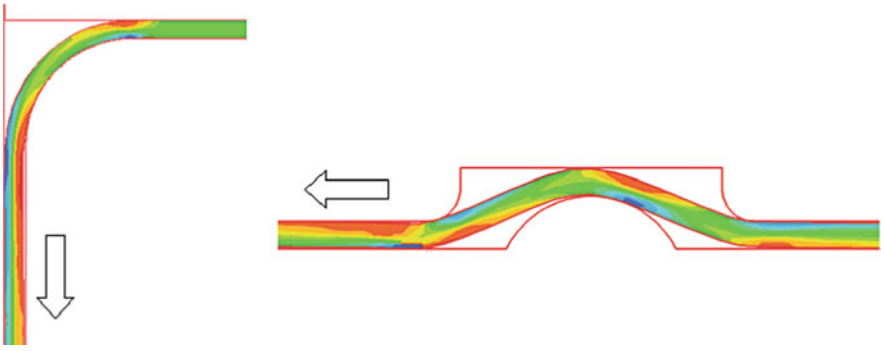

Fig. 2.25 Reversal tension-compression loading (*red* for the tension stress) during passing over a tool radius (*left*) or through a draw bead. *Arrows* show the direction of drawing

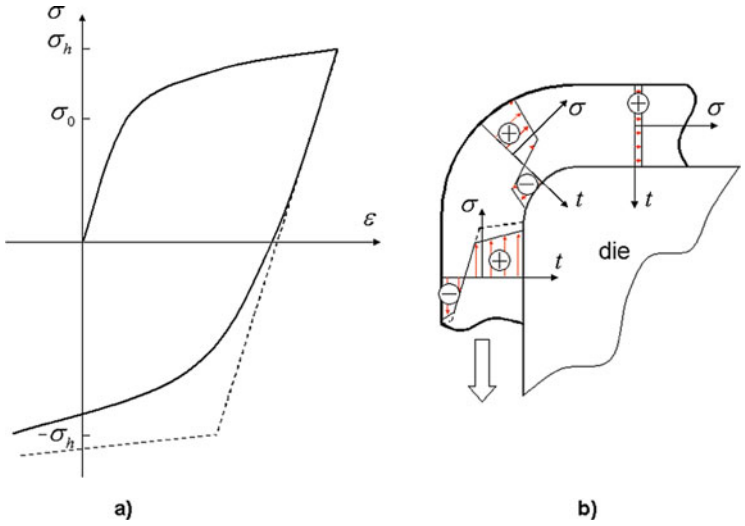

Fig. 2.26 Schematic of the Bauschinger effect (**a**) and its influence on the stress evolution during passing over a die radius (**b**)

test. First material hardens in tension to the stress σ_h and then loaded in compression. Plastic deformation occurs before negative yield strength (dashed line presents material behavior without the Bauschinger effect). Similar reversal stress-strain history occurs when material passes over a die radius (Fig. 2.26b). During the first bending there is a tension on the outer side of a sheet and a compression inside. During the second unbending the stress state over the sheets thickness reverses and is influenced directly by the Bauschinger effect.

Especially for a springback prediction an accurate description of the material behavior during reversal loading is essential: on the one hand it is important to know the exact stress distribution at the end of the forming process before unloading starts, on the other hand it is necessary to model unloading with the proper stress-strain response [103]. Since the magnitude of a springback depends on the yield strength and the Young's modulus, more proper material modeling including the Bauschinger effect has become necessary particularly for the new materials like high strength steels and aluminium alloys.

2.8.2 Experimental Observations

The experimental procedure in order to get cyclic tension-compression curves for sheet metals is complex as sheet metal tends to buckle during compression loading. This makes the measurement delicate, especially for large strains. Several techniques to perform such tests have been developed recently [103–105]. Based on these investigations one can separate the Bauschinger effect into three partial effects: early re-plastification, transient softening and workhardening stagnation leading to

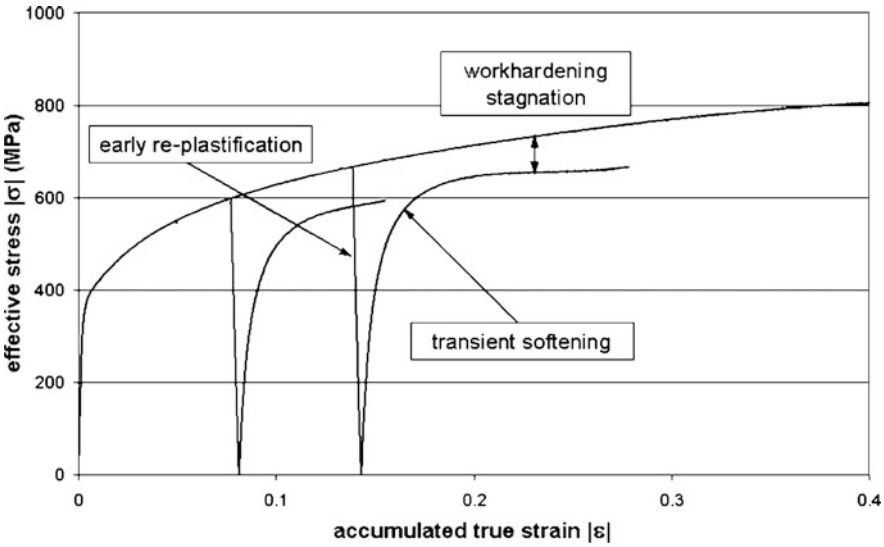

Fig. 2.27 Uniaxial tension and tension-compression curves with different pre-strains for DP600 steel

reduced yielding. Figure 2.27 shows tension and two tension-compression curves at different pre-strains of 8 and 14% for the high strength steel DP600. A special representation of the compression curves as the positive effective stress over the accumulated true strain permits the observation of the workhardening stagnation, which is typical for many materials and looks like a delay in the hardening for a certain amount of strain.

Noticeable there is a non-linear character on the stress-strain curve directly after the load reversal, so that the tangential modulus is lower than the elastic modulus. One call this phenomena can early re-yielding or early re-plastification [104–106].

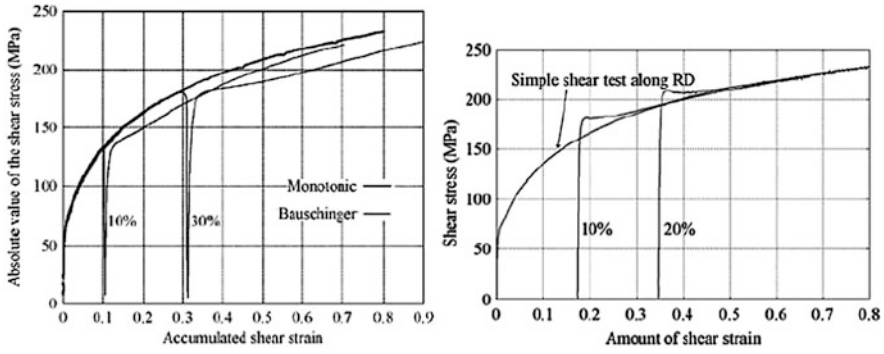

Fig. 2.28 The Bauschinger effect during reversal shear loading and the cross effect during orthogonal loading for mild steel DC06 [107]

Another phenomenon related to the Bauschinger effect is the so-called reduction of the Young's modulus depending on the pre-strain. In [104, 105] it has been shown that the initial modulus typically reduces exponentially with the accumulated pre-strain. In [107] not only the sign of the loading but also its direction has been verified. During the orthogonal loading (uniaxial tension followed by simple shear) the increase of the yield stress has been observed (see Fig. 2.28). This phenomena is the so-colled cross effect.

2.8.3 Physical Nature of the Bauschinger Effect

Before dealing with phenomenological modeling of the Bauschinger effect, it is advisable to get a good understanding of the physical origin of it, what may lead to more refined plasticity models and may ultimately improve the simulation results. As for the metal plasticity at room temperature in general, the main source for the Bauschinger effect is a dislocation structure.

As deformation occurs, dislocations move, activating slip on the energetically favorable slip systems, and the dislocation density increases gradually. Dislocations overlap, accumulate at obstacles producing dislocation tangles and pile-ups (Fig. 2.29). This increases the resistance to further dislocation motions and causes a hardening of the metal.

The Bauschinger effect can be generally ascribed to long-range effects, such as internal stresses due to dislocation interactions, dislocation pile-ups at grain boundaries or Orowan loops around strong precipitates, and to short-range effects, such as directionality of mobile dislocations in their resistance to motion or annihilation of the dislocations during the reverse loading.

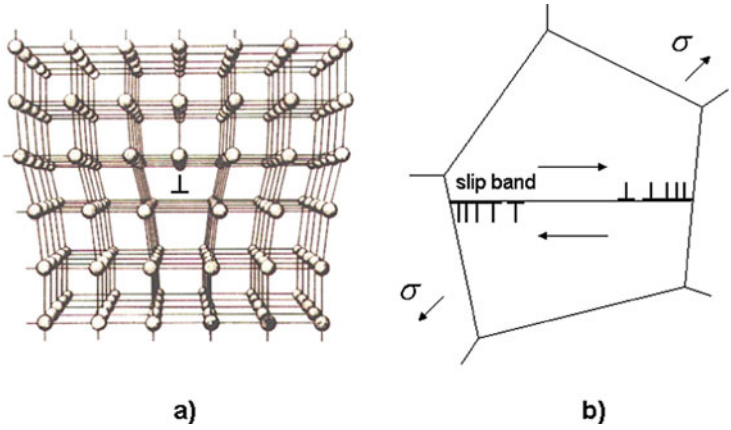

Fig. 2.29 Edge dislocation (**a**) and dislocation pile-ups on the grain boundaries (**b**)

The primary driving force of the Bauschinger effect can be explained by the motion of the less stable dislocation structures such as pile-ups. Pile-up occurs as a cluster of dislocations is unable to move past the barrier. As accumulated dislocations generate microscopic back-stresses, they will assist the movement of dislocations in the reverse direction and the yield strength becomes lower. This occurs directly after the change of load direction or during unloading and takes place simultaneously with elastic deformation. With this microscopic mechanism one can explain such macroscopic phenomena as the transient softening, the early re-plastification and the reduction of the Young's modulus.

Another mechanism is, when the strain direction is reversed, dislocations of the opposite sign can be produced from the same source that produced the slip-causing dislocations in the initial direction. Dislocations with opposite signs can attract and annihilate each other. Since strain hardening is related to an increased dislocation density, reducing the number of dislocations reduces strength.

The workhardening stagnation can be explained by the partial disintegration of the performed dislocation cell structures and the subsequent resumption of work-hardening to the formation of new dislocation structures [105, 107].

The so-called cross effect during orthogonal loading is referred to the fact that the dislocation structures which developed during pre-loading in a given direction act as obstacles to slip on systems activated in the orthogonal direction after the change of loading direction [107].

Other mechanisms beside the crystallographic slip can also macroscopically contribute to the Bauschinger effect. Twinning is crucial particularly for the metals with hexagonal close-packed lattice such as magnesium or zircon. During the cold forming of the magnesium alloys the twinning under compression can occur, which leads to the essential reduction of the yield strength. Other factors which contribute to such material behavior on the macroscopic level could be a change of the crystallographic texture during plastic deformation, stress induced phase transformation or porosity evolution.

2.8.4 Phenomenological Modelling

The Bauschinger effect is usually being predicted by using the anisotropic (also known as distortional) hardening, which describes in general a transformation of the yield surface during the plastic deformation. However, as the experimental observations show, the distortion of the yield surface is very complex and includes its translation and change of its size and shape [108]. To describe such a behavior phenomenologicaly a large amount of experiments is needed, however with reasonable effort one can describe the translation of the yield surface (kinematic hardening) and the change of its size (isotropic hardening, Fig. 2.30).

It is necessary to distinguish between the aspects: the word isotropic can be related to both yield criteria and to the evolution of yield surface, while kinematic is applied only to the evolution. A position of the yield surface will be described with the back-stress tensor $\boldsymbol{\alpha}$. It is obvious, that as soon as plastic pre-strain occurs

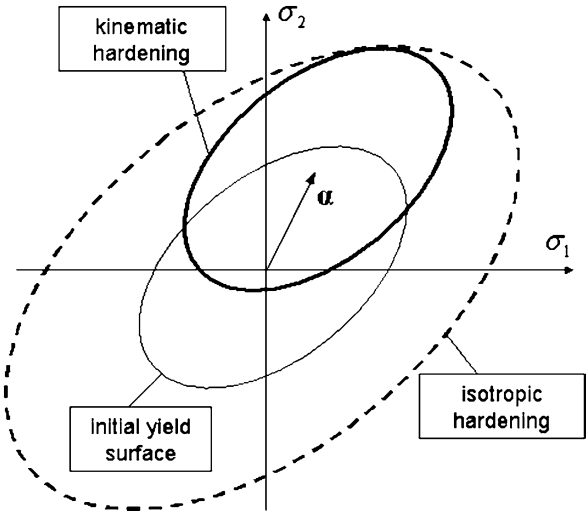

Fig. 2.30 Kinematic hardening—translation of the yield surface with the same shape and size

and the back-stress tensor has a value, the kinematic hardening leads to the plastic anisotropy even if isotropic yield criterion is used.

Before starting with particular models describing kinematic hardening, let us first refer to the classical framework usually being used for elastoplastic modeling with isotropic hardening.

Assuming small elastic and large plastic deformations for metals, the rate of deformation can be decomposed into elastic and plastic parts as

$$\dot{\boldsymbol{\varepsilon}} = \dot{\boldsymbol{\varepsilon}}_e + \dot{\boldsymbol{\varepsilon}}_p \tag{2.309}$$

The stress-strain response in elastic range is assumed to be linear

$$\dot{\sigma} = \mathbf{C}\mathbf{:}\,\dot{\boldsymbol{\varepsilon}}_e \tag{2.310}$$

where **C** is the elasticity tensor.

The plastic flow occurs when the yield criterion is valid:

$$f = \phi(\boldsymbol{\sigma}) - R - \sigma_0 = 0 \tag{2.311}$$

where σ_0 is the initial yield stress, R is the scalar function, which introduces hardening and ϕ is the homogeneous function, which indicates the form of the yield surface. For simplicity, let us assume the von Mises isotropic yield function derived from the second invariant of the stress tensor

$$\phi = \mathrm{J}_2(\boldsymbol{\sigma}) = \sqrt{\frac{3}{2}}\,\|\mathbf{S}\| \tag{2.312}$$

where **S** is stress deviator tensor.

The consistency condition during the plastic flow is

$$\dot{f} = \frac{\partial f}{\partial \boldsymbol{\sigma}} : \dot{\boldsymbol{\sigma}} + \frac{\partial f}{\partial R}\dot{R} = 0 \tag{2.313}$$

The relation between plastic strains and stresses is defined by the flow rule:

$$\dot{\boldsymbol{\varepsilon}}_p = \dot{\lambda}\frac{\partial \Phi}{\partial \boldsymbol{\sigma}} \tag{2.314}$$

where λ is the Lagrange multiplier and ϕ is the plastic potential, which defines the direction of plastic flow. From (2.314) follows the normality of $\dot{\boldsymbol{\varepsilon}}_p$ to the yield surface for the associated flow rule ($\Phi = f$).

The equivalent plastic strain rate is defined as

$$\dot{p} = -\dot{\lambda}\frac{\partial \Phi}{\partial R} \tag{2.315}$$

For the associated flow rule and von Mises plasticity one can now derive the plastic multiplier

$$\dot{\lambda} = \dot{p} = \sqrt{\frac{2}{3}}\left\|\dot{\boldsymbol{\varepsilon}}_p\right\| \tag{2.316}$$

Finally substituting (2.315) into (2.310) one can write

$$\dot{\boldsymbol{\sigma}} = \mathbf{C} : (\dot{\boldsymbol{\varepsilon}} - \dot{\lambda}\frac{\partial \Phi}{\partial \boldsymbol{\sigma}}) \tag{2.317}$$

Additionally, the hypothesis of plastic incompressibility (independence on the hydrostatic stress) will be assumed:

$$\frac{\partial \Phi}{\partial (tr[\boldsymbol{\sigma}])} = 0 \tag{2.318}$$

2.8.4.1 Prager's Model

The hardening in this formulation corresponds to the pure translation of the yield surface in stress space and will be described by the back-stress tensor $\boldsymbol{\alpha}$. The yield condition in this case is

$$f = \sqrt{\frac{3}{2}}\left\|\mathbf{S} - \boldsymbol{\alpha}\right\| - \sigma_0 = 0 \tag{2.319}$$

In the theory of Prager, it is assumed that during loading the back-stress develops in the same direction as the plastic strain increment [108]:

$$\dot{\boldsymbol{\alpha}} = c\dot{\boldsymbol{\varepsilon}}_p \tag{2.320}$$

where c is a material constant. This model is the simplest case of the pure kinematic hardening. However, it can not accurately describe material behavior using the linear hardening.

2.8.4.2 Model of Armstrong and Frederick

To get a better description of a hardening and to make a smoother transition from elastic to inelastic behaviour, Armstrong and Frederick [109] suggested to enhance the evolution equation (2.320) to one of the Bailey-Orowan type:

$$\dot{\alpha} = c\left(\frac{2}{3}a\dot{\varepsilon}_p - \alpha\dot{p}\right) \tag{2.321}$$

where c and a are the material parameters. The additional recovery term with the accumulated plastic strain p describes a kind of memory effect and leads to an exponential evolution character of the back-stress, which corresponds much better to experimental observations.

2.8.4.3 Chaboche's Model

The previous models described the hardening only by the translation of the yield surface. With further improvement, Chaboche presented a mixed hardening rule as a superposition of nonlinear isotropic and kinematic hardening [108, 110].

Then the yield criterion is

$$f = \sqrt{\frac{3}{2}}\|\mathbf{S} - \boldsymbol{\alpha}\| - R - \sigma_0 = 0 \tag{2.322}$$

with the back-stress

$$\dot{\boldsymbol{\alpha}} = c(\frac{2}{3}a\dot{\boldsymbol{\varepsilon}}_p - \boldsymbol{\alpha}\dot{p}) \tag{2.323}$$

and the isotropic part of the hardening

$$\dot{R} = b(Q - R)\dot{p} \tag{2.324}$$

where c, a, b and Q are the material constants.

As it has been mentioned in [110] one non-linear term of the back-stress is not sufficient for the description of large-strain hardening. To improve it one can use several back-stresses simultaneously

$$\boldsymbol{\alpha} = \sum_{m=1}^{M} \boldsymbol{\alpha}^{(m)} \tag{2.325}$$

$$\dot{\boldsymbol{\alpha}}^{(m)} = c^{(m)}(\frac{2}{3}a^{(m)}\dot{\boldsymbol{\varepsilon}}_p - \boldsymbol{\alpha}^{(m)}\dot{p}) \tag{2.326}$$

including one linear

$$\dot{\boldsymbol{\alpha}}^{(M)} = \frac{2}{3}H\dot{\boldsymbol{\varepsilon}}_p \tag{2.327}$$

The model of Chaboche with many back-stress components is able to describe the transient softening quite accurately. However, the phenomena of the early re-plastification and the workhardening stagnation are still uncovered.

2.8.4.4 Yoshida–Uemori Model

The model of Yoshida and Uemori [105, 111] is a further improvement of the Chaboche's model which additionally describes the early re-plastification and the workhardening stagnation.

This model assumes two surfaces: the yield surface f develops within the bounding surface F. Based on the wide experimental investigations Yoshida and co-workers apply the pure kinematic hardening for the yield surface since the early re-plastification occurs at a very early stage of load reversal. At the same time the bounding surface has mixed isotropic-kinematic hardening:

$$f = \sqrt{\frac{3}{2}}\,\|\mathbf{S} - \boldsymbol{\alpha}\| - \sigma_0 = 0 \tag{2.328}$$

$$F = \sqrt{\frac{3}{2}}\,\|\mathbf{S} - \boldsymbol{\beta}\| - R - B = 0 \tag{2.329}$$

where $\boldsymbol{\beta}$ denotes the center of the bounding surface, and B and R are its initial size and isotropic hardening.

The flow rule is defined as

$$\dot{\boldsymbol{\varepsilon}}_p = \dot{\lambda}\frac{\partial f}{\partial \boldsymbol{\sigma}} \tag{2.330}$$

One can write the back-stress as the sum

$$\boldsymbol{\alpha} = \boldsymbol{\alpha}_* + \boldsymbol{\beta} \tag{2.331}$$

where $\boldsymbol{\alpha}_*$ is the relative motion of the yield surface with respect to the bounding surface

$$\dot{\boldsymbol{\alpha}}_* = \sqrt{\frac{2}{3}}ca(\mathbf{n}_p - \sqrt{\frac{\bar{\alpha}_*}{a}}\mathbf{n}_*)\dot{p} \tag{2.332}$$

in terms of the non-dimensional measures

$$\mathbf{n}_p = \frac{\mathbf{S} - \boldsymbol{\alpha}}{\|\mathbf{S} - \boldsymbol{\alpha}\|}, \quad \mathbf{n}_* = \frac{\boldsymbol{\alpha}}{\|\boldsymbol{\alpha}\|} \tag{2.333}$$

with

$$\dot{p} = \sqrt{\frac{2}{3}} \left\| \dot{\boldsymbol{\varepsilon}}_p \right\|, \quad \bar{\alpha}_* = \sqrt{\frac{3}{2}} \|\boldsymbol{\alpha}_*\|, \quad a = B + R - \sigma_0 \tag{2.334}$$

Kinematic hardening for the bounding surface is

$$\dot{\boldsymbol{\beta}} = m \left(\sqrt{\frac{2}{3}} b \mathbf{n}_p - \boldsymbol{\beta} \right) \dot{p} \tag{2.335}$$

and its isotropic hardening

$$\dot{R} = m(R_{sat} - R)\dot{p} \tag{2.336}$$

To describe the workhardening stagnation Yoshida and Uemori proposed to modify the evolution of the bounding surface by providing a new surface g in the stress space

$$g = \sqrt{\frac{3}{2}} \|\mathbf{S} - \mathbf{q}\| - r = 0 \tag{2.337}$$

where $\mathbf{q}$ and r denote the center and the size of the surface.

It will be assumed that the center of the bounding surface $\boldsymbol{\beta}$ exists either on or inside of the surface g and the isotropic hardening of the bounding surface R takes place when $\boldsymbol{\beta}$ stays on the surface g, namely $\dot{R} > 0$ when

$$g = \sqrt{\frac{3}{2}} \|\boldsymbol{\beta} - \mathbf{q}\| - r = 0 \,\text{and}\, \frac{\partial g}{\partial \boldsymbol{\beta}} : \dot{\boldsymbol{\beta}} > 0 \tag{2.338}$$

and $\dot{R} = 0$ otherwise (see Fig. 2.31).

The kinematic motion of the surface g is defined as

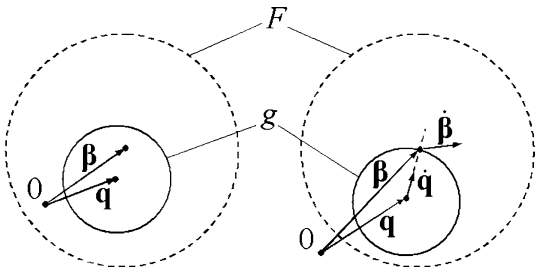

Fig. 2.31 Schematic illustration of the surface g in stress space

$$\dot{\mathbf{q}} = \mu(\boldsymbol{\beta} - \mathbf{q}) \tag{2.339}$$

with

$$\mu = \frac{\Gamma - \dot{r}}{r} \text{and} \Gamma = \frac{3(\boldsymbol{\beta} - \mathbf{q}) : \dot{\boldsymbol{\beta}}}{2r} \tag{2.340}$$

the evolution of r is

$$\begin{array}{l} \dot{r} = h\Gamma \text{ when } \dot{R} > 0 \\ \dot{r} = 0 \quad \text{when } \dot{R} = 0 \end{array} \tag{2.341}$$

where $h(0 \leq h \leq 1)$ is a material parameter.

After analysing the ability of the above model to describe experimental results it was found that the early re-plastification phenomenon can not be covered well enough. The proposed solution is to use the variable Young's modulus as a function of the accumulated plastic strain p:

$$E = E_0 - (E_0 - E_a)\left(1 - e^{-\xi p}\right) \tag{2.342}$$

where E_0 and E_a are the values of Young's modulus for virgin and infinitely large pre-strained material, respectively, and ξ is a material parameter. For the definition of the Young's modulus Yoshida suggests an average value in the stress range $0 \leq \sigma \leq 0.95\sigma_r$, where σ_r indicates the stress reversal point.

2.8.4.5 AutoForm-Model

To improve the springback prediction a novel approach to model the Bauschinger effect has been developed and implemented in the commercial code AutoForm [112]. The main idea of the model is to use the same evolution equation for the entire unloading and reverse loading path, including the area, which is treated as an elastic in conventional models. As the model is part of an undisclosed research, the principal of it will be presented here for the uniaxial tension-compression case using fictive values of the reversal stress σ_r and the reversal strain ε_r with the coordinate center in the point of load reversal

$$\varepsilon_r = \frac{\sigma_r}{E_l(p)} + K \, arctan \, h^2 \left(\frac{\sigma_r}{2\sigma_h(p)}\right)^2 \tag{2.343}$$

with $\sigma_h(p)$ as hardening stress used to describe tension curve (see Fig. 2.32) and E_l as the initial Young's modulus at the moment of load reversal. Analog to the Yoshida-Uemori model E_l is a function of the accumulated plastic strain p:

$$E_l = E\left(1 - \gamma\left(1 - e^{-\chi p}\right)\right) \tag{2.344}$$

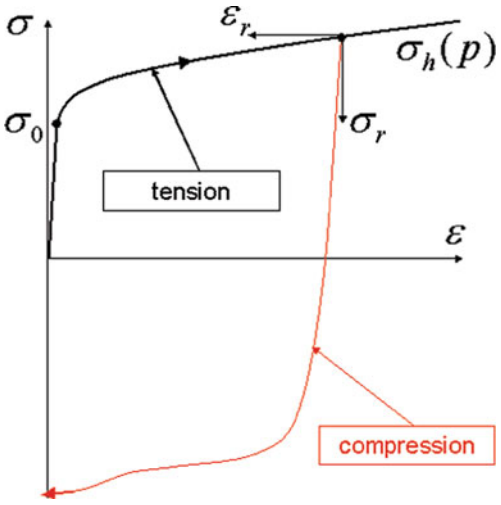

Fig. 2.32 Schematic of the tension-compression curve with reversal stress and strain

where γ and χ are two material parameters and E is the elastic modulus.

One can then write the definition for tension and compression parts of the curve

$$\sigma = \begin{cases} \sigma_h(p) & for \quad tension \\ \sigma_h(p) - \sigma_r & for \quad compression \end{cases} \tag{2.345}$$

On the contrary to the previous models, here the evolution equations for the hardening stress and for the back-stress are much more decoupled. The definition of the hardening during proportional loading is independent from the definition of the back-stress and hardening curve can be defined even in tabular form.

As in the model of Yoshida-Uemori, the pure kinematic hardening is assumed here. However, the model in AutoForm uses the non-linear stress-strain response within the yield surface and can describe the early re-plastification very accurately.

In order to model the workhardening stagnation, the accumulated equivalent plastic strain p is replaced by a new hardening parameter p_d, which behaves as follows: p_d is identical with p during proportional deformation and develops slower than p during reverse or non-proportional deformation. To determine if a deformation is reverse or non-proportional, a storage surface g is introduced (Fig. 2.33). During the initial proportional loading (time t), the progression of plastic strain extends the storage surface and the strain-like variable $\mathbf{q}$ lies on the surface g. During the further reverse or non-proportional loading (time $t + \Delta t$), the tensor $\mathbf{q}$ traverses the storage surface; during the time it is inside, the variable p_d develops slower than p. This behavior is controlled by a material parameter $\xi (0 \leq \xi \leq 1)$, which characterizes the fraction of forward strain that can be reversed with the delay of work hardening.

The set of equations is:

$$\dot{p}_d = f \cdot \dot{p} \tag{2.346}$$

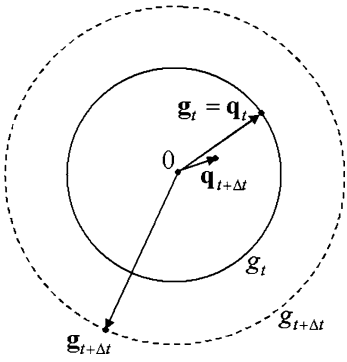

Fig. 2.33 Schematic illustration of the storage surface g

$$f = sign(\tilde{f})\tilde{f}^2 \tag{2.347}$$

$$\tilde{f} = 1 - \frac{3}{4}\frac{r}{g} \tag{2.348}$$

In the beginning is $g = 0$ and growths proportionally to $\dot{p}_d$:

$$\dot{g} = \xi \dot{p}_d \tag{2.349}$$

r in Eq. (2.348) is a scalar value

$$r = \phi\,(\mathbf{g} - \mathbf{q}) \tag{2.350}$$

where $\mathbf{q}$ is a tensor representing the position within the surface g

$$\dot{\mathbf{q}} = \dot{\mathbf{g}} + \dot{p}\left[\frac{\partial r}{\partial \mathbf{g}}\right]^{-1} \tag{2.351}$$

and

$$\dot{\mathbf{g}} = \frac{\dot{g}}{\varphi(\sigma)}\sigma \tag{2.352}$$

Considering Eqs. (2.350) and (2.351) and since $\mathbf{q}$ can not exceed the surface g, one derive the rate of r as

$$\begin{aligned} \dot{r} &= -\dot{p} \text{ when } r > 0 \\ \dot{r} &= 0 \quad \text{when } r = 0 \end{aligned} \tag{2.353}$$

Finally, assuming all the discussed above phenomena, the model is able to describe accurately experimental tension-compression curves. Figure 2.34a shows the uniaxial tension and tension-compression data for the high-strength steel DP600

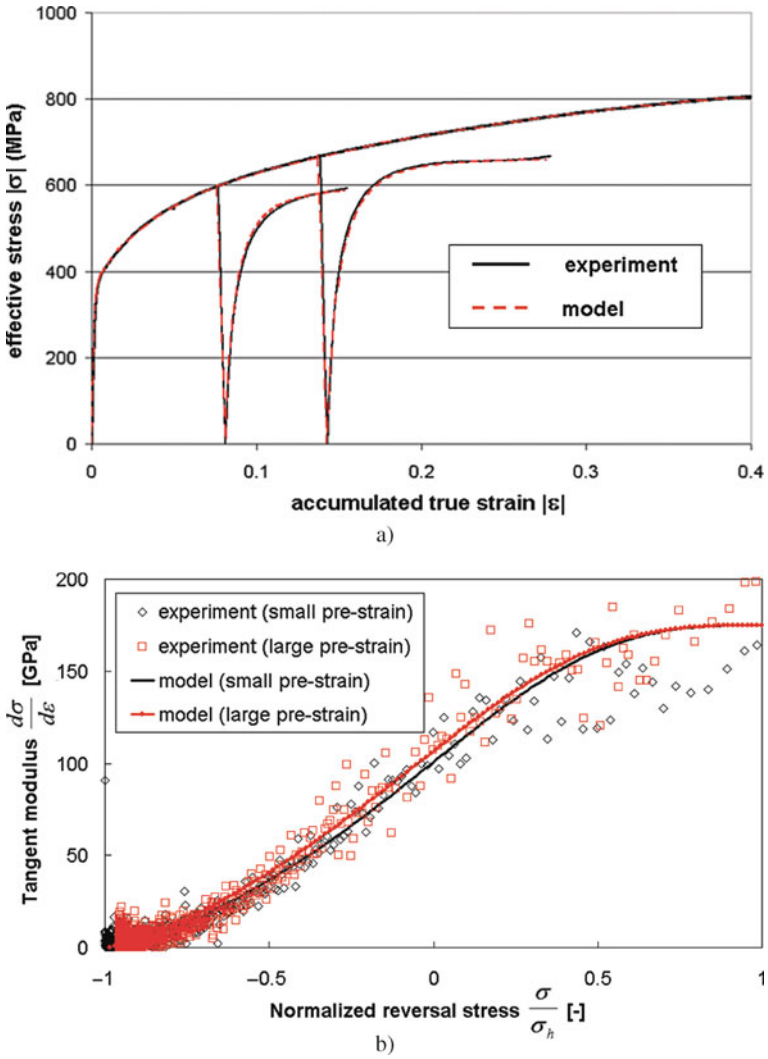

Fig. 2.34 Uniaxial tension and tension-compression curves (**a**) and evolution of the tangential modulus (**b**) during compression for DP600 steel calculated with AutoForm-model together with experimental results

Table 2.5 Kinematic hardening parameters for DP600 steel

K	ξ (–)	γ (–)	χ	E_l (GPa)
0.011	1	0.13	30	200

for two tests with different pre-strains of 8 and 14%. The second picture on the figure presents the evolution of tangent modulus starting from the reversal point, which allows to see the non-linear character of the stress-strain response directly after the load reversal.

Table 2.5 presents the model parameters for the DP600 steel. For the description of tensile hardening curve tabulated data from the tension test has been used.

References

1. Lankford WI, Snyder SC, Bauscher JA (1950) New criteria for predicting the press performance of deep-drawing sheets. Transaction ASM 42:1196–1232
2. Wech PI, Radtke L, Bunge HJ (1983) Comparison of plastic anisotropy parameters. Sheet Metal Industries 60:594–597
3. Siegert K, TALAT Lecture 3705 (http://www.eaa.net/eaa/education/TALAT/index.htm)
4. Choi Y, Walter ME, Lee JK, Han CS (2006) Observations of anisotropy evolution and identification of plastic spin parameters by uniaxial tensile tests. International Journal of Solids and Structures 1:303–325
5. Barlat F, Brem JC, Yoon JW, Chung K, Dick RE, Choi SH, Pourboghrat F, Chu E, Lege DJ (2003) Plane stress yield function for aluminium alloy sheets – Part 1: Theory. International Journal of Plasticity 19:297–319
6. Banabic D, Wagner S (2002) Anisotropic behaviour of aluminium alloy sheets. Aluminium 78:926–930
7. Pöhlandt K, Banabic D, Lange K (2002) Equi-biaxial anisotropy coefficient used to describe the plastic behavior of sheet metal. Proceedings of the ESAFORM Conference, Krakow, 723–727
8. Findley WN, Michno MJ (1976) A historical perspective of yield surface investigations for Metals. International Journal of Non-Linear Mechanics 11:59–80
9. Zyczkowski M (1981) Combined loadings in the theory of plasticity. Polish Scientific Publishers, Warsaw
10. Barlat F, Lege DJ, Brem JC (1991) A six-component yield function for anisotropic materials. International Journal of Plasticity 7:693–712
11. Tresca H (1864) On the yield of solids at high pressures. Comptes Rendus Academie des Sciences 59:754 (in French)
12. Huber MT (1904) Przyczynek do podstaw wytorymalosci. Czasopismo Techniczne 22: 34–81
13. Mises R (1913) Mechanics of solids in plastic state. Göttinger Nachrichten Mathematical Physics 4:582–592 (in German)
14. Hencky H (1924) On the theory of plastic deformations. Zeitschrift für Angewandte Mathematik und Mechanik 4:323–334 (in German)
15. Timoshenko SP (1953) History of strenght of materials. McGraw-Hill, New York, NY
16. Drucker DC (1949) Relations of experiments to mathematical theories of plasticity. Journal of Applied Mechanics 16:349–357
17. Norton FH (1929) The creep of steel at high temperatures. McGraw-Hill, New York, NY
18. Bailey RW (1929) Creep of steel under simple and compound stresses and the use of high initial temperature in steam power plants. Transmission in Tokyo Section Meeting World Power Conference, Konai-kai Publishing, Tokyo
19. Hershey AV (1954) The plasticity of an isotropic aggregate of anisotropic face centred cubic crystals. Journal of Applied Mechanics 21:241–249
20. Hosford WF (1972) A generalised isotropic yield criterion. Journal of Applied Mechanics 39:607–609

21. Karafillis AP, Boyce MC (1993) A general anisotropic yield criterion using bounds and a transformation weighting tensor. Journal of the Mechanics and Physics of Solids 41:1859–1886
22. Yu MH (2002) Advances in strength theories for materials under complex stress state in the 20th century. Applied Mechanics Reviews 55:198–218
23. von Mises RV (1928) Mechanics of plastic deformation of crystals. Zeitschrift für Angewandte Mathematik und Mechanik 8:161–185 (in German)
24. Olszak W, Urbanowski W (1956) The orthotropy and the non-homogeneity in the theory of plasticity. Polska Archiwum Mechaniki Stosowanej 8:85–110
25. Hill R (1948) A theory of the yielding and plastic flow of anisotropic metals. Proceedings of the Royal Society London A 193:281–297
26. Woodthrope J, Pearce R (1970) The anomalous behaviour of aluminium sheet under balanced biaxial tension. International Journal of Mechanical Sciences 12:341–347
27. Pearce R (1968) Some aspects of anisotropic plasticity in sheet metals. International Journal of Mechanical Sciences 10:995–1001
28. Banabic D, Müller W, Pöhlandt K (1998) Determination of yield loci from cross tensile tests assuming various kinds of yield criteria. Sheet Metal Forming Beyond 2000, Brussels, 343–349
29. Hill R (1979) Theoretical plasticity of textured aggregates. Mathematical Proceedings of the Cambridge Philosophical Society 85:179–191
30. Lian J, Zhou D, Baudelet B (1989) Application of Hill's new theory to sheet metal forming – I. Hill's 1979 criterion and its application to predicting sheet forming limits. International Journal of Mechanical Sciences 31:237–244
31. Hosford WF (1979) On yield loci of anisotropic cubic metals. In: Proceedings of the 7th North American Metalworking Conference (NMRC), SME, Dearborn, MI, 191–197
32. Chu E (1995) Generalization of Hill's 1979 anisotropic yield criteria. Journal of Materials Processing Technology 50:207–215
33. Zhou W (1990) A new non-quadratic orthotropic yield criterion. International Journal of Mechanical Sciences 32:513–520
34. Müller W (1996) Characterization of sheet metal under multiaxial load. Berichte aus dem Institut für Umformtechnik, Universität Stuttgart, Nr. 123, Springer, Berlin (in German)
35. Bassani JL (1977) Yield characterisation of metals with transversally isotropic plastic properties. International Journal of Mechanical Sciences 19:651–654
36. Bishop JFW, Hill R (1951) A theory of the plastic distortion of polycrystalline agregates under combined stress. Philosophical Magazine 42:414–427
37. Zhou W (1994) A new orthotropic yield function describable anomalous behaviour of materials. Transactions of Nonferrous Metals Society of China 4:431–449
38. Montheillet F, Jonas JJ, Benferrah M (1991) Development of anisotropy during the cold rolling of aluminium sheet. International Journal of Mechanical Sciences 33:197–209
39. Hill R (1990) Constitutive modelling of orthotropic plasticity in sheet metals. Journal of the Mechanics and Physics of Solids 38:405–417
40. Lin SB, Ding JL (1996) A modified form of Hill's orientation-dependent yield criterion for orthotropic sheet metals. Journal of the Mechanics and Physics of Solids 44:1739–1764
41. Chung K, Shah K (1992) Finite element simulation of sheet metal forming for planar anisotropic metals. International Journal of Plasticity 8:453–476
42. Leacock AG (2006) A mathematical description of orthotropy in sheet metals. Journal of the Mechanics and Physics of Solids 54:425–444
43. Hill R (1993) A user-friendly theory of orthotropic plasticity in sheet metals. International Journal of Mechanical Sciences 15:19–25
44. Stout MG, Hecker SS (1983) Role of geometry in plastic instability and fracture of tubes sheet. Mechanics of Materials 2:23–31
45. Logan R, Hosford WF (1980) Upper-bound anisotropic yield locus calculations assuming (111) – Pencil glide. International Journal of Mechanical Sciences 22:419–430

46. Hosford WF (1985) Comments on anisotropic yield criteria, International Journal of Mechanical Sciences 27:423–427
47. Hosford WF (1993) The mechanics of crystals and textured polycrystals. Oxford University Press, Oxford
48. Hosford WF (1996) On the crystallographic basis of yield criteria. Texture and Microstructures 26–27:479–493
49. Barlat F, Richmond O (1987) Prediction of tricomponent plane stress yield surfaces and associated flow and failure behaviour of strongly textured FCC polycrystalline sheets. Materials Science and Engineering 91:15–29
50. Barlat F, Lian J (1989) Plastic behaviour and stretchability of sheet metals (Part I): A yield function for orthotropic sheet under plane stress conditions. International Journal of Plasticity 5:51–56
51. Banabic D, Balan T, Comsa DS (2000) A new yield criterion for orthotropic sheet metals under plane-stress conditions. Proceedings of the 7th Conference 'TPR2000', Cluj Napoca, Romania, 217–224
52. Banabic D, Kuwabara T, Balan T, Comsa DS, Julean D (2003) Non-quadratic yield criterion for orthotropic sheet metals under plane-stress conditions. International Journal of Mechanical Sciences 45:797–811
53. Banabic D, Aretz H, Comsa DS, Paraianu L (2005) An improved analytical description of orthotropy in metallic sheets. International Journal of Plasticity 21:493–512
54. Choi SH et al. (1999) Prediction of yield surfaces of textured sheet metals. Metallurgical and Materials Transactions 30A:377–379
55. Lian J, Chen J (1991) Isotropic polycrystal yield surfaces of BCC and FCC metals: Crystallographic and continuum mechanics approaches. Acta Metallurgica 39:2285–2294
56. Barlat F et al. (1997) Yielding description for solution strengthened aluminium alloys. International Journal of Plasticity 13:185–401
57. Hayashida Y et al. (1995) FEM analysis of punch stretching and cup drawing tests for aluminium alloys using a planar anisotropic yield function. In: Shen SF, Dawson PR (eds) Simulation of materials processing-theory, methods and applications. AA Balkema, Rotterdam, 712–722
58. Barlat F et al. (1997) Yield function development for aluminium alloy sheets. Journal of the Mechanics and Physics of Solids 45:1727–1763
59. Yoon JW et al. (1999) A general elasto-plastic finite element formulation based on incremental deformation theory for planar anisotropy and its application to sheet metal forming. International Journal of Plasticity 15:35–67
60. Bron F, Besson J (2004) A yield function for anisotropic materials. Application to aluminium alloys. International Journal of Plasticity 20:937–963
61. Wang D-A, Pan J (2006) A non-quadratic yield function for polimeric foams. International Journal of Plasticity 22:434–458
62. Budiansky B (1984) Anisotropic plasticity of plane-isotropic sheets. In: Dvorak GJ, Shield RT (eds) Mechanics of material behavior. Elsevier, Amsterdam, 15–29
63. Tourki Z et al. (1994) Orthotropic plasticity in metal sheets. Journal of Materials Processing Technology 45:453–458
64. Gotoh M (1977) A theory of plastic anisotropy based on a yield function of fourth order. International Journal of Mechanical Sciences 19:505–520
65. Hill R (1950) The mathematical theory of plasticity. Oxford University Press, Oxford
66. Barlat F et al. (2000) Constitutive modeling for aluminium sheet forming simulations. In: Khan AS, Zhang H, Yuan Y (eds) Plastic and viscoplastic response of materials and metal forming. Proceedings of the 8th International Symposium in Plasticity and its Current Applications, Whistley, Canada, Neat Press, Fulton, MD, 591–593
67. Aretz H, Barlat F (2004) General orthotropic yield function based on linear stress deviator transformations. In: Ghosh S, Castro GC, Lee JK (eds) Materials processing and design:

Modelling, simulation and applications. Proceedings of the NUMIFORM 2004 Conference, Columbus, OH, 147–151
68. Barlat F et al. (2005) Linear transformation-based anisotropic yield functions. International Journal of Plasticity 21:1009–1039
69. Yoon JW et al. (2006) Prediction of six or eight ears in a drawn cup based on a new anisotropic yield function. International Journal of Plasticity 22:174–193
70. Cosovici GA (2006) Implementation of the new yield criteria in the FE programs for sheet metal forming simulation. PhD Thesis, Cluj Napoca, Romania (in Romanian)
71. Paraianu L (2006) Modelling of the FLC using the large deformation theory. PhD Thesis, Cluj Napoca, Romania (in Romanian)
72. Press WH et al. (1992) Numerical recipes in C. The art of scientific computing. Cambridge University Press, Cambridge
73. Aretz H (2005) A non-quadratic plane stress yield function for orthotropic sheet metals. Journal of Materials Processing Technology 168:1–9
74. Barlat F, Yoon JW, Cazacu O (2006) On linear transformations of stress tensors for the description of plastic anisotropy. International Journal of Plasticity 22:876–896
75. Cazacu O, Barlat F (2001) Generalization of Drucker's yield criterion in orthotropy. Mathematics and Mechanics of Solids 6:613–630
76. Cazacu O, Barlat F (2003) Application of representation theory to describe yielding of anisotropic aluminium alloys. International Journal of Engineering Science 41:1367–1385
77. Cazacu O, Barlat F (2004) A criterion for description of anisotropy and yield differential effects in pressure-insensitive metals. International Journal of Plasticity 20:2027–2045
78. Liu C, Huang Y, Stout MG (1997) On the asymmetric yield surface of plastically orthotropic materials: A phenomenological study. Acta Materialia 45:2397–2406
79. Cazacu O, Plunkett B, Barlat F (2006) Orthotropic yield criterion for hexagonal close packed metals. International Journal of Plasticity 22:1171–1194
80. Vegter H, Drent P, Huetink J (1995) A planar isotropic yield criterion based on material testing at multi-axial stress state. In: Shen SF, Dawson PR (eds) Simulation of materials processing-theory, methods and applications. AA Balkema, Rotterdam, 345–350
81. Vegter D, van den Boogaard AH (2006) A plane stress yield function for anisotropic sheet material by interpolation of biaxial stress states. International Journal of Plasticity 22: 557–580
82. Mollica F, Srinivasa AR (2002) A general framework for generating convex yield surfaces for anisotropic metals. Acta Mechanica 154:61–84
83. Hu W (2003) Characterized behaviors and corresponding yield criterion of anisotropic sheet metals. Materials Science and Engineering A345:139–144
84. Hu W (2005) An orthotropic yield criterion in a 3-D general stress state. International Journal of Plasticity 21:1771–1796
85. Hu W (2007) A novel quadratic yield model to describe the feature of multi-yield-surface of rolled sheet metals. International Journal of Plasticity 23:2004–2028
86. Comsa DS (2006) Numerical simulation of the sheet metal forming prodesses using a new yield criterion. PhD Thesis, Tehnical University of Cluj Napoca (in Romanian)
87. Comsa DS, Banabic D (2007) Numerical simulation of sheet metal forming processes using a new yield criterion. Key Engineering Materials 344:833–840
88. Soare S (2007) On the use of homogeneous polynomials to develop anisotropic yield functions with applications to sheet metal forming. PhD Thesis, University of Florida
89. Soare S, Yoon JW, Cazacu O (2007) On using homogeneous polynomials to design anisotropic yield functions with tension/compression symmetry/asymmetry. In: Cesar de Sa JMA, Santos AD (eds) Materials processing and design: Modeling, simulation and applications. Proceedings of the NUMIFORM 2007 Conference, Porto, 607–612
90. Oller S, Car E, Lubliner J (2003) Definition of a general implicit orthotropic yield criterion. Computer Methods in Applied Mechanics and Engineering 192:895–912

91. Comsa DS, Banabic D (2008) Plane-stress yield criterion for highly-anisotropic sheet metals. In: Hora P (ed) Proceedings of the 7th International Conference and Workshop on Numerical Simulation of 3D Sheet Metal Forming Processes, NUMISHEET 2008, Interlaken, Switzerland, 43–48
92. Banabic D, Cazacu O, Barlat F, Comsa DS, Wagner S, Siegert K (2002) Recent anisotropic yield criteria for sheet metals. Proceedings of the Romanian Academy 3:91–99
93. Barlat F, Banabic D, Cazacu O (2002) Anisotropy in sheet metals. In: Yang D-Y, Oh SI, Huh H, Kim YH (eds) Design inovation through virtual manufacturing. Proceedings of the NUMISHEET 2002 Conference, Jeju Island, Korea, 515–524
94. Paraianu L, Banabic D (2006) Predictive accuracy of different yield criteria. Proceedings of the SISOM Conference, Bucharest, 465–574
95. Chaparro BM, Alves JL, Menezes LF, Fernandes JV (2007) Optimization of the phenomenological constitutive models parameters using genetic algorithms. In: Banabic D (ed) Advanced methods in material forming, Springer, Heidelberg, 35–54
96. Barlat F, Cazacu O, Zyczkowski M, Banabic D, Yoon J-W (2004) Yield surface plasticity and anisotropy. In: Raabe D, Chen L-Q, Barlat F, Roters F (eds) Continuum scale simulation of engineering materials fundamentals-microstructures-process applications. Wiley-VCH, Weinheim, 145–185
97. Banabic D, Tekkaya EA (2006) Forming Simulation. In: Hirsch J (ed) Virtual fabrication of aluminum alloys: Microstructural modeling in industrial aluminum production. Wiley-VCH, Weinheim, 275–302
98. Yoon JW, Barlat F (2006) Modeling and simulation of the forming of aluminium sheet alloys. In: Semiatin SL (ed) ASM handbook, Vol 14B, Metalworking: Sheet forming. ASM International, Materials Park, OH, 792–826
99. Barlat F (2007) Constitutive modeling for metals. In: Banabic D (ed) Advanced methods in material forming, Springer, Heidelberg, 1–18
100. Banabic D, Barlat F, Cazacu O, Kuwabara T (2007) Anisotropy and formability. In: Chinesta F, Cueto E (eds) Advances in material forming-ESAFORM 10 years on. Springer, Heidelberg, 143–173
101. Barlat F (2007) Constitutive descriptions for metal forming simulations, In: Cesar de Sa JMA, Santos AD (eds) Materials processing and design: Modeling, simulation and applications. Proceedings of the NUMIFORM 2007 Conference, Porto, 3–22
102. ABAQUS (2004), Analysis user's manual, Version 6.4. Hibbit, Karlsson & Sorensen Inc., Providence, RI
103. Krasovskyy A (2005) Verbesserte Vorhersage der Rückfederung bei der Blechumformung durch weiterentwickelte Werkstoffmodelle. PhD Thesis, University of Karlsruhe (in German)
104. Yoshida F, Urabe M, Toropov VV (1998) Identification of material parameters in constitutive model for sheet metals from cyclic bending test. International Journal of Mechanical Sciences 40:237–249
105. Yoshida F, Uemori T, Fujiwara K (2002) Elastic-plastic behavior of steel sheets under in-plane cyclic tension-compression at large strain. International Journal of Plasticity 18: 633–659
106. Cleveland RM, Ghosh AK (2002) Inelastic effects on springback in metals. International Journal of Plasticity 18:769–785
107. Peeters B, Kalidindi SR, Teodosiu C, Van Houtte P, Aernoudt E (2002) A theoretical investigation of the influence of dislocation sheets on evolution of yield surfaces in single-phase B.C.C. polycrystals. Journal of the Mechanics and Physics of Solids 50:783–807
108. Lemaitre J, Chaboche JL (1990) Mechanics of solid materials. Cambridge University Press, Cambridge
109. Armstrong PJ, Frederick CO (1996) A mathematical representation of the multiaxial Bauschinger effect. GEGB Report RD/B/N731. Berkeley Nuclear Laboratories

110. Chaboche JL, Rousselier G (1983) On the plastic and viscoplastic constitutive equations – Part 1: Rules developed with internal variable concept. Journal of Pressure Vessel Technology 105:153–158
111. Yoshida F, Uemori T (2002) A model of large-strain cyclic plasticity describing the Bauschinger effect and workhardening stagnation. International Journal of Plasticity 18:661–686
112. Kubli W, Krasovskyy A, Sester M (2008) Advanced modeling of reverse loading effects for sheet metal forming processes. In: Hora P (ed) Proceedings of the 7th International Conference and Workshop on Numerical Simulation of 3D Sheet Metal Forming Processes, NUMISHEET 2008, Interlaken, Switzerland, 479–484

Chapter 3
Formability of Sheet Metals

List of Special Symbols

a, b, c	material constants in the Cayssials model
D	blank diameter
d	cup diameter
d_{m}	mean cup diameter
E_0	coefficient in the eMMFC model
e_{u}	ultimate strain
F	formability index; Force
f, f_0, f_1	yield function; non-homogeneity coefficients in MK and HN models
$g_{11,22,12}$	partial derivatives
k	material constant in the Hollomon and Swift strain-hardening laws
m	strain-rate sensitivity index
n	hardening coefficient
p	exponent in the eMMFC model
r	normal anisotropy (Lankford) coefficient
s	thickness
s_0	initial thickness
t	time parameter
$T_{11,22,\ 12,\ 21}$	tensors
Y	yield function
α	loading ratio
β	drawing ratio
β	strain rate ratio
$\Delta(t, \varepsilon, \sigma)$	increment of time, strain or stress
ε	logarithmic strain
$\bar{\varepsilon}$	effective strain
$\dot{\bar{\varepsilon}}$	effective strain rate
$\dot{\varepsilon}_{11,22}$	principal strain rates
$\dot{\varepsilon}_{12,21}$	angular strain rates

D. Banabic, *Sheet Metal Forming Processes*, DOI 10.1007/978-3-540-88113-1_3,

ε_0	pre-deformation in the Swift strain-hardening law
$\varepsilon_{1,2}$	major and minor strains
ε_3	principal strain in sheet thickness direction
ε^*_{10}	limit strain corresponding to the plane strain
$\varepsilon^*_{11,\,22}$	major and minor limit strains
ζ	principal stress ratio
$\mu_{p,d}$	friction coefficients
φ	angle of the geometrical non-homogeneity
ρ	ratio of incremental strains or principal strain rates
σ_{max}	maximum principal stress
σ_e, $\bar{\sigma}$	effective stress
σ	stress
$\sigma_{1,2}$	principal stresses

3.1 Introduction

The formability is the capability of sheet metal to undergo plastic deformation to a given shape without defects. The defects have to be considered separately for the fundamental sheet metal forming procedures of deep-drawing and stretching. The difference between these types of stamping procedures is based on the mechanics of the forming process. For deep-drawing, the usual defects of the produced parts are presented in Fig. 3.1 [1].

Some of these defects are caused by the forming tools (types 5, 9, 10, 14), by the friction regime (types 4, 13) or by the mechanical and metallurgical properties of the material as well as by geometrical parameters (types 1, 2, 3, 6, 7, 8, 11, 12). Only the defects of type 3, 6, 8 are related to stretching processes, the others are specific to deep-drawing. Concerning the defect type 3 (e.g. in hemispherical punch stretching), the tear is oriented along the circumference and located near the pole. Tearing is usually preceded by strain localization (necking) which causes a reduction of the part's strength, worsens its appearance and is a reason for rejecting it. Necking, tearing, wrinkling, modification of the roughness or a poor appearance are factors that generally define a limit to the deformation by stretching (see also [2–8]).

Necking is a limiting criterion not only for stretching but also for other processes leading to similar strain states in the plastic zone (Fig. 3.2).

Figure 3.3 demonstrates that formability is a complex characteristic.

As an example, the influence of various parameters on the formability in deep drawing is presented in Fig. 3.4.

The formability, expressed by the drawing ratio $\beta = D/d$ (D being the blank diameter and d the cup diameter, depends on the strain limiting criterion as well as on a process parameter (blank holding pressure p).

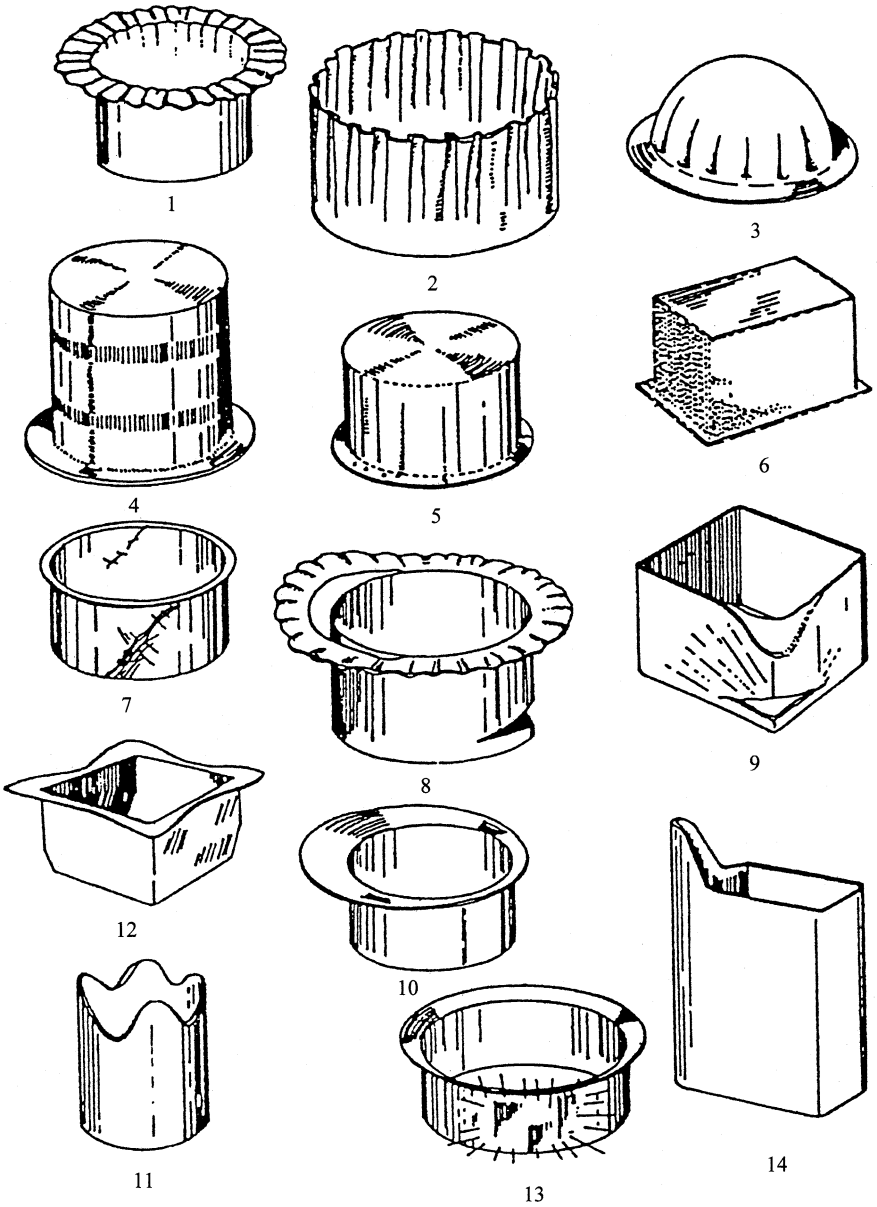

Fig. 3.1 Defects in deep-drawing: 1—flange wrinkling; 2—wall wrinkling; 3—part wrinkling; 4—ring prints; 5—traces; 6—orange skin; 7—Lüders strips; 8—bottom fracture; 9—corner fracture; 10, 11, 12—folding; 13, 14—corner folding [1]

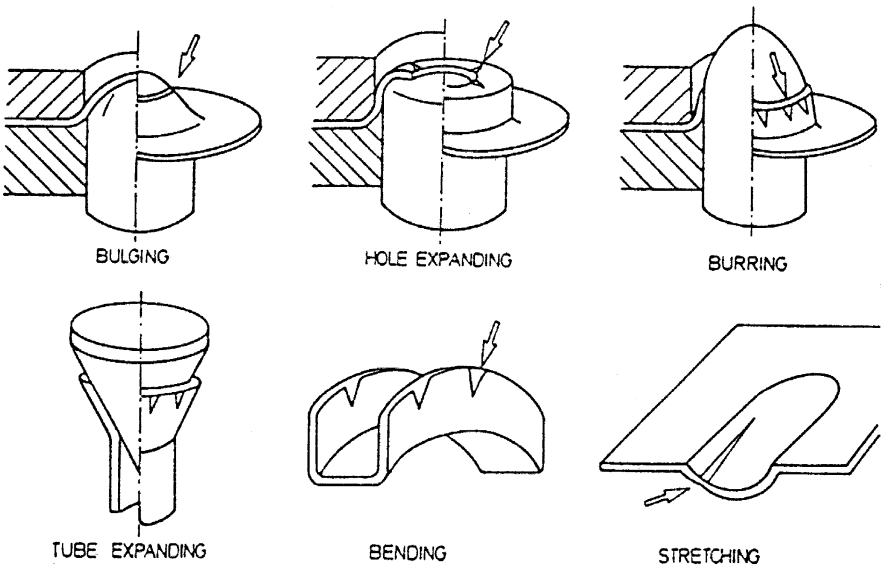

Fig. 3.2 Examples of processes where deformation is limited by necking [7]

Marciniak [4–8] developed the idea of Cockcroft and Latham [9] by introducing formability indices depending on the type of the simulating test as well as the strain bounding criterion.

Of course, these indices depend also on the mechanical parameters of the material:

$$F_{\mathrm{kl}} = F(n, m, r, e_{\mathrm{u}}, f) \tag{3.1}$$

where n is the hardening coefficient, m the strain rate sensitivity, r the anisotropy coefficient, e_{u} the ultimate strain, and f the non-homogeneity coefficient.

The increment of the formability index may be expressed as

$$dF = \frac{\partial F}{\partial n}dn + \frac{\partial F}{\partial m}dm + \frac{\partial F}{\partial r}dr + \frac{\partial F}{\partial \varepsilon_u}d\varepsilon_u + \frac{\partial F}{\partial f}df \tag{3.2}$$

Each derivative in this equation can be determined theoretically or experimentally for a given sheet forming process [5]. Figure 3.5 shows the factors influencing the formability index for some important sheet forming processes. In this figure, μ_{p} and μ_{d} are the friction coefficients at the interface between blank and punch and blank and die, respectively.

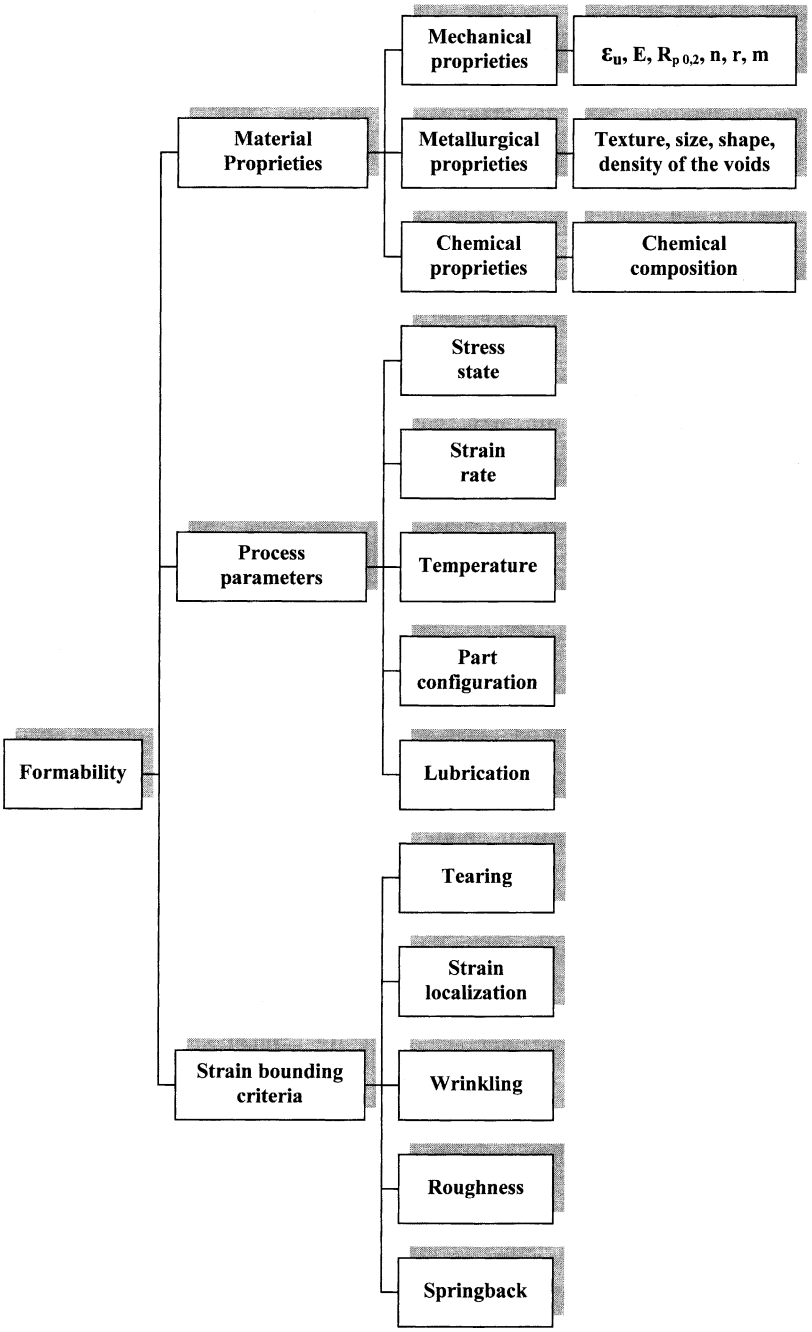

Fig. 3.3 Parameters influencing sheet metal formability

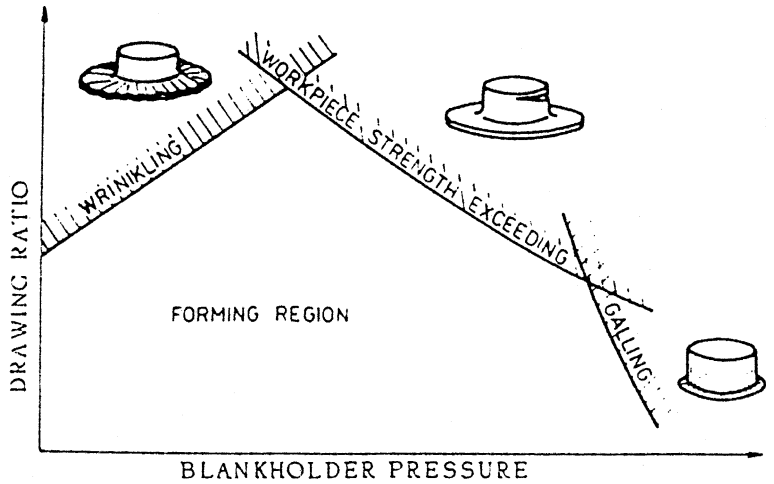

Fig. 3.4 Influence of various parameters on formability in deep-drawing [6]

Crite -rion	FORMING OPERATION	
Workpiece strength exceeded by forming load	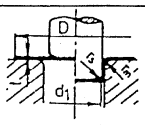	DEEP DRAWING $F_{2,1}\,[(n, r)\,\mu_d\,(D, d, t, r_S, r_m)]$
	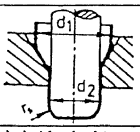	REDRAWING $F_{2,2}\,[(n, r)\,\mu_d\,\mu_p\,(D, d, d_2, t, r_S)]$
	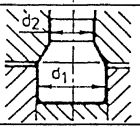	SWAGING $F_{2,3}\,[(n, r, R_{02}, R_m)\,\mu_d\,(D, d_1, d_2, t)]$
Localized necking	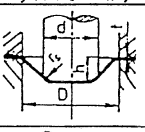	STRETCHING /BULGING/ $F_{5,4}\,[(n, r_m)\,\mu_p\,(D, d, t, r_S, h)]$
	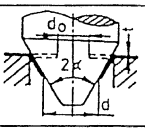	BURRING $F_{5,5}\,[(n, r_m)\,\mu_p\,(d, d_0, \alpha, t)]$
	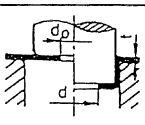	HOLE EXPANDING $F_{5,6}\,[(n, r_m)\,\mu_p\,(d, d_0, t)]$

Fig. 3.5 Factors influencing the formability index for the most important sheet metal forming processes [7]

3.2 Evaluation of the Sheet Metal Formability

At the end of the nineteenth century, due to the development of the sheet forming technology, sheet metal formability became a research topic. A detailed presentation of this research can be found in [10–13]. Some of the first researchers interested in this field were Bessemer and Parkes, Adamson, Considere [14] and Erichsen [15].

Since then, various method for evaluating sheet metal formability have been developed. One may subdivide them into four classes:

- simulating tests
- methods based on mechanical tests
- method of the limiting dome height
- methods based on forming limit diagrams.

3.2.1 Methods Based on Simulating Tests

Sheet metal forming processes can be characterized by two basic types of deformation patterns: drawing and bending [16]. Concerning drawing one has to distinguish stretching ($\varepsilon_1 > 0; \varepsilon_2 > 0$) and deep drawing ($\varepsilon_1 > 0; \varepsilon_2 < 0$), see Fig. 3.6.

Various formability tests specific to each of these deformation patterns have been developed. In the case of drawing processes there are simulating tests for stretching, deep-drawing and combined drawing. A detailed presentation of the simulating tests is given in [10, 13, 17–32].

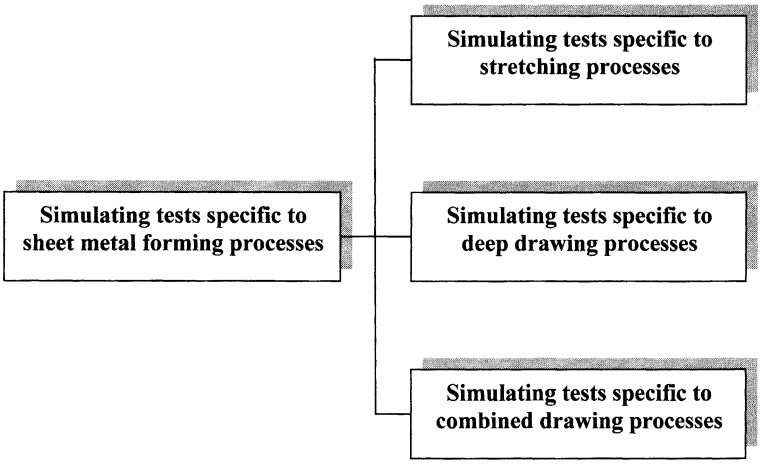

Fig. 3.6 Deformation patterns specific to sheet metal forming processes

3.2.1.1 Typical Punch-Stretching Methods

The first test for evaluating the formability of sheet metals was proposed by Erichsen [15]. The test consists in stretching a sheet specimen by means of a hemispherical punch until the occurrence of fracture, see Fig. 3.7.

The depth of the punch indentation in the specimen expressed in millimetres is the so-called Erichsen index (IE). This is the most commonly used parameter for expressing the formability of sheet metals. Various researchers have analyzed the accuracy, the limits of applicability as well as the factors influencing the test results [12, 25, 33–37]. Olsen [38] introduced a test similar to that proposed by Erichsen but with a different size of the tools.

The index established using these methods has a low accuracy due to the small size of the tools, the impossibility of ensuring a sound fixing of the specimen and poor lubrication.

In order to diminish these errors Hecker [39] proposed a formability test based on stretching a punch having a greater diameter than that in the Erichsen and Olsen tests. In this case the blank is also held by draw-beads whereby there is a dry friction regime between punch and specimen. Like for the Erichsen and Olsen test the formability index is expressed by the depth of the punch indentation at the beginning of fracture.

Since most of the defects in deep-drawing of complex parts are located near the region on plane stretching (plane strain), Ghosh [40] proposed a modification of the Hecker test in the order of simulating this state of strain. For this purpose he used Hecker's device with strip specimens of various widths. This test, called the limit dome height test (LDH), will be described in Sect. 3.3.2.

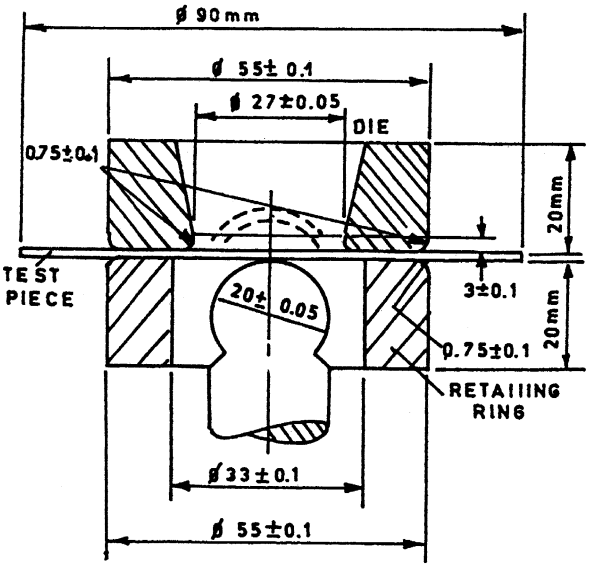

Fig. 3.7 Scheme of Erichsen test

Jovignot [41] proposed a testing method based on the hydraulic bulge test. Siebel and Pomp [42] developed a test consisting of deep-drawing a circular specimen with a central circular hole until the occurrence of fracture. The formability index is expressed as the diameter of the hole at the initiation of fracture.

3.2.1.2 Typical Deep-Drawing Methods

Sachs [43] proposed a test based on tensioning a specimen having the shape of a wedge. This simulates the straining of a longitudinal strip as a part of a cup during a deep-drawing process.

The research initiated by Sachs was continued by Swift [44] and Guyot [45] who proposed different shapes of the specimens. Swift also established a linear relationship between the maximum traction load and the drawing ratio.

The advantage of wedge drawing tests is the simple shape of the specimen and the suitability of general-purpose machines for carrying out the tests. The outstanding disadvantage is the fact that the mechanics of straining is rather different from that of real deep-drawing processes since neither bending nor the effect of friction are simulated in the test.

Chung and Swift [46] published the first coherent and complete mathematical model of the deep-drawing process which also was confirmed by experiments [47, 48]. Swift proposed a deep-drawing test method of his own. This test consists of deep-drawing cylindrical parts having different diameters (Fig. 3.8) and determining the limit drawing ratio LDR, i.e. the ratio of the maximum diameter of the workpiece that is drawn without tearing and the diameter of the punch:

$$\mathrm{LDR} = \frac{D_{\max}}{d} \tag{3.3}$$

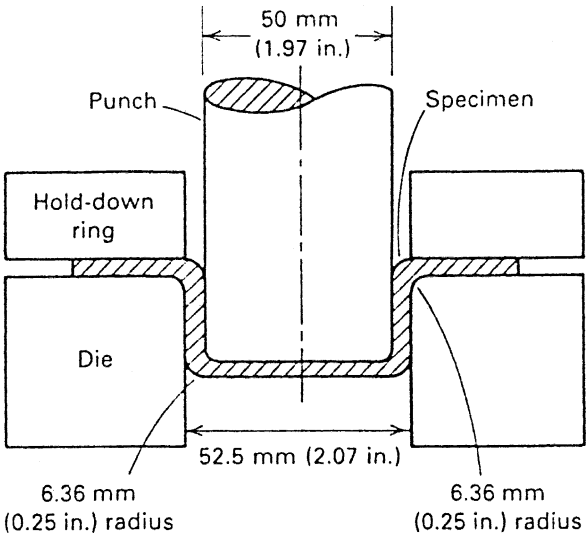

Fig. 3.8 Swift's cup-drawing test

Sometimes a percent expression of the LDR is used:

$$\frac{D_{\max} - d}{D_{\max}} 100[\%] \tag{3.4}$$

Swift's method has been widely used and is considered as a standard test by the International Deep-Drawing Research Group (IDDRG) [16, 29]. However, the efforts of Swift and co-workers in order to find a unique formability index which can be obtained by a single test have been unsuccessful. Further research was carried out by Willis [49]. Siebel and co-workers analyzed the factors such as lubrication, drawing speed influencing the limit drawing ratio [13]. Fukui [50] proposed a deep-drawing test using a conical die. The advantage of this method is that the 'diameter ratio' D/D_0 ($D =$ upper diameter of the part at fracture) as a measure of formability may be established by a single test.

The results of Japanese research in this field are summarized in [51, 52].

From all the above-mentioned experiments the one proposed by Swift is the most accurate one, giving the most reliable results.

3.2.1.3 Combined Deep-Drawing Methods

Real sheet metal forming processes usually are a combination of the basic processes of deep-drawing and stretching. For simulating this, combined tests have been developed. Sachs [43, 53] developed a method based on the use of a conical punch with a flat bottom. After tearing the test is continued until the occurrence of fracture at the edge of the hole obtained previously.

Petrasch [27] proposed a method of evaluating the formability from the deformation energy. At first the specimen is drawn by impact whereby the deformation energy is obtained as a measure of deep-drawability. After this the upper edge of the cup is enlarged until the occurrence of fracture. The ratio of the maximum diameter and the diameter of the cylindrical section of the part is a measure of stretch formability.

Swift stated that deep-drawing with a hemispherical punch gives more comprehensive information about the suitability for combined deep-drawing [48]. In this test deformation takes place by stretching at the centre of the part and by deep-drawing in the region of the blank. Fukui obtained a similar conclusion by using a hemispherical punch and a conical die. The formability is expressed as the ratio of the bottom diameter of the cone (corresponding to the occurrence of fracture) and of the diameter of the workpiece.

Eisenkolb [54, 55] proposed a test consisting of forming a cup on the wall of another cup that had already been produced by deep-drawing. By this a residual formability is determined.

Engelhardt [56] introduced the so-called 'deep-drawing potential' as a measure of safety against failure by bottom cracks. This method has obtained some practical

importance. Compared to the cupping test by Swift [48] this test is easier to carry out since only one specimen is needed.

3.2.2 Limit Dome Height Method

This method combines advantages of simulating tests and of the forming limit diagram. Based on observations by Drewes [57], Ghosh [40] proposed to represent the heights of the parts as functions of the minimum strains occurring in rectangular specimens (of Nakazima type) stretched on a hemispherical punch until fracture. By drawing a curve through the experimental points obtained with specimens of different width, a diagram like shown in Fig. 3.9 is obtained [11]. Later on, the method has been modified by English researchers under the name of Strip Stretch Test and by American researchers, named Limiting Dome Height test.

The height of the part corresponding to plane strain is a formability index denoted by LDH_0. This is the minimum compared to the heights obtained for other states of strain. The width of the specimen corresponding to plane strain is a characteristic of the material. In spite of its advantages the method has been little used in industry, due to the large dispersion of the LDH_0 values and the large amount of experimental work.

More recently, Wagoner [58] introduced the OSUFT method in order to overcome the applicability limits of the LDH method. For this purpose the shape of the tools was optimized by FE simulations aiming to achieve as close as possible a state of plane strain. The results showed a reduced dispersion and good agreement with industrial practice. Also the amount of experimental work is reduced.

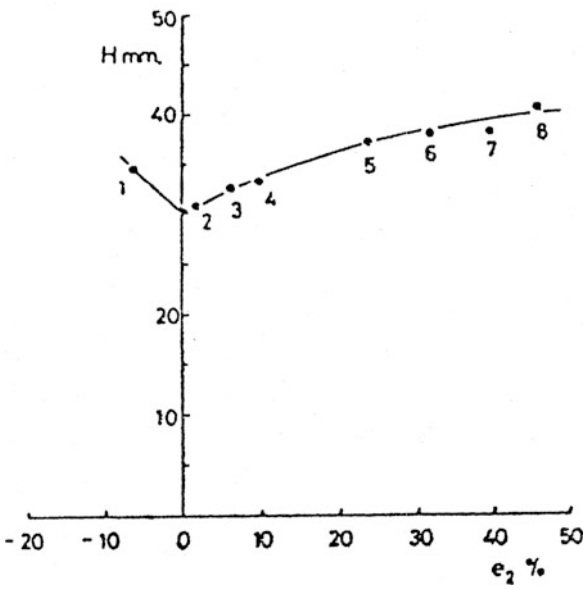

Fig. 3.9 Limit dome height curve

3.3 Forming Limit Diagram

3.3.1 Definition: History

The maximum values of the principal strains ε_1 and ε_2 can be determined by measuring the strains at failure (necking, fracture, wrinkling etc.) on sheet components covered with grids of circles. The research in this field was pioneered by Keeler [59], based on the observations of Gensamer [60] that instead of using global indices the local deformations have to be considered (Fig. 3.10).

During forming the initial circles of the grid become ellipses. Keeler plotted the major strains against the minor strains obtained from such ellipses at fracture of parts after biaxial stretching ($\varepsilon_1 > 0; \varepsilon_2 > 0$) [59] (Fig. 3.11).

For numerous materials the critical area between the domains has been detected both by means of laboratory tests and by forming of industrial components. These measurements were conducted for various materials. The excellent correlation of the results was a proof that the forming limits in sheet metal forming can be evaluated very well by determining the Forming Limit Curve (FLC).

Later, Goodwin [62] plotted the curve for the tension/compression domain ($\varepsilon_1 > 0; \varepsilon_2 < 0$) by using different mechanical tests. In this case, transverse compression allows for obtaining high values of tensile strains like in rolling or drawing.

The diagrams of Keeler (right side) and Goodwin (left side) are currently called the Forming Limit Diagram (FLD), see Fig. 3.12. Connecting all of the points corresponding to limit strains leads to a Forming Limit Curve (FLC). The FLC splits

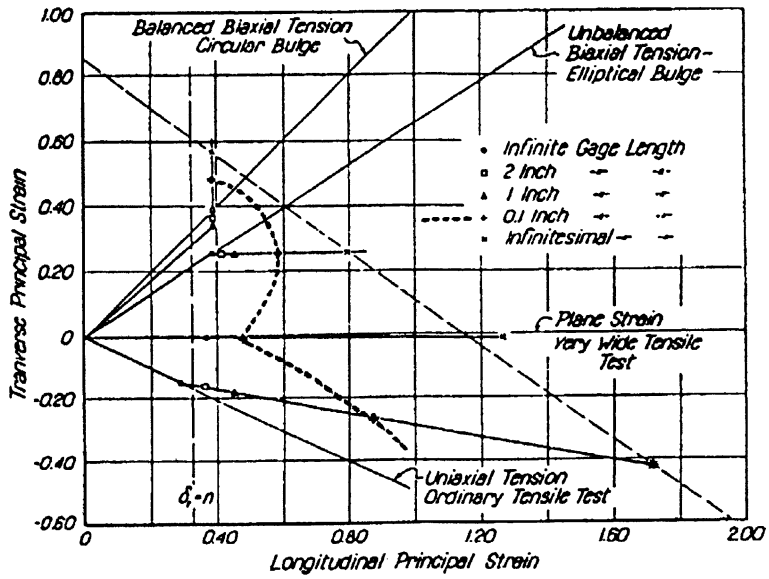

Fig. 3.10 The original Forming limit diagram defined by Gensamer [60]

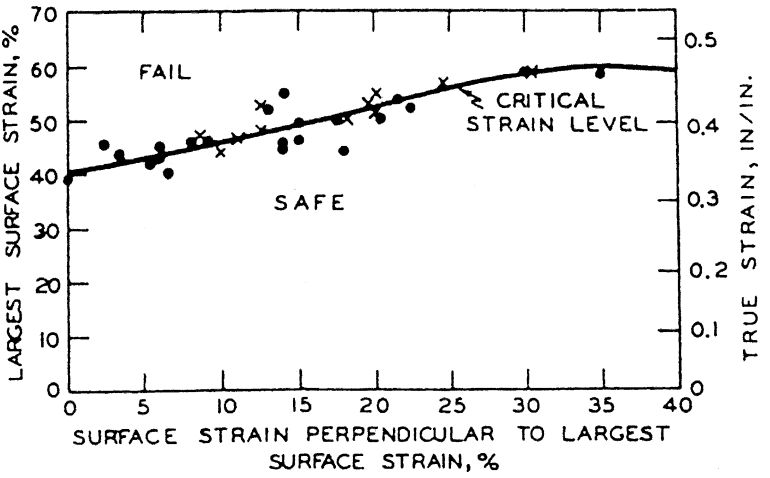

Fig. 3.11 Forming limit diagram defined by Keeler [61]

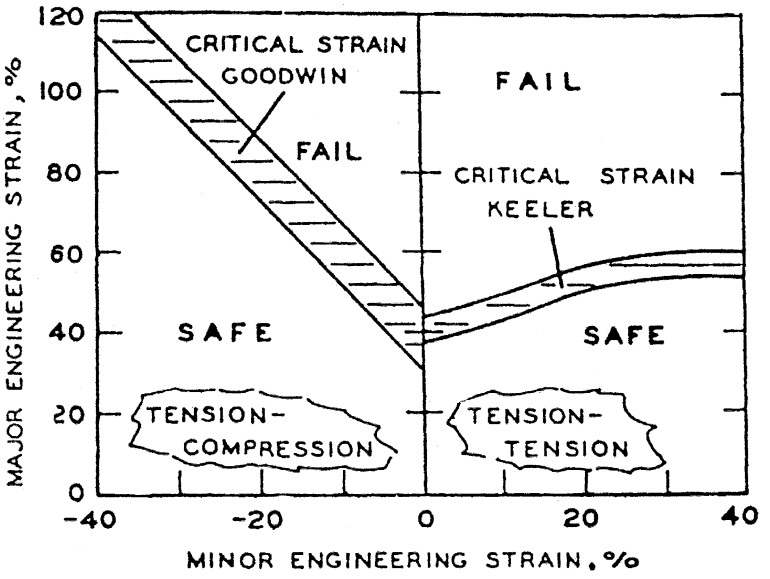

Fig. 3.12 Forming limit diagrams defined by Keeler and Goodwin [62]

the 'fail' (i.e. above the FLC) and 'save' (i.e. below the FLC) regions. The Forming Limit Curve (FLC) is plotted on a Forming Limit Diagram (FLD). The intersection of the limit curve with the vertical axis (which represents the plane strain deformation ($\varepsilon_2 = 0$)) is an important point of the FLD and is noted FLD_0. The position of this point depends mainly on the strain hardening coefficient and also on thickness (see Sect. 3.3.4).

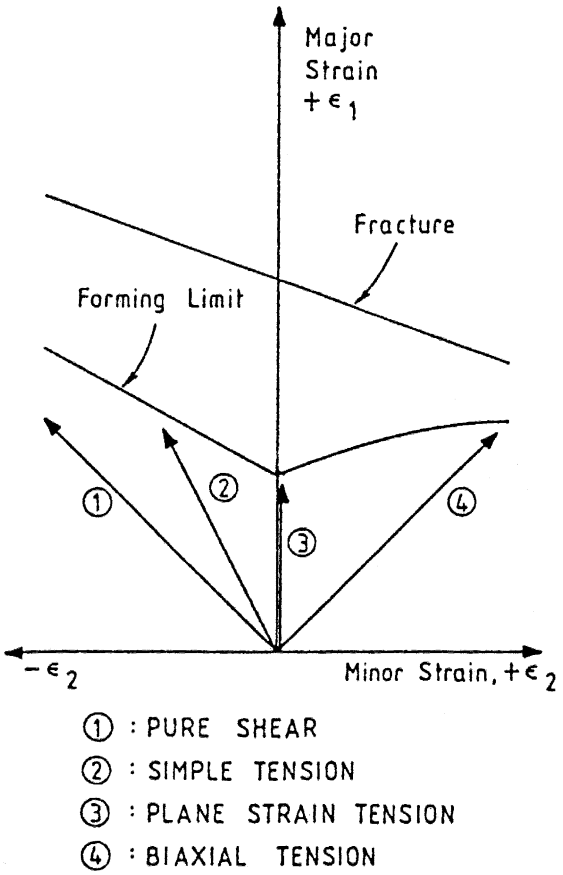

Fig. 3.13 Forming limit diagrams for necking and for fracture

Today, depending on the kind of limit strains that is measured different types of FLD's are determined: for necking and for fracture, see Fig. 3.13.

From subsequent experimental and theoretical research, even two more types of FLDs have emerged: the wrinkling limit diagram by Havranek (Fig. 3.14) [63] and the Stress Forming Limit Diagram (SFLD) by Arrieux (Fig. 3.15) [64]. The latter is not sensitive to the strain path.

In order to extend the application of stress limit curves to a 3-D stress state (presence of through-thickness components of compressive stress), Simha et al. [65] has introduced a new concept, namely Extended Stress-Based Limit Curve (XSFLC). The XSFLC represents the equivalent stress and mean stress at the onset of necking during in-plane loading. Figure 3.16 shows the three formulations of the Forming Limit Curve concept, namely: strain-based FLC (εFLC), stress-based FLC (σFLC) and Extended Stress-Based FLC (XSFLC), respectively. The Equivalent stress and the Mean stress are obtained through the expressions

$$\sigma_{\text{eq}} = \sqrt{\sigma_1^2 + \sigma_2^2 - \sigma_1\sigma_2}; \tag{3.5}$$

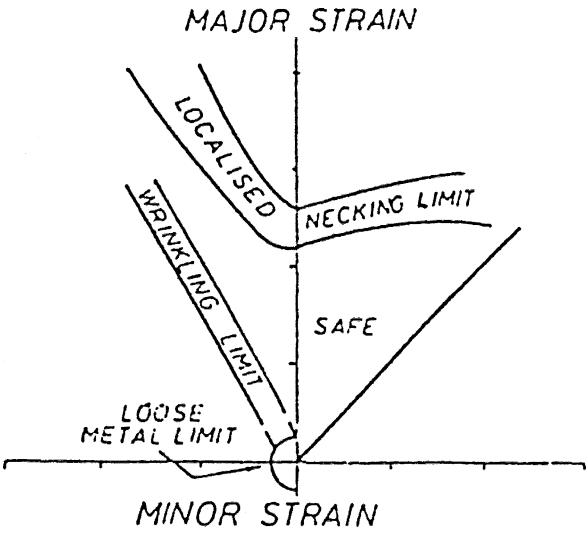

Fig. 3.14 Forming limit diagram for wrinkling [63]

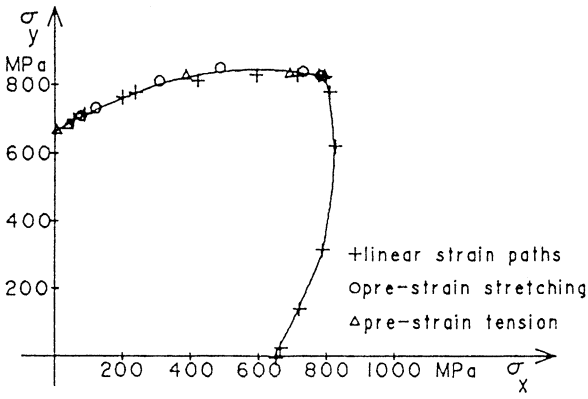

Fig. 3.15 Stress forming limit diagram defined by Arrieux [64]

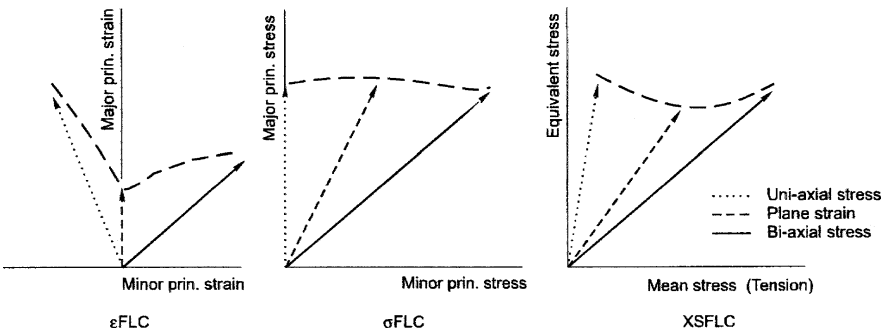

Fig. 3.16 Schematic of the strain-based forming limit curve (εFLC), the stress-based forming limit curve (σFLC) and the extended stress-based forming limit curve (XSFLC) [66]

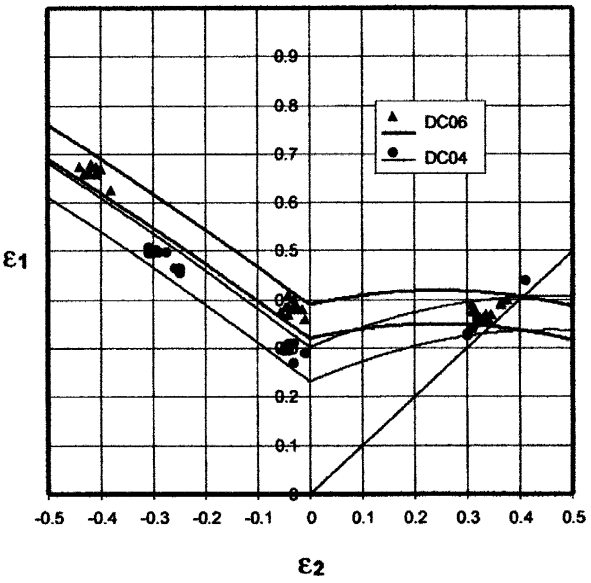

Fig. 3.17 Forming limit band (FLB) for two steel grades [67]

$$\sigma_{\text{mean}} = \frac{\sigma_1 + \sigma_2}{3}, \tag{3.6}$$

where σ_{eq} is the equivalent stress, and σ_{mean} the mean stress, which is assumed to be positive in tension.

Figure 3.16 also presents the loading paths for the three cases: uniaxial stress, plane strain and biaxial stress. A thorough analysis of the conditions for the use of the XSFLC as a Formability Limit Curve under three-dimensional loading is presented in [66].

Forming Limit Curves are valid for one particular material alloy, temper and gauge combination. However material properties vary from batch to batch due to variation in the production process. Therefor a single Forming Limit Curve cannot be an exact description of the forming limit. Janssens et al. [67] have proposed a more general concept, namely the Forming Limit Band (FLB) as a region covering the entire dispersion of the Forming Limit Curves (Fig. 3.17).

3.3.2 Experimental Determination of the FLD

3.3.2.1 Experimental Tests

FLDs must cover as much as possible the strain domain which occurs in industrial sheet metal forming processes. The diagrams are established by experiments that provide pairs of values of the limit strains ε_1 and ε_2 obtained for various loading patterns (equibiaxial, biaxial, uniaxial etc.). In order to determine a FLD one must generate load paths ranging from equibiaxial tension ($\varepsilon_1 = \varepsilon_2$) to pure shear

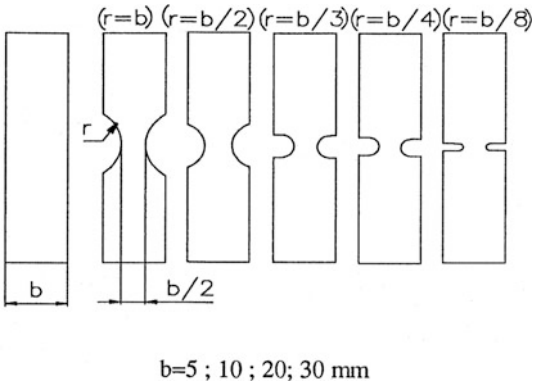

Fig. 3.18 Rectangular specimens with and without notches

($\varepsilon_1 = -\varepsilon_2$). In practice the state of simple tension ($\varepsilon_1 = -2\varepsilon_2$ for isotropic materials) is never exceeded in the blank holder region.

It is necessary to deform the specimen along a linear strain path, i.e. the trajectory followed by a point in the $\varepsilon_1, \varepsilon_2$ -plane until reaching the forming limit must be a straight line.

3.3.2.2 Uniaxial Tensile Test

This test allows determining a section of the FLD in the range $\varepsilon_2 < 0$. For obtaining different strain paths, specimens with different shapes and sizes with and without notches are used, see Fig. 3.18 [68].

The advantages of the tensile test for determining FLDs are that the specimens are easy to manufacture and a general purpose testing machine can be used; furthermore the specimens remain plane during the test which facilitates measurement. However, only the negative section of the forming limit diagram ($\varepsilon_2 < 0$) can be determined.

3.3.2.3 Hydraulic Bulge Test

This test was first proposed by Olsen [38]. For varying the strain path elliptical dies of different shape can be used, see Fig. 3.19. The most important advantage of the test is the absence of friction. The disadvantage is that only the section of the forming limit diagram for positive values of ε_2 can be obtained.

3.3.2.4 Punch Stretching Test

This test was first proposed and used by Keeler himself. It consists of stretching a specimen (2) clamped between a blank-holder (3) and a die (4) using a spherical of elliptical punch, see Fig. 3.20. The strain path is mainly varied by using specimens of different width; is can also be varied by varying the punch radius and the lubricant. Instead of using rectangular specimens Hasek applied specimens with circular recesses.

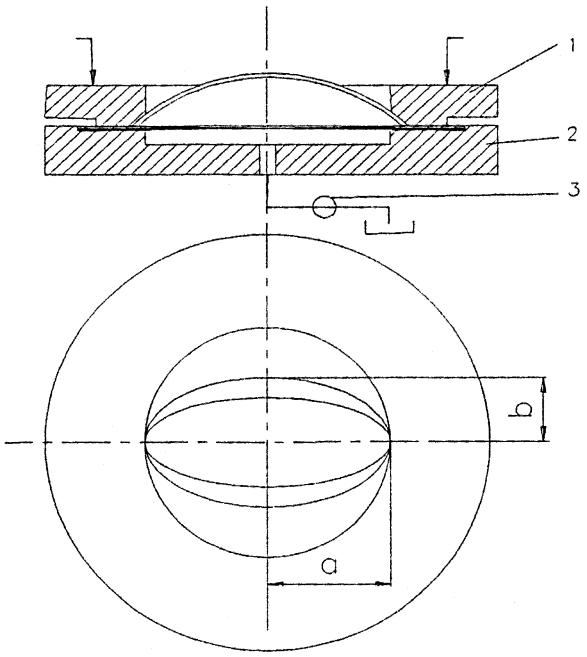

Fig. 3.19 Scheme of hydraulic bulge test with elliptical dies

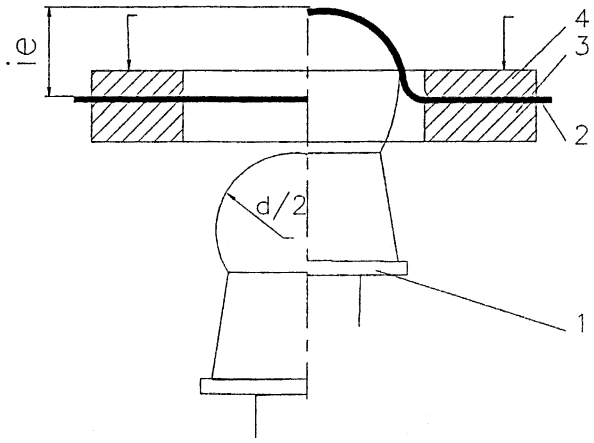

Fig. 3.20 Schematic layout of the punch stretching test

3.3.2.5 Keeler Test

This test consists in the use of punches having different radii in order to vary the stress state, see Fig. 3.21. Disadvantages of the test are the large amount of experimental work; only the positive section of the forming limit diagram is obtained, and the shape and position of the forming limit is influenced by the punch radii.

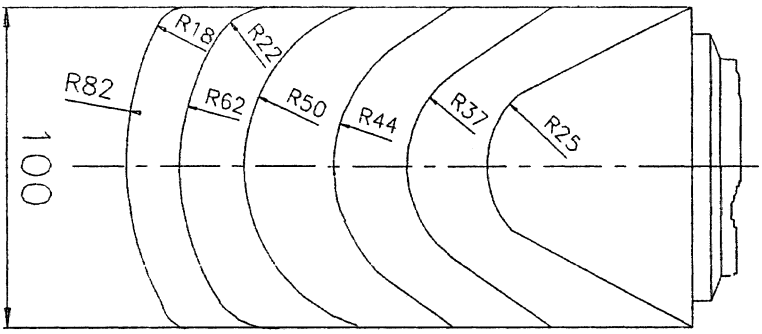

Fig. 3.21 Punches used in the Keeler test

3.3.2.6 Hecker Test

In this test [69] only one type and size of punch and specimen is needed whereby the friction regime is varied by varying the lubricant for obtaining different strain paths. A disadvantage is that only the positive region of the forming limit diagram is determined.

3.3.2.7 Marciniak Test

In deep-drawing with a flat bottom punch tearing of the part usually occurs at the connection between the bottom and the cylindrical wall.

In order to produce the tearing at the planar bottom of the cup, Marciniak proposed [4] to use a hollow punch and an intermediate part having a circular hole placed between punch and workpiece, see Fig. 3.22.

To obtain different strain paths are used punches with different cross sections (circular, elliptical, rectangular). The advantage of this test is that tearing appears at

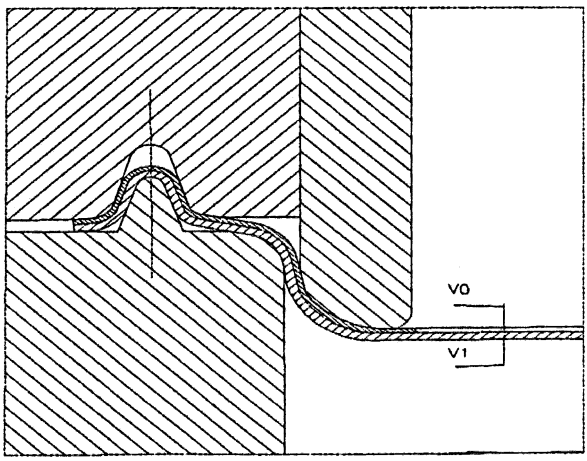

Fig. 3.22 Schematic layout of the device used in the Marciniak test

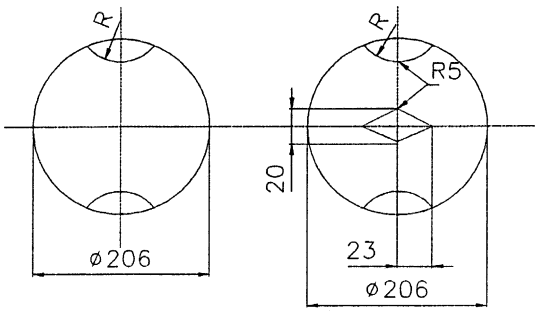

Fig. 3.23 Shapes of the specimens and the intermediate part

the planar bottom of the part thus eliminating the errors of measurement caused by a curvature. Disadvantages are the complex shapes of punch and die and the limitation of the test to the positive domain of the forming limit diagram. In order to overcome these drawbacks, the test can be modified by using specimens and intermediate parts having different shapes, see Fig. 3.23. By varying the radius of the recesses the entire domain of the FLD is obtained using only one ring punch.

3.3.2.8 Nakazima Test

The test [70, 71] consists of drawing rectangular specimens having different widths using a hemispherical punch and a circular die. By varying the width of the specimen and the lubricant one may obtain both the positive and the negative domain of the FLD. The shape of the specimen recommended by ISO 12004 standard is presented in the Fig. 3.24. The recommended length is longer than 25% of punch diameter. For the punch diameter and the die diameter are recommended the values 100 and 105 mm, respectively.

Advantages of the test are the simplicity of the tools, the simple shape of the specimens and the possibility of covering the entire domain of the FLDs. Disadvantages are the possibility of wrinkling and errors of measurement caused by the curvature

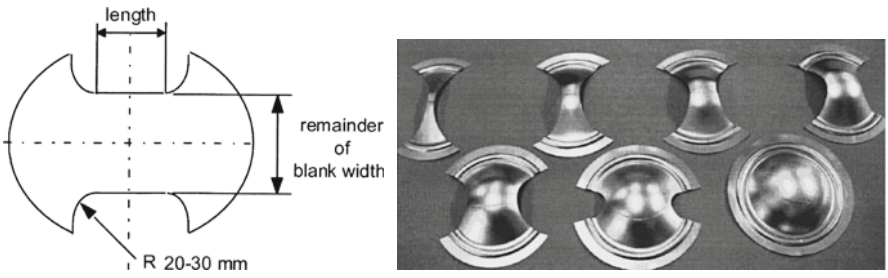

a) b)

Fig. 3.24 (**a**) Shape of the specimens used in the Nakazima test [70]; (**b**) the photo of a set of specimens for a complete FLD (courtesy by GOM company)

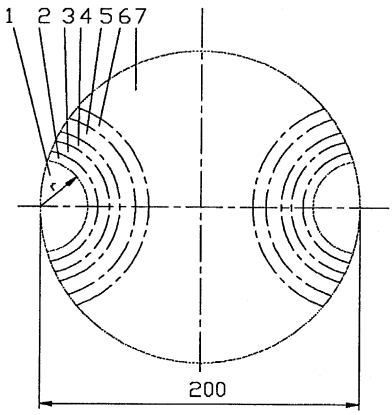

Fig. 3.25 Shape of the specimens used in the Hasek test [73]

Nr.	1	2	3	4	5	6	7
r(mm)	0	4	5	57,5	65	72,5	80

of the punch. This method is used actually as standard method by the ISO 12004 standard 'Metallic materials. Determination of the forming limit curves' [72].

3.3.2.9 Hasek Test

In order to avoid wrinkling of the specimens Hasek proposed [23] the use of circular specimens with recesses of different radii, see Fig. 3.25. This requires an increased amount of work for manufacturing the specimens.

3.3.2.10 Comparison of Different Tests

In addition to the above described methods there are some other tests but their use is limited to a reduced number of strain states (Myauchi test using shearing, Marciniak

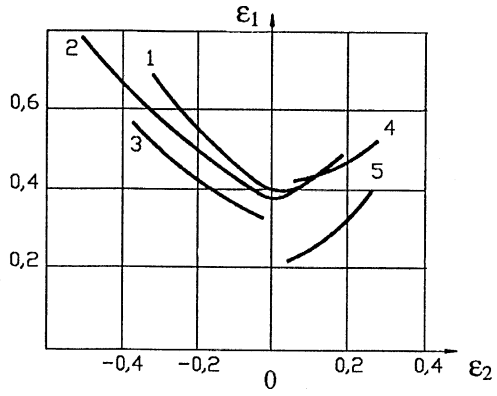

Fig. 3.26 FLDs established using different testing methods: 1—Hasek; 2—Nakazima; 3—uniaxial tension; 4—Keeler; 5—hydraulic bulge test [73]

test using sheet torsion etc.). Hasek [73] published a systematic study of the influence of the testing method upon the obtained FLDs. The key results are summarized in Fig. 3.26.

From the tests described above, the following ones are be recommended: Marciniak test or hydraulic bulge test for eliminating friction; uniaxial test if simplicity is sought for; Nakazima test for covering a great variety of strain paths.

3.3.3 Methods of Determining the Limit Strains

Defining the limit strains of sheet metals has been a constant preoccupation of several IDDRG workgroups. Almost all methods known until now have been developed in these groups. The Benelux [74, 75], French [76, 77], Japan [22] and the German [78, 79] IDDRG groups were very active in this area (see also [19, 80–82]).

Next we will briefly present the most well known methods developed over the years.

Takashina and his co-workers [83] first proposed a simply method to determine the limit strains (so-called 'three circle method'). The method has been improved by Veerman [84, 85]. Bragard [86] developed in 1972 a more precise method of determining the limit strains based on interpolation (Fig. 3.27).

This method is later improved (1975) by D'Haeyer and Bragard [87] using the name of 'the double profile method'. In 1972 Hecker proposed a method [69, 88] based on the determination of three types of ellipses around the fracture: fractured, necked and acceptable (Fig. 3.28). The method consists in determining the major and minor strains of the different types of ellipses in the neighborhood of the

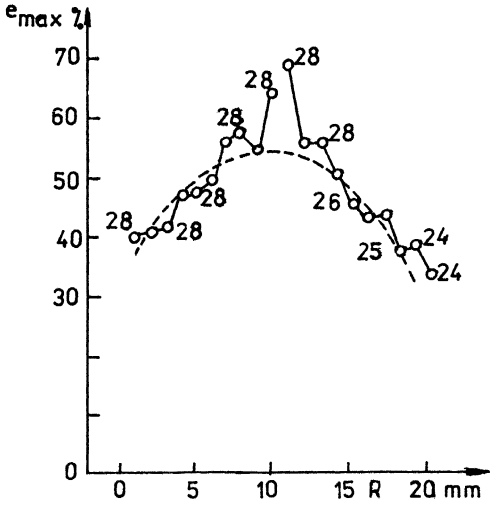

Fig. 3.27 Bragard (interpolation) method to determine the limit strain

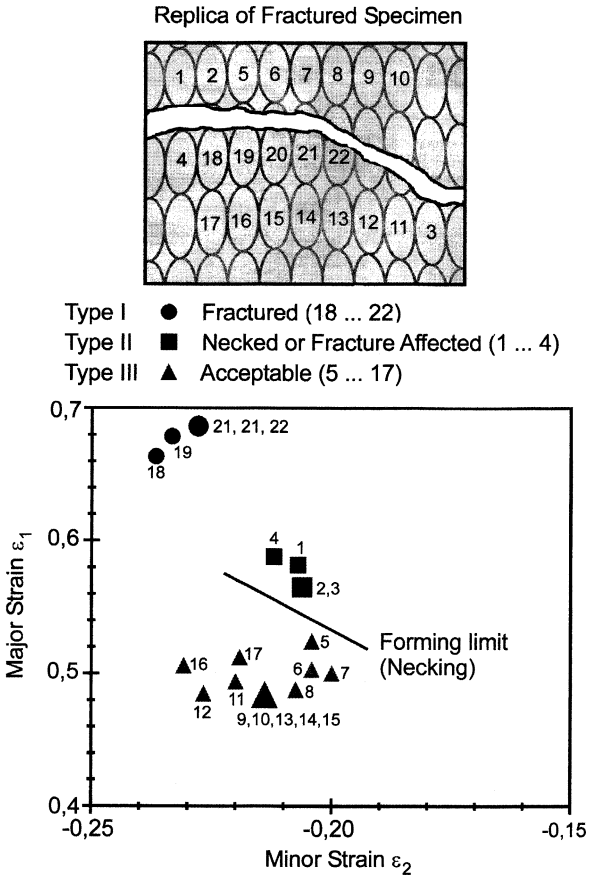

Fig. 3.28 Hecker method to determine the limit strain

fracture on the deformed piece and transposing them on FLD. The limit curve is traced between the point corresponding to the ellipses affected by necking and the acceptable ones (Fig. 3.28). The method has been used on a large scale because of simplicity.

Kobayashi [89] defines the limit strain based on the accelerated increase of the roughness in the necking area. The Zurich meeting in 1973 of the IDDRG workgroup, following an analysis of several versions of limit strain determination, recommends using an improved version of the Bragard method. This is known as the 'Zurich Nr.5 method' [90].

Together with the development 'of online' video strain measuring methods, new methods if determining the limit strains have been proposed in the last years.

A new criterion based on the evolution of the strain rate as a function of time during the forming process has been proposed by the SOLLAC team [91]. The method is based on the observation than the beginning of the necking is accompanied by a considerable increase of the strain rate. According with this method

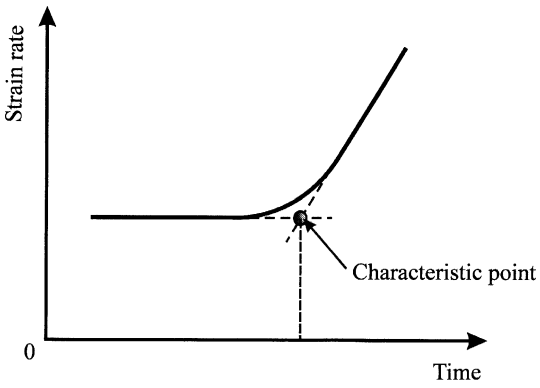

Fig. 3.29 Strain-rate versus time

the start necking point corresponds to the dramatically changing in the strain-rate versus time variation (characteristic point). This point could be determined by the intersection of the two straight lines corresponding to the first and the last sector of the curve (Fig. 3.29). The strain—rate evolutions are automatically determined by images analysis. The strain-rate method has been used recently by Volk [92]. He used the idea to identify a regular grid for the optical measurement as a typical mesh of a finite element method.

The Nakajima workgroup of the IDDRG has developed a new method [78], the so-called 'in-process measurement' method (Fig. 3.30).

A guideline for the determination of FLC based on this method is presented in the paper [93]. It is describe in detail the geometry and the number of the specimens, the geometry of the tool, testing conditions (punch velocity, blank holding force lubricant) as well as measurement and mathematical analysis of the deformed specimen. The method is similar with the Bragard one. Using a video camera system, a film of the forming process is made. Based on the film of the forming process, the development of the strain distribution starting from the onset of necking and finally up

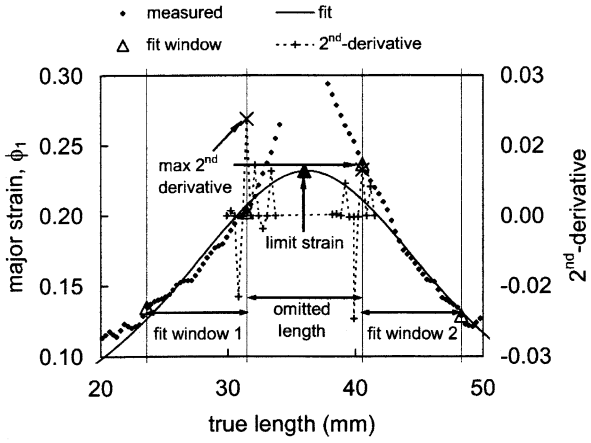

Fig. 3.30 IDDRG method to determine the limit strain [78]

to the fracture is analyzed. The method is a very robust one and gives a very good repeatability of the results. Base of this achievements, the expert group of Nakajima workgroup proposed a revision of the ISO 12004 standard 'Metallic materials-sheet and strip-Determination of the forming limit curves' [72].

Based on the video camera measurement some systems have been developed by the commercial company to determine automatically the FLC. CAMSYS company has developed the first automatically system (ASAME—Automated Strain Analysis and Measurement Environment) used on the large scale, both in research laboratory and industry [94]. The INSA Lyon developed a FLD determination system (IcaForm) based on the spray of a random pattern of paint at the surface of the sample to determine strain distribution [95]. An opto-mechanical device adaptable allows determining easily the FLD. An objective criterion to identify the start of local necking automatically has been proposed recently [96]. The 'Autogrid' system developed by Vialux company offer the possibility to determine the limit strains automatically and independent of any operator. The methodology used to define the limit strain is presented in details in the paper [97]. GOM Company has developed for the FLC determination so-called ARAMIS system [98]. The methodology used is according with the Nakajima workgroup recommendation. For an FLC are used five different geometries, for each geometry three specimens and for each specimen three to five parallel sections. The FLC determination procedure can be done automatically.

3.3.4 Factors Influencing the FLC

3.3.4.1 Sheet Thickness

Besides using sheet of higher quality, the most common solution for the success of difficult sheet metal forming processes is to increase the sheet thickness. The influence of the sheet thickness on the limit strains has been studied by Haberfield [99], Romano [100], Hiam [101], Kleemola [102] etc.

The influence of sheet thickness on the FLD is characterized by the following relationships:

- the FLD for necking depends on sheet thickness (t_0)(see Fig. 3.31 [103])
- as the thickness rises, the curve rises on the plot ($\varepsilon_1; \varepsilon_2$)
- the influence is high for pure expansion and vanishes for pure compression
- the influence of the thickness on the FLD_0 increases linearly (see Fig. 3.32 [104])
- along a linear strain path the rise of the FLD is proportional to the increase of thickness but this influence vanishes above a critical value.

The engineer can decide if an unsuccessful forming process may be improved by increasing the sheet thickness. This is especially important if the stress acting during the forming process is tensile in both principal directions.

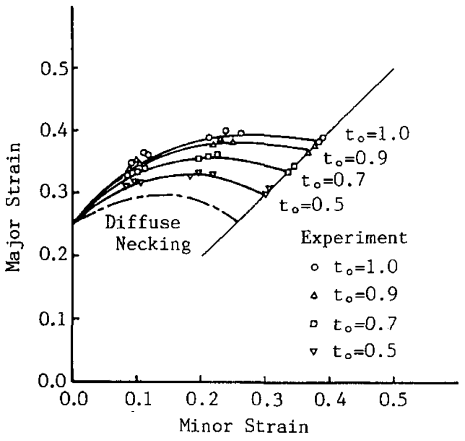

Fig. 3.31 Influence of the thickness on the FLC [103]

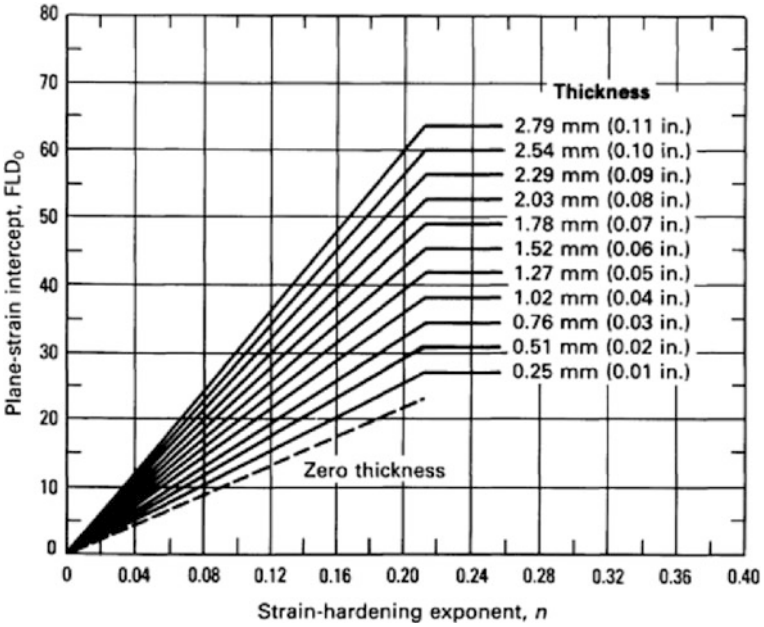

Fig. 3.32 Influence of the thickness and strain hardening coefficient on the FLD_0 [104]

3.3.4.2 Grid Size

If the circles of the initial grid have a diameter d, the measured strain is a mean value averaged over a distance equal to d. Hence, in presence of a strain gradient, a smaller grid size improves the resolution.

When determining the FLD for necking, the strain gradients are rather low; in this case the effect of the grid size on the test results is only weak. However, when determining the FLD for fracture, higher strain gradients occur [105].

Grumbach and Sanz [105] studied the influence of the diameter d on the obtained values of ε_1 and ε_2, using grids with radii in the range from 5 to 0.5 mm. The results confirmed that the circle diameter of the grid has a strong influence on the strain obtained in the direction of the strain gradient whereas the lateral strain may be obtained without any gradient at all.

The data obtained for various circle diameters of the grid allow for an extrapolation of the principal strains to a diameter of zero diameters. If the strain values for this ideal grid are denoted by ε_1^* and ε_2^* one can write:

$$\varepsilon_1^* + \varepsilon_2^* + \varepsilon_3^* = 0 \tag{3.7}$$

where ε_3^* is the strain in thickness direction. Assuming that there is a strain gradient only in the direction of ε_1 the strains in the two other directions are independent of the grid diameter: $\varepsilon_2^* = \varepsilon_2$ and $\varepsilon_3^* = \varepsilon_3$. Hence

$$\varepsilon_1^* = -(\varepsilon_2 + \varepsilon_3) \tag{3.8}$$

As a consequence, the high dispersion of ε_1 one side and the other of the vertical axis $\varepsilon_2 = 0$ disappears. From this point of view several authors [26, 105] proposed the use of an intrinsic FLD, representing the fracture FLD determined using a grid

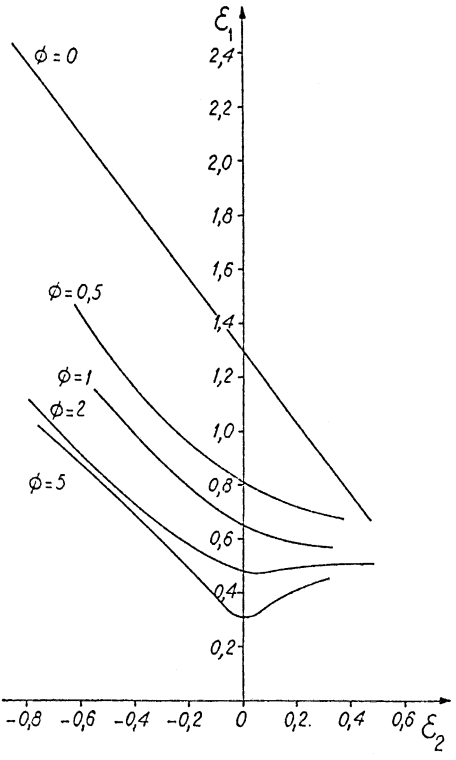

Fig. 3.33 Intrinsic forming limit diagram [105]

of infinitely small size. The plot of this intrinsic curve is very close to a straight line, see Fig. 3.33 [105].

3.3.4.3 Strain Path

When the limit strains are sought, the path of deformation can be plotted, showing the successive strains (ε_1; ε_2) imposed to the circle where fracture eventually occurs. These paths always start at the origin of the two axes.

The curves in Fig. 3.34 were plotted using simple laboratory tests which are used for determining limit diagrams. These tests were:

I ISO 50—simple tensile test using standard specimen
II TPE 1—tensile test using thinned specimen
III Swift 50—cylindrical cup $\Phi = 50$ mm with flat bottom
IV hydraulic expansion through circular die (Jovignot).

The following conclusions have been formulated:

- the paths are practically linear as long as necking does not appear; in this case the size of the grid circles has an influence on the measured values as shown above
- the slope of the path corresponding to the simple tensile test follows from the relation

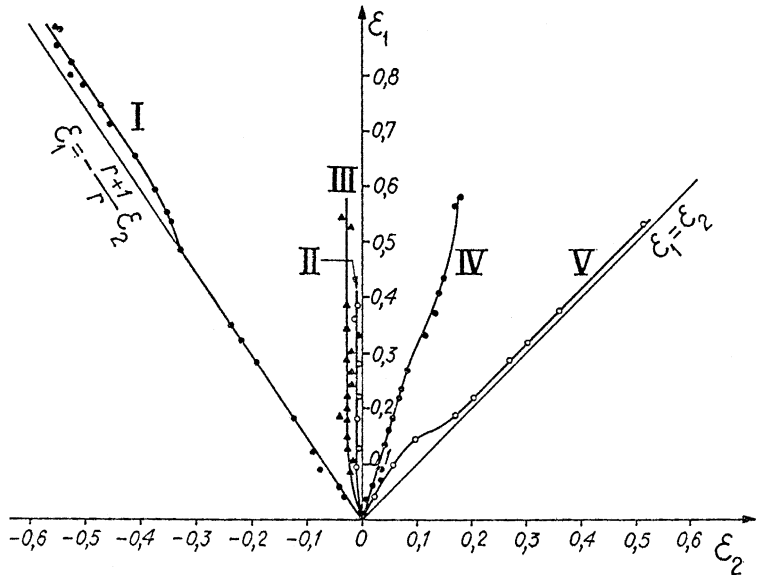

Fig. 3.34 Strain paths used in different tests [105]

$$\varepsilon_1 = -\frac{1+r}{r}\varepsilon_2 \tag{3.9}$$

- the slope of the path corresponding to the hydraulic bulge test using a circular die (Jovignot) is equal unity due to the equibiaxial tensile stress.

Kikuma [106] showed the influence of the strain path on the FLDs (Fig. 3.35).

For industrial sheet metal forming processes which require several passes (e.g. in the automotive industry), Japanese authors have shown that, as long as the deformation pattern changes from one pass to another, the strain path is a broken line [52]. If a tensile load path is followed by a compressive one the limit strains are smaller than the ones corresponding to the FLD; on the other hand, a compressive load preceding a tensile one improves the limit strain values. Yet, engineers from industry always proceed first with a tensile or a compressive deformation, and only eventually apply expansion.

The complex strain paths undergone by industrial parts during multi-pass forming can be simulated in laboratory tests by applying to the same specimen successively two different load paths, for example, a tensile test followed by deep-drawing or biaxial expansion followed by a local tensile test. The analysis of the specimens provides results similar to those for real industrial components:

- a path change has a strong influence on FLDs both for necking and fracture
- as long as the initial deformation implies $\varepsilon_2 < 0$ (compression test, simple tensile test) followed by biaxial expansion, the limit curve II is higher than the FLD I (corresponding to simple, linear load paths, see Fig. 3.35)
- on the contrary, if $\varepsilon_2 > 0$ during the first stage and compression or simple tensile load follows later the limit curve III is below the FLD I for simple paths.

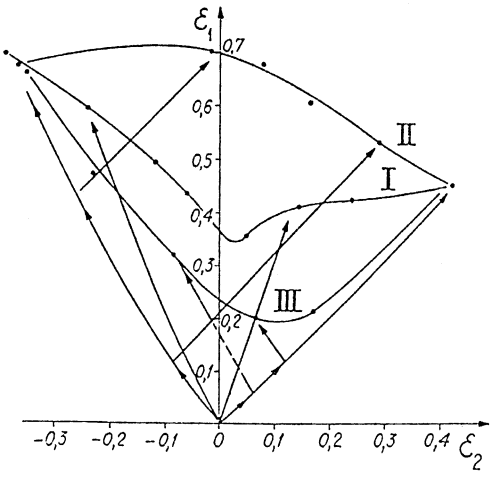

Fig. 3.35 Influence of strain path on the forming limit curve [106]

These results confirm the practical rule mentioned above. Actually, the residual formability depends on the strain evolution. It is well known that the defects induced by plastic deformation are a consequence of voids developing at the matrix/inclusion interface; their growth and coalescence also depend on the strain history.

3.3.4.4 Mechanical Properties

The numerous determinations of forming limit diagrams realized after Keeler and Goodwin first published their results confirmed their conclusion that for materials with relatively close mechanical properties the experimental FLDs are close as well. Using the load path plots, it has been possible to determine the influence of the mechanical properties not only on the position of the FLD, but also on the position of the limit state corresponding to the part of interest. Woodthorpe [107] and Pearce [108] have studied the influence of the mechanical parameters (strain hardening, n, and anisotropy coefficients, r) on the FLC for the first time. Later, Haberfield [99], Hiam [101] and Conrad [109] have extended Woodthorpe's research. For example, Conrad [109] studied the influence of the strain rate sensitivity exponent, m, on the limit strains.

Since the strain paths for simple tensile tests are straight lines having the slope—(1+r)/r in the $\varepsilon_1, \varepsilon_2$ -plane the load paths will shift to the left by increasing r. Higher values of r also allow for higher values of the final strain ε_1. This influence has been outlined in [110], see Fig. 3.36.

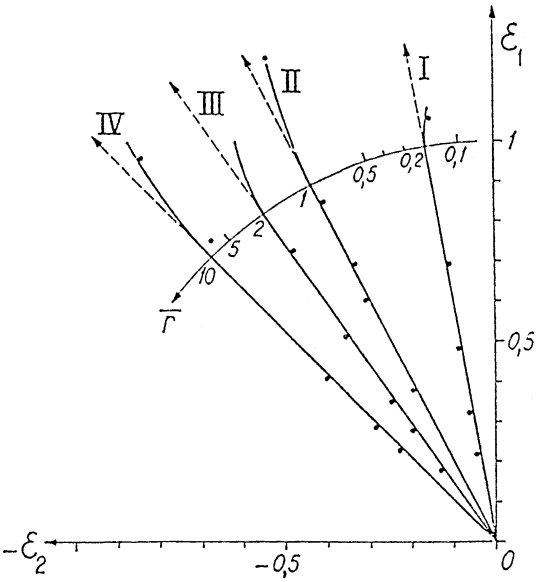

Fig. 3.36 Influence of anisotropy on strain path [110]

In the same manner, if n is increasing (at a given r), one may notice that the uniform elongation and the ultimate elongation increase and the point designating fracture moves to higher values of ε_1.

It has also been shown that in the range of expansion ($\varepsilon_1 > 0; \varepsilon_2 > 0$) with the increase of n, the corresponding point of the FLD is shifted to the right i.e. to higher values of equivalent strain. This may be explained by the delayed initiation of necking whereby the strain path remains linear for a longer period. As a conclusion, even if the FLDs for different materials are close to each other they are shifted in accordance with the values of the mechanical properties (r and n).

3.3.4.5 Influence of the Punch Curvature

Ghosh and Hecker [111] showed that the choice of the experimental method used for the FLC determination (in-plane versus out-of-plane) influences the position of the limit curves. The influence of the punch curvature on the stretching limits has been studied first by Charpentier [112]. He used punches having different curvature radii (ranging from the infinite radius—in-plane stretching—to a relatively small radius—15.85 mm) and noticed that the decrease of the radius was accompanied by an increase of the formability (upwards motion of the FLC). Shi and Gerdeen [113] performed a theoretical analysis of this influence using the Marciniak–Kuckzinsky model (see Sect. 3.4.3) (Fig. 3.37).

3.3.4.6 Influence of the Temperature

The influence of the temperature on the limit strains was studied first by Lange [114] and later by Ayres [115], Kumpulainen [116], Li and Ghosh [117], Abedrabbo [118], van den Boogaard [119] etc. According to these researchers, the temperature has a different influence on the formability of different metallic alloys. For example, the formability of the AA 5754 alloy has a significant increase when the temperature rises even with small amounts (from 250 to 350°C) (Fig. 3.38 [117]), while temperature variations in the same range have a very little influence on the formability of the AA 6111-T4 alloy (Fig. 3.39 [117]). The increase of the formability by raising the temperature of the material is frequently used in the case of the sheet metals having a poor formability at room temperature (some aluminum or magnesium alloys, high-strength steels, etc.).

3.3.4.7 Influence of the Strain Rate

Drewes [120] followed later by Ayres [115] and Percy [121] have analyzed the influence of the strain rate on the limit strain. In general, the increase of the strain rate causes a downward displacement of the FLC, that is a diminishment of the formability. Such an example is shown in Fig. 3.40 [121] and corresponds to the SPCEN-SD steel. The difference between the strain rates is 10^4. Similar results were also obtained by Ayres [115]. On the other hand, more recently, Balanethiram

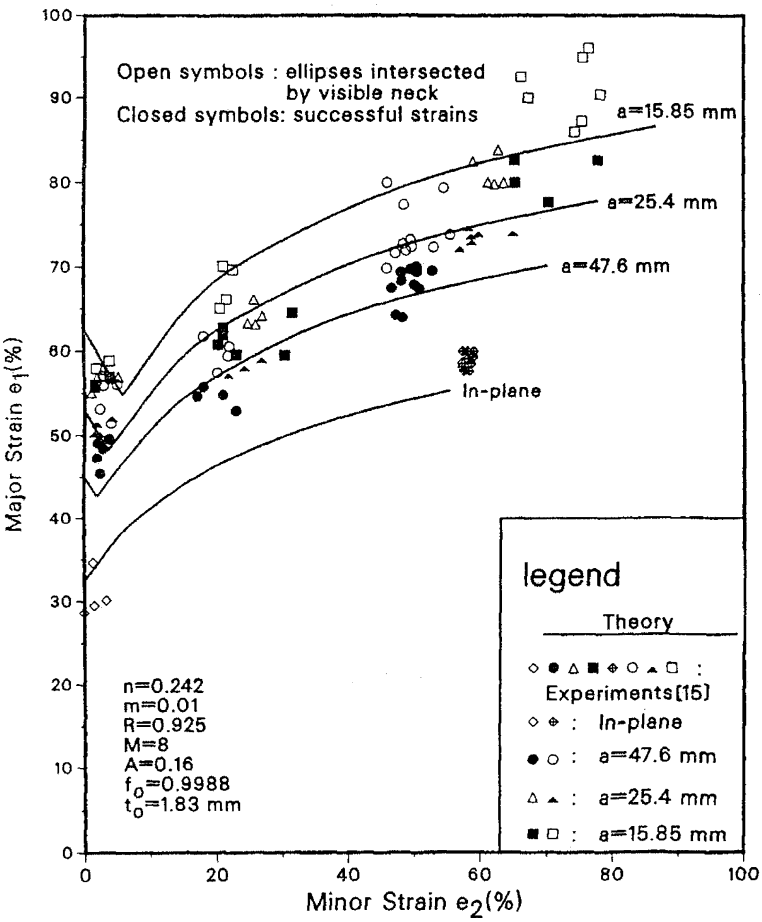

Fig. 3.37 Influence of punch curvature on the FLC [113]

and Daehn [122] have reported a significant increase of the formability when the strain rate is also increased for an OFHC copper. Gerdooei and Dariani [123] have explained this effect based on the Johnson–Cook law (see Fig. 3.41). The different behavior of the metallic materials from this point of view is a consequence of the different values of the strain-rate sensitivity index, as well as of the different mechanical response when the strain rate is modified.

3.3.4.8 Influence of the Normal Pressure

The effect of the normal pressure on the formability of sheet metals is well know and already used from long time ago in industry [124]. During some forming operations (hydrostatic forming, incremental forming) the sheet is subjected to a significant normal pressure. The increase in formability is usually explained by the closing of

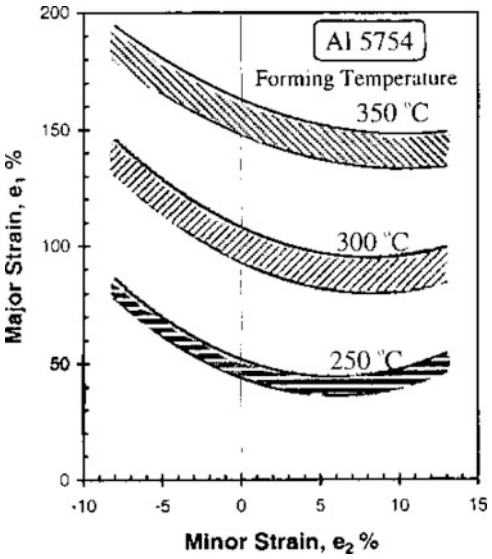

Fig. 3.38 Influence of the temperature on the FLC for the 5754 aluminium alloy [117]

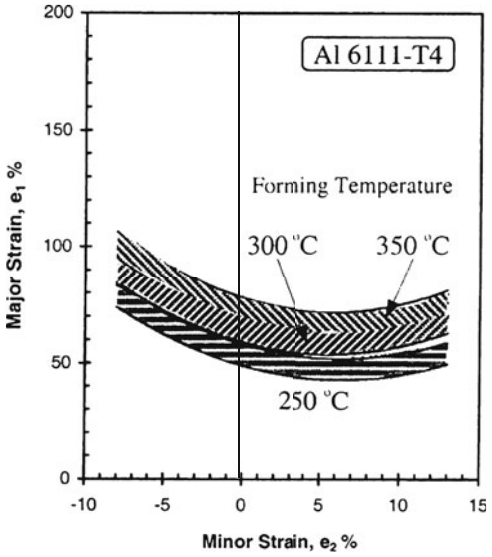

Fig. 3.39 Influence of the temperature on the FLC for the 6111-T4 aluminium alloy [117]

the micro-voids in the sheet and the slowing down of the nucleation of new ones due to the normal pressure exerted by the surrounding fluid [125]. But, an analysis of sheet failure under normal pressure without assuming ductile damage has been done in the last period. Such an analysis was performed by using Swift Hill models by Gotoh [126], Smith [127] and Matin [128]. Recently, Banabic and Soare [129], Wu et al. [130] and Alwood and Shouler [131] have analyzed the influence of the normal pressure on the Forming Limit Curve using an enhanced Marciniak model.

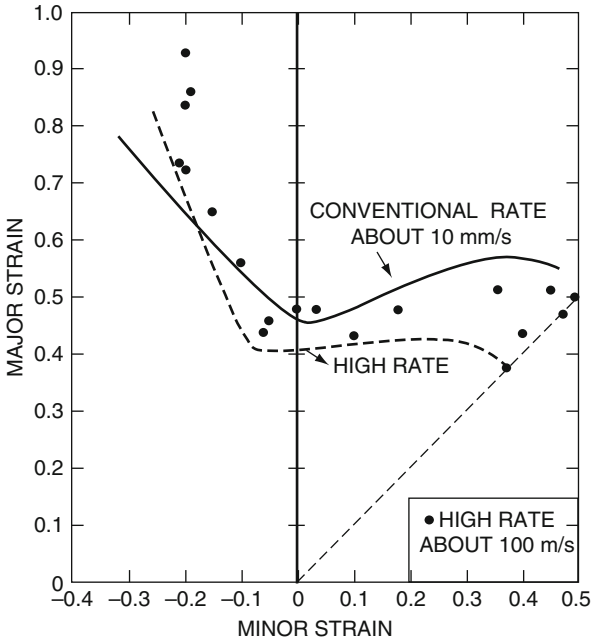

Fig. 3.40 Influence of the strain-rate on the FLC for SPCEN-SD steel [121]

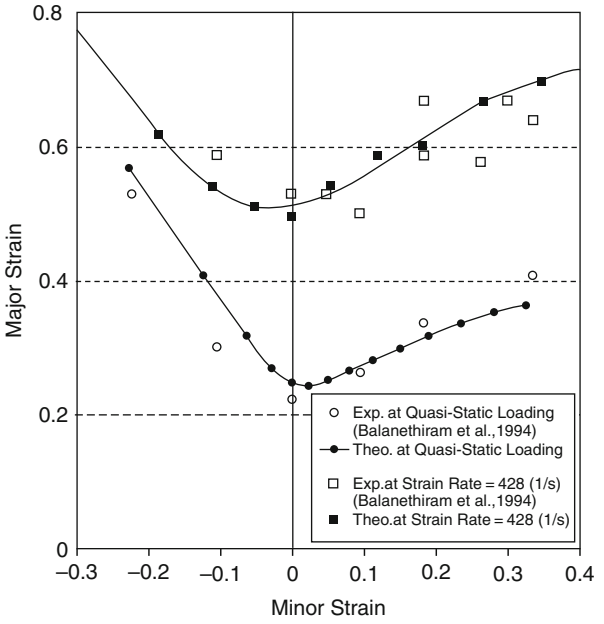

Fig. 3.41 Influence of the strain-rate on the FLC for OFHC copper [123]

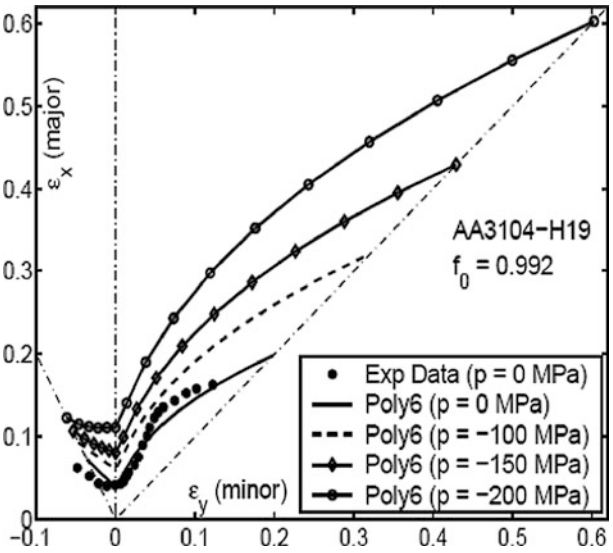

Fig. 3.42 Forming limit curves for several values of the normal pressure for AA3104-H19 aluminium alloy [129]

The results presented in the last papers are very closed one to another one. In the Fig. 3.42 is presented this influence based on the modified Marciniak model.

3.3.4.9 Other Parameters

Besides the influencing factors listed above some other parameters have an effect on the FLCs, see [1, 3, 16, 18, 23, 31, 82, 81, 132–137].

3.3.5 Use of Forming Limit Diagrams in Industrial Practice

The most realistic and efficient way to estimate the technological possibilities of producing a part and to avoid unsuccessful design is to apply the FLD method. This enables to determine

- the range of safety for deep-drawing
- the critical zones where necking or fracture are most likely to occur
- the strain level
- the favorable working conditions (blank holding, lubrication etc.).

In practice this method is applied as follows. After the shape, dimensions and material quality of a given part have been prescribed by the designer the forming technology and the tools have to be designed. For this purpose the maximum

strains in the part must be known as well as the forming limit diagram of the material.

By comparing the points corresponding to the maximum strains in the parts with the FLD one can estimate whether fracture or necking could appear during forming.

If no defect is to be expected one has information about how far from the limit the material is deformed.

If the points defined by the maximum strain are beyond the limit curve, some modifications have to be made of

- working conditions (blank-holding, lubrication)
- design of the part itself (fillet radii, angles etc.)
- material (quality, thickness).

The effect of these modifications is illustrated by Fig. 3.43. In the first two cases the characteristic point is shifted either from A to A′ or A″ or from B to B′ or B″. In the third case the forming limit curve itself is shifted to the dashed line.

The FLD method also gives an estimation of the severity of deformation through the so-called severity index [138]. This parameter is defined as shown in Fig. 3.44. If the point of the maximum strain is below and far from the forming limit curve, the severity index is small and the safety margin is so large that material is wasted (point C in Fig. 3.43).

Therefore it is possible either to modify the forming process by increasing the strains (move from C to C′) or to use a material having a lower forming limit curve (yet still beyond the point of maximum strains). A good compromise between reasonable safety margins and prevention of material waste appears to be in the zone where the severity index is 7–8. The safety margin depends on the quality

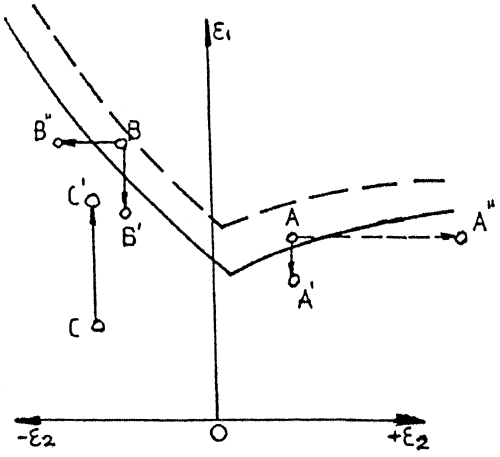

Fig. 3.43 Examples of the shifting of critical points

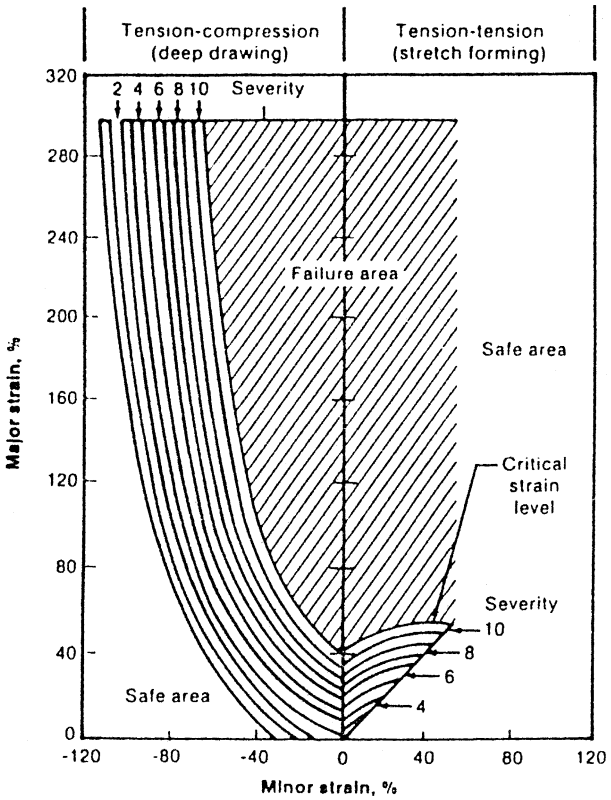

Fig. 3.44 Definition of the severity indices [138]

of the material as well as on the process parameters. The choice of the material not only influences the FLD but also the strain path and the deformation front.

The determination of the maximum strains to compare with the FLD can be difficult for complex parts, since the deformations cannot be calculated by analytical methods. In such cases two other methods are available for the estimation of the maximum strains: experimental studies on small scale models or numerical simulation. In the past experimental methods have been most widely used. However, in the last two decades numerical simulation has become more and more the method of choice. On the other hand, important progress has been achieved in numerical solution methods, especially the finite element method.

The structure of an expert system for the analysis of sheet metal formability is illustrated by Fig. 3.45. The steps of process design in sheet metal forming, based on formability analysis, are presented in Fig. 3.46 [139].

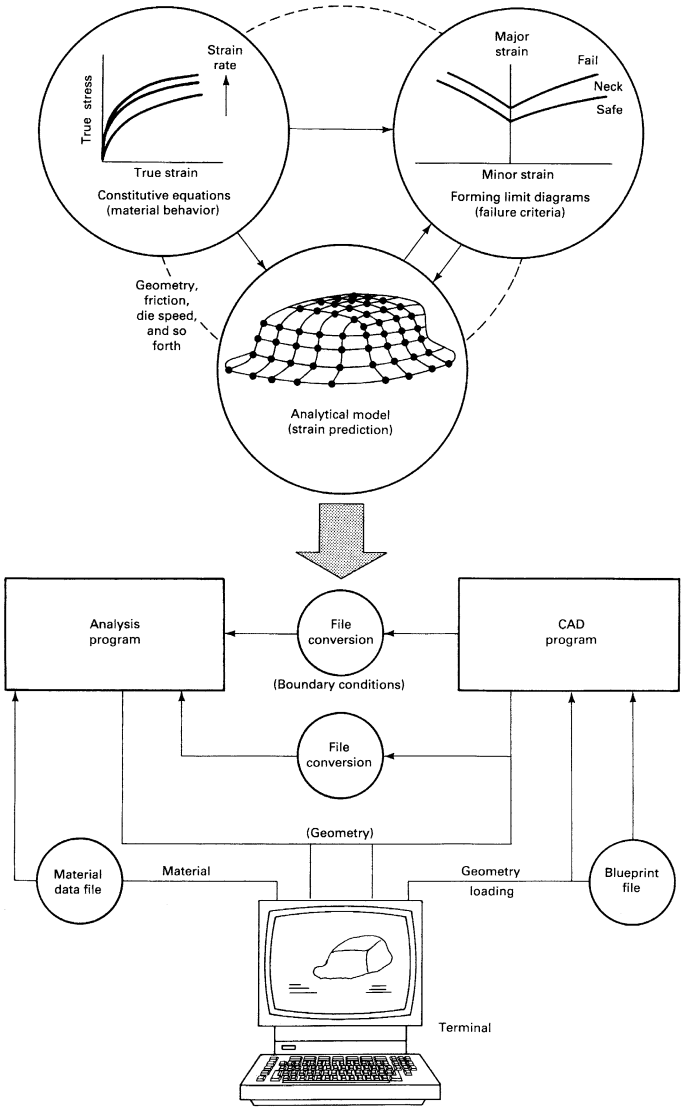

Fig. 3.45 Structure of an expert system for the analysis of sheet metal formability [139]

Besides software packages of finite element analysis and CAD, computer aided process design also requires databases with FLDs for various working conditions. Experimental testing is a very valuable input for these databases, but it is also rather expensive. The mathematical modeling based on theoretical developments described in the Sect. 3.4 is also used for this purpose. A detailed presentation of the way the FLD concept is used in FE simulation software is made in Sect. 4.3.

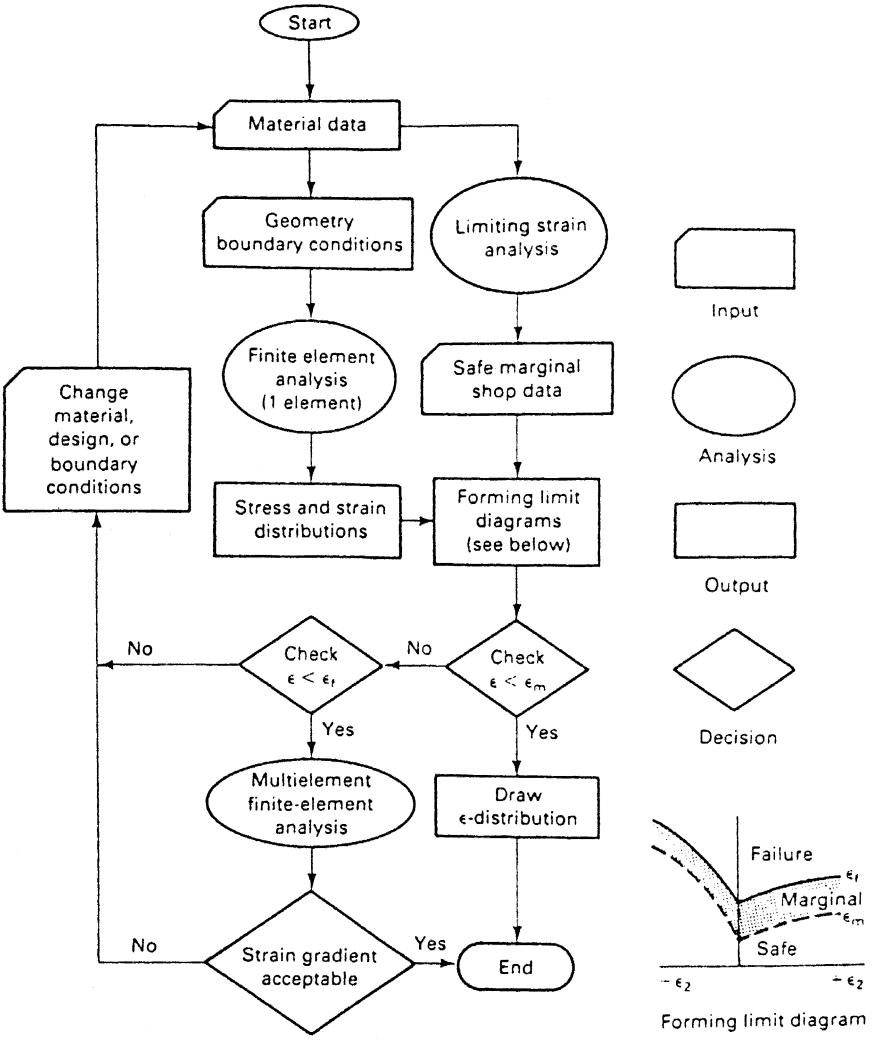

Fig. 3.46 Flowchart of technological design process in sheet metal forming on the basis [139]

3.4 Theoretical Predictions of the Forming Limit Curves

Various theoretical models have been developing for the calculation of forming limit curves (Fig. 3.47). The first ones were proposed by Swift [140] and Hill [141] assuming homogeneous sheet metals (the so-called models of diffuse necking and localized necking), respectively). The Swift model has been developed later by Hora (so-called Modified Maximum Force Criterion-MMFC) [142]. Marciniak [143] proposed a model taking into account that sheet metals are non-homogeneous from both the geometrical and the structural point of view. Storen and Rice [144] have

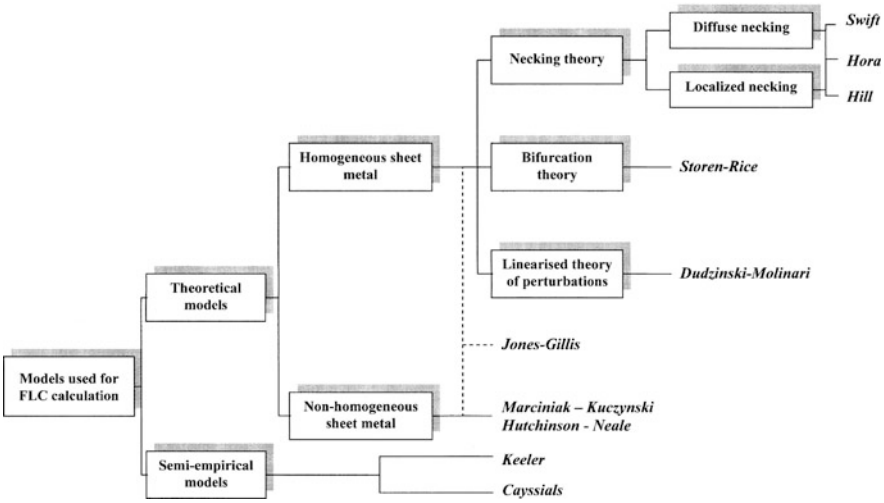

Fig. 3.47 Theoretical models used in FLC calculation

been developed a model based on the bifurcation theory. Dudzinski and Molinari [145] used the method of linear perturbations for analyzing the strain localization and computing the limit strains.

Since the theoretical models are rather complex and need a profound knowledge of continuum mechanics and mathematics while their results are not always in agreement with experiments, some semi-empirical models have been developed in recent years.

In the next sections the most commonly used models are presented briefly with the focus on those based on the necking phenomenon (Swift and Hill), the Marciniak–Kuczynski and MMFC model, respectively.

3.4.1 Swift's Model

Considère [146] approached for the first time the problem of plastic instability in uniaxial tension. In the case of ductile materials, two domains may be distinguished in the region of plastic straining. In the first domain the hardening influence on the traction force is stronger than the influence of the cross-section reduction. This is the so-called 'domain of stable plastic straining', being characterized by the fact that an increase of the traction force is needed in order to obtain an additional deformation of the specimen. In the second domain material hardening cannot compensate the decrease of the traction force due to the reduction of the specimen's cross-section. This is the so-called 'domain of unstable plastic straining', being characterized by a decrease of the traction force, although the stress continues to increase.

The beginning of necking corresponds to the maximum of the traction force. From the mathematical point of view, this condition can be written in the form

$$dF = 0 \tag{3.10}$$

By simple mathematical manipulations the following condition of plastic instability is obtain:

$$\frac{d\sigma}{d\varepsilon} = 1 + \sigma \tag{3.11}$$

Assuming a Ludwik–Hollomon strain-hardening law,

$$\sigma = k\bar{\varepsilon}^n \tag{3.12}$$

then the condition (3.11) becomes

$$\bar{\varepsilon} = n \tag{3.13}$$

Hence, according to Considère's criterion, a material obeying the Ludwick–Hollomon hardening law starts to neck when the strain is equal to the hardening coefficient.

Swift [140] used the Considère criterion in order to determine the limit strains in biaxial tension. He analysed a sheet element loaded along two perpendicular directions and applied the Considère criterion for each direction. Assuming a strain hardening described by Eq. (3.12), he obtained the following expressions for the limit strains:

$$\varepsilon_1^* = \frac{\sigma_1 \left(\frac{\partial f}{\partial \sigma_1}\right)^2 + \sigma_2 \left(\frac{\partial f}{\partial \sigma_2}\right)\left(\frac{\partial f}{\partial \sigma_1}\right)}{\sigma_1 \left(\frac{\partial f}{\partial \sigma_1}\right)^2 + \sigma_2 \left(\frac{\partial f}{\partial \sigma_2}\right)^2} n \tag{3.14}$$

$$\varepsilon_2^* = \frac{\sigma_2 \left(\frac{\partial f}{\partial \sigma_1}\right)^2 + \sigma_1 \left(\frac{\partial f}{\partial \sigma_1}\right)\left(\frac{\partial f}{\partial \sigma_2}\right)}{\sigma_1 \left(\frac{\partial f}{\partial \sigma_1}\right)^2 + \sigma_2 \left(\frac{\partial f}{\partial \sigma_2}\right)^2} n \tag{3.15}$$

where f is the yield function.

By using different yield functions, it is possible to evaluate the limit strains as functions of the loading ratio α and the mathematical parameters of the material (hardening coefficient n, anisotropy coefficient r, strain-rate sensitivity m, etc.). As an example, if the Hill 1948 criterion is used (Eq. 2.63), the limit strains are as follows:

$$\varepsilon_1^* = \frac{[1 + r(1-\alpha)]\left(1 - \frac{2r}{1+r}\alpha + \alpha^2\right)}{(1+r)(1+\alpha)\left[1 - \frac{1+4r+2r^2}{(1+r)^2}\alpha + \alpha^2\right]} n \tag{3.16}$$

$$\varepsilon_2^* = \frac{[(1+r)\,\alpha - r]\left(1 - \frac{2r}{1+r}\alpha + \alpha^2\right)}{(1+r)\,(1+\alpha)\left[1 - \frac{1+4r+2r^2}{(1+r)^2}\alpha + \alpha^2\right]} n \tag{3.17}$$

The expressions of the limit strains associated to some other yield criteria (such as Hill 1979 and Hill 1993) are presented in [147].

By computing the values of $\varepsilon_1{}^*$ and $\varepsilon_2{}^*$ for different loading ratios α and recording them in a rectangular coordinate system ε_1, ε_2 the necking limit curve is obtain.

3.4.2 Hill's Model

In the case of uniaxial tension, the localized necking develops along a direction, which is inclined with respect to the loading direction. Hill [141] assumed that the necking direction is coincident with the direction of zero-elongation and thus the straining in the necking region is due only to the sheet thinning.

The method used for obtaining the limit strains in this case is presented in [10]. The expressions of these strains are as follows:

$$\varepsilon_1^* = \frac{\frac{\partial f}{\partial \sigma_1}}{\frac{\partial f}{\partial \sigma_1} + \frac{\partial f}{\partial \sigma_2}} n \tag{3.18}$$

$$\varepsilon_2^* = \frac{\frac{\partial f}{\partial \sigma_2}}{\frac{\partial f}{\partial \sigma_1} + \frac{\partial f}{\partial \sigma_2}} n \tag{3.19}$$

It can be seen that

$$\varepsilon_1^* + \varepsilon_2^* = n \tag{3.20}$$

This is the equation of a line parallel with the second bisectrix of the rectangular coordinate system ε_1, ε_2 and intersecting the vertical axis at the point $(0, n)$.

According to Eq. (3.20), the FLC computed on the basis of the Hill's model does not depend on the yield criterion, but only on the value of the hardening coefficient.

3.4.3 Marciniak–Kuckzynski (M–K) and Hutchinson–Neale (H–N) Models

On the basis of the experimental investigations concerning the strain localization of some specimens subjected to hydraulic bulging or punch stretching, Marciniak [148] has concluded that the necking is usually initiated by a geometrical or structural non-homogeneity of the material. This non-homogeneity may be associated to a

variation of the sheet thickness (geometrical non-homogeneity) or some defects of the lattice (structural non-homogeneity).

The analysis of the necking process has been performed assuming a geometrical non-homogeneity in the form of a thickness variation. This variation is usually due to some defects in the technological procedure used to obtain the sheet metal. The thickness variation is generally gentle. However, the theoretical model assumes a sudden variation in order to simplify the calculations (Fig. 3.48).

The theoretical model proposed by Marciniak assumes that the specimen has two regions: region A having a uniform thickness $s_0{}^{(A)}$, and region B having the thickness $s_0{}^{(B)}$ (Fig. 3.48). The initial geometrical non-homogeneity of the specimen is described by the so-called 'coefficient of geometrical non-homogeneity', f, expressed as the ratio of the thickness in the two regions:

$$f = \frac{s_0^{(B)}}{s_0^{(A)}} \tag{3.21}$$

The strain and stress states in the two regions are analysed with respect to the principal strain $\varepsilon_1{}^{(B)}$ in region B and the principal strain $\varepsilon_1{}^{(A)}$ in region A. When the ratio $\varepsilon_1{}^{(B)}/\varepsilon_1{}^{(A)}$ becomes too high (infinite in theory, above 10 in practice), one may consider that the deformation of the specimen is localized in region B (Fig. 3.49).

The shape and position of the curve $\varepsilon_1{}^{(B)}(\varepsilon_1{}^{(A)})$ depend on the value of the coefficient f. If $f = 1$ (geometrically homogeneous sheet), the curve becomes coincident with the first bisectrix. Thus this theory cannot model the strain localization for geometrically homogeneous sheets.

The value of the principal strain $\varepsilon_1{}^{(A)}$ in region A corresponding to non-significant straining of this region as compared to region B (the straining being localized in region B) represents the limit strain $\varepsilon_1{}^{(A)*}$ (Fig. 3.49). This strain together

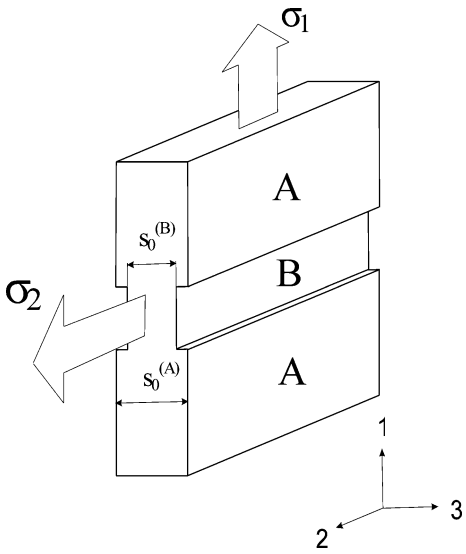

Fig. 3.48 Geometrical model of the M–K theory

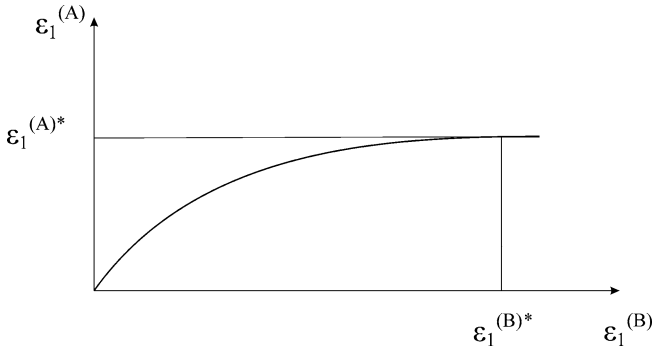

Fig. 3.49 The dependence $\varepsilon_1{}^{(B)}/\varepsilon_1{}^{(A)}$

with the second principal strain $\varepsilon_2{}^{(A*)}$ in region A define a point of the forming limit curve. By varying the strain ratios $\rho = d\,\varepsilon_2{}^{(A)}/d\,\varepsilon_1{}^{(A)}$, different points on the FLC are obtained. By scrolling the range $0 < \rho < 1$, the FLC for biaxial tension ($\varepsilon_1 > 0$, $\varepsilon_2 > 0$) is obtained. In this range the orientation of the geometrical non-homogeneity with respect to the principal directions is assumed to be the same during the entire forming process.

The Marciniak model was further developed by Marciniak and Kuczynski [143] and Marciniak, Kuczynski and Pokora [149], usually being briefly denominated the M–K model.

The M–K model was extended to the negative range of the FLD's ($\varepsilon_2 < 0$) by Hutchinson and Neale (H–N model) [150–152]. According with the original paper of Hutchinson and Neale [151], the inclination of the non-homogeneity varies with the main strains by a law having the form:

$$\tan(\varphi + d\varphi) = \frac{1 + d\varepsilon_1^{(A)}}{1 + d\varepsilon_2^{(A)}} \tan\varphi \tag{3.22}$$

and the non-uniformity coefficient varies by a law having the form:

$$f_1 = f_0 \left(d\,\varepsilon_3^{(B)} - d\,\varepsilon_3^{(A)} \right), \tag{3.23}$$

where, f_1 and f_0 are the current and initial non-uniformity coefficients, respectively.

The M–K and H–N models are thoroughly described in [153–155] together with the numerical algorithms. The explicit algorithms are usually used to solve the M–K and H–N models. Newton's method is used to solve the non linear system of equations. Since Newton's method usually has a non-convergence problem, different methods are used (for example, backtracking algorithm [155]) to eliminate this drawback. However, the use of such an algorithm significantly increases the computation time. A synthetic presentation of the M–K and H–N models' evolution is given in [156, 157].

In order to increase the robustness of the algorithms used to solve the M–K and the H–N models, an implicit formulation of the models is proposed in [158]. This formulation is presented in detail in the next section.

3.4.4 Implicit Formulation of the M–K and H–N Models

Both M–K and H–N models assume that the strain localization is caused by a thickness imperfection represented as a groove in Fig. 3.50 [143, 150]. According to this hypothesis, two regions of the sheet metal should be distinguished: A – non-defective zone; B – groove. At different stages of the straining process (identified by the time parameter t), the ratio

$$ {}^{t}f = {}^{t}s^{(B)} \Big/ {}^{t}s^{(A)} , \quad 0 < {}^{t}f < 1 \tag{3.24} $$

is used to describe the amplitude of the imperfection ($ {}^{t}s^{(A)} $ and $ {}^{t}s^{(B)} $ denote the current thickness of regions A and B, respectively – see Fig. 3.50).

Throughout this section, the sheet metal is considered to behave as an orthotropic membrane under the plane-stress conditions

$$ \begin{aligned} {}^{t}\sigma_{i3} &= {}^{t}\sigma_{3i} = 0, \quad i = 1, 2, 3, \\ {}^{t}\dot{\varepsilon}_{\alpha 3} &= {}^{t}\dot{\varepsilon}_{3\alpha} = 0, \quad \alpha = 1, 2. \end{aligned} \tag{3.25} $$

The constraints written above are valid both for region A and region B. Eq. (3.25) involves the components of the stress and strain-rate tensors expressed in the plastic orthotropy frame (1 and 2 are the indices associated to the rolling and transverse

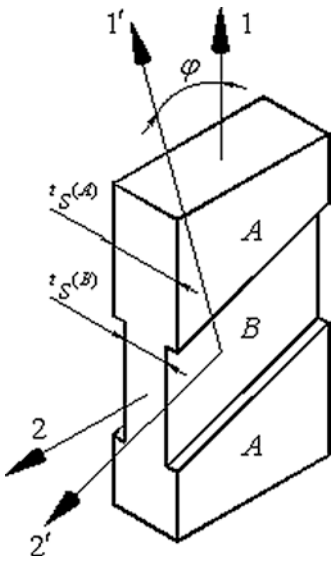

Fig. 3.50 Schematic view of the thickness imperfection assumed by the H–N model

directions, respectively – see Fig. 3.50, while 3 is the index corresponding to the normal direction – not shown in Fig. 3.50).

We also assume that the sheet metal is subjected to loads which do not produce tangential stresses and strains in the plastic orthotropy frame:

$$ {}^t\sigma_{12} = {}^t\sigma_{21} = 0, \quad {}^t\dot{\varepsilon}_{12} = {}^t\dot{\varepsilon}_{21} = 0. \tag{3.26} $$

This constraint will be applied not only to the non-defective zone (as in the classical formulation of the Hutchinson–Neale model), but also to the groove. Under such circumstances, the diagonal components of the stress and strain-rate tensors automatically become eigenvalues. In order to emphasize their significance, the following notations will be used:

$ {}^t\sigma_i \ (i = 1, 2, 3)$ – principal stresses $\left({}^t\sigma_1 = {}^t\sigma_{11}, {}^t\sigma_2 = {}^t\sigma_{22}, {}^t\sigma_3 = {}^t\sigma_{33} = 0\right)$
$ {}^t\dot{\varepsilon}_i \ (i = 1, 2, 3)$ – principal strain rates $\left({}^t\dot{\varepsilon}_1 = {}^t\dot{\varepsilon}_{11}, {}^t\dot{\varepsilon}_2 = {}^t\dot{\varepsilon}_{22}, {}^t\dot{\varepsilon}_3 = {}^t\dot{\varepsilon}_{33}\right)$.

The mechanical response of the sheet metal will be described by a rigid-plastic model. The main ingredient of the constitutive model is the yield criterion:

$$ {}^t\overline{\sigma}\left({}^t\sigma_1, {}^t\sigma_2\right) = {}^tY\left({}^t\overline{\varepsilon}\right). \tag{3.27} $$

Equation (3.27) involves the following quantities:

- $ {}^t\overline{\sigma} = {}^t\overline{\sigma}\left({}^t\sigma_1, {}^t\sigma_2\right) \geq 0$ – equivalent stress (homogeneous function of the first degree)
- $ {}^t\overline{\varepsilon} \geq 0$ – equivalent (plastic) strain
- $ {}^tY = {}^tY\left({}^t\overline{\varepsilon}\right) > 0$ – yield parameter controlled by a strictly increasing hardening law.

The non-zero components of the strain-rate tensor (considered fully plastic) are defined by the flow rule

$$ {}^t\dot{\varepsilon}_\alpha = {}^t\dot{\overline{\varepsilon}}\frac{\partial {}^t\overline{\sigma}}{\partial {}^t\sigma_\alpha}, \quad \alpha = 1, 2, \tag{3.28} $$

and the incompressibility constraint

$$ {}^t\dot{\varepsilon}_3 = -{}^t\dot{\varepsilon}_1 - {}^t\dot{\varepsilon}_2. \tag{3.29} $$

In order to preserve the simplicity of the formulation, we assume that region A evolves along linear strain paths defined as follows:

$$ {}^t\dot{\varepsilon}_1^{(A)} > 0, \quad {}^t\dot{\varepsilon}_2^{(A)} = \rho^{(A)} \cdot {}^t\dot{\varepsilon}_1^{(A)}, \quad -1 < \rho^{(A)} \leq 1. \tag{3.30} $$

Each strain path investigated when calculating a forming limit curve will be identified by a constant value of the parameter $\rho^{(A)}$. Eq. (3.30) automatically implies that ${}^t\dot{\varepsilon}_2^{(A)}$ has the status of a minor principal strain-rate.

As shown in Fig. 3.50, the orientation of the groove is described by the angular parameter φ. We adopt the hypothesis $0° \leq \varphi < 45°$, thus considering that the necking band is closer to the direction of the minor principal strain-rate ${}^t\dot{\varepsilon}_2^{(A)}$. In order to find a formula for the calculation of the angular parameter φ, we define a local frame associated to the groove. Its planar axes are identified by the indices $1'$ and $2'$, being oriented as in Fig. 3.50. Let

$$ {}^t\dot{\varepsilon}_{2'2'}^{(A)} = {}^t\dot{\varepsilon}_1^{(A)} \sin^2\varphi + {}^t\dot{\varepsilon}_2^{(A)} \cos^2\varphi = {}^t\dot{\varepsilon}_1^{(A)} \left[\sin^2\varphi + \rho^{(A)} \cos^2\varphi\right] \tag{3.31} $$

be the strain-rate along the necking band. If $-1 < \rho^{(A)} \leq 0$, Eq. (3.31) could be used to find a zero-extension direction. Indeed, by enforcing

$$ {}^t\dot{\varepsilon}_{2'2'}^{(A)} = {}^t\dot{\varepsilon}_1^{(A)} \left[\sin^2\varphi + \rho^{(A)} \cos^2\varphi\right] = 0, \quad -1 < \rho^{(A)} \leq 0, \tag{3.32} $$

one obtains

$$ \tan^2\varphi + \rho^{(A)} = 0, \quad -1 < \rho^{(A)} \leq 0, \tag{3.33} $$

i.e.

$$ \varphi = \arctan\sqrt{-\rho^{(A)}}, \quad -1 < \rho^{(A)} \leq 0. \tag{3.34} $$

Equation (3.34) defines the orientation of the necking band for the left branch of the forming limit curve. In fact, this formula is similar to that found by Hill for the same type of strain paths [141].

If $0 < \rho^{(A)} \leq 1$, Eq. (3.31) does not allow the existence of zero-extension directions in the plane of the sheet metal. In such cases, as in the classical M–K model, we assume that the necking band is oriented along the direction of the minor principal strain-rate ${}^t\dot{\varepsilon}_2^{(A)}$:

$$ \varphi = 0°, \quad 0 < \rho^{(A)} \leq 1. \tag{3.35} $$

Equations (3.34) and (3.35) can be unified in the general formula

$$ \varphi = \arctan\sqrt{\max\left[-\rho^{(A)}, 0\right]}, \quad -1 < \rho^{(A)} \leq 1. \tag{3.36} $$

It is easily noticeable that, for linear strain paths $\left(\rho^{(A)} = \text{const.}\right)$, Eq. (3.36) implies the constancy of the angular parameter φ.

For any load state having the property ${}^t\sigma_1 > 0$, the equivalent stress could be expressed as follows:

$$ {}^{t}\overline{\sigma} = {}^{t}\sigma_1 \cdot F\left({}^{t}\zeta\right), \quad {}^{t}\zeta = {}^{t}\sigma_2 \big/ {}^{t}\sigma_1 , \quad {}^{t}\sigma_1 > 0. \tag{3.37} $$

Equation (3.37) results from the fact that ${}^{t}\overline{\sigma}$ is a first-degree homogeneous function. The partial derivatives $\partial {}^{t}\overline{\sigma} \big/ \partial {}^{t}\sigma_\alpha$ $(\alpha = 1, 2)$ are also homogeneous functions but of zero-degree. As a consequence, they are expressible in the form

$$ \frac{\partial {}^{t}\overline{\sigma}}{\partial {}^{t}\sigma_\alpha} = G_\alpha\left({}^{t}\zeta\right), \quad {}^{t}\zeta = {}^{t}\sigma_2 \big/ {}^{t}\sigma_1, \quad {}^{t}\sigma_1 > 0, \quad \alpha = 1, 2. \tag{3.38} $$

The functions F and G_α $(\alpha = 1, 2)$ are related only to the particular formulation of the equivalent stress adopted in the model. Equations (3.37) and (3.38) lead to the following expressions of the yield criterion and flow rule (see also Eqs. (3.27) and (3.28)):

$$ {}^{t}\sigma_1 \cdot F\left({}^{t}\zeta\right) = {}^{t}Y\left({}^{t}\overline{\varepsilon}\right), \quad {}^{t}\zeta = {}^{t}\sigma_2 \big/ {}^{t}\sigma_1 , \quad {}^{t}\sigma_1 > 0, \tag{3.39} $$

$$ {}^{t}\dot{\varepsilon}_\alpha = {}^{t}\dot{\overline{\varepsilon}} \cdot G_\alpha\left({}^{t}\zeta\right), \quad {}^{t}\zeta = {}^{t}\sigma_2 \big/ {}^{t}\sigma_1, \quad {}^{t}\sigma_1 > 0, \quad \alpha = 1, 2. \tag{3.40} $$

The linear strain paths defined as in Eq. (3.30) fulfil the condition ${}^{t}\sigma_1^{(A)} > 0$. Under these circumstances, Eq. (3.40) can be applied to region A:

$$ {}^{t}\dot{\varepsilon}_\alpha^{(A)} = {}^{t}\dot{\overline{\varepsilon}}^{(A)} \cdot G_\alpha\left[{}^{t}\zeta^{(A)}\right], \quad {}^{t}\zeta^{(A)} = {}^{t}\sigma_2^{(A)} \Big/ {}^{t}\sigma_1^{(A)} , \quad {}^{t}\sigma_1^{(A)} > 0, \quad \alpha = 1, 2. \tag{3.41} $$

Equations (3.41) and (3.30) allow to obtain a relationship between $\rho^{(A)}$ and ${}^{t}\zeta^{(A)}$:

$$ G_2\left[{}^{t}\zeta^{(A)}\right] = \rho^{(A)} \cdot G_1\left[{}^{t}\zeta^{(A)}\right]. \tag{3.42} $$

It is again noticeable that, for linear strain paths $\left(\rho^{(A)} = \text{const.}\right)$, Eq. (3.42) implies the constancy of the principal stress ratio, i.e.

$$ {}^{t}\zeta^{(A)} = {}^{t}\sigma_2^{(A)} \Big/ {}^{t}\sigma_1^{(A)} = \zeta^{(A)} = \text{const.} \tag{3.43} $$

At the level of region A, Eqs. (3.39) and (3.40) can thus be written in the particular forms

$$ {}^{t}\sigma_1^{(A)} \cdot F\left[\zeta^{(A)}\right] = {}^{t}Y\left[{}^{t}\overline{\varepsilon}^{(A)}\right], \tag{3.44} $$

$$ {}^{t}\dot{\varepsilon}_\alpha^{(A)} = {}^{t}\dot{\overline{\varepsilon}}^{(A)} \cdot G_\alpha\left[\zeta^{(A)}\right], \quad \alpha = 1, 2. \tag{3.45} $$

Because the stress state in region B also fulfils the condition ${}^{t}\sigma_1^{(B)} > 0$, we can define the corresponding ratio

$$ {}^{t}\zeta^{(B)} = {}^{t}\sigma_2^{(B)} \Big/ {}^{t}\sigma_1^{(B)}, \quad {}^{t}\sigma_1^{(B)} > 0. \tag{3.46} $$

As we shall see below, ${}^t\zeta^{(B)}$ generally varies even if the strains in the non-defective zone evolve along a linear path. Due to this fact, Eqs. (3.39) and (3.40) should be written as follows when making reference to region B:

$$ {}^t\sigma_1^{(B)} \cdot F\left[{}^t\zeta^{(B)}\right] = {}^tY\left[{}^t\overline{\varepsilon}^{(B)}\right], \tag{3.47} $$

$$ {}^t\dot{\varepsilon}_\alpha^{(B)} = {}^t\dot{\overline{\varepsilon}}^{(B)} \cdot G_\alpha\left[{}^t\zeta^{(B)}\right], \quad \alpha = 1, 2. \tag{3.48} $$

As in the classical formulation of the H–N model, two sets of constraints will be enforced at the interface between the regions A and B (see Fig. 3.50):

- Continuity of the strain-rate along the necking band

$$ {}^t\dot{\varepsilon}_{2'2'}^{(A)} = {}^t\dot{\varepsilon}_{2'2'}^{(B)} \tag{3.49} $$

- Equilibrium of the normal and tangential loads acting on the interface from both sides

$$ {}^t\sigma_{1'1'}^{(A)} \cdot {}^ts^{(A)} = {}^t\sigma_{1'1'}^{(B)} \cdot {}^ts^{(B)} \tag{3.50} $$

$$ {}^t\sigma_{1'2'}^{(A)} \cdot {}^ts^{(A)} = {}^t\sigma_{1'2'}^{(B)} \cdot {}^ts^{(B)} \tag{3.51} $$

By making use of the thickness non-homogeneity parameter ${}^tf$ (see Eq. (3.24)), we write Eqs. (3.50) and (3.51) in the equivalent forms

$$ {}^t\sigma_{1'1'}^{(A)} = {}^tf \cdot {}^t\sigma_{1'1'}^{(B)} \tag{3.52} $$

$$ {}^t\sigma_{1'2'}^{(A)} = {}^tf \cdot {}^t\sigma_{1'2'}^{(B)} \tag{3.53} $$

The rotated tensor components involved in Eqs. (3.52) and (3.53) can be also expressed in terms of the principal stresses, thus obtaining

$$ {}^t\sigma_1^{(A)}\cos^2\varphi + {}^t\sigma_2^{(A)}\sin^2\varphi = {}^tf \cdot \left[{}^t\sigma_1^{(B)}\cos^2\varphi + {}^t\sigma_2^{(B)}\sin^2\varphi\right] \tag{3.54} $$

$$ \left[{}^t\sigma_1^{(A)} - {}^t\sigma_2^{(A)}\right]\sin\varphi \cdot \cos\varphi = {}^tf \cdot \left[{}^t\sigma_1^{(B)} - {}^t\sigma_2^{(B)}\right]\sin\varphi \cdot \cos\varphi \tag{3.55} $$

Because $0^\circ \leq \varphi < 45^\circ$, we are allowed to rewrite the above relationships as follows:

$$ {}^t\sigma_1^{(A)} + {}^t\sigma_2^{(A)}\tan^2\varphi = {}^tf \cdot \left[{}^t\sigma_1^{(B)} + {}^t\sigma_2^{(B)}\tan^2\varphi\right] \tag{3.56} $$

$$ \left[{}^t\sigma_1^{(A)} - {}^t\sigma_2^{(A)}\right]\tan\varphi = {}^tf \cdot \left[{}^t\sigma_1^{(B)} - {}^t\sigma_2^{(B)}\right]\tan\varphi \tag{3.57} $$

At last, with the help of the principal stress ratios associated to regions A and B (see Eqs. (3.43) and (3.46)), Eqs. (3.56) and (3.57) become

$$ {}^{t}\sigma_1^{(A)} \cdot \left[1 + \zeta^{(A)} \tan^2 \varphi\right] = {}^{t}f \cdot {}^{t}\sigma_1^{(B)} \cdot \left[1 + {}^{t}\zeta^{(B)} \tan^2 \varphi\right] \tag{3.58} $$

$$ {}^{t}\sigma_1^{(A)} \cdot \left[1 - \zeta^{(A)}\right] \tan\varphi = {}^{t}f \cdot {}^{t}\sigma_1^{(B)} \cdot \left[1 - {}^{t}\zeta^{(B)}\right] \tan\varphi \tag{3.59} $$

In general, Eq. (3.58) cannot degenerate to the trivial case $0 = 0$. Under such circumstances, it is possible to divide Eq. (3.59) by Eq. (3.58). After some simple manipulations, we obtain the following relationship between the principal stress ratios associated to regions A and B:

$$ \left[\zeta^{(A)} - {}^{t}\zeta^{(B)}\right] \sin\varphi = 0. \tag{3.60} $$

For the strain paths characterized by the condition $-1 < \rho^{(A)} < 0$, Eq. (3.36) defines an angular parameter $0° < \varphi < 45°$. In this case, Eq. (3.60) enforces ${}^{t}\zeta^{(B)} = \zeta^{(A)} = \text{const}$. The principal stress ratios associated to regions A and B are thus rigorously coincident and constant when $-1 < \rho^{(A)} < 0$.

The plane-strain path $\rho^{(A)} = 0$ needs a separate discussion, as in this case Eq. (3.36) defines an angular parameter $\varphi = 0°$ and Eq. (3.60) degenerates to the trivial form $0 = 0$. Anyhow, when $\varphi = 0°$, the local frame associated to the groove is superimposed to the plastic orthotropy frame ($1 = 1'$ and $2 = 2'$). The constraints given by Eqs. (3.32) and (3.49) now reduce to ${}^{t}\dot{\varepsilon}_2^{(A)} = {}^{t}\dot{\varepsilon}_2^{(B)} = 0$, meaning that region B evolves along the same plane-strain path and enforcing again the constancy of the principal stress ratio: ${}^{t}\zeta^{(B)} = \zeta^{(A)} = \text{const}$. We are able to conclude that

$$ {}^{t}\zeta^{(B)} = \zeta^{(A)} = \text{const.}, \quad \text{if } -1 < \rho^{(A)} \leq 0. \tag{3.61} $$

For all the strain paths characterized by the condition $0 < \rho^{(A)} \leq 1$, Eq. (3.36) defines an angular parameter $\varphi = 0°$. In this case, Eq. (3.60) also degenerates to the trivial form $0 = 0$, but Eq. (3.49) will not enforce the constancy of the stress ratio in region B as it takes the more general form ${}^{t}\dot{\varepsilon}_2^{(A)} = {}^{t}\dot{\varepsilon}_2^{(B)}$.

One may notice that, whatever is the value of the parameter $\rho^{(A)}$ in the range $-1 < \rho^{(A)} \leq 1$, the equilibrium constraint given by Eq. (3.58) reduces to

$$ {}^{t}\sigma_1^{(A)} = {}^{t}f \cdot {}^{t}\sigma_1^{(B)}, \tag{3.62} $$

due to Eqs. (3.61) and (3.36). For all the strain paths characterized by the condition $-1 < \rho^{(A)} \leq 0$, the above relationship becomes even simpler when combined with Eqs. (3.44), (3.47) and (3.61):

$$ {}^{t}Y\left[{}^{t}\overline{\varepsilon}^{(A)}\right] = {}^{t}f \cdot {}^{t}Y\left[{}^{t}\overline{\varepsilon}^{(B)}\right], \quad \text{if } -1 < \rho^{(A)} \leq 0. \tag{3.63} $$

Equation (3.63) makes redundant the second equilibrium constraint expressed by Eq. (3.59). In fact, Eq. (3.63) has been deduced using Eq. (3.61) which is a corollary of Eq. (3.59).

In the case $0 < \rho^{(A)} \leq 1$, Eqs. (3.44) and (3.47) can be exploited to reformulate Eq. (3.62) as follows:

$$ {}^{t}Y\left[{}^{t}\overline{\varepsilon}^{(A)}\right] \Big/ F\left[\zeta^{(A)}\right] = {}^{t}f \cdot {}^{t}Y\left[{}^{t}\overline{\varepsilon}^{(B)}\right] \Big/ F\left[{}^{t}\zeta^{(B)}\right], \quad \text{if } 0 < \rho^{(A)} \leq 1. \tag{3.64} $$

Again, Eq. (3.64) should not be accompanied by Eq. (3.59) because the second equilibrium constraint now degenerates to the trivial form $0 = 0$.

The strain-compatibility enforced by Eq. (3.49) also deserves a discussion. In the case $-1 < \rho^{(A)} \leq 0$, this constraint becomes trivial ($0 = 0$) and redundant due to Eqs. (3.36) and (3.61) already included in the model. For the remaining strain paths $0 < \rho^{(A)} \leq 1$, Eq. (3.49) reduces to the simpler formulation (see also Eqs. (3.35), (3.45) and (3.48))

$$ {}^{t}\dot{\overline{\varepsilon}}^{(A)} \cdot G_2\left[\zeta^{(A)}\right] = {}^{t}\dot{\overline{\varepsilon}}^{(B)} \cdot G_2\left[{}^{t}\zeta^{(B)}\right], \quad \text{if } 0 < \rho^{(A)} \leq 1. \tag{3.65} $$

Equation (3.65) is non-trivial and accompanies Eq. (3.64) in the model used to calculate the right branch of the forming limit curve.

We shall focus now on the presentation of the computational strategy. The evolution of the sheet metal up to the necking is analyzed for individual strain paths. Each of these paths is defined by a constant value of the parameter $\rho^{(A)}$ in the range $-1 < \rho^{(A)} \leq 1$. The straining process is analyzed in an incremental manner. Let $[T, T + \Delta T]$ be the discrete time interval corresponding to one of the steps performed in the analysis. All the parameters associated to the T moment are known quantities both for the non-defective area and the groove. The corresponding configuration of the sheet metal is thus taken as a reference state. In particular, the parameters associated to the moment $T = 0$ are defined by the conditions ${}^{0}\overline{\varepsilon}^{(A)} = {}^{0}\overline{\varepsilon}^{(B)} = 0$, and ${}^{0}\varepsilon_{\alpha}^{(A)} = {}^{0}\varepsilon_{\alpha}^{(B)} = 0$ ($\alpha = 1, 2$). The initial value of the thickness ratio $0 < {}^{0}f < 1$ is also prescribed. As concerns the parameters corresponding to the $T + \Delta T$ moment, they are unknown quantities and should be evaluated.

The computation is conducted by applying small increments of the equivalent strain to region A. In order to obtain sufficiently accurate results, these increments should remain small. During the numerical tests performed by the author, $\Delta\overline{\varepsilon}^{(A)} = 10^{-3} \div 10^{-4}$ has proven to be a good selection range.

Due to the fact that $\rho^{(A)}$ uniquely defines the ratio of the principal stresses in region A, the parameter $\zeta^{(A)}$ should be evaluated only once, namely at the beginning of each strain path. This task is accomplished by solving the equation (see Eqs. (3.42) and (3.43))

$$ \rho^{(A)} \cdot G_1\left[\zeta^{(A)}\right] - G_2\left[\zeta^{(A)}\right] = 0 \tag{3.66} $$

with respect to the unknown $\zeta^{(A)}$. In general, numerical procedures must be used to evaluate $\zeta^{(A)}$. During the tests performed by the author, the bisection method has worked very well, especially when combined with a bracketing strategy.

As soon as $\zeta^{(A)}$ is known, the increments of the principal strains in region A can be evaluated from Eq. (3.45) rewritten as

$$\Delta\varepsilon_\alpha^{(A)} = \left[\Delta\overline{\varepsilon}^{(A)}\right] \cdot G_\alpha \left[\zeta^{(A)}\right], \quad \alpha = 1, 2. \tag{3.67}$$

One may also notice that, for a given strain path, $\Delta\varepsilon_\alpha^{(A)}$ $(\alpha = 1, 2)$ are constant quantities and should be computed only once.

At this stage, the parameters associated to the non-defective area of the sheet metal can be updated using the formulae

$$^{T+\Delta T}\overline{\varepsilon}^{(A)} = {}^{T}\overline{\varepsilon}^{(A)} + \Delta\overline{\varepsilon}^{(A)}, \quad {}^{T+\Delta T}\varepsilon_\alpha^{(A)} = {}^{T}\varepsilon_\alpha^{(A)} + \Delta\varepsilon_\alpha^{(A)}, \quad \alpha = 1, 2. \tag{3.68}$$

We are now prepared to evaluate the groove parameters corresponding to the $T + \Delta T$ moment. If $-1 < \rho^{(A)} \leq 0$ (left branch of the forming limit curve), the principal stress ratios are the same in regions A and B (see Eq. (3.61)). In this case, only the increment of the equivalent strain $\Delta\overline{\varepsilon}^{(B)}$ should be found as a solution of Eq. (3.63) written for the $T + \Delta T$ moment:

$$^{T+\Delta T}Y\left[{}^{T+\Delta T}\overline{\varepsilon}^{(A)}\right] = {}^{T+\Delta T}f \cdot {}^{T+\Delta T}Y\left[{}^{t}\overline{\varepsilon}^{(B)} + \Delta\overline{\varepsilon}^{(B)}\right], \quad \text{if } -1 < \rho^{(A)} \leq 0, \tag{3.69}$$

where the current thickness ratio $^{T+\Delta T}f$ is expressible from Eqs. (3.24) and (3.29)

$$\begin{aligned} {}^{T+\Delta T}f = \frac{^{T+\Delta T}s^{(B)}}{^{T+\Delta T}s^{(A)}} = {}^{0}f \exp\left[{}^{T+\Delta T}\varepsilon_3^{(B)} - {}^{T+\Delta T}\varepsilon_3^{(A)}\right] = \\ {}^{0}f \exp\left[{}^{T+\Delta T}\varepsilon_1^{(A)} + {}^{T+\Delta T}\varepsilon_2^{(A)} - {}^{T}\varepsilon_1^{(B)} - {}^{T}\varepsilon_2^{(B)} - \Delta\varepsilon_1^{(B)} - \Delta\varepsilon_2^{(B)}\right] \end{aligned} \tag{3.70}$$

with $\Delta\varepsilon_\alpha^{(B)}$ $(\alpha = 1, 2)$ resulting from Eqs. (3.48) and (3.61):

$$\Delta\varepsilon_\alpha^{(B)} = \left[\Delta\overline{\varepsilon}^{(B)}\right] \cdot G_\alpha \left[\zeta^{(A)}\right], \quad \text{if } -1 < \rho^{(A)} \leq 0, \quad \alpha = 1, 2. \tag{3.71}$$

Equation (3.69) can be solved only in a numerical manner. During the tests performed by the author, the bisection method has proven excellent performances in combination with a bracketing strategy. After $\Delta\overline{\varepsilon}^{(B)}$ is determined, the increments of the principal strains in region B can be easily evaluated from Eq. (3.71).

In the case $0 < \rho^{(A)} \leq 1$ (right branch of the forming limit curve), the principal stress ratio associated to region B is no longer constant. As a consequence, two unknown quantities should be determined. They are the current principal stress ratio $^{T+\Delta T}\zeta^{(B)}$ and the increment of the equivalent strain $\Delta\overline{\varepsilon}^{(B)}$. Fortunately, the strain-rate along the necking band does not vanish if $0 < \rho^{(A)} \leq 1$. Under such circumstances, Eq. (3.65) can be put in an incremental form and used to express

$\Delta\overline{\varepsilon}^{(B)}$ as a dependency on ${}^{T+\Delta T}\zeta^{(B)}$ (see also Eq. (3.67)):

$$\Delta\overline{\varepsilon}^{(B)} = \frac{\Delta\varepsilon_2^{(A)}}{G_2\left[{}^{T+\Delta T}\zeta^{(B)}\right]}, \quad \text{if } 0 < \rho^{(A)} \leq 1. \tag{3.72}$$

$\Delta\overline{\varepsilon}^{(B)}$ given by Eq. (3.72) should be replaced in Eq. (3.64) written for the $T+\Delta T$ moment. We thus obtain

$$\begin{aligned} &{}^{T+\Delta T}Y\left[{}^{T+\Delta T}\overline{\varepsilon}^{(A)}\right] \Big/ F\left[\zeta^{(A)}\right] = \\ &\quad {}^{T+\Delta T}f \,.\, {}^{T+\Delta T}Y\left[{}^{T}\overline{\varepsilon}^{(B)} + \frac{\Delta\varepsilon_2^{(A)}}{G_2\left[{}^{T+\Delta T}\zeta^{(B)}\right]}\right] \Big/ F\left[{}^{T+\Delta T}\zeta^{(B)}\right], \quad \text{if } 0 < \rho^{(A)} \leq 1. \end{aligned} \tag{3.73}$$

The current thickness ratio ${}^{T+\Delta T}f$ is still defined by Eq. (3.70), but the principal strain increments $\Delta\varepsilon_\alpha^{(B)}$ $(\alpha = 1, 2)$ result now from a more complicated flow rule (see Eqs. (3.48) and (3.72)):

$$\Delta\varepsilon_1^{(B)} = \left[\Delta\varepsilon_2^{(A)}\right]\frac{G_1\left[{}^{T+\Delta T}\zeta^{(B)}\right]}{G_2\left[{}^{T+\Delta T}\zeta^{(B)}\right]}, \quad \Delta\varepsilon_2^{(B)} = \Delta\varepsilon_2^{(A)}, \quad \text{if } -1 < \rho^{(A)} \leq 0. \tag{3.74}$$

In conclusion, Eqs. (3.70) and (3.74) will bring Eq. (3.73) to a formulation involving only ${}^{T+\Delta T}\zeta^{(B)}$ as unknown. Again, the numerical solution can be found using the bisection method combined with a bracketing strategy. After ${}^{T+\Delta T}\zeta^{(B)}$ is determined, Eqs. (3.72) and (3.74) allow the evaluation of the increments $\Delta\overline{\varepsilon}^{(B)}$ and $\Delta\varepsilon_\alpha^{(B)}$ $(\alpha = 1, 2)$, respectively.

At this stage, the parameters associated to the defective area of the sheet metal can be updated using the formulae

$${}^{T+\Delta T}\overline{\varepsilon}^{(B)} = {}^{T}\overline{\varepsilon}^{(B)} + \Delta\overline{\varepsilon}^{(B)}, \quad {}^{T+\Delta T}\varepsilon_\alpha^{(B)} = {}^{T}\varepsilon_\alpha^{(B)} + \Delta\varepsilon_\alpha^{(B)}, \quad \alpha = 1, 2. \tag{3.75}$$

The procedures described above with reference to the left and right branches of the forming limit curve are simple and efficient. In all cases, the problem consists in solving a unique non-linear equation. At the level of region A, it is always possible to find a solution by numerical techniques. Region B needs a more careful treatment from this point of view. Generally, strains accumulate faster in the groove. As described above, the model tries to enforce the equilibrium of the tractions along the interface with the non-defective area of the sheet metal. At higher strain levels, the bearing capability of the groove can be limited by the hardening law. In such cases, it is not possible to find the solution at the level of region B. The bearing limitation can be trapped by testing the value of the equivalent strain increment $\Delta\overline{\varepsilon}^{(B)}$ during the bracketing procedure. If the search for an initial guess fails even for very large increments $\Delta\overline{\varepsilon}^{(B)}$, we can be sure that region B has already attained its bearing limit. From the mechanical point of view, this situation corresponds to the occurrence of the necking phenomenon in the groove. As a consequence, the current values of the

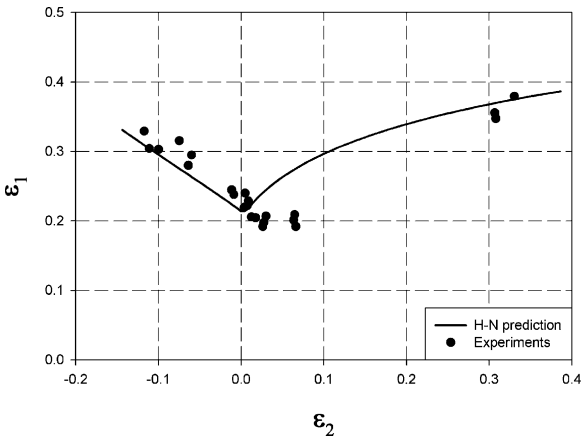

Fig. 3.51 H–N prediction versus experiments [159] for AA5182-T4 aluminium alloy

principal strains in region A should be considered as defining the limit state of the sheet metal.

The occurrence of the necking must be also checked after finding a numerical solution for the groove. Normally, the ratio $\Delta\overline{\varepsilon}^{(B)}/\Delta\overline{\varepsilon}^{(A)}$ should be tested. If this quantity becomes very large ($\Delta\overline{\varepsilon}^{(B)}/\Delta\overline{\varepsilon}^{(A)} > 100$, for example), we may conclude that the necking has been initiated. The inspection of the strain path should be stopped as the current values of the principal strains in region A define the limit state. If the ratio $\Delta\overline{\varepsilon}^{(B)}/\Delta\overline{\varepsilon}^{(A)}$ is not great enough, the computation will continue after applying a new increment of the equivalent plastic strain $\Delta\overline{\varepsilon}^{(A)}$ to region A.

Different formulations of the equivalent stress (von Mises, Hill48, Barlat89, and BBC 2005) and hardening laws (Hollomon, Swift, Voce, Ghosh, Hockett-Sherby, and AutoForm) have been implemented in the strain localization model presented above. In all cases, the numerical tests have shown a very good stability and robustness of the solution procedure. In order to validate the performances of the computational algorithm, its predictions have been compared with the experimental data corresponding both to steel and aluminium alloys [158]. As an example, Fig. 3.51 shows the comparison between the numerical results and the experimental data included in the Benchmark 1 of the NUMISHEET 2008 conference [159] for the case of the AA5182-T4 aluminium alloy.

3.4.5 Linear Perturbation Theory

Dudzinski and Molinari [145] proposed the use of the linearized theory of stability in order to determine the limit strains. Boudeau [160] has used this theory for calculating the FLC's. Localized necking is considered in this analysis as a local instability problem associated with local equilibrium equations and cotitutive equations of the material for a given state of strain and stress.

3.4.6 Modified Maximum Force Criterion (MMFC)

The 'Modified Maximum Force Criterion' (MMFC) for diffuse necking proposed by Hora et al. [142] is based on Considère's maximum force criterion. The idea behind the MMFC-Model is to factor in an additional increase in hardening, which is triggered by the deviation from the initial, homogeneous stress condition—e.g. uniaxial tension—to the stress condition of local necking and with this to the point of plane strain (Fig. 3.52) [161].
The mathematical expression of the criterion is:

$$\frac{\partial \sigma_{11}}{\partial \varepsilon_{11}} + \frac{\partial \sigma_{11}}{\partial \beta} \frac{\partial \beta}{\partial \varepsilon_{11}} = \sigma_{11} \tag{3.76}$$

Herein, β represents the strain rate ratio given by

$$\beta = \frac{\dot{\varepsilon}_{22}}{\dot{\varepsilon}_{11}} \tag{3.77}$$

The MMFC model will be written ina form independent of the yield criterion, i.e. it can accommodate any yield criterion. According to Hora et al. [142] the following relations are defined:

$$\alpha = \frac{\sigma_{22}}{\sigma_{11}}, \quad \bar{\sigma} = \frac{\sigma_{11}}{f(\alpha)}, \quad \bar{\varepsilon} = g(\beta)\, \varepsilon_{11}. \tag{3.78}$$

The stress ratio α takes the values $0 \leq \alpha \leq 1$, i.e. it ranges from uniaxial tension ($\alpha = 0$) to equibiaxial tension ($\alpha = 1$). $\bar{\sigma}$ is the equivalent stress defined by the yield criterion which is utilized in the necking analysis, see below. $\bar{\varepsilon}$ is the equivalent plastic strain.

$$g(\alpha) = f(\alpha)\,[1 + \alpha \cdot \beta(\alpha)] \tag{3.79}$$

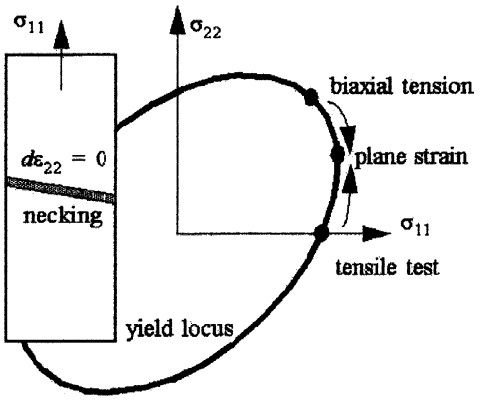

Fig. 3.52 Basic principle of the MMFC criterion [161]

The function $f(\alpha)$ is obtained from:

$$f(\alpha) = \frac{1}{\bar{\sigma}\,(\sigma_{11} = 1, \sigma_{22} = \alpha)} \tag{3.80}$$

Assuming the instantaneous yield stress is represented by the Swift hardening law Hora's necking criterion then reads [142]

$$Y'(\bar{\varepsilon}) \cdot f(\alpha) \cdot g(\alpha) - Y(\bar{\varepsilon}) \cdot \frac{f'(\alpha) \cdot g(\alpha) \cdot \beta(\alpha)}{\beta'(\alpha)\bar{\varepsilon}} = f(\alpha)\, Y(\bar{\varepsilon}) \tag{3.81}$$

with $\beta' = d\beta/d\alpha$, $f' = df/d\alpha$, $Y' = dY/d\bar{\varepsilon}$.

The primary unknown variable $\bar{\varepsilon}$ can easily be calculated as the root of the necking criterion given in Eq. (3.81) (which is, in general, a non-linear equation) by means of Newton's method. Once the equivalent plastic strain at the onset of necking for a chosen linear strain path is calculated from Eq. (3.81) the major and minor plastic in-plane strains corresponding to the onset of necking are found from

$$\varepsilon_{11}^{*} = \frac{\bar{\varepsilon}^{*}}{g}, \quad \varepsilon_{22}^{*} = \beta \cdot \varepsilon_{11}^{*} \tag{3.82}$$

$\bar{\varepsilon}^{*}$ is the root of the necking criterion Eq. (3.81).

In order to take into account the influence of the thickness on the limit strains, an enhanced MMFC (eMMFC) has been proposed recently by Hora and his co-workers [162]. A term is added to the original formulation (3.76). The eMMFC is expressed as

$$\frac{\partial \sigma_{11}}{\partial \varepsilon_{11}} \left[1 + \frac{t}{2r} + e(E,t)\right] + \frac{\partial \sigma_{11}}{\partial \beta} \frac{\partial \beta}{\partial \varepsilon_{11}} \geq \sigma_{11} \tag{3.83}$$

where, t is the thickness, r is the sheet curvature radius and $e(t, E = \text{const}) = E_0 \left(\frac{t}{t_0}\right)^p$ represent the influence of the thickness. The parameters E_0, p and t_0 are determining using experimental data [161].

Banabic and Soare [163] make more precise statements about the nature of the numerical instability of the MMFC model, asses the predictive capabilities of the criterion, and introduce a fitting parameter for its plane strain calibration. In order to improve the prediction of limit strains using MMFC model, Paraianu et al. [164] chose to introduce two fitting coefficients in the original model.

The advantage of the MMFC criteria can be found in their independence of the inhomogeneity assumption. This criterion could be used to calculate FLC for non-linear strain path. A drawback of the MMFC models is the fact that it contains a singularity that emerges if the yield locus contains straight line segments, like Barlat 2000 or BBC 2005, respectively [165]. Comsa and Banabic [166] removed this limitation of the MMFC criterion by modifying the initial formulation. As an

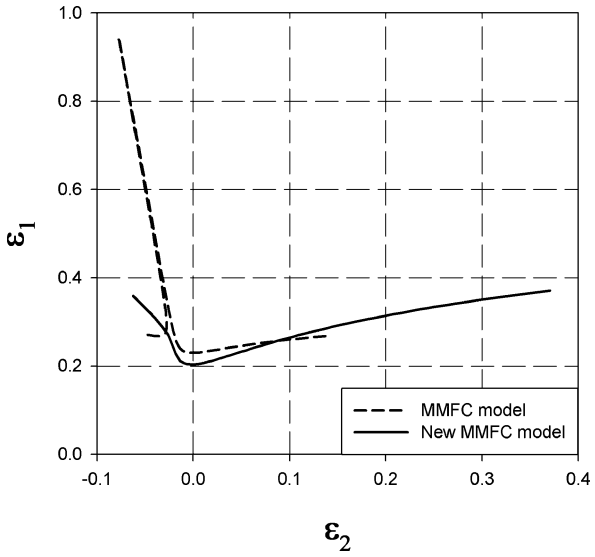

Fig. 3.53 FLC of the AA2090-T3 aluminium alloy predicted by classic and new MMFC models

example, the singularity noticed by Aretz [165] in the case of the AA2090-T3 aluminum alloy is no more present when using the new formulation proposed in [166] (see Fig. 3.53).

3.5 Commercial Programs for FLC Prediction

Based on the above mentioned models have been developed more commercial programs for the limit strains prediction.

Hora and his co-workers (http://www.forminnotech.ethz.com) have developed MATFORM code based on the MMFC model [142, 161, 162]. This code is able to calculate and plot the limit strains and also the visualization of the strain hardening curve and yield loci using Hill 1948, Hill 1979, Hill 1990 and Barlat 1989 criteria. The program is useful for evaluation of most common experiments like tensile, bulge, Miauchi, torsion dilatometer and tube hydroforming tests. The program is very well documented and is able to export the constitutive models in FEM specific form for the application in the mostly spread FEM-codes like AutoForm or PamStamp.

Using the CRACH algorithm (based on the Marciniak–Kuczynski model), Gese and Dell [167] have developed two software: CrachLAB, a product for prediction of the initial FLC and CrachFEM a product for coupling with the FEM codes. Criteria for ductile and shear fracture have been included in CrachFEM to cover the whole variety of fracture modes for sheet materials. The material model used to calculate instability describes: the initial anisotropy (using Hill 1948 criterion), the combined isotropic-kinematic hardening and the strain rate sensitivity. CrachFEM is now included in the FEM codes PamStamp and PamCrash of ESI Group.

3.5.1 FORM-CERT Program

Based on a Marciniak–Kuckzynski model, Jurco and Banabic [168–170] have developed so-called FORM-CERT commercial code. The BBC 2005 yield criterion is implemented in this model. This yield criterion can be reduced to simpler formulations (Hill 1948, Hill 1979, Barlat 1989, etc). In this way, the yield criterion can be also used in the situations when only 2, 4, 5, 6, or 7 mechanical constants are available. The program consists in four modules: a graphical interface for input, a module for the identification and visualization of the yield surfaces, of the strain hardening laws and a module for calculating and visualizing the forming limit curves. The numerical results can be compared with experimental data, using the import/export facilities included in the program. FORM-CERT can be used as a standalone application for calculating FLC's and comparing them with experimental data, or as an auxiliary tool for the finite-element simulation of sheet metal forming processes. In its current structure, the program offers useful functionalities both for research and industrial laboratories. A short description of this program will be presented in the next sections.

The program FORM-CERT developed in the CERTETA research centre consists in the following modules:

- Identification module associated to the yield criterion (responsible for evaluating the coefficients of the yield criterion, as well as for the graphical output of the yield locus and planar distribution of the yield stress and *r*-coefficient)
- Module for calculating and displaying the strain hardening law
- Module for calculating and displaying the forming limit diagram.

Figure 3.54 shows a structural diagram of the program. This diagram presents the modules mentioned above, as well as their interaction. We shall describe next the functionality of each module.

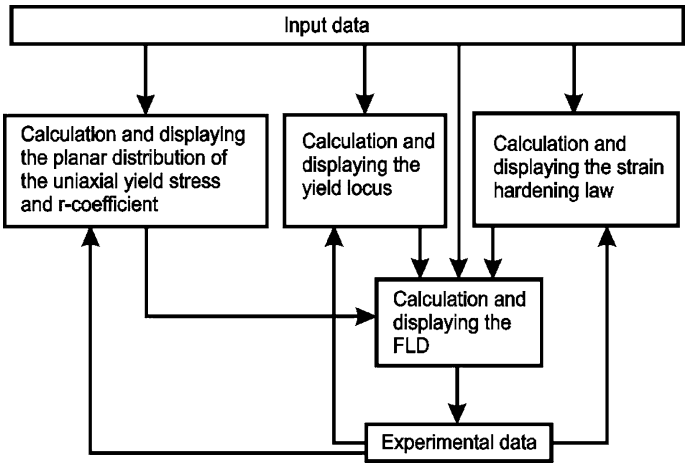

Fig. 3.54 Structure of the FORM-CERT program

3.5.1.1 Identification Module Associated to the Yield Criterion

The yield surface is described in a general manner using the BBC 2005 yield criterion [2.53]. The BBC 2005 yield criterion can be reduced to simpler formulations (Hill 1948, Barlat 1989, etc.) by enforcing equalities between some of its coefficients (see Sect. 2.5.3). In this way, the general yield criterion can be also used in the situations when only 2, 4, 5, 6, or 7 mechanical constants are available. The performances of the BBC 2005 yield criterion for different identification strategies have been evaluated and presented in [171, 172]. Figure 3.55 shows the user graphical interface of this module. Here is the place where the user can choose the identification strategy by specifying the number of mechanical parameters available for input. The input boxes can be filled from keyboard but the program also offers the possibility to import data from an ASCII file. The module performs the identification, displays the values of the coefficients and stores them into an ASCII output file. Optionally, the values of the coefficients can be passed to the FLC calculation module.

The identification module also offers the possibility to plot the computed yield locus. Different yield loci obtained from different identification strategies (with more or less coefficients) can be superimposed on the same diagram. A separate panel of the graphical interface ('Experimental data') can be accessed for importing experimental points from ASCII files. This data is also shown on the same diagram. In this way, the user has the possibility to evaluate the performances of the

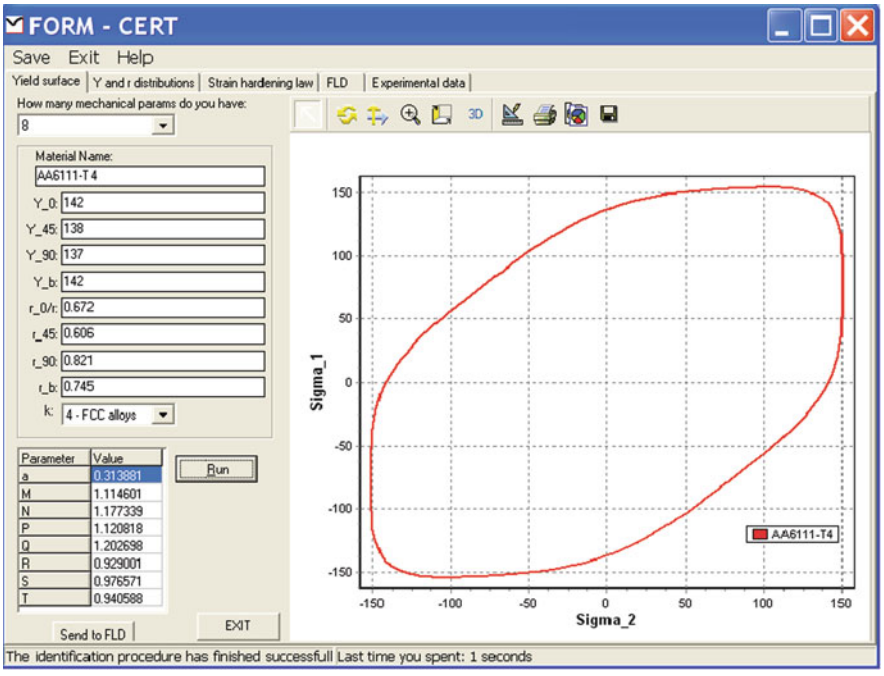

Fig. 3.55 Graphical user interface of the identification module

yield criterion in different identification cases and to select the best formulation. The identification module also allows studying the sensitivity of the yield locus to the variation of the input data.

3.5.1.2 Calculation and Displaying the Planar Distribution of the Uniaxial Yield Stress and *r*-Coefficient

As it is well known (see Chap. 2), the knowledge of the yield locus is not sufficient for evaluating the performances of a yield criterion. The planar distribution of the uniaxial yield stress and *r*-coefficient offers useful information related to this aspect. The accuracy of the constitutive models is strongly dependent on their capability to describe such variations. In fact, the residual stresses, the springback and the thickness distribution obtained from FE calculation is closely connected to the performances of the yield criterion. As a consequence, the program developed by the authors includes a module that computes and displays the distribution of the uniaxial yield stress and *r*-coefficient in the plane of the sheet metal (see Fig. 3.56). Of course, the diagrams are calculated using the type of the yield criterion selected in the identification module. A detailed description of the computational procedure is given in Ref. [53] from Chapter 2. Again, experimental points can be superimposed on the same diagram by accessing the panel 'Experimental data'. The module also offers the possibility to perform a sensitivity analysis of the curves to the variation of the input data (coefficients of the yield criterion).

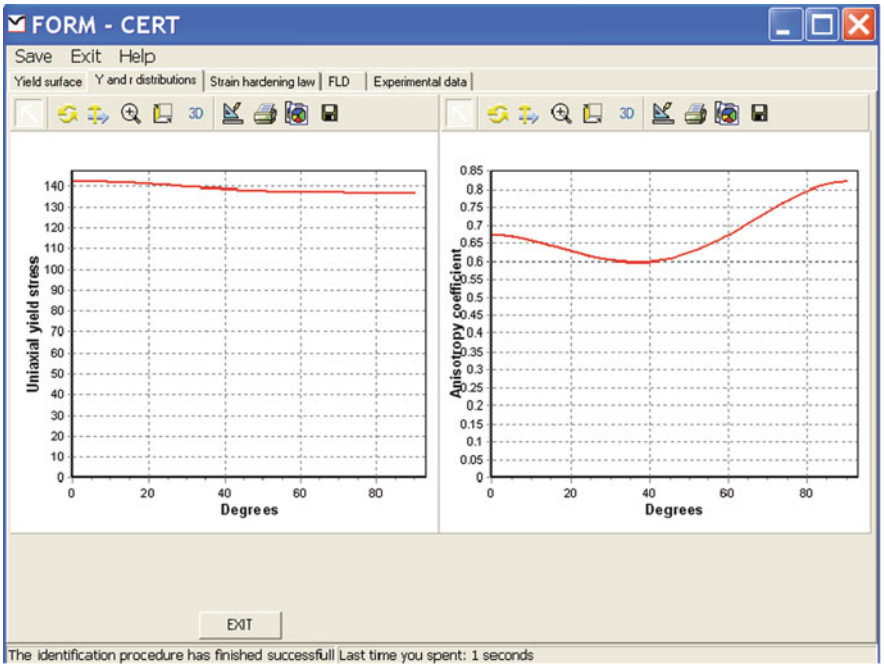

Fig. 3.56 Graphical user interface of the module used for displaying uniaxial yield stresses and *r*-coefficient distributions

3.5.1.3 Calculation and Displaying the Strain Hardening Law

A separate module of the program has been developed for calculating and displaying to types of hardening laws: Swift and Voce, respectively.

The expression of the hardening laws are as follows:

- Swift:

$$Y(\bar{\varepsilon}^p) = K(\bar{\varepsilon}^0 + \bar{\varepsilon}^p)^n \tag{3.84}$$

- Voce:

$$Y(\bar{\varepsilon}^p) = B - (B - A)e^{(-m\bar{\varepsilon}^p)} \tag{3.85}$$

In Eqs. (3.84) and (3.85), K, n, $\bar{\varepsilon}^0$, B, A and m are material parameters. In these formulations, Y is chosen to be the uniaxial yield stress associated to the rolling direction.

The graphical interface allows the user to choose the type of the hardening law and plots the associated curve (see Fig. 3.57). The predictions offered by different hardening laws can be superimposed on the same graph and also compared with experimental data (acquired via the 'Experimental data' panel). This module offers the possibility to adopt the most accurate hardening law.

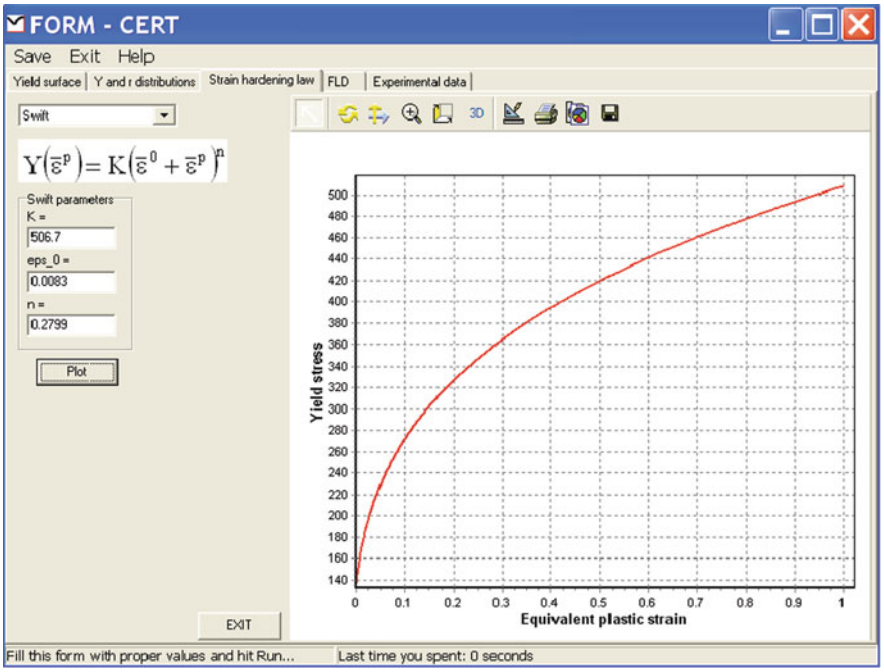

Fig. 3.57 Graphical user interface of the module used for calculating and displaying the strain hardening rule

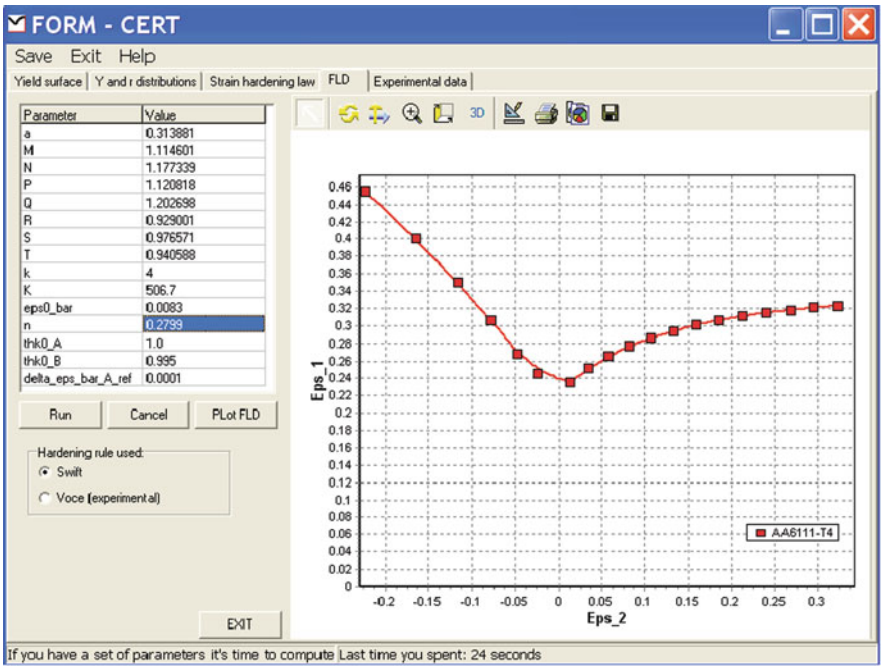

Fig. 3.58 Graphical user interface of the FLD module

3.5.1.4 Calculation and Displaying the FLC

This is the main module of the program. The Hutchinson-Neale model (see Sect. 3.4.4) of the strain localization process has been implemented in the FORM-CERT program.

The graphical user interface provided by this module is divided in two regions (Fig. 3.58). The first one receives the input data: coefficients of the yield criterion and strain hardening law calculated by the modules mentioned bellow, a parameter specifying the thickness non-homogeneity factor and also the value of the strain increment used for computing the FLC.

At present, the FLD module works only for linear strain paths. The second region of the graphical user interface is used for plotting the FLC predicted. Several curves can be superimposed on the same diagram and also compared with experimental data (imported from ASCII files via the 'Experimental data' panel).

3.5.1.5 'Experimental Data' Module

This module is structured as a panel for acquiring input data (Fig. 3.59). The user has the possibility to type this data or to import it from ASCII files. The data can be plotted on diagrams or exported to other modules of the FORM-CERT

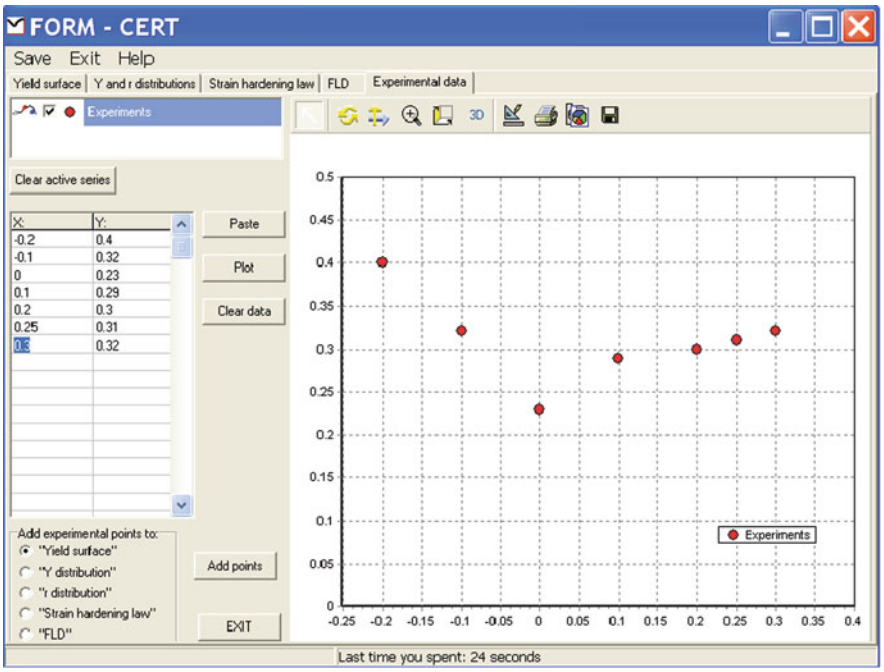

Fig. 3.59 Graphical user interface of the 'experimental data' module

program. All the diagrams generated by the modules mentioned above can be processed and also exported in different graphical formats (Bitmap, Windows Metafile, GIF, JPEG, Postscript, PDF, etc.). In addition, the results of the computations can be exported in a numerical format (via ASCII, XML, Excel, and HTML files).

3.6 Semi-empirical Models

Despite all the recent enhancements of the computational models (see Sect. 3.4), they are not able to give very accurate predictions of the limit strains in all the cases encountered in practical applications (different materials, thickness, forming rates, temperatures, strain paths, etc.). Due to this fact, the commercial finite-element codes still make use of experimental FLD's or FLD's calculated with semi-empirical models. Some of the widely-used semi-empirical models will be presented next.

Keeler and Brazier [104] proposed an empirical relationship for calculating the limit strains corresponding to plane strain, ε_{10}:

$$\varepsilon_{10}(\%) = (23.3 + 14.13 \cdot t)\,\frac{n}{0.21} \tag{3.86}$$

where t is the sheet thickness ($t \leq 3$ mm).

Assuming that the shape of the FLD remains the same and having determined the value of ε_{10}, it is possible to obtain the FLD by translating the Keeler–Goodwin curve along the vertical coordinate axis.

Cayssials [173, 174] developed the Keeler–Brazier model by including both the coefficient of strain-rate sensitivity m and the 'internal damage' parameters. The limit strain is the solution of the equation

$$a\,(\varepsilon_{10} - n)^3 + b\,(\varepsilon_{10} - n)^2 + c\,(\varepsilon_{10} - n) - 10 \cdot mt = 0 \tag{3.87}$$

where *a, b* and *c* are material constants. As a first approximation, ε_{10} can be expressed as follows:

$$\varepsilon_{10} = n + 5mt \tag{3.88}$$

Cayssials and Lemoine [175] have extended the formulation (3.87) by including the anisotropy coefficient and has been obtained:

$$a(\varepsilon_{10} - n)^3 + b(\varepsilon_{10} - n)^2 + c(\varepsilon_{10} - n) - -14\frac{\sqrt{(2+4r)}}{\sqrt{(r+1)(r+2)}}mt = 0 \tag{3.89}$$

where, r is the anisotropy coefficient.

More, by coupling the former model with the Stören and Rice model [144] has been possible the extension of the new model also for drawing and stretching areas. So, the new model is able to predict the FLC for the complete domain, both for linear and non-linear strain paths, using only the mechanical parameters (yield stress, strain hardening coefficient, strain rate sensitivity index and anisotropy coefficient) and thickness of the material. The results obtained are in very good agreement with the experimental data for new grades of steel alloys (UHSS, DP, TRIP etc.) [175].

References

1. Eary DF (1974) Techniques of press working sheet metals. Prentice Hall, London
2. Dieter GE, Kuhn HA, Semiatin SL (2003) Handbook of workability and process design. ASM International, Metals Park, OH
3. Kumpulainen J (1984) Factors limiting the formability of sheet metals. PhD Thesis, Helsiki University of Technology, Helsinki
4. Marciniak Z (1965) Stability of plastic shells under tension with kinematic boundary condition. Archiwum Mechaniki Stosorwanej 17:577–592
5. Marciniak Z (1971) Limits of metal sheets formability. WNT, Warsaw (in Polish)
6. Marciniak Z (1978) Sheet metal forming limits. In: Koistinen DP, Wang NM (eds) Mechanics of sheet metal forming. Plenum Press, New York/London, 215–235
7. Marciniak Z (1984) Assessment of material formability. In: Advanced Technology of Plasticity. Proceeding of the 2nd ICTP, Tokyo, 685–694
8. Marciniak Z, Duncan JL, Hu SJ (2002) Mechanics of sheet metal forming. Butterworth-Heinemann, Oxford
9. Cockroft MG, Latham DJ (1968) Ductility and the workability of metals. Journal of the Institute of Metals 96:33–39

10. Banabic D, Dörr RI (1992) Formability of thin sheet metals. OIDICM, Bucharest (in Romanian)
11. Pearce R (1978) Sheet metal testing – From the 19th century until now. Proceedings of the Biennial Congress of the IDDRG, Warwick, 355–362
12. Pearce R (1982) 4000 Years of sheet metal forming. In: Newby JR, Niemeier BA (eds) Formability of metallic materials 2000 AD, ASTM, Chicago, 3–18
13. Siebel E, Beisswanger H (1955) Deep-drawing. Carl Hanser, München (in German)
14. Considere A (1985) Application of iron and steel in constructions. Annales des Ponts et Chaussees 9:574–575 (in French)
15. Erichsen AM (1914) A new test for thin sheets. Stahl und Eisen 34:879–882 (in German)
16. Pomey G (1976) Formability of thin sheet, Vols 1–3, Collection I.R.S.I.D.-O.T.U.A, Paris (in French)
17. Averkiev AI (1985) Formability methods for metal sheets. Masinostroenie, Moscow (in Russian)
18. Banabic D, Dörr RI (1995) Modeling of the sheet metal forming. Transilvania Press, Cluj Napoca (in Romanian)
19. Banabic D et al. (2000) Formability of metallic materials. Springer, Heidelberg
20. Col A (2000) Forming limit diagrams: A survey. In: Banabic D (ed) Proceedings of the Cold Metal Forming Conference, Printek, Cluj Napoca, 100–118
21. Ghosh AK, Hecker SS, Keeler SP (1985) Sheet metal forming and testing. In: Dieter FE (ed) Workability testing technique. ASM, Metals Park, OH, 135–195
22. Hayashi H (1997) Co-operative research on forming limit diagram in JDDRG. IDDRG WG Meeting, Haugesund
23. Hasek V (1973) On the strain and stress states in drawing of large un-regular sheet metal components. Berichte aus dem Institut für Umformtechnik, Universität Stuttgart, Nr. 25, Girardet, Essen (in German)
24. Miles M (2006) Formability testing of sheet metals. In: Semiatin SL (ed) ASM handbook, Vol 14B, Metalworking: Sheet metal. ASM International, Materials Park, OH, 673–698
25. Narashimhan K, Nandedkar VM (1996) Formability testing of sheet metals. Transactions of the Indian Institute of Metals 49:659–676
26. Parniere P, Sanz G (1976) Formability of thin sheet. In: Baudelet B (ed) Metal forming of the metals and alloys. Editions CNRS, Paris, 305–330 (in French)
27. Petrasch W (1951) Deep-drawing test by impact. Mitt. Forsch.-ges. Blechbearbeitung, 209–211 (in German)
28. Pöhlandt K (1989) Materials testing for the metal forming industry. Springer, Heidelberg
29. Pomey G, Parniere P (1980) Formability of thin sheet. Techniques de l'ingenieur, M 695:1–16, M 696:1–19 (in French)
30. Ragupathi RS (1985) Sheet metal properties and testing methods. In: Lange K (ed) Handbook of metal forming. SME, Dearborn, MI
31. Taylor B (1988) Evaluation of formability for secondary (sheet) forming. In: Semiatin SL (ed) Metals handbook, Vol 14, Forming and forging, 9th edn. ASM, Metals Park, OH, 877–900
32. Xu Y (2006) Modern formability. Measurement, analysis and applications. Hanser Gardner Publications, Cincinnati, OH
33. Esser H, Arend H (1940) Anz. Machinenwesen 87:140–144
34. Kaftanoglu B, Alexander JM (1961–62) An investigation of the Erichsen test. Journal of the Institute of Metals 90:457–470
35. Kayseler H (1934) On the proprieties of sheet steels. Mitt. Forsch. 2:39–42 (in German)
36. Kokkonen V, Hygren G (1959) Investigation into the accuracy of the Erichsen cupping test. Sheet Metal Industries 36:167–178
37. Yokai M, Alexander JM (1967) A further investigation of the Erichsen test. Sheet Metal Industries 44:466–475

38. Olsen TY (1920) Machines for ductility testing. Proceedings of the American Society for Testing and Materials 20:398–403
39. Hecker SS (1974) A cup test for assessing stretchability. Metals Engineering Quarterly 14:30–36
40. Ghosh AK (1975) The effect of lateral drawing-in on stretch formability. Metals Engineering Quarterly 15:53–64
41. Jovignot C (1930) Method and testing device for the study the fracture of the sheet metals (in French). Revue de Metallurgie 27:287–291
42. Siebel E, Pomp A (1929) A new test for thin sheets. Mitt. K.W.I. 11:287–291 (in German)
43. Sachs G (1930) A new testing device for deep-drawing. Metallwirtschaft 9:213–218 (in German)
44. Loxley EM, Swift HW (1945) The wedge drawing test. Engineering 159:38–40, 77–80, 136–138
45. Guyot J (1962) Deep-drawability of thin sheets. Dunod, Paris (in French)
46. Chung SY, Swift HW (1951) Cup-drawing from a flat blank. Proceedings of the Institution of Mechanical Engineers 165:199–223
47. Swift HW (1954) The mechanism of a simple drawing operation. Engineering 178:431–435
48. Swift HW (1954) The mechanism of a simple deep-drawing operation. Sheet Metal Industries 31:817–828
49. Willis J (1954) Deep-drawing: A review of the practical aspects of professor H. W. Swift's researches. Butterworths Scientific Publications, London
50. Fukui S, Yoshida K, Abe K (1960) Correlation among experimental values obtained in various formability tests. Scientific Papers of the Institute of Physical and Chemical Research 54:199–205
51. Yoshida K (1959) Classification and systematization of sheet-metal press-forming process. Scientific Papers of the Institute of Physical and Chemical Research 53:126–187
52. Yoshida K, Hayashi Y (1979) Developments in research into sheet-metal forming process in Japan. Sheet Metal Industries 55:14–17, 56:261–270
53. Sachs G (1934) Sheet metal testing with the Erichsen device. Metallwirthschaft 13:78–91 (in German)
54. Eisenkolb F (1932) Research on the assessment of the formability of thin sheets. Stahl und Eisen 52:357–364 (in German)
55. Eisenkolb F (1949) Testing of thin sheets. Stanzereischriften 5 (in German)
56. Engelhardt W (1961) Development and first evaluation of a new method for testing deep-drawability. PhD Thesis, TU Dresden (in German)
57. Drewes EJ et al. (1972) Forming limit diagrams and application to actual press forming. IDDRG Meeting Group 1, Amsterdam
58. Miles MP, Siles JL, Wagoner RH, Narasimhan K (1993) A better formability test. Metallurgical Transactions 24A:1143–1151
59. Keeler SP (1961) Plastic instability and fracture in sheet stretched over rigid punches, PhD Thesis, Massachusetts Institute of Technology, Boston
60. Gensamer M (1946) Strength and ductility. Transactions of the American Society for Metals 36:30–60
61. Keeler SP, Backofen WA (1963) Plastic instability and fracture in sheets stretched over rigid punches. Transactions of the American Society for Metals 56:25–48
62. Goodwin GM (1968) Application of strain analysis to sheet metal forming problems in the press shop. Society of Automotive Engineers No. 680093, 380–387
63. Havranek B (1977) The effect of mechanical properties on wrinkling in conical shells. Journal of Mechanical Working Technology 1:115–129
64. Arrieux R (1981) Contribution to the determination of forming limit curves of titanium and aluminum. Proposal of an intrinsic criterion. PhD Thesis, INSA, Lyon (in French)
65. Simha CHM, Gholipour J, Bardelcik A, Worswick MJ (2007) Prediction of necking in tubular hydroforming using an extended stress-based FLC. ASME Journal of Engineering Materials and Technology 129:136–147

66. Simha CHM, Grantab R, Worswick MJ (2007) Computational analysis of stress-based forming limit curves. International Journal of Solids and Structures 44:8663–8684
67. Janssens K, Lambert F, Vanrostenberghe S, Vermeulen M (2001) Statistical evaluation of the uncertainty of experimentally characterised forming limits of sheet steel. Journal of Materials Processing Technology 112:174–184
68. Brozzo P, De Luca B, Rendina R (1972) A new method for the prediction of the formability limits of metal sheets. Proceedings of the 7th Biannual Congress of the IDDRG, Amsterdam
69. Hecker S (1972) A simple forming limit curve technique and results on aluminum alloys. Proceedings of the IDDRG Congress, Amsterdam, 5.1–5.8
70. Nakazima K, Kikuma T (1967) Forming limits under biaxial stretching of sheet metals. Testu-to Hagane 53:455–458 (in Japanese)
71. Nakazima K, Kikuma T, Hasuka K (1971) Study on the formability of steel sheets. Yawata Technical Report No. 284, 678–680
72. ISO 12004 (2006) Metallic materials. Sheet and strip. Determination of the forming limit curves. Part 2: Determination of forming-limit curves in the laboratory. ISO, Geneva
73. Hasek V (1978) Research and theoretical description concerning the influences on the FLDs. Blech Rohre Profile 25:213–220, 285–292, 493–499, 617–627 (in German)
74. Montfort G (1997) Summary of experimental FLD work. BDDRG Working Group Report, Haugesund
75. Novello F, Montfort G (1999) Summary of experimental FLD work-BDDRG working group, IDDRG Meeting, WGIII, Birmingham, 3.1–3.14
76. Col A (2005) Forming limit curves: Are we at a turn? In: Boudeau N (ed) Proceedings of the 24th IDDRG Congress, University of Franche Comte, Besancon, 25.1–25.10
77. Geoffrey JL (2003) Standardization of forming limit curves. IDDRG Conference, Bled
78. Hotz W (2006) European efforts in standardization of FLC. In: Hora P (ed) Numerical and experimental methods in prediction of forming limits in sheet forming and tube hydroforming processes. ETH Zürich, Zürich, 24–25
79. Hotz W, Timm J, Keller S (2001) Measurement of forming limit diagrams: Activities regarding the harmonization in the aluminum industry. IDDRG German Group Meeting, Düsseldorf
80. Hora P, Tong L (2006) Prediction of forming limits in virtual sheet metal forming-yesterday, today and tomorrow. In: Hora P (ed) Numerical and experimental methods in prediction of forming limits in sheet forming and tube hydroforming processes. ETH Zürich, Zürich, 8–17
81. Till ET (2001) Parameters affecting forming limits in steel sheet. Nr. 575, VDI Verlag, Düsseldorf (in German)
82. Till ET, Walch C, Pauli H (2006) A note on forming limits and forming limit stress diagrams. In: Santos AD, Barata da Rocha A (eds) Proceedings of the 25th IDDRG Congress, Porto, 11–18
83. Takashina K et al. (1968) Relation between the manufacturing conditions and the average strain according to the scribed circle tests in steel sheets. La Metallurgia Italiana 8:757–765
84. Veerman C et al. (1971) Determination of appearing and admissible strains in cold-reduced sheets. Sheet Metal Industries 687–694
85. Veerman C, Neve PF (1972) Some aspects of the determination of the FLD-onset of localized necking. Sheet Metal Industries 421–423
86. Bragard A, Baret JC, Bonnarens H (1972) A simplified technique to determine the FLD at onset of necking. Centre for Research in Metallurgy 33:53–63
87. d'Hayer R, Bragard A (1975) Determination of the limiting strains at the onset of necking. Centre for Research in Metallurgy 42:33–35
88. Hecker SS (1975) Simple technique for determining forming limit curves. Sheet Metal Industries 52:671–676
89. Kobayashi T, Ishigaki H, Tadayuki A (1972) Effect of strain ratios on the deforming limit of steel sheet and its application to the actual press forming. Proceedings of the IDDRG Congress, Amsterdam, 8.1–8.4

90. ∗∗∗ (1983) Methods of determining the forming limit curve. Proceedings of the IDDRG WG III Meeting, Zurich
91. Marron G et al. (1997) A new necking criterion for the forming limit diagrams, Proceedings of the IDDRG 1997 WG Meeting, Haugesund
92. Volk W (2006) New experimental and numerical approach in the evaluation of the FLD with the FE-method. In: Hora P (ed) Numerical and experimental methods in prediction of forming limits in sheet forming and tube hydroforming processes. ETH Zürich, Zürich, 26–30
93. Liebertz H et al. (2004) Guideline for the determination of forming limit curves. Proceedings of the IDDRG Conference, Sindelfilgen, 216–224
94. Lewison DJ, Lee D (1999) Determination of forming limits by digital image processing methods. Proceedings of International Body Engineering Conference and Exposition (IBEC), Detroit, MI (Paper 01–3168)
95. Brunet M, Morestin F (2001) Experimental and analytical necking studies of anisotropic sheet metals. Journal of Materials Processing Technology 112:214–216
96. Schatz M, Keller S, Feldmann P (2005) Experimental determination of the FLD for sheet thickness from 2.5 to 5.0 mm. UTF Science III:1–8 (in German)
97. Feldmann P, Schatz M (2006) Effective evaluation of FLC-tests with the optical in-process strain analysis system AUTOGRID. In: Hora P (ed) Numerical and experimental methods in prediction of forming limits in sheet forming and tube hydroforming processes. ETH Zürich, Zürich, 69–73
98. Friebe H et al. (2006) FLC determination and forming analysis by optical measurement system. In: Hora P (ed) Numerical and experimental methods in prediction of forming limits in sheet forming and tube hydroforming processes. ETH Zürich, Zürich, 74–81
99. Haberfield AB, Boyles MW (1973) Laboratory determined the FLC of sheet steel. Sheet Metal Industries 50:400–411
100. Romano G, Rault D, Entringer M (1976) Utilization des courbes limites de formage et du mode de repartition des deformations comme critere de jugement de l'amptitude d'un acier extradoux a l'emboutissage. Mem. Sci. Rev. Mettalurgie 73:372–383
101. Hiam J, Lee A (1978) Factors influencing the FLC of sheet steel. Sheet Metal Industries 50:400–411
102. Kleemola HJ, Kumpulainen JO (1980) Factors influencing the FLD. Influence of sheet thickness. Journal of Mechanical Working Technologies 3:303–311
103. Fukui Y, Nakanishi K (1988) Effects of sheet thickness on the in-plane sterch forming limit in an aluminium sheet. JSME International Journal 31:679–685
104. Keeler SP, Brazier WG (1975) Relationship between laboratory material characterization and press-shop formability. Proceedings of the Micro alloying Conference, New York, NY, 21–32
105. Grumbach M, Sanz G (1972) Influence of various parameters on forming limit curves. Revue de Metallurgie 61:273–290 (in French)
106. Kikuma T, Nakazima K (1971) Aspects of deforming conditions and mechanical properties in the stretch forming limits of sheet metals. Transactions of the Iron and Steel Institute of Japan 11:827–830
107. Woodthorpe J, Pearce R (1970) The effect of the r and n upon the FLD of sheet steel. Proceedings of the ICSTIS Conference, Tokyo, 822–827
108. Pearce R (1971) A user guide to FLD. Sheet Metal Industries 48:943–949
109. Conrad H, Demeri MY, Bhatt D (1978) Effects of material parameters including strain-rate sensitivity of the flow stress on the stretch formability of sheet metal. In: Hecker SS, Ghosh AK, Gegel HL (eds) Formability: Analysis modeling and experimentation. Metal Society of AIME, New York, NY, 208–231
110. Rault D (1976) Description of the deep-drawing end connected problems (in French). In: Baudelet B (ed) Metal forming of the metals and alloys. CNRS, Paris, 297–303

111. Ghosh AK, Hecker SS (1975) Stretching limits in sheet metals: In-plane versus out-of-plane deformations. Metallurgical Transactions 5A:2161–2164
112. Charpentier PL (1975) Influence of the punch curvature on the stretching limits of sheet steel. Metallurgical Transactions 6A:1665–1669
113. Shi MF, Gerdeen JC (1991) Effect of strain gradient and curvature on forming limit diagrams for anisotropic sheets. Journal Material Shaping Technology 9:253–268
114. Lange E (1975) Die Bedeutung von Kennwerten und Verfahren zur Beurteilung des Umformverhaltens beim Tiefziehen von Feinblechen (I). Baender Blech Rohre 5:511–514
115. Ayres RA, Wenner ML (1978) Strain and strain-rate hardening effect on punch stretching of 5182-0 aluminium at elevated temperature. Sheet Metal Industries 55:1208–1216
116. Kumpulainen JO, Ranta-Eskola AJ, Rintamaa RHO (1983) Effects of temperature an deep-drawing of sheet metals. Transactions of ASME. Journal of Engineering Materials and Technology 105:119–127
117. Li D, Ghosh AK (2004) Biaxial warm forming behavior of aluminum sheet alloys. Journal of Materials Processing Technology 145:281–293
118. Abedrabbo N, Pourboghrat F, Carsley J (2006) Forming of aluminum alloys at elevated temperatures – Part 2: Numerical modeling and experimental verification. International Journal of Plasticity 22:342–373
119. van den Boogaard AH (2002) Thermally enhanced forming of aluminium sheet. Modeling and experiments. PhD Thesis, University of Twente, Enschede
120. Drewes EJ, Martini A (1976) Einfluss der Umformgeschwindigkeit auf die Grenzformaenderungen und die Formaenderungsverteilung von Feinblech. Archiv fuer Eissenhuettenwessen 47:167–172
121. Percy JH (1980) The effect of strain rate on the FLD for sheet metal. Annals of CIRP 29:151–152
122. Balanethiram VS, Daehn GS (1994) Hyperplasticity-Increased forming limits at high workpiece velocities. Scripta Metallurgica 31:515–520
123. Gerdooei M, Mollaei Dariani B (2009) Strain rate-dependent forming limit diagrams for sheet metals. Journal of Engineering Manufacture 222:1651–1659
124. Keeler SP (1970) La formabilité est améliorée par pression hydrostatique. Machine Moderne 43–45
125. Padwal SB, Chaturvedi RC, Rao US (1992) Influence of superimposed hydrostatic tension on void growth in the neck of a metal sheet in biaxial stress fields (I, II). Journal of Materials Processing Technology 32:91–107
126. Gotoh M, Chung T, Iwata N (1995) Effect of out-of-plane stress on the forming limit strains of sheet metals. JSME International Journal 38:123–132
127. Smith LM et al. (2003) Influence of transverse normal stress on sheet metal formability. International Journal of Plasticity 19:1567–1583
128. Matin PH, Smith LM (2005) Practical limitations to the influence of through-thickness normal stress on sheet metal formability. International Journal of Plasticity 21:671–690
129. Banabic D, Soare S (2008) On the effect of the normal pressure upon the forming limit strains. In: Hora P (ed) Proceedings of the 7th International Conference and Workshop on Numerical Simulation of 3D Sheet Metal Forming Processes, Interlaken, 199–204
130. Wu PD et al. (2008) Effects of superimposed hydrostatic pressure on sheet metal formability. International Journal of Plasticity 25:1711–1725
131. Allwood JM, Shouler DR (2008) Generalised forming limit diagrams showing increased forming limits with non-planar stress states. International Journal of Plasticity 25: 1207–1230
132. Bleck W et al. (1998) A comparative study of the forming limit diagram models for steel sheets. Journal of Materials Processing Technology 83:223–228
133. Bressan JD (1997) The influence of material defects on the forming ability of sheet metal. Journal of Materials Processing Technology 72:11–14

134. Hiroi T, Nishimura H (1997) The influence of surface defects on the forming-limit diagram of steel sheet. Journal of Materials Processing Technology 72:102–109
135. Sowerby R, Johnson W (1975) A review of texture and anisotropy in relation to metal forming. Materials Science and Engineering 20:101–111
136. Keeler SP (1988) Fifty years of sheet metal formability – Has science replaced the art? Proceedings of the SAE Conference, Detroit, 197–204
137. Taylor B (1985) Sheet formability testing. In: Newby JR (ed) Metals handbook, Vol 8, Mechanical testing, 9th edn. ASM, Metals Park, OH, 547–570
138. Chatfield DA, Keeler SP (1971) Technology for using sheet steel designing for formability. Metal Progress 99:60–63
139. Lee D, Majlessi SA, Vogel JH (1988) Process modelling and simulation for sheet forming. In: Semiatin SL (ed) Metals handbook, Vol 14, Forming and forging, 9th edn. ASM, Metals Park, OH, 911–927
140. Swift HW (1952) Plastic instability under plane stress. Journal of the Mechanics and Physics of Solids 1:1–18
141. Hill R (1952) On discontinuous plastic states with special reference to localized necking in thin sheets. Journal of the Mechanics and Physics of Solids 1:19–30
142. Hora P, Tong L (1994) Prediction methods for ductile sheet metal failure using FE-simulation. In: Barata da Rocha A (ed) Proceedings of the IDDRG Congress, Porto, 363–375
143. Marciniak Z, Kuckzynski K (1967) Limit strains in the process of stretch-forming sheet metal. International Journal of Mechanical Sciences 9:609–620
144. Storen S, Rice JR (1975) Localized necking in thin sheets. Journal of the Mechanics and Physics of Solids 23:421–441
145. Dudzinski D, Molinari A (1991) Perturbation analysis of thermoviscoplastic instabilities in biaxial loading. International Journal of Solids and Structures 5:601–628
146. Considère M (1885) L'emploi du fer et Lacier Dans Les Constructions. Annales Des Ponts et Chausses 9:574–775
147. Banabic D, Dannenmann E (2001) The influence of the yield locus shape on the limits strains. Journal of Materials Processing Technology 109:9–12
148. Marciniak Z (1965) Stability of plastic shells under tension with kinematic boundary condition. Archiwum Mechaniki Stosorwanej 17:577–592
149. Marciniak Z, Kuczynski K, Pokora T (1973) Influence of the plastic properties of a material on the FLD for sheet metal in tension. International Journal of Mechanical Sciences 15:789–805
150. Hutchinson RW, Neale KW (1978) Sheet necking I. In: Koistinen DP, Wang NM (eds) Mechanics of sheet metal forming. Plenum Press, New-York/London, 111–126
151. Hutchinson RW, Neale KW (1978) Sheet necking II. In: Koistinen DP, Wang NM (eds) Mechanics of sheet metal forming. Plenum Press, New-York/London, 127–153
152. Hutchinson RW, Neale KW (1978) Sheet necking III. In: Koistinen DP, Wang NM (eds) Mechanics of sheet metal forming. Plenum Press, New York/London, 269–285
153. Banabic D et al. (2004) FLD theoretical model using a new anisotropic yield criterion. Journal of Materials Processing Technology 157–158:23–27
154. Butuc MC, Barata da Rocha A, Gracio AA, Ferreira Duarte J (2002) A more general model for forming limit diagrams prediction. Journal of Materials Processing Technology 125–126:213–218
155. Ganjiani M, Assempour A (2008) Implementation of a robust algorithm for prediction of forming limit diagrams. Journal of Materials Engineering and Performance 17:1–6
156. Banabic D, Barlat F, Cazacu O, Kuwabara T (2007) Anisotropy and formability. In: Chinesta F, Cueto E (eds) Advances in material forming – ESAFORM 10 years on. Springer, Heidelberg, 143–173
157. Banabic D, Barlat F, Cazacu O, Kuwabara T (2010) Advances in anisotropy and formability. International Journal of Materials Forming (accepted)

158. Bichis I, Dragos G, Paraianu L, Comsa DS, Banabic D (2010) Robust algorithm for the solution of the Marciniak–Kuczynski strain localization model (in preparation).
159. Volk W, Illig R, Kupfer H, Wahlen A, Hora P, Kessler L, Hotz W (2008) Benchmark 1 – Virtual forming limit curves. In: Hora P (ed) Proceedings of the 7th International Conference and Workshop on Numerical Simulation of 3D Sheet Metal Forming Processes, Part 2, Interlaken, 3–9
160. Boudeau N (1995) Prediction of instability in local elasto-plastic instabilities. PhD Thesis, University of Franche-Compte, Besancon (in French)
161. Hora P, Tong L (2006) Numerical prediction of FLC using the enhanced modified maximum force criterion (eMMFC). In: Hora P (ed) Numerical and experimental methods in prediction of forming limits in sheet forming and tube hydroforming processes. ETH Zürich, Zürich, 31–36
162. Hora P, Tong L, Reissner J (2003) Mathematical prediction of FLC using macroscopic instability criteria combined with micro structural crack propagation models. In: Khan A (ed) Proceeding of Plasticity'03 Conference, Neat Press, Fulton, MD, 364–366
163. Banabic D, Soare S. (2009) Assessment of the modified maximum force criterion for aluminum metallic sheets. Key Engineering Materials 410–411:511–520
164. Paraianu L, Dragos G, Bichis I, Comsa DS, Banabic D (2009) An improved version of the modified maximum force criterion (MMFC) used for predicting the localized necking in sheet metals. Proceedings of the Romanian Academy 10:237–243
165. Aretz H (2004) Numerical restrictions of the modified maximum force criterion for prediction of forming limits in sheet metal forming. Modelling and Simulation in Materials Science and Engineering 12:677–692
166. Comsa DS, Banabic D (2010) A new formulation of the modified maximum force criterion to avoid the numerical instabilities (in preparation)
167. Gese H, Dell H (2006) Numerical prediction of FLC with the program CRACH. In: Hora P (ed) Numerical and experimental methods in prediction of forming limits in sheet forming and tube hydroforming processes. ETH Zürich, Zürich, 43–49
168. Banabic D (2006) Numerical prediction of FLC using the M-K-Model combined with advanced material models. In: Hora P (ed) Numerical and experimental methods in prediction of forming limits in sheet forming and tube hydroforming processes. ETH Zürich, Zürich, 37–42
169. Jurco P, Banabic D (2005) A user-frienldy program for calculating forming limit diagrams. In: Banabic D (ed) Proceedings of the 8th ESAFORM Conference on Material Forming, Cluj Napoca, 423–427
170. Jurco P, Banabic D (2005) A user-friendly program for analyzing the anisotropy and formability of sheet metals. In: Boudeau N (ed) Proceedings of the IDDRG 2005 Conference, Besancon, 26.1–26.8
171. Banabic D, Paraianu L, Cosovici G, Jurco P, Comsa DS, Vos M (2003) Performances of the BBC 2003 yield criterion when using data obtained from different mechanical tests. In: Gyenge C (ed) Proceedings of the MTeM 2003 Conference, Cluj-Napoca, 23–26
172. Banabic D, Comsa DS, Paraianu L, Cosovici G, Jurco P (2003) Prediction of the yield loci for anisotropic materials using uniaxial and plane-strain tensile tests. Proceedings of the MSE2003 Conference, Sibiu, 11–15
173. Cayssials F (1998) A new method for predicting FLC. Proceedings of the IDDRG Congress Meeting Working Group III, Brussel, 1–6
174. Cayssials F (1999) The version of the 'Cayssials' FLC model. Proceedings of the IDDRG Meeting Working Group III, Birmingham, 1–7
175. Cayssials F, Lemoine X (2005) Predictive model for FLC (Arcelor model) upgraded to UHSS steels. In: Boudeau N (ed) Proceedings of the IDDRG Conference, Besancon, 17.1–17.8

Chapter 4
Numerical Simulation of the Sheet Metal Forming Processes

List of Special Symbols

a, m, p	exponents in the Swift-Hockett/Sherby strain hardening law
C	coefficient in the Swift-Hockett/Sherby strain hardening law
M	exponent in the BBC 2005 yield criterion
R_{m}	tensile strength
$R_{\mathrm{p0.2}}$	yield stress
r_0, r_{45}, r_{90}	anisotropy coefficients in the rolling, diagonal and transversal directions
r_{b}	biaxial anisotropy coefficient
α	coefficient in the Swift/Hockett/Sherby strain hardening law
ε_0	pre-strain
$\varepsilon_{\mathrm{pl}}$	plastic strain
σ	equivalent stress
σ_{b}	biaxial yield stress
σ_{i}	initial stress
σ_{Sat}	saturation stress
σ_0, σ_{45}, σ_{90}	yield stresses in the rolling, diagonal and transversal directions

4.1 AutoForm Solutions

4.1.1 The Role of Simulation in Process Planning

Much attention is given to the theoretical and technological methods behind stamping simulation models; however the applicability of these models in the productive completion of a comprehensive digital process plan is often overlooked. The role that simulation models play in the development process must consider the alignment of software usage, the available inputs, and the desired outputs supporting the work process, in addition to the software capabilities.

Each of the finite element analysis technologies discussed in previous chapters of this book describes the technological differences between the available stamping

D. Banabic, *Sheet Metal Forming Processes*, DOI 10.1007/978-3-540-88113-1_4,

simulation solvers. Beyond the technology of the solvers, the time at which these tools are applied greatly changes the utility of these tools in achieving the desired outcome. Using finite element analysis to determine if a sheet metal part can be formed requires inputs and boundary conditions for the definition of the mathematical model. As a digital process layout evolves the availability of information and assumptions to be used in the pre-processing of the simulation model greatly determines if the output from the simulation code can be trusted or useful. Certainly, no software code will provide any result if the inputs are incomplete and some solver methodologies require fewer inputs to converge. To this end, we should perhaps not discuss solver technology but rather the types of desired simulation outcomes:

- Part Feasibility (geometry check)
- Manufacturability (process validation)
- Process Capability (production robustness)

Each of these outcomes does potentially benefit from the application of different simulation tools, but the most distinguishing characteristics are the assumptions and included inputs to the simulation model. The broader the assumptions, regardless of the selected solver methodology, the more likely it is that reality will differ from the simulation predictions. The earlier simulation is attempted, the broader the assumptions must be; as the process matures assumptions lead to design decisions and production process parameterization, thereby allowing for improved accuracy in the simulation. The more realistic the alignment of simulation assumptions with the reality of the stamping environment, the more accurate the simulation results can be—this is not a solver technology constraint but instead a condition of defining the modeled environment.

Simulation results viewed outside the context of the simulation inputs and assumptions made in compiling without inputs cannot be trusted to fulfill any of the above desired outcomes. It is the existence of the results in light of the assumed conditions of the simulation that make the simulation results valuable. The availability of input and output data varies with time in the design process. The known or assumed parameters at the time of simulation define and differentiate the following levels of maturity of simulation outcome

- Part feasibility: Feasibility Solution evaluating part geometry and material specification to deliver the product function
- Manufacturability: Tooling and Tryout Solution evaluating part and tooling geometry, planned production process, and material specification
- Process capability: Robustness Solution demonstrating consistent manufacturability in a variable production environment; a sustainable process can be defined and maintained amid the expected production variability

Within the realm of possible outcomes for a given product design, we can identify that some but not all will be recognized as feasible, as illustrated in Fig. 4.1. Part

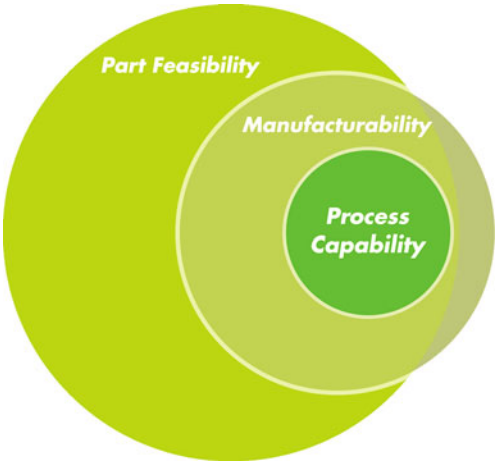

Fig. 4.1 Potential process layout outcomes

Feasibility demonstrates that the part could be made safely—within the forming limits of the material—without regard to the manufacturing process. Manufacturability indicates that the part can be successfully made in a well defined manufacturing process. Process Capability shows that the selected process will produce acceptable parts over the range of variation likely for the selected manufacturing environment and specifications. Process Capability is a subset of those process layouts that produce manufacturability. Manufacturability is often a subset of what is feasible, but as shown in the Fig. 4.1 it can occur that a product design that is at first recognized as infeasible will later prove—through the ingenuity and diligence of skilled tool makers and designers—to be manufacturable. While this is a possibility that those designs that are deemed infeasible will later prove manufacturable, via process means not recognized during feasibility (geometry) checks, it is a limited potential that is usually recognized easily with some input from manufacturing personnel.

As with any recognizable subset relationship, Part Feasibility does not guarantee either manufacturability or process capability, nor does manufacturability guarantee process capability. It is most likely that a capable process will be based upon a manufacturable process and that manufacturable process is often a result of a recognized feasible product. Therefore it is easy to state that any effort to reduce the number of infeasible products early in the design process will, greatly improve the likelihood of the desirable outcome of a fully capable manufacturing process.

4.1.2 Material Data in Digital Process Planning

Part function, as determined by the product designer/engineer, typically specifies a combination of 3-dimensional product geometry and material grade. The selected combination of product geometry and material grade serve the part function—structural strength, assembly, packaging, crash worthiness, stiffness, ride

and handling, etc.—and are presumed to have been specified for sound reasons and are considered to be a requirement of the part design.

To achieve the product function, a near infinite number of possibilities exist for the process layout—manufacturing tool and process design—however, not all the possible process layouts would deliver the specified product while achieving optimal quality, cost, and production delivery (lead time) goals. Certainly, nearly any part design can be made, given enough time and money; but as the concept of inexhaustible time and resources is not reasonable, it must be considered that compromises to the acceptable quality or the desired part function must be considered. The alternative is that the product is deemed impractical or too expensive; and never realized.

At the time a product is first being designed its effect on cost, quality, and delivery are often not considered by the product designer. The sole concern of the designer is attainment of the functional or styling requirements of the product. However, to design blindly is a waste of resources and time: to that end a simple set of feasibility assumptions can be made in order to weed out many truly infeasible design concepts. Later, as manufacturing decisions regarding the process layout are made, the prior assumptions and therefore feasibility assessment may no longer be valid. This has, in the past, been used as an indictment of the technology applied during the feasibility solution. This could not be farther from the truth; it is merely testimony to the fact that, as the process matures the rules of the game change.

At the time the product is first designed, the limitations that the product geometry places on quality, cost, and lead time are not quantified. Without feedback the product designer will create products that suit their function only. However, as the product is prepared for manufacturing—digital process layout planning—it may become apparent that the part is not practical perhaps due to forming difficulties, process costs or quality reasons. At this time the product will either have to be changed, or the process or product is sub-optimized.

In Fig. 4.2 note the comparison between a stamped component for a premium quality niche vehicle and that same component in a quality high production vehicle. In the figure, the outer ring (5) represents optimal attainment of the defined target criteria, as the points shift toward the center (1) they are either compromised or rendered sub-optimal. In the premium quality niche vehicle, note that no compromise was taken in regard to part *quality* characteristics or *function* characteristics, however this is likely the result of compromises in the area of *cost* and lead *time*. It takes more time and money to achieve the highest level of product performance and quality to design intent.

We see for the quality high production vehicle; compromises are made regarding part geometry and function, as well as some measures of *quality*—Fig. 4.2. This may be the result of an uncompromised pursuit of optimal production *costs* and minimized *lead time*. During early feasibility, a component design for the two vehicles would most likely be recognized as feasible for their original product functions and specified material. As the manufacturing targets are more accurately defined, a component for the higher production vehicle—with its optimized targets for production costs—will have different tooling and production restraints, which

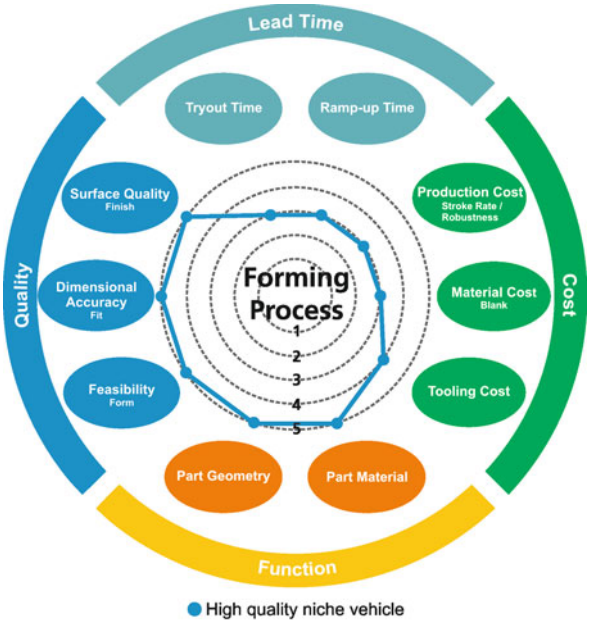

a)

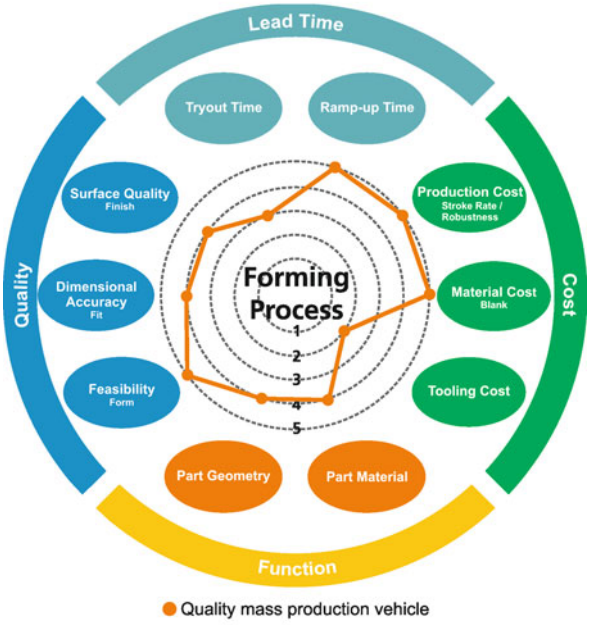

b)

Fig. 4.2 Comparison of impact of digital process plans on function, quality, cost, and lead time for: (**a**) high quality niche vehicle; (**b**) quality mass production vehicle

might render the original product design poorly manufacturable. Is the simulation tool, or the simulation analyst, to blame when the process planning forces product concessions to assist in manufacturing? Neither. At the time, the part seemed feasible for the selected geometry and material grade. But in the light of the new information and limitations placed on the tooling and tryout solution, the analysis outcome is different.

Assessing the forming of the part, without considering production requirements, may lead to unreliable results; later when the reality of these constraints is placed upon the part, or the process, the resulting prediction will seemingly contradict an earlier outcome. However, there is still great value in assessing the forming of the part based upon whatever reasonable assumptions can be made at the time. This value should be tempered with an understanding that the subsequent evolution of the process layout may alter the initial predictions. Finite element analysis of the stamping process layout is but one piece of the larger question: can a particular component be made with the required function and acceptable quality, at a reasonable cost, on time? The future of Digital Process Planning relies on a push towards the comprehensive analysis of quality, cost, and production metrics.

4.1.3 Feasibility (Part Feasibility)

4.1.3.1 Applied Technology

The earliest application of simulation in the evolution of process layout is the evaluation of the part feasibility. Traditionally, Inverse One-Step methods have served as the primary early feasibility tool. The solver technology and the assumptions that MUST be made to utilize the solver relegate inverse one-step solvers to this outcome. The *minimum* user inputs for an inverse one-step code are a 3D model of the sheet metal part and a material grade specification. Some argue that, with additional boundary conditions added, the inverse one-step can perform advanced feasibility analyses and even tooling and tryout solutions (manufacturability). However, even with added boundary conditions, the solution is but a potential reality, because the effect of physical responses such as tool timing, gravity induced sag, and realistic stamping reactions cannot be fully modeled in the inverse one-step model.

While inverse one-step solver technology has been associated primarily with feasibility; a broader definition of feasibility could include full incremental analysis. The richer feedback that is available from incremental analysis can be highly useful when attempting to narrow a given product design to the most feasible geometry; but rapid incremental simulations performed during the feasibility stage may later be contradicted by simulations later performed during the Tooling and Tryout solution phase. This is not due to limitations of the rapid incremental simulation technology, but instead recognition of the fact that simulation outcome validity is primarily a function of the modeled process inputs rather than solver technology. Simulations run at later stages in product development benefit from a more complete definition

of production variables, such as the blank shape and precise tooling geometry, and that is what differentiates feasibility from manufacturability.

The application of different incremental simulation solver methods—Dynamic Explicit and Quasi-static Implicit solvers—and the presumed accuracy of each method, have relegated these codes to highly specialized usage in some organizations. Simulation outcomes have been deemed manufacturable based solely on the solver methodology used, with little discussion manufacturing environment or the inputs used. It must be understood that even the most accurate solver will provide improbable outcome if using improbable assumptions—safe or failing results based on incorrect process inputs do not make the design any safer. The accuracy of the simulation has to be matched with the accuracy of the available input data. If we do not consider the accuracy of our process inputs, discussion over solver accuracy becomes a moot point.

We propose to define part feasibility analyses not based on the simulation technology used, but on the precision of the simulation inputs. For example, if one runs incremental simulations with a blank that does not reflect design intent, then those results can only be used to determine feasibility at best—not a proof of manufacturability or a tooling and tryout solution. Conversely, if a competent solver is used to simulate a stamping process with the precise process inputs matching the intent of the tools, then the resultant prediction can indicate the manufacturability of the part.

This differentiation of part feasibility from process feasibility (manufacturability) is analogous to the use of prototype 'soft' tools versus production 'hard' tools. While the existence of parts that were produced from prototype tools can be taken as a proof of part feasibility, the means by which the prototypes are produced is often not acceptable for full scale production. The prototype tooling may use tooling geometry that is not optimal for production stamping, lubrication may be non-standard, trimming conducted using lasers, and final flanges hand-bent. Similarly, we must distinguish between simulations that faithfully represent the production environment (Manufacturability or Process feasibility) from those simulations that make less accurate although reasonable assumptions (Part feasibility or geometry check).

4.1.3.2 Input Data

3D CAD data and the material grade specification comprise the minimum required inputs for early feasibility. The material model requires a hardening curve, yield surface model, and forming limit. The CAD data should be the latest design intent data fully faced and complete. Other optional, but value added, inputs can include desired manufacturing orientation, boundary conditions (sheet restraint and friction) and addendum (tool layout geometry). If an incremental software code is to be used for an advanced feasibility solution, then additional inputs such as the 3D tooling proposal, applied external forces and initial blank outline are required.

One unfortunate reality of the part feasibility analysis is that the reliability of mechanical properties for the specified material grade varies. In some cases, the material selection is made primarily on the product function of the finished part with little or no regard to the method of manufacture for the part. Also, the information shared with the product designer regarding their material selection may be limited to stiffness, minimum initial yield and tensile strengths, and total elongation—properties pertinent to product function but not sufficient to run finite element forming analysis. Broad assumptions, regarding the specifics of the material model, result in predictions of feasibility that are often times overly optimistic. Product designers select material grades that, to their knowledge, suit the final performance requirements of their design. There may be a host of material grade specifications that might deliver the similar initial yield and tensile strengths, but the manufacturing behavior of the available materials may not be comparable, or even compatible. Additionally, the necessary methods to make the part from the specified material grade may not be in balance with the process layout goals for the part in regards to cost, lead time, or the attainable product quality.

External boundary conditions can be input—such as restraint of the sheet edge, friction, symmetry, etc.—but the correct values to use in determination of feasibility can be difficult to ascertain, as the tooling design used to attain such restraint is still to be defined. Moreover, the physical conditions required to achieve such boundary conditions may be unrealistic. A limitation of the use of these boundary conditions is that the application and distribution of these forces may be unknown by the product feasibility engineer. At best, the product designer may be reduced to assuming a uniform distribution of some amount of restraint, or a variable distribution of restraints about the sheet boundary. It is easy to see how arbitrary the resultant feasibility assessment can become.

For parts where drawing is the likely forming method, one potential methodology for ensuring part feasibility is to run a number of iterations with uniform restraint conditions varied between free (no restraint applied) to full (boundary is fully restrained), the resultant outputs could then be reviewed to assess at which forming condition an observed formability anomaly is recognized as an issue for escalation. This technique which substitutes the arbitrary constraints added to the sheets boundary for the development of full process layout tooling surfaces—binder and addendum—has been successfully applied by a number of Automotive OEMs. These OEMs have shown the use of an inverse one-step as a product feasibility test can dramatically increase the ability to define formability concerns. The formability concerns are ultimately addressed through direct product intervention by the product designer, or through escalation to advanced feasibility support from manufacturing engineering.

Inverse one-step results of drawn parts can be further improved if the input is geometry representative of a potential draw addendum and binder. The addition of the draw die geometry can improve the validity of the resultant feasibility as well as blank outline; however the creation of such geometry requires some tooling knowledge and process awareness, as well as some ability to digitally model reasonable tooling geometry—see Fig. 4.3 below. The additional effort can pay dividends through improved precision in the predicted material utilization and blank

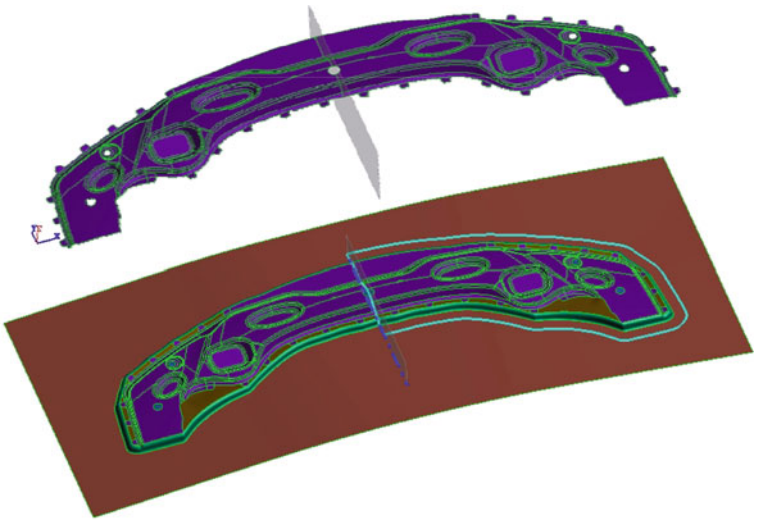

Fig. 4.3 Prediction of part feasibility could be run to consider plausible tooling

nesting, in addition to highlighting forming issues that may be a result of the product geometry's influence on the tooling layout; however, results can be skewed if the process layout geometry proposed is inappropriate. The ability to augment the analyzed product geometry with some tooling geometry—that follows some typical norms and rules for stamping—without the product engineer having to wait others, will allow multiple product geometry to be assessed prior to the release of the product data.

If the solver method is an inverse one-step, then there is another input implicit to the applied solver methodology—the part geometry is to be achieved in one action. This limitation—that the plastic deformation will be achieved in one-step—is clear from the description of the solver method. In cases where the part is to be formed in multiple operations, e.g. draw with a secondary trim then reform, the results of the inverse one-step simulation may indeed be very misleading. Consultation with appropriate manufacturing personnel may indicate that an alternative process is required. This too should bring about an escalation to advanced feasibility and the use of an incremental solver to ascertain the part feasibility.

In the case of an incremental 'advanced-feasibility' solution the selection of element formulation as an input becomes relevant. For accuracy, it may be argued that a solid 'brick' element is potentially the most accurate available element formulation, but most agree that it is computationally inefficient for forming analysis of a typical stamped part—the gain in result 'accuracy' is not proportional to the increased modeling, computing, and post processing requirements. Additionally, at the time of an advanced feasibility solution, the accuracy of some of the selected process inputs is in doubt. An 'accurate' simulation of a process condition that is incomplete in its assumptions is not an accurate model at all. Therefore, at the time of feasibility determination it is possible to benefit from computational efficiencies in the element

formulation: provided that the use of the alternate element formulation does not contradict the physical conditions of the assumed stamping environment. Significant gains in computational speed can be achieved by using situation optimized element formulations, such as Bending-Enhanced Membrane elements for draw operations that use a full blank holder to constrain the sheet edge. Such adaptations, made in the light of an understanding of the other inherent assumptions of the feasibility solution, are acceptable if forming concerns can be identified during the design phase, when the greatest opportunity for cost effective correction exists.

4.1.3.3 Output Data

In the instance of using inverse one-step solvers, sometimes the best the user can do is use the software to identify forming issues to escalate to those who run the advanced-feasibility models. Again, this is due to the nature of the early feasibility solution. Based on the inputs used for the inverse one-step solution, the likely combination of inputs and results may not be fully known. Attempts to resolve all the issues via product modification may be unnecessary and only add cost to the engineering process while not achieving the improvement in process layout that is desired.

Recognition of these escalation issues is easily achieved via an FLD based output differentiating the forming modes of the part and risk of failure. Formability plots with such summary views are attainable in most commercially available inverse one-step solvers. The forming tendencies of the part for safe, marginal, splitting failure, compression, wrinkling, or lack of stretch will often be shaded on the simulation mesh in different colors, coded for easy recognition.

A significant shortcoming in the inverse one-step feasibility method is recognizing at which boundary condition the issues should be identified. At free boundary restraint very few splits should be found—those that can be immediately recognized as critical geometry issues or indication that process modification may be needed. Eventually for many parts complete splitting failure can be attained by increasing the restraint until the sheet edges are locked. Does this mean that every part is safe and unsafe at the same time? At which condition would one pronounce that the forming issue exists?

The challenge is not only to identify that forming issues exist, but more importantly which restraints was the most likely stamping condition. The condition in the real production tool is likely to be something in between the ‘free’ and ‘locked’ restraints. The tool and die makers would tune the die to ensure that the part was stretched enough to avoid wrinkles but not so much that the part will split. A system can be devised to allow the feasibility engineer to identify a minimum threshold of stretching—between free and locked—that should be achieved. As the boundary restraint is increased from free to fully constrained the amount of compression and thickening related issues will decrease while the amount of thinning and splitting issues will increase, see Fig. 4.4 above. If splitting issues arise and compression and thickening issues still exist then one could conclude that the tools that would

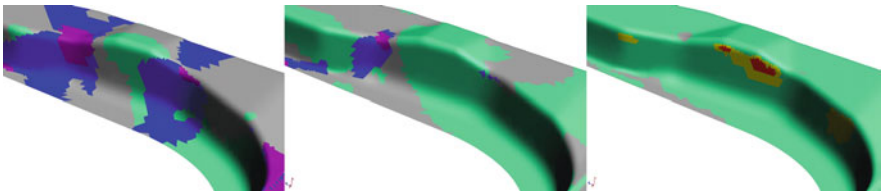

Fig. 4.4 With different restraint conditions the 'safety' of the part changes

later be built to manufacture the product would likely induce such failure potential. The question of forming feasibility is never a simple yes or no proposition, instead it must be proposed with many conditions. The result should be presented in the context of the assumptions that lead to the outcome—i.e. the part is feasible at a stretching threshold of 2% thinning on a majority of the part surface, the part is not feasible at the minimum threshold of stretch, the part is feasible if produced from a fully developed blank, the part is not feasible in a single forming operation, etc.

The feasibility prediction attained can be used to highlight the geometry based forming issues and potential resolution (i.e. product concessions, larger radii, open walls, shallow geometry), however, it should be noted that failure to qualify the part geometry as 'feasible' does not automatically disqualify product geometry as being non-manufacturable. In the case of a feasibility result from an inverse one-step solver, if the part is manufactured in a series of drawing or forming operations there is a strong likelihood that the product could be successfully made if the proper tooling and tryout solution is applied. Therefore the numerical results gathered during the feasibility assessment may need to be taken with some skepticism. Similarly, some parts that are deemed feasible should be dismissed when reviewed for tooling and tryout, because the methods required to achieve the feasible product design are undesirable. To put it simply: just because a product can be made, does not mean that it should be made.

Feasibility, as much as we might wish it would be, is not a binary output. That a part has passed feasibility is a statement that should be highly qualified with a complete list of conditions—assumptions, inputs, and boundary conditions. The part is feasible if these conditions are met. In the case of inverse one-step technology the conditions include the assumption that the part is formed in only one forming operation, that the blank will be a fully developed shape, that the tool contact is uniform, consistency of material parameters exactly as modeled, that the external forces don't change over time or distance. Knowing that the actual delivered parts will very likely be manufactured differently than modeled should inform our decisions on how to use the available results—see Table 4.1. In the case of advanced feasibility, assumptions will include but are not limited to the user defined blank outline, the binder pressure, friction (lube), material parameters exactly as modeled, draw bead effect and location, and process layout geometry.

Table 4.1 Feasibility solution outputs

Output	Reliability		Caveats	Action
	Feasibility	Advanced feasibility		
Formability splitting failure issues	Moderate	Moderate	Some splits may be correctable via process adjustment (i.e. different blank outline, holding condition, multi-stage forming)	Escalate if immediate geometry adjustment does not resolve or improve. Obtain review from process or method planning
Formability compression/wrinkling issues	Low	Moderate (process layout dependent)	Wrinkling behavior strongly controlled by process layout	Escalate all known wrinkling tendencies so process layout can plan accordingly
Blank outline	High (crash form) Low (draw parts)	Moderate to High (process layout dependent)	Blank outline from inverse one-step is a reasonable start for process determination (tooling and tryout). Part only blanks from one-step risk severe under quote material requirements	Run inverse one-step using tooling geometry and desired boundary of formed sheet. Embed or nest and escalate to advanced feasibility to achieve higher confidence in the blank size estimate. Nesting and embedding into shear blank improves material utilization prediction (advanced feasibility or tooling and tryout solution)
Thickness (mm) and thinning (%)	Low	Low to Moderate (process layout dependent)	Thinning distribution will change with the process layout	Inverse one-step thinning results are better than assumed nominal for FEA/CAE functionality testing, however advanced feasibility results will achieve superior results
Springback	None	Low	Stresses from feasibility based inputs are highly questionable—dependence on process layout	No actionable steps regarding springback can be taken

4.1.4 Manufacturability (Process Validation)

4.1.4.1 Applied Technology

What is feasible is not always possible given circumstances limited by budget or manufacturing capabilities. This may sound like semantic double speak, but instead speaks to the difference between what we can model, and what can actually be accomplished in today's world. Further along in the manufacturing development of the sheet metal stamped part is the process definition, tooling development and design stage. Simulations performed during this stage of the product life cycle are presumably defined to determine the manufacturability of the production intent sheet metal stamped part. At this point in the product development process some simulation solver technologies are more viable than others. Inverse one-step has for the most part outlived its usefulness when moving on to consider manufacturing feasibility—incremental solvers are the generally accepted technology to determine manufacturability.

Incremental simulations may have already been performed on the component, but if the process inputs used were not production intent then that resultant prediction of forming was only a validation of the part feasibility. Once the appropriated inputs are defined and used for conduct of an incremental simulation we can then recognize that the outcome of the simulation is a validation to the manufacturing feasibility—manufacturability—of the part.

What truly distinguishes part manufacturability from part feasibility is not the simulation technology to be used, but instead the precision required in the selection and definition of the pre-processing inputs provided. The goal of a tooling and tryout solution is to provide timely feedback on the viability of the manufacturing process layout plan. In this regard, we can see that many process layouts that are deemed manufacturable were a subset of those product geometries that are deemed feasible, though some exceptions may exist. However, not all feasible parts will be deemed manufacturable. The characteristic that separates these two outcomes is the flexibility of the constraints in the manufacturing process layout.

Now that the inputs have been improved to emulate the production intent of the manufacturing environment, some of the earlier assumptions made during the advanced-feasibility also may need to be amended. Using the better inputs with speed-optimized FEA parameters—like coarse mesh and situational optimized element formulations—should make way for use of finer mesh and more specific element formulations. Indeed, we still see the use of a solid element for most sheet stamping simulations as overkill, but now the use of a full shell element can be seen as value added, provided that the process being simulated has already shown reasonable convergence potential with the adapted inputs. It would be unwise to immediately throw out the speed benefit of bending enhanced membrane, when a passing result is still several iterations away; however, once a reasonable outcome is found, a final validation run using an Elastic-Plastic shell is a prudent step to ensure the highest level of confidence as we move forward.

4.1.4.2 Input Data

The use of production intent input data is the key distinguishing factor that separates a Tooling and Tryout Solution for manufacturability from a Feasibility Solution for part feasibility. Without recognition of the inputs used as the production intent the value of the simulation outcome is limited—part feasibility. Instead we propose that the goal of a Tooling and Tryout solution for manufacturability is to validate the production tooling prior to tool build. This end can only be achieved by means of simulation that emulates in a very accurate manner the conditions that will be present in the tooling tryout and eventual production.

At this time we start to see the larger influence of the decisions made in regard to the comprehensive digital process plan. The blank that may have been used for an advanced feasibility simulation may have been run without full knowledge of the planned production line, stamping process, or material utilization targets.

Listed in Table 4.2 are many of the required inputs that must be determined—with the goals set out for the digital process plan in consideration, at present it is not possible to enter directly into the simulation software the cost per blank goals of the part, nor production robustness goals and have the simulation set itself up to achieve these ends. Instead the human operator makes value decisions regarding the attainment of these goals and selects the inputs that appear to further the pursuit of those goals. Returning to the goals of the digital process plan we can assume that for lower production vehicles one-time costs such as initial tooling costs may have greater influence on the selected blank shape than a high volume-low cost vehicle, where material utilization may far exceed the initial tooling cost for importance. It is no longer acceptable to determine if the part CAN be made, we now seek to prove

Table 4.2 Inputs for a manufacturability analysis-tooling and tryout solution

Tooling Geometry inputs	Blank inputs	Environment variables
3D tooling surface data	Full material description • N • R • YS (min-max) • TS (min-max) • Yield Surface • Rolling direction • FLC	Effective friction data Lube, coating, substrate combination
3D trim lines	Blank shape and location • In coil • In die	Applied tool forces (pad/blankholder/binder)
3D flanging tools	Initial Thickness	Die closing timing
3D net points for springback analysis		Cushion travel/blank support
Bead Profile (effective restraint)		
Bead centerline		

that the part will be made in our plants, using our tooling standards, to our accepted level of part quality.

Example Case

Using a feasibility solution an automotive b-pillar was deemed a feasible product design, the feasibility assessment was performed using inverse one-step technology and advanced feasibility was performed using quasi-static implicit incremental solver. As inputs to the advanced feasibility a simple draw development was designed and a blank outline was calculated using the inverse one-step blank prediction. Formability assessment and thinning strain predictions indicated that the b-pillar appeared to be feasible—Fig. 4.5.

Upon release for tooling and tryout, the draw development used in advanced feasibility was re-worked to support the following tooling operations in the process layout plan (i.e. trimming without use of cams and flanging) which required some alterations to the draw development. Additionally, the blank used in the tooling and tryout solution was planned as a sheared blank with a trapezoidal profile—Fig. 4.6. When simulation was completed no passing result could be attained without further compromising on compressive and wrinkling behaviors in critical areas—Fig. 4.7. The part was determined to be poorly manufacturable and sent back to product design for concessions in the latch area. The reason for the change in blank was the manufacturing cost of the shaped blank in production. Shaped blanks require

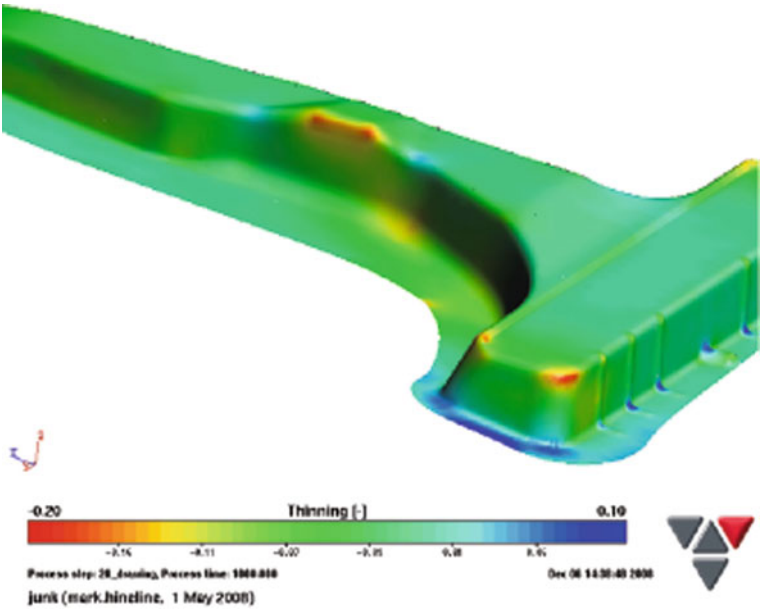

Fig. 4.5 Advanced feasibility—arbitrary blank

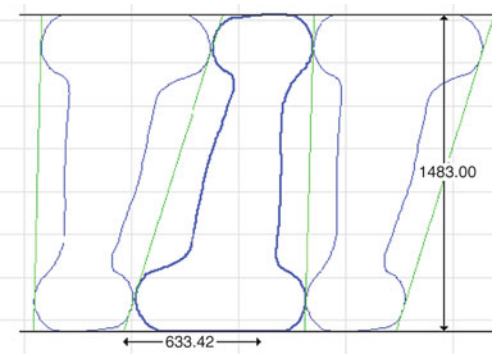

Fig. 4.6 Blank nesting to achieve target costs

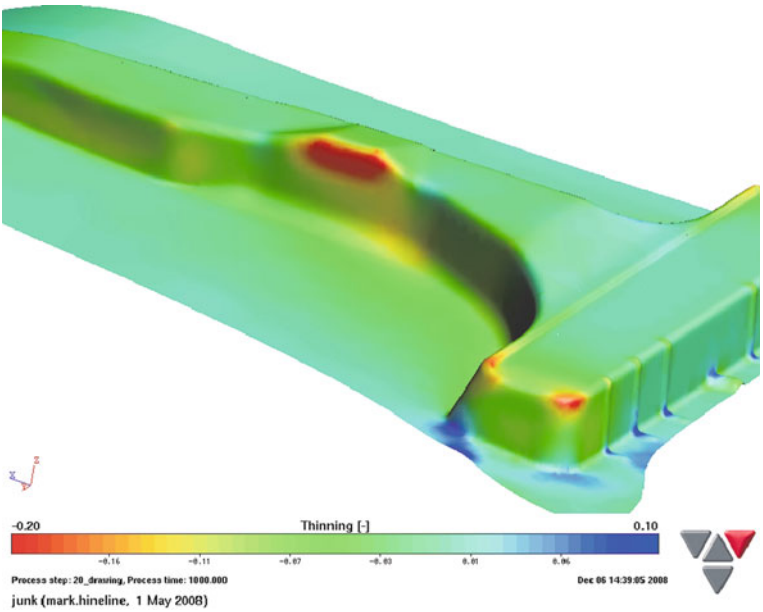

Fig. 4.7 Manufacturability using shear blank

blanking dies, blanking dies often require offline production of blanks, and offline blank-production may drive the use of special pallets for the blanks. The product engineer responsible for the feasibility analyses may lack the foreknowledge to select the appropriate blank shape, or the decision to use a shear blank had not been made yet by the manufacturing department.

The manufacturability of the sheet metal part is often compromised by goals made for the production stamping environment: such as production cost controls, corporate guidelines for tool processing, material utilization goals, production plant limitations, or other factors. Earlier recognition of this fact allows for potential to alter other contributing factors, such as minor product concessions, additional

process steps (draw-redraw), or lowered expectations for finished part quality. This difference exists regardless of the incremental simulation technology utilized, therefore it is clear that the 'accuracy' of a given simulation solution is driven by the simulation input precision and the predictive reliability of the solver results.

With this is mind, the difference between feasibility and manufacturability—tooling and tryout solutions—can be seen as less of a technological barrier but due to a limitation of process knowledge and information. The 'quality' of the output from sheet metal stamping simulation therefore lies in the ability of the operator to use the software to best emulate the intended production environment. This may entail ensuring that production intent inputs are used, accurate depiction of the blanks mechanical properties (i.e. hardening curve, yield surface, failure criteria), and appropriate element formulation. If the condition of having realistic production intent inputs is not met then solver technology is a moot argument. Given the definition of the production intent environment, the results from the solver can be considered reasonable proofs of the likelihood of safe manufacturing of the part, for the production variables as modeled.

An outcome of predicted manufacturability is, as with feasibility a conditional assertion: if the production environment delivers the tools as engineered and the blanks shipped to match the mechanical properties used in the incremental analysis, and the set-up of the tool is the same as modeled, the production tool should deliver results matching the simulation. That being said, it is most likely that when a discrepancy exists between the prediction from the Finite Element Analysis and the physical tooling that immediate reactions should first be to look at the as built condition of the die, the blank used in the die, and the set-up of the die in the press environment before looking to blame the quality of the analysis outcome.

4.1.4.3 Output Data

The types of outputs that are expected from the tooling and tryout solution for manufacturability are much the same as we see in feasibility analysis, only now with the use of improved inputs the reliability of those results is much improved. An outcome of predicted manufacturability validates that a desirable outcome will be reached in the built tool if built to the engineering specifications as modeled.

Strain distributions, and therefore the nearness to failure, resultant from tooling and tryout solutions are far more reliable, and can provide to the tool and die designer and eventually the tool maker a reasonable target for tool build conditions. These strain distributions if used in CAE modeling of vehicle structural performance can provide enhanced realism when compared to results from CAE models that assume conditions based upon the nominal designed stock thickness and initial material strengths.

With improved strain distribution as well as strain path, the stress distribution of the part is now more realistic than achievable when compared to any stress result from advanced feasibility. Again it is important to recognize that this expected improvement in the stress distribution is not so much a factor of the simulation technology used, but that we expect that the inputs used to run the tooling and

tryout solution for manufacturability to be used when the dies are actually built for production. The resultant stress distribution should result in improved springback prediction reliability, and possibly the ability to predict shape fixation in the finished part and begin the process of engineering countermeasures for the elastic deformation of the part.

As we saw with feasibility the predicted outcome is conditional upon the inputs that were used. It is meaningless to state that the part can be manufactured without defining the boundary conditions that are required to deliver that outcome. For many output variables that would be used to establish the outcome of manufacturability (process feasibility) establishing that the process yields a 'safe' result is fairly straightforward—one can over engineer for avoidance of splits or wrinkles in the finish product. However, other quality attributes such as springback and surface quality cannot simply be defined as 'safe'. These attributes can be highly variable with even minor fluctuations in the process inputs (i.e. material, lube, in-die forces) and there is no 'over-engineering' to avoid negative ramifications of this variability. To this end we see that merely validating that the single set of process inputs used to validate the manufacturability of the stamping process is insufficient to assure that production of the part can proceed with confidence.

4.1.5 Capability (Robustness)

4.1.5.1 Applied Technology

The ultimate goal of the use of computer aided engineering tools is the virtual production of the stamped product so as to eliminate the need for time consuming and expensive tryout. At present there are many examples where this expectation has already been met, many examples can be found where the outcome was not so reliable and the tryout of the tool progressed slowly and may have never achieved a 'safe' panel. When the computer aided engineering models yield results different from the physical tools, the difference is not due to the failings of technology, but perhaps a failure to recognize a fundamental issue: The world is variable while deterministic computer simulation models are fundamentally fixed—run from a single set of selected inputs that represent singular instance, a specific sheet of metal with a single idealized set of mechanical parameters, blank shape, tonnage application, friction, bead effect, etc—based on one possible process state.

The result of an incremental tooling and tryout solution for manufacturability is constrained by the concept that the simulated part and process is formable if exact conditions are achieved in the manufacturing environment. The outcome is highly conditional, and often we may find that if the input conditions change even slightly the result of the simulation may change from acceptable to unacceptable, safe to failing, within specification or out of specification. The results of the simulation after many hours of modeling by the analyst and perhaps multiple iterations achieves a passing result, however once the passing result is reached it is unclear how stable and repeatable that result may be.

During physical tryout this fact is evident, few tool and die makers would sell a tool on the basis of a single successful panel produced during tryout; instead multiple successful panels must be made and proven to be acceptable to the customer. However, many users of simulation will pass off on a simulation of a single successful iteration or 'hit'. That single passing simulation is a result of a perfect collection of events, which may or may not be achievable in the actual production environment.

To retain the value brought to the engineering of the sheet metal stamped part from computer simulation, the simulation analyst must consider and include in the analysis the very real potential for variation in the assumptions made during the analysis. Much debate could be made over the claim that many make when defending the validity of their own feasibility or manufacturability analyses, 'the simulation was run using the worst case inputs'—the necessary question to this comment is what are the 'worst case' inputs and does that by default illustrate the worst case outcomes. The answer to this query is that what appears to be 'worst case' cannot be assumed in a consistent manner nor can the effect of that assumption be recognized in advance—see Fig. 4.8. If the effect of these changes was predictable in advance computer, simulation would be entirely trivial.

The fact is that in a variable environment any difference from the assumed inputs will yield some difference, and whether or not that difference is significant is the root of the problem. A simple design of experiments using multiple manufacturability simulations with user adjusted inputs to represent the variation could potentially yield valuable feedback, but this feedback will be skewed again by the users' assumptions and predetermined suspicions over which variables are 'worst case'. One could attempt to derive some design of experiments to seed multiple iterations of the simulation model to attain results that could represent the outcome of the variable stamping environment. However, the data collected would be only as reliable as the design of experiments, which for the reasons listed above may be difficult to design as one must already have a clear idea which variable should be changed and the potential for influence of these changes in order to select the combination of variables to test. Also interpretation of such vast amounts of data would be overwhelming.

The perception that we can produce an accurate simulation result from finite element analysis software now must always address the range of inputs that were used, and are those ranges of inputs a likely condition that we might see in production. For

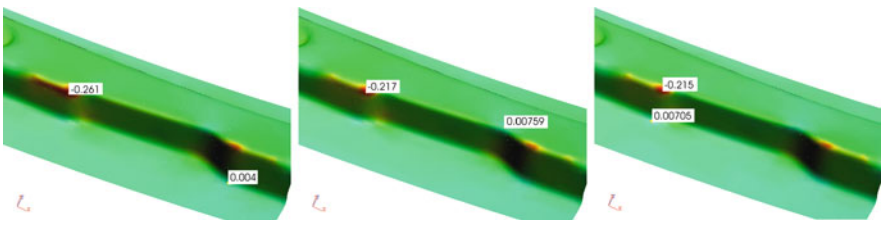

Fig. 4.8 Thinning results from small set of analyses with different but acceptable inputs

if the ranges used are not a precise representation of the probable production ranges then the outcome of the simulation(s) will not predict the likely or probable results. The outcome of process capability from a robustness solution is instead an entirely new paradigm for simulation where the user can input ranges of inputs that are probable, and the simulation solver automatically and statistically randomizes the variables, combines the variables into reasonable input decks, manages the running of the multiple simulations, and most importantly is able to represent the outcome in a meaningful way. Stochastic analyses—based upon larger sets of incremental results—can provide the technological answer to the issue at hand when trying to ascertain the capability of the designed part in the approved process.

4.1.5.2 Input Data

Similar to feasibility and manufacturability outcomes the capability of a part and process is constrained by the available inputs. In a capability analysis the input variables are now represented as ranges of potential values. The recognition of these possible ranges is typically not available at the time of early feasibility or manufacturability, nor would it be reasonable to attempt a full capability analysis at the time of product conception and design. These variables are a direct result of production decisions and assumptions that may not be known or available until closer to the time of production. These variables can be the result of the steel coil, the selected blanking process, the design of the forming tool, press selection, and compromises made in the 3D process layout throughout the planning process.

The material inputs used to determine manufacturability we most likely a 'typical' or minimum acceptable value. But it is known that the material shipped to the stamping plant, like any other manufactured good is subject to variation potential from the manufacturing source. The goal of the robustness solution is to determine if the defined process is still capable of producing parts within this variation potential. Figure 4.9 illustrates how over a 23 lot production run the material at one stamping plant varied greatly in terms of the delivered materials mechanical properties. If the robustness solution is conducted using reasonable ranges of material properties that emulate the expected normal distribution of the expected values, then the resulting simulation outcome can illustrate the potential for variation within the manufacturing environment.

Other assumptions that can be considered questionable from the previous solutions is the assumption of the blanks initial location, the distribution and effective ness of the lubrication, the size and shape of draw beads, the amount of pressure applied by the binder or pad systems, and many other critical design elements that up to this point are considered design decisions and constants. But in the production environment, the attainment and maintenance of these 'constants' is not certain.

4.1.5.3 Output Data

The resulting outcome from running so many simulations with the varied inputs and assumptions will be a very rich amount of data that, if reviewed properly, can indicate which variables have influence over which output results. From one

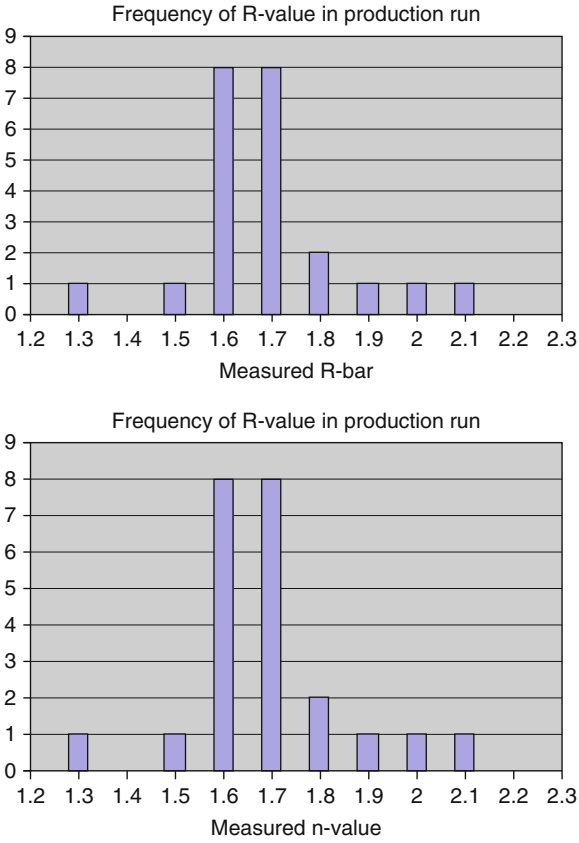

Fig. 4.9 Material property variation potential gathered from 23 real production lots

simulation to another, if a single attribute of the material changes, the influence of variation in the inputs and their effect on the outcome can be derived; however when more than one variable changes from run to run, it is not obvious which of the inputs influence the outcome—Fig. 4.10. To manually inspect the simulation for prediction of process capability, it may be nearly impossible to arrive at any reasonable conclusion. However, using advanced techniques to interrogate the response surface generated from the battery of simulations it will be possible to derive relationships between the observed changes in the output variables and the associated changes in the design inputs.

Ultimately, the goal is to arrive at a capable process; not always a likely event. For this reason, another useful outcome from a seemingly failing robustness analysis is the ability to recognize relationships between the output variables and the input factors that may have led up to the undesirable result (Table 4.3). Provided there are enough simulations in the response set to be statistically sound, it is possible to derive which input variables are influential for generating any response. If an input is influential then the sensitivity to the input variation we can be gauged—Fig. 4.11. This information can be used to conduct a 'robust engineering' of the process—an engineering process by which the robustness solution is used to identify not only

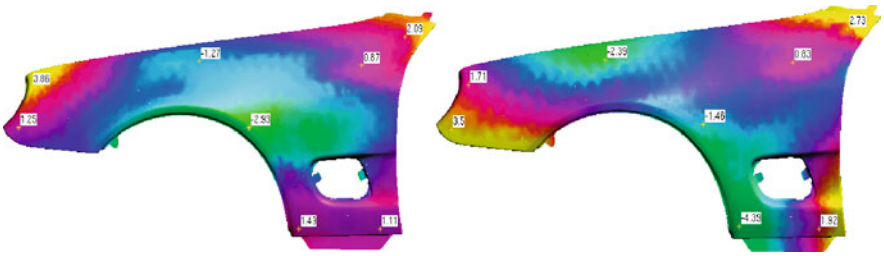

Fig. 4.10 Springback results from two slightly different materials in same process

Table 4.3 Input variation possible for robustness analysis to capture production noise

Input	Production variation	Range	Influence/effect
Yield strength	Varies with the mill and processor: chemistry, mechanical processing, and annealing	Suppliers normal distribution or ± 20 MPa	High influence on hardening behavior, yield surface, effectiveness of beads and pads, springback
Tensile strength	Variable with chemistry, and mechanical processing	Suppliers normal distribution or ± 20 MPa	Influences hardening (with YS)
N value	Variable with chemistry, mechanical processing, and annealing	Fluctuates with variation of yield and tensile strength	Hardening behavior, forming limit,
R value	Hot roll vs cold roll, mechanical processing, coil rolling direction	± 20% (steel) ± 10% (aluminium)	Yield surface, strain/stress distribution
Lube (friction coef.)	Varies over sheet surface, varies over blank batch, performance is variable in production (beginning to end)	± 10%	Strain distribution, material flow, stress distribution
Blank location	May shift as result of automation and gauging, varies with coil width (shear blank)	± 1 mm or tolerance	Binder force distribution, bead effect, lubrication effect, tooling contact
Binder/pad pressure	Varies through the stroke, varies with die setting, varies during production run	± 10%	Force distribution, bead effect (full set), tooling contact
Blank thickness	Varies with coil/blank	± 10%	Tool contact, force distribution, contact pressure

that a process is capable or not, but to point the designer towards the design inputs that may result in a more capable outcome.

Through the application of a robustness solution, the designer can engineer a design that ensures that not only has the part and process been designed to achieve a

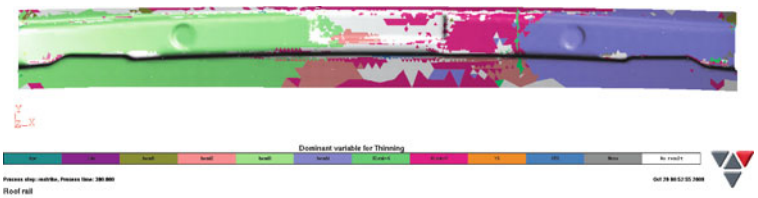

a)

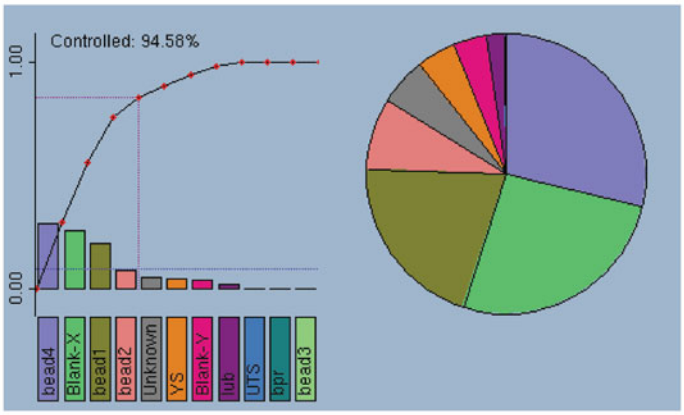

b)

Fig. 4.11 Determination of which inputs influenced thinning result: (**a**) roof rail; (**b**) influences

'safe' and feasible result, but furthermore that the process will continue to produce acceptable results throughout production, if the inputs are held within the window of variation provided by the robustness solution. With such data at the readily available, the designer will be able to predict if any changes are forced to the process layout, or in some cases merely look up from the body of simulation the expected results

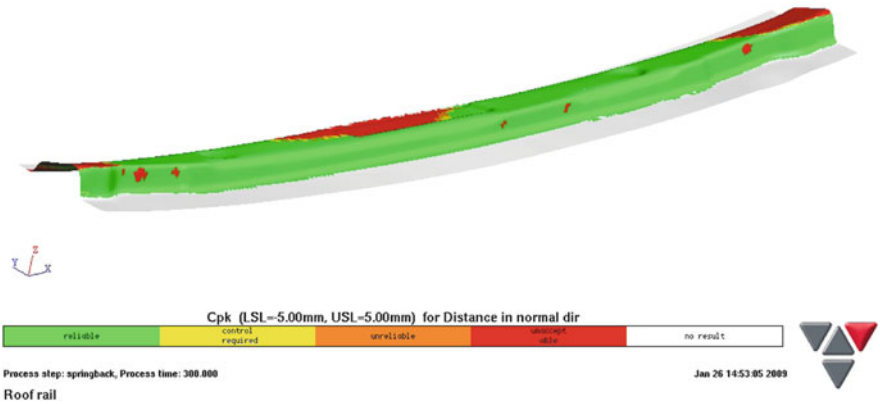

Fig. 4.12 Sampling the large result set allows for recognition of process capability

from some specific set of input variables and their on the overall forming safety, or capability, of an alternative process—Fig. 4.12.

Changes to the blank, stamping process layout or product specifications will have quantifiable ramifications for the 'quality' of the part. A 'production map' of sorts can be developed to be referenced as a guide during tooling tryout or part production, so that in the event of some system change (new splitting failures, parts out of tolerance) the robustness results can be polled to find which inputs are most likely to have slipped outside of acceptability to identify a list of 'usual suspects' in the loss of 'quality'.

4.1.6 Simulation Result 'Quality'

As forming simulation technology has matured, most of the attention to the quality of the process layout has been measured in how closely the simulation results matched the results in press, often forgetting that the manufacturing process inputs cannot be assumed to match exactly the simulated inputs. Also, the focus has been on the attainment of simulation results that accurately depict some already known result of a single fixed and fully measured input data set.

A great deal of energy has been dedicated to discussion and determination of appropriate element formulations, contact algorithms, solver methodologies, and material models which surely has advanced the science of sheet metal stamping. August institutions devote time and resources to the pursuit of improved simulation of the effect of sheet metal stamping. Certainly, the yield surface model can deeply influence the reliability of the forming simulation. However the observable differences from material modeling subtleties and finite element nuance, pales in comparison to the differences yielded when the engineering environment does not match the production environment—varied blank shape, bead location, or applied pressure. Little consideration is given to whether or not the result came from a process layout that could be approved for cost, and even more difficult to measure has been whether the result could be reliably achieved in the ever changing production environment. Only by implementing a robustness solution in pursuit of a capable process can a truly comprehensive assessment of the part function, quality, cost, and delivery capability be made.

4.1.7 Comprehensive Digital Process Planning

Many significant decisions need to be made throughout the development of the digital process layout that will directly affect the 'quality' of the part—the safety margin from splitting or wrinkling, the shape repeatability, assembly fit, and surface quality. These changes are made in the pursuit of meeting cost targets for material utilization, tool cost, or process simplification. The effect of these changes is rarely, if ever, quantified. Computer Aided Engineering, if it is to truly achieve the goal of

eliminating the need for physical modeling, will have to overcome this limitation by creating a platform in which this data is tabulated and compared. Stamping simulation cannot live isolated from the measurement calculation of cost or repeatability. The quality of a panel cannot be blindly pursued over the real world implications of tooling manufacturing costs, and the need to ensure rapid and on time delivery of tools and parts of those tools. Similarly every cost initiative must be assessed for potential impact on the resulting part quality.

Using the computer simulation to prove that part geometry is possible (feasibility) for the selected material, while providing value during product development, is not enough. Production concerns that constrain the blank process layout, such as blank shape, number and type for stamping operations are made for concerns of cost, quality, and lead time goals. Figures 4.13 and 4.14 illustrate the potential relationship between the desire to achieve 'better' resulting process layout and risk to other attributes. These process layout changes reduce the number of feasible designs to those that are recognized as manufacturable. Without great cost the production environment cannot assure that all process variables will be constant or stable over time—die maintenance, material variation, production environment all influence the process layout reducing the number of viable designs to those that may be capable. Recognizing whether a process layout can deliver the product as designed on time, at cost, and to the required level of quality is the ultimate goal in stamping simulation. Accuracy in simulation is the ability to predict process capability in a reliable and timely manner, such that production issues can be averted.

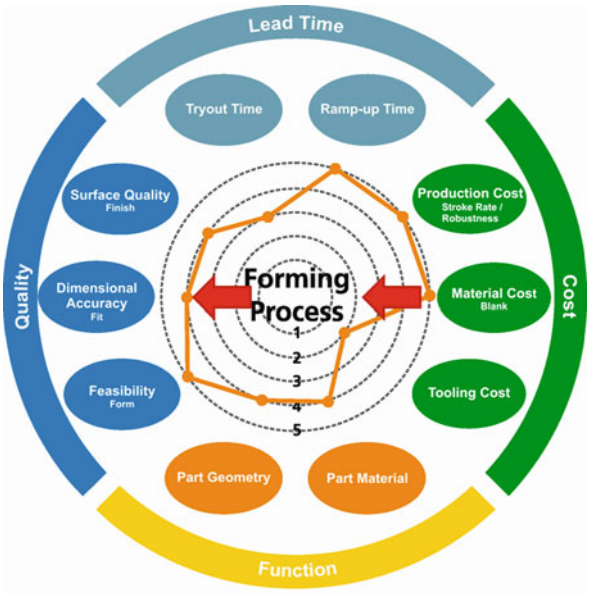

Fig. 4.13 Improvements to 'fit' may drive material costs from optimum

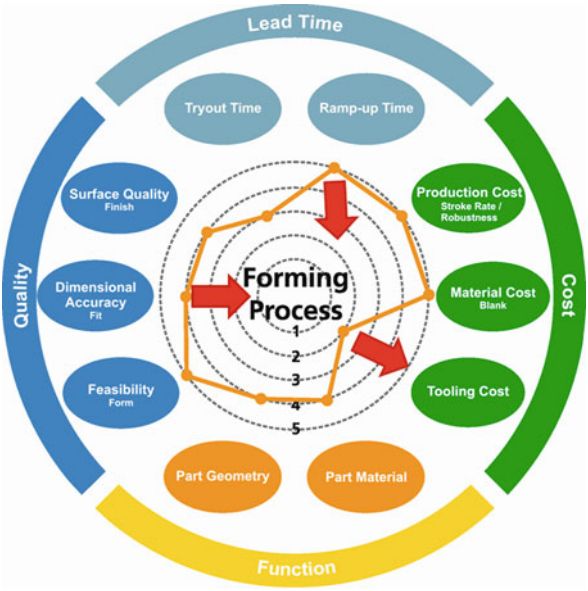

Fig. 4.14 Reducing tooling cost may affect quality or ramp-up time adversely

4.2 Simulation of the Elementary Forming Processes

4.2.1 Simulation of the Bulge Forming Process

In an European research project concerning inverse modeling [1], an experimental program was conducted consisting of tensile tests and cruciform tests for material characterization, complemented by bulge tests for validation. In the following, results for DC04-IF (0.81 mm sheet thickness) are presented.

4.2.1.1 Hardening Description

Hardening parameters for a combined Swift-Hockett/Sherby law, Eq. (4.1), were fitted to the results of tensile tests in rolling direction and are given in Table 4.4. All stress units are in MPa.

$$\sigma = (1-\alpha)\left\{C\left(\varepsilon_{\mathrm{pl}}+\varepsilon_0\right)^m\right\}+\alpha\left\{\sigma_{\mathrm{Sat}}-\left(\sigma_{\mathrm{Sat}}-\sigma_i\right)e^{-a\varepsilon_{\mathrm{pl}}^p}\right\}. \qquad (4.1)$$

Table 4.4 Hardening parameters of DC04-IF

Material	α	ε_0	m	C (MPa)	σ_{i} (MPa)	σ_{Sat} (MPa)	a	p
DC04-IF	0.50	0.0044	0.27	580	140	432	5.47	0.76

4.2.1.2 Yield Surface Description

From the tensile tests, the three yield stresses σ_0, σ_{45}, σ_{90} and the three r-values r_0, r_{45}, r_{90} are known (see Table 4.5). From the cruciform tests, the biaxial yield stress σ_b can be derived. In these tests, no strain measurement was performed. Therefore, the r_b-value is not known.

The strategy used in AutoForm to identify the coefficients in the BBC 2005 criterion is described in Table 4.6. Grey fields denote given experimental data. White fields denote values that are defined by the model. For example, for the Hill 1948 model in Table 4.6, r_0, r_{45}, r_{90} and σ_0 are input and r_b, σ_{45}, σ_{90} and σ_b are output parameters. The exponent M is chosen to be $M = 6$.

In Fig. 4.15, the yield surfaces of the above yield functions are displayed in the principal stress plane. The BBC 2005-8 formulation is missing because a measured r_b value is not available. The data points correspond to an equivalent plastic strain (evaluated with Hill 1948 yield criterion) of 0.05.

Within the Hill 1948 model, the biaxial yield stress is fully determined by the r-values. This fact results in a biaxial yield stress that is too large compared to the measured value, see Fig. 4.15. On the other hand, the BBC 2005-7 model can take the measured biaxial yield stress into account exactly, and also the rest of the cruciform test data is described much better by the BBC 2005-7 model than by the BBC 2005-6, the BBC 2005-4 and the Hill 1948 models, respectively.

4.2.1.3 Bulge Tests

In the frame of the European project 'Material parameters for sheet metal forming simulations by means of optimization algorithms' [1], the bulge equipment had an internal diameter of 100 mm and a tool radius of 2 mm. The sheets were gridded to allow optical strain measurements. For the DC04-IF sheets, the bulge height of 20 mm was reached at an internal pressure of 7.75 MPa.

Table 4.5 Yield stresses and r-values of DC04-IF

Material	σ_0 (MPa)	σ_{45} (MPa)	σ_{90} (MPa)	σ_b (MPa)	r_0	r_{45}	r_{90}	r_b
DC04	137	142	142	154	1.9	1.8	2.5	–

Table 4.6 Strategy to define the coefficients of the BBC 2005 model for steel for cases where not all input is available: missing experimental input (white fields) for BBC model is filled up with Hill 1948 data

Availability of test results	Model	M	σ_0	σ_{45}	σ_{90}	σ_b	r_0	r_{45}	r_{90}	r_b
All data available	BBC 2005-8	6								
Biaxial test available but r_b not given	BBC 2005-7	6								
Biaxial test not available	BBC 2005-6	6								
Only r_0, r_{45}, r_{90} given, σ_0 arbitrary	BBC 2005-4	6								
Only r_0, r_{45}, r_{90} given, σ_0 arbitrary	Hill 1948	2								

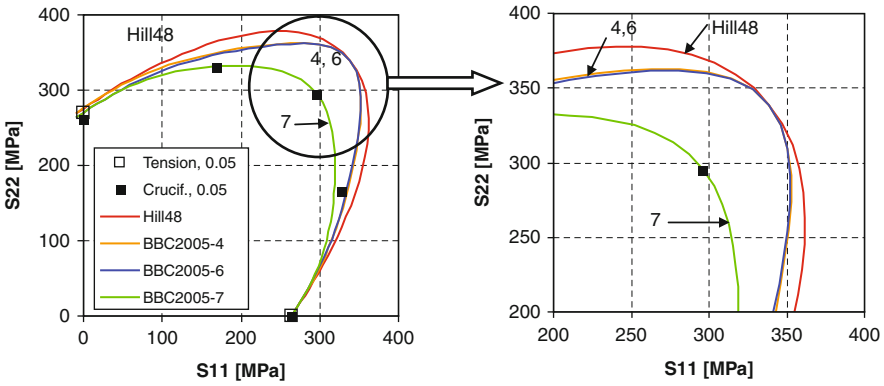

Fig. 4.15 Yield surfaces of the DC04-IF material in principal stress space. Yield functions: Hill 1948, BBC 2005-4, BBC 2005-6 and BBC 2005-7

4.2.1.4 Bulge Simulations

The bulge simulations are run with the 'Hydromech' functionality of the module AutoForm-Incremental of AutoForm 4.1 [2], both with the Hill 1948 and the BBC 2005 models. Three node shell elements with 5 integration points through the thickness are used. The initial element size is set to 4 mm in all simulations, and the adaptive refinement settings are chosen according to the AutoForm recommendations for final validation simulations [2]. In the simulation, the final internal pressure of 7.75 MPa is prescribed, and the strain distribution at the final (unknown) bulge height is computed.

In Fig. 4.16, measured minor and major strain values are plotted as data points over the distance s from the center of the specimen. Simulations are run with the Hill 1948, the BBC 2005-4, BBC 2005-6 and the BBC 2005-8 yield surface models, and the results are displayed with lines.

At the distance $s \approx 60$ mm the sheet was clamped in the experiments with help of a step bead. In the simulation, this clamping is not modeled in detail, so that for $s > 60$ mm the computed and measured strain values should not be compared.

4.2.1.5 Discussion

In a bulge test, the material near to the center of the specimen is in a biaxial stress state. On the other hand, the material at the edge where the sheet is clamped is in a plane strain state. Therefore, in a bulge test all material points are between a state of plane strain and biaxial stress, and it is to be expected that the simulation results are very sensitive to the choice of the biaxial stress point in the yield surface model. In fact, the simulation with the BBC 2005-7 model differs from the simulations with the other yield surface models.

Only the BBC 2005-7 model is able to describe the measured strain values accurately, whereas the other models give strain values that are too low, see Fig. 4.16.

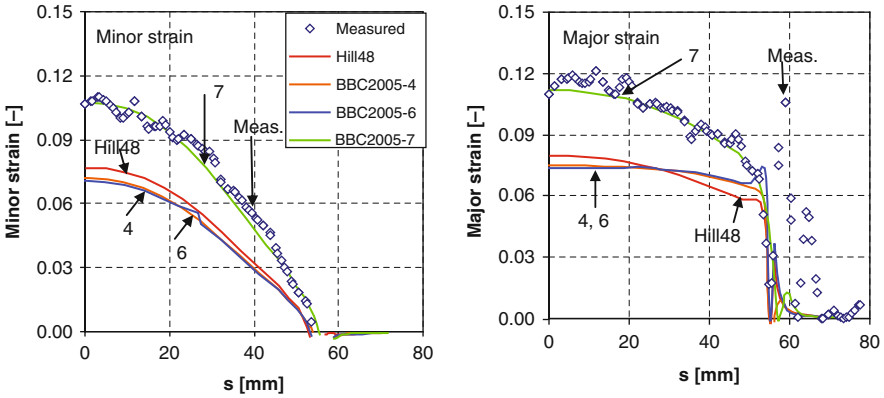

Fig. 4.16 Measured and computed principal strain for DC04-IF: (**a**) minor strain; (**b**) major strain. Yield functions: Hill 1948, BBC 2005-4, BBC 2005-6 and BBC 2005-7

Table 4.7 Computed final bulge height for an internal pressure of 7.75 MPa from Hill 1948, BBC 2005-4, BBC 2005-6 and BBC 2005-7 model

	Hill 1948	BBC 2005-4	BBC 2005-6	BBC 2005-7	Meas.
Final bulge height (mm)	17.1	17.2	17.3	20.2	20

Also the final bulge height is matched well by the BBC 2005-7 model and not by the others, see Table 4.7.

It is concluded that for hydroforming processes where an important fraction of the part is loaded near the equibiaxial stress state the usage of the BBC 2005-7 model can significantly improve the prediction of material flow, localization and final failure.

4.2.2 Simulation of Stretch Forming of Spherical Cup

In order to verify the accuracy of the determined parameters for a material model, we need information from some experiment the produces strain paths that are deviating from those paths used to determine the parameters, i.e. uni-axial and equi-biaxial strain paths. It is also an open question which values the exponent M should take for each material. Therefore, the idea with the current experiment is to achieve a strain path somewhere between plane strain and equi-biaxial stretching (Vegter H, 2006–2008, private communication). In order to achieve this, a circular blank is stretch formed with spherical punch. The diameter of the punch is 100 mm and during the experiment the edge of the blank is locked with a lock bead and a very high blank holder force. The blank is cleaned before the test and then no other lubrication is added to the blank.

Table 4.8 Experimentally determined anisotropy parameters of H180BD

σ_0 (MPa)	σ_{45} (MPa)	σ_{90} (MPa)	σ_b (MPa)	r_0	r_{45}	r_{90}	r_b
188	205	193	229	2.01	1.02	2.72	0.97

The material used in this example is H180BD bake hardening material. The experimentally determined anisotropy parameters are presented in Table 4.8. These parameters have been determined at Volvo Cars with experimental data from tensile test and viscous bulge test [3].

The opinion among almost every researcher and sheet metal forming simulation engineer in the world is that the exponent M is equal to six for all steel grades. This is based on results from Hosford [4]. But since he based his conclusions from studies on an isotropic material, one could question if this is also valid for an anisotropic material like the one used in this example. Therefore simulations have been performed with BCC 2005 material model using all parameters in Table 4.8 and two values of the exponent, namely M equals to five and M equals to six. For comparison the simulations have also been performed with the Hill 1948 material model.

Figure 4.17 presents several interesting results. First of all, the Hill 1948 material model overestimates both the punch force and the formability of the material since the simulation doesn't start to localise. The overestimate of the punch force is due to the fact that Hill 1948 overestimates the equi-biaxial yield stress for all materials with high Lankford coefficients. In order to explain why the localisation is delayed we also need to look at the BBC 2005 results. With the exponent M equal to five we observe that the simulation punch force curve slope changes almost at the same depth as the experimental curve slope changes. On the other hand, with the exponent M equal to six the change in slope is earlier in the simulations than in the experiments, i.e. an increase of the exponent reduces the punch depth where localisation starts in the simulation, see Mattiasson et al. [5]. The value of exponent M is also the explanation for why the Hill 1948 model localises too late, since the Hill 1948 model is exactly the same as using the BBC 2005 model with only the longitudinal yield stress together with the three uni-axial r-values as input and an exponent M equal to two. The final conclusion is therefore that it is important to have an accurate value of the exponent in the material model if it is too small the localisation in the simulations will start too late and if it is too large the simulation will localise too early.

In order to further analyse the difference between the material models, the major and minor strains at 27 mm punch depth are compared in a cross section through the centre of the punch. These results are displayed in Figs. 4.18 and 4.19. For both major and minor strains, the Hill 1948 predicts larger strains than was measured in the experiments. On the other hand, with an exponent M equals to six, the simulations predict smaller major and minor strains than in the experiments, while with an exponent M equals to five the agreement between simulations and experiments is very good.

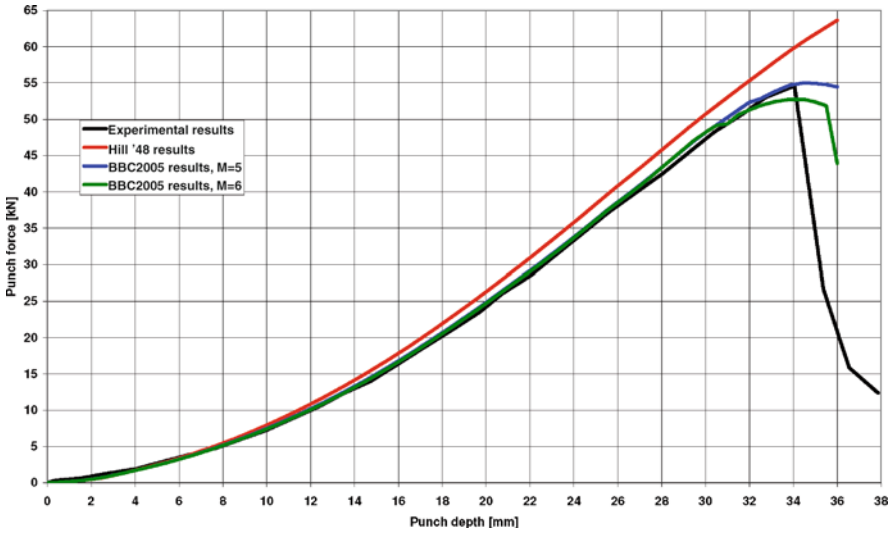

Fig. 4.17 Punch force versus punch displacement in both experiments and simulations with different material models

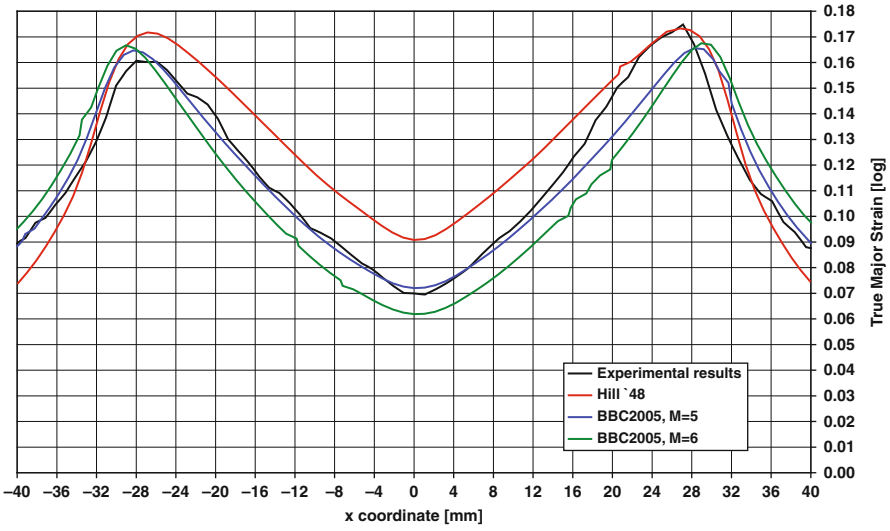

Fig. 4.18 Major strains at 27 mm punch depth

This example illustrates a few important facts that must be taken into consideration in the sheet metal forming simulations. First of all, the exponent M is not equal to six for all steel grades. In fact, studies at Volvo Cars have shown that the exponent M is different for different type of materials and in some cases also different for the same material from different suppliers. It has the lowest values for mild steel grades

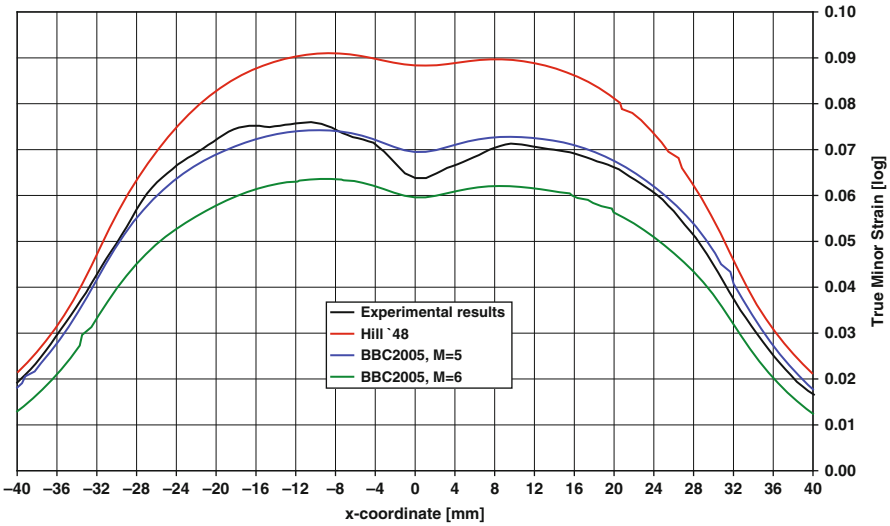

Fig. 4.19 Minor strains at 27 mm punch depth

with high formability and as the formability of the material diminishes, the value of exponent *M* increases. For some AHSS materials it is close to six and for some other AHSS material it is even larger than six. Furthermore, in order get the highest accuracy of the simulation one must use all parameters in Table 4.8 and perform simulations of some experiment to determine the appropriate value of the exponent *M*. If the simulation engineer uses the standard values, i.e. *M* equals to six for steel grades and *M* equals to eight for aluminium alloys, he or she will predict a different strain state than the real one and, what is even more important, predict localisation earlier than in reality, i.e. a too conservative prediction. But it is also important to emphasize that the BBC 2005 model with an exponent equal to six in this case has better agreement with experiments than the Hill 1948 material model.

4.2.3 Simulation of Cross Die

The measurements used in this section were performed in the European project 'Forming of metallic materials' (FOMM). In this project, the cross die geometry was used to assess the simulation accuracy of commercial finite element packages [6].

Raw data for a 0.79 mm thick DC04 material and a 1.01 mm thick Ac121-T4 material is available from these material characterization tests:

- uniaxial tensile tests under 0, 45 and 90° from RD
- bulge tests
- plane strain tests

For the simulation of the cross die, CAD data of the real tool and blank geometry is available, together with information about the process conditions (lubrication, blank holder force, tool movement etc.)

4.2.3.1 Hardening Description

The parameters of a combined Swift-Hockett/Sherby approach (Eq. 4.1) are approximated from hardening curves measured in the 0° tensile tests. The approximated hardening parameters are listed in Table 4.9:

Table 4.9 Hardening parameters of DC04 and Ac121-T4

Material	α	ε_0	m	C (MPa)	σ_i (MPa)	σ_{Sat} (MPa)	a	p
DC04	0.50	0.0061	0.26	561	153	415	6.13	0.8
Ac121-T4	0.50	0.0070	0.29	492	130	330	9.08	0.96

The yield stress σ_0 computed from these parameters is identical with the value used in the yield surface description.

4.2.3.2 Yield Surface Description

From the tensile tests, the three yield stresses σ_0, σ_{45}, σ_{90} and the three r-values r_0, r_{45}, r_{90} are known (see Table 4.10). From the load-deflection curves measured in the bulge tests, the biaxial yield stress σ_b can be derived. In the bulge tests, no strain measurement was performed. Therefore, the r_b-values of the materials are not known. The plane strain test data is not used.

The different strategies used in AutoForm to identify the coefficients in the BBC 2005 criterion are described in Tables 4.11 and 4.12. The exponent M is M=6 for steel and M=8 for aluminum.

In these tables, grey fields denote given experimental data. White fields denote values that are defined by the model. For example, for the Hill 1948 model in Table 4.3, r_0, r_{45}, r_{90} and σ_0 are input and r_b, σ_{45}, σ_{90} and σ_b are output parameters.

In the next figures, the yield surfaces of the above yield functions are displayed in the principal stress plane. The BBC 2005-8 formulation is missing because a measured r_b value is not available.

For the DC04 material, the yield surface of the Hill 1948 model is plotted in addition to the various forms of the BBC 2005 model (Fig. 4.20). Uniaxial yield stresses σ_0 and σ_{90} from the tensile tests and biaxial yield stress σ_b from the bulge

Table 4.10 Yield stresses and r-values of DC04 and Ac121-T4

Material	σ_0 (MPa)	σ_{45} (MPa)	σ_{90} (MPa)	σ_b (MPa)	r_0	r_{45}	r_{90}	r_b
DC04	151	166	163	192	1.83	1.39	2.11	–
Ac121-T4	126	122	121	137	0.65	0.40	0.77	–

Table 4.11 Strategy to define the coefficients of the BBC 2005 model for steel for cases where not all input is available: missing experimental input (white fields) for BBC model is filled up with Hill 1948 data

Availability of test results	Model	M	σ_0	σ_{45}	σ_{90}	σ_b	r_0	r_{45}	r_{90}	r_b
All data available	BBC 2005-8	6								
Biaxial test available but r_b not given	BBC 2005-7	6								
Biaxial test not available	BBC 2005-6	6								
Only r_0, r_{45}, r_{90} given, σ_0 arbitrary	BBC 2005-4	6								
Only r_0, r_{45}, r_{90} given, σ_0 arbitrary	Hill 1948	2								

Table 4.12 Strategy to define the coefficients of the BBC 2005 model for aluminium for cases where not all input is available: missing experimental input (white fields) for BBC model is filled up with Hill 1948 data

Availability of test results	Model	M	σ_0	σ_{45}	σ_{90}	σ_b	r_0	r_{45}	r_{90}	r_b
All data available	BBC 2005-8	8								
Biaxial test available but r_b not given	BBC 2005-7	8								
Biaxial test not available	BBC 2005-6	8								
Only r_0, r_{45}, r_{90} given, σ_0 arbitrary	BBC 2005-4	8								
Only r_0, r_{45}, r_{90} given, σ_0 arbitrary	Hill 1948	2								

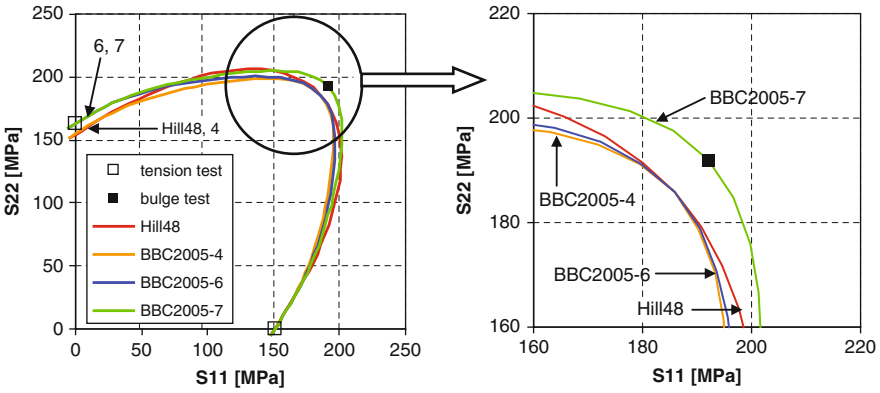

Fig. 4.20 Yield surfaces of the DC04 material in principal stress space. Yield functions: Hill 1948, BBC 2005-4, BBC 2005-6 and BBC 2005-7

test are plotted as data points. All yield functions use the given r-values as input. This is why the slopes of the yield surfaces in the uniaxial points are the same for all models.

The BBC 2005-7 model describes all measured yield stresses exactly because all of them are used as input parameters for the model. The BBC 2005-6 model matches only the measured σ_{90} value but not the σ_b value. Finally, the BBC 2005-4 curve and the Hill 1948 curve do not pass σ_{90} and σ_b but only σ_0.

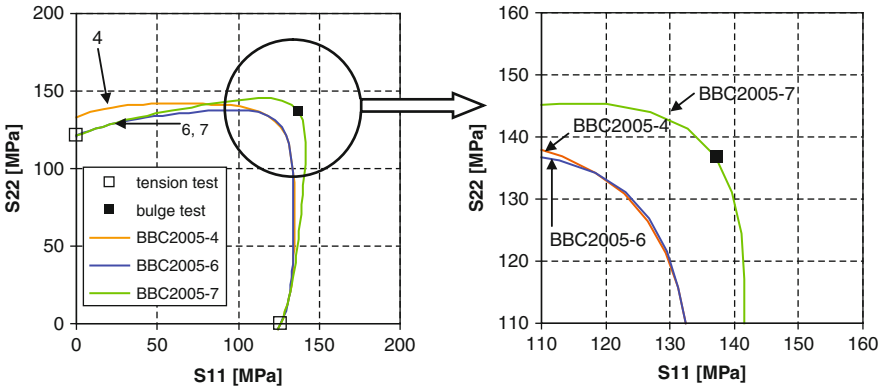

Fig. 4.21 Yield surfaces of the Ac121-T4 material in principal stress space. Yield functions: BBC 2005-4 (identical with Barlat 1989), BBC 2005-6 and BBC 2005-7

The Hill 1948 model is a special case of the BBC 2005-4 model with $M = 2$ instead of $M = 6$. Therefore, these models have the same uniaxial and biaxial yield stresses. The biggest differences between the Hill 1948 curve and the BBC 2005-4 curve is in the plane strain region.

For the yield surfaces of the Ac121-T4 material shown in Fig. 4.21, the previous discussion of the data in Fig. 4.20 holds as well. The only difference is that only the BBC 2005 models are displayed. This is because the Barlat 1989 model is identical with the BBC 2005-4 model, see Table 4.12.

4.2.3.3 Cross Die Experiments

The geometry of the cross die example is shown in Fig. 4.22 and Table 4.13.

In the experiments the sheet dimensions and the blank holder force were chosen such that a punch stroke of 60 mm could be reached without fracture, see Table 4.14.

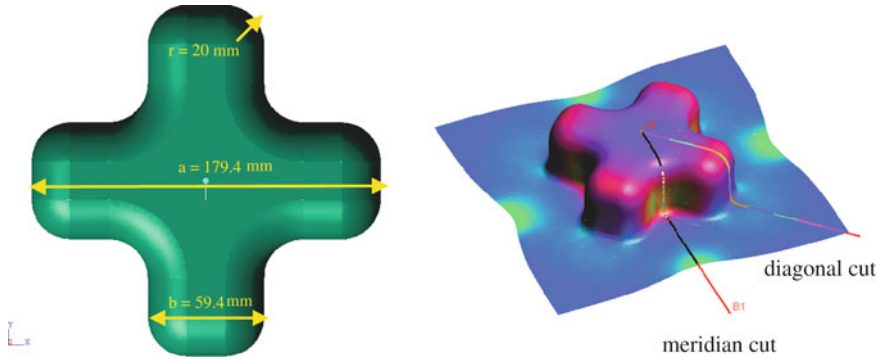

Fig. 4.22 *Left*: Punch geometry from above. *Right*: Sheet at punch stroke 60 mm, with sections for draw in measurements and thickness measurements

Table 4.13 Geometrical parameters of punch and die. The clearance between punch and die is 2.3 mm. Thus, on the die (not shown in Fig. 4.22) each radius has the value 22.3 mm

a_{punch} (mm)	b_{punch} (mm)	r_{punch} (mm)	a_{die} (mm)	b_{die} (mm)	r_{die} (mm)
59.4	179.4	20	64	184	22.3

Table 4.14 Experimental parameters for DC04 andAc121-T4

Material	Blank holder force (kN)	Sheet dimensions (mm)	Lubrication
DC04	350	330 × 330	Grease
Ac121-T4	116	260 × 260	Grease/teflon

After stopping the forming after 60 mm punch stroke, the draw in and the thickness were measured along the two sections displayed in Fig. 4.22.

4.2.3.4 Cross Die Simulations

The simulations of the cross die forming experiments were run with the module AutoForm-Incremental of AutoForm 4.1, employing three node shell elements with 5 integration points through the thickness. The initial element size was set to 11 mm in all simulations. The adaptive refinement settings were chosen following the AF recommendations for final validation simulations [2]. Typically, this resulted in 35 solution increments with 2,200 elements at the beginning and 12,000 elements at the end of the simulation.

First of all, in simulations using the BBC 2005-7 yield surface model the coefficient of Coulomb's friction law and the elastic stiffness of the tools were adjusted to measured draw in values along the diagonal and the meridian cut. A value of 0.05 for Coulomb's friction coefficient was found to give a satisfactory agreement between measured and computed draw in both for DC04 and Ac121-T4. Note that the experiments were carried out with special lubrication, see Table 4.14. The elastic stiffness of the blankholder was increased by a factor of 20 compared to the AutoForm default value. This was necessary because in the experiments the binder was not ground (or spotted) for sheet thickening. The following simulations with different yield surface models were run with these settings fixed.

In Figs. 4.23 and 4.24, thickness measurements are compared with computed thickness distributions for the yield surfaces displayed in Figs. 4.20 and 4.21. The distance s runs from the centre of the cross specimen outwards along the diagonal cut and the meridian cut as displayed in Fig. 4.22.

For the DC04 material, the simulation with the BBC 2005-7 model matches the thickness measurements very well. Especially, the minimum thickness is predicted accurately. All the other yield surface descriptions yield higher deformations and, thus, overestimate the risk of failure for that part.

For the Ac121-T4 material, the BBC 2005-7 simulation matches the thickness measurements rather well, especially in the meridian cut. In the diagonal cut, the

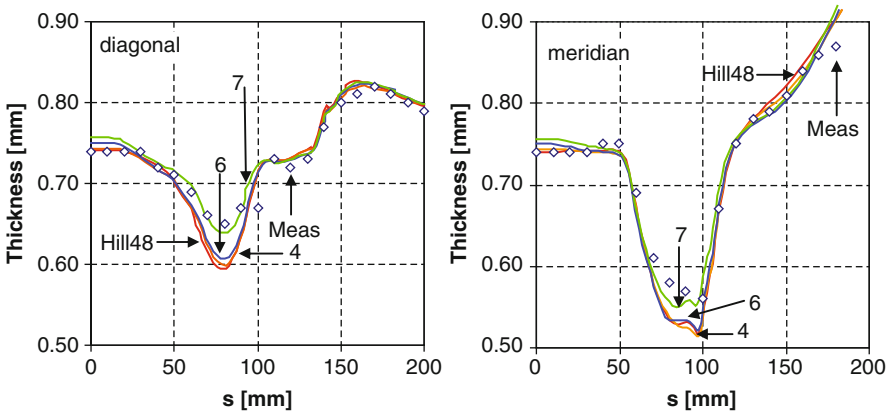

Fig. 4.23 Measured and computed thickness for DC04. Yield functions: Hill 1948, BBC 2005-4, BBC 2005-6 and BBC 2005-7

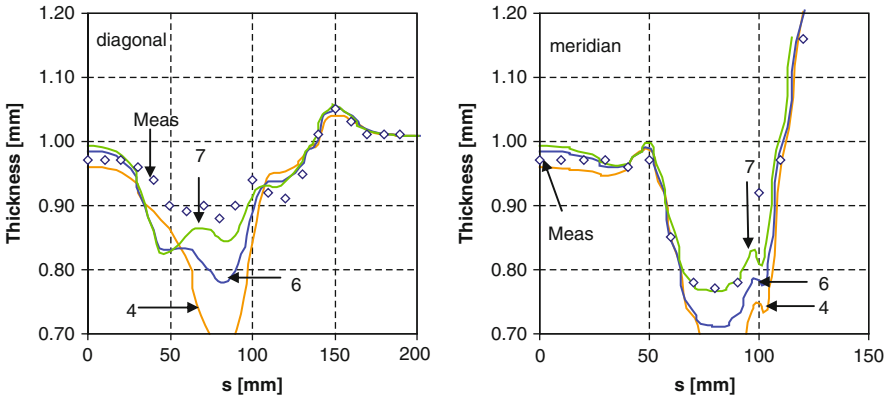

Fig. 4.24 Measured and computed thickness for Ac121-T4. Yield functions: BBC 2005-4 (identical with Barlat 1989), BBC 2005-6 and BBC 2005-7

agreement between measured and computed thickness is not as good as it is for the DC04 material in Fig. 4.23. Anyway, the data is described much better by the BBC 2005-7 model than by BBC 2005-6 and BBC 2005-4 (which is identical with the Barlat 1989 model). The widely used Barlat 1989 model largely overestimates the risk of failure for that part.

4.2.3.5 Discussion

Although the differences between the various yield surface models do not seem to be very large at first sight (see Figs. 4.20 and 4.21), the cross die test is by far best described with help of the BBC 2005-7 model. The results demonstrate that for an accurate failure prediction it is crucial to take not only the uniaxial yield stresses and

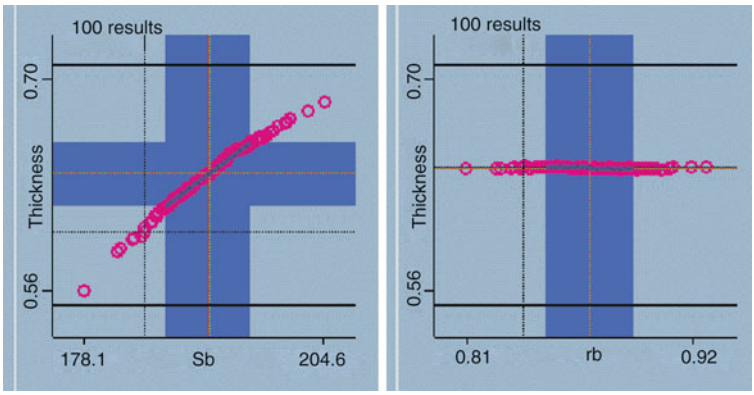

Fig. 4.25 Measured and computed thickness for DC04, diagonal cut, $s = 80$ mm. *Left*: Variation of σ_b. *Right*: Variation of r_b

r-values into account but also the biaxial yield stress σ_b. The question remains if the prediction could be further improved by taking also the r_b value into account with help of the BBC 2005-8 model. Since no measured r_b value is available, this question was tackled with a purely numerical sensitivity analysis using the the module AutoForm-Sigma of AutoForm 4.1.

Two series of simulations were performed for the DC04 material. In the first series, only the σ_b value was varied while keeping the other material parameters fixed. In the second series, the same procedure was applied to the r_b value. The computed thickness is evaluated in the diagonal cut at the position of minimum thickness ($s \approx 80$ mm). The results are compared in Fig. 4.25.

The dependency between the computed thickness and the biaxial yield stress σ_b is nearly linear, especially in the range 192 MPa $\pm$ 4.8 MPa that is indicated by the vertical blue band in the left part of Fig. 4.25. The value of 4.8 MPa was input as standard deviation for the SIGMA analysis. Since no statistical information was available for the DC04 material, the value was arbitrarily chosen to be 2.5% of the value 192 MPa.

The assumed standard deviation for the biaxial anisotropy parameter r_b is 0.02175 (2.5% of the value 0.87). The effect on the result is hardly visible. This means that even if r_b would have been measured and used in the simulation, it had no significant impact on the computed minimum thickness.

In this light, for the cross die simulation the usage of the BBC 2005-7 model is proven to be sufficiently accurate.

4.3 Simulation of the Industrial Parts Forming Processes

The first example studies the different material models for a H180BD bake hardening material. The experimentally determined anisotropy parameters are presented in Table 4.15. These parameters have been determined at Volvo Cars with experimental data from tensile test, viscous bulge test [3] and stretch forming test with a spherical punch. This is the same material as in Sect. 4.2.2

Table 4.15 Experimentally determined anisotropy parameters of H180BD

σ_0 (MPa)	σ_{45} (MPa)	σ_{90} (MPa)	σ_b (MPa)	r_0	r_{45}	r_{90}	r_b	M
188	205	193	229	2.01	1.02	2.72	0.97	5.0

Generally, not all data in Table 4.15 are always available for all materials in the industry. Therefore, it is interesting to compare three different set-ups:

- Hill 1948 material model in which measured σ_0, r_0, r_{45} and r_{90} are used as input and M equals 2. This is how the majority of industrial simulations are done today. All other parameters, i.e. σ_{45}, $\sigma_{90,}$ σ_b and r_b, are in this case predicted by the material model. For this particular material, the Hill 1948 material model overestimates both the σ_{45} and σ_{90} values while r_b is lower than the measured value, see Table 4.16.
- BBC 2005 with six parameters measured in tensile tests: σ_0, σ_{45}, $\sigma_{90,}$ r_0, r_{45} and r_{90}. Here σ_b and r_b are then values predicted by AutoForm which in this case means the same values as for Hill 1948. In this set-up M is equal to 6 for steel grades and 8 for aluminium alloys. This set-up is called AF in Table 4.16.
- BBC 2005 with all data in Table 4.16.

Table 4.16 Anisotropy parameters used in the simulations

	σ_0 (MPa)	σ_{45} (MPa)	σ_{90} (MPa)	σ_b (MPa)	r_0	r_{45}	r_{90}	r_b	M
Hill 1948	188	246	197	248	2.01	1.02	2.72	0.74	2.0
BBC 2005-6	188	205	193	248	2.01	1.02	2.72	0.74	6.0
BBC 2005-8	188	205	193	229	2.01	1.02	2.72	0.97	5.0

4.3.1 Simulation of an Outer Trunklid

The differences between the yield loci with these three different settings are small, it is only in the plane and equi-biaxial strain part of the yield locus that the three set-ups are different. It is therefore easy to come to the conclusion that they should produce similar results. In order to test this conclusion, simulations of the forming of an outer trunklid with all three set-ups have been performed in AutoForm 4.1.1. In these simulations all other inputs, e.g. friction coefficients, draw bead restraining forces and hardening curves are identical. The results from the simulations are also compared with results from trials of the same material in Volvo Cars production.

The forming experiments revealed no major forming problems but in two areas on the addendum surfaces the comparisons between experimental and numerical results are extremely interesting. The first area was at the rear upper corner of the part. Here a small failure occurred in the experiments, but this fracture could easily be removed with a small modification of the addendum in this area. This area

is called Area A in Fig. 4.26. The second area is the transition area between the horizontal part and the vertical part of the trunklid. In this area the material was subjected to very large strains but there was no failure. This area is called Area B in Fig. 4.26.

Generally, the simulation results with the three different set-ups are very similar when compared. But in the two areas mentioned above, the three different set-ups produce quite different results.

The strain signatures for Area A with the three different simulation set-ups are displayed in Fig. 4.27. In this area, the Hill 1948 and the BBC 2005 material model will all experimental parameters produces similar results and with both set-ups the maximum principal strains are far above the FLC curve. The strain state is more severe with the BBC 2005 model, but both material models clearly predict a fracture in the simulation is this area which corresponds well with experimental results. In the BBC 2005 model using only tensile test data, the so called AutoForm set-up, all major strains in this area are below the FLC and therefore no fracture in the part according to this set-up.

In the Area B, the two BBC 2005 set-ups are producing similar results, see Fig. 4.28. It also seems that BBC 2005 using all data from Table 4.15 predicts a

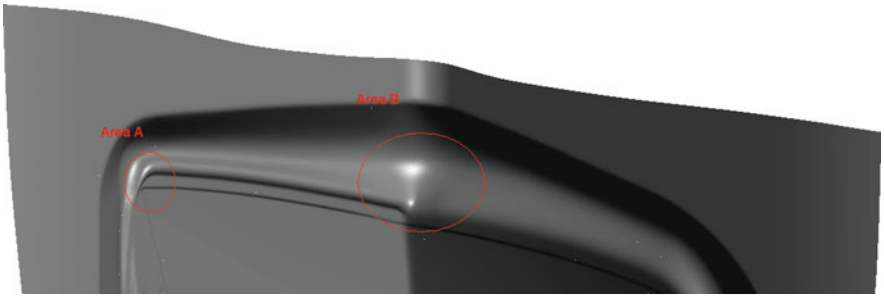

Fig. 4.26 The two studied areas

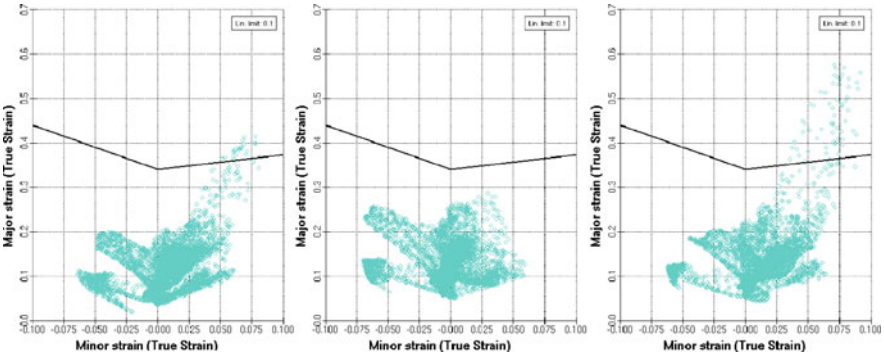

Fig. 4.27 Strain signatures for the Area A with Hill 1948 (*left*), BBC 2005 with tensile test data (*middle*) and BBC 2005 with all parameters (*right*)

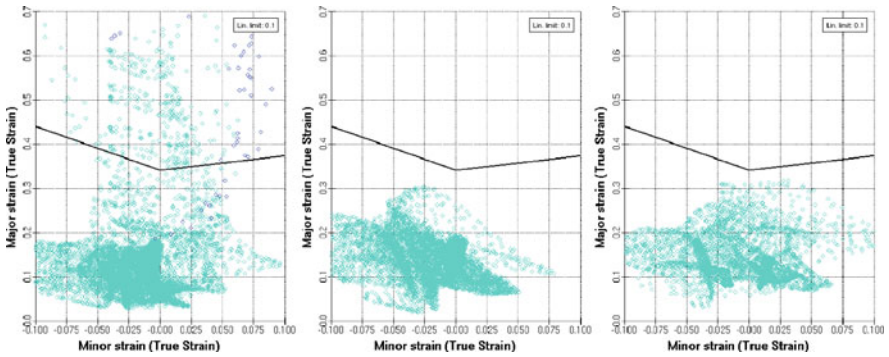

Fig. 4.28 Strain signatures for the area B with Hill 1948 (*left*), BBC 2005 with tensile test data (*middle*) and BBC 2005 with all parameters (*right*)

slightly more severe strain state than BBC 2005 using only tensile test data. These results are also in good agreement with experimental observations where very large deformations were observed without any fracture. The Hill 1948 set-up yields a completely different strain signature. The major strains are far above the FLC curve and the strains are so large that the software removes elements in this area. There is therefore no doubt that there would be a fracture in this area according to the Hill 1948 material model.

The final conclusion is that although the yield loci are similar in this case, the BBC 2005 model predictions are much closer to the test results than the Hill 1948 predictions in the studied areas. The explanation for the difference is that the two strain states studied are close to plane strain see Figs. 4.27 and 4.28, and here the differences between the three yield loci are large.

The BBC 2005 model with all parameters as input models the equi-biaxial and plane strain part of the yield locus with high accuracy since it is using the measured equi-biaxial stress as input. The choice of M-value then determines stress state at plane strain. By comparing experimental and simulation results from e.g. stretch forming experiments with friction, an appropriate value of M for each material could be determined, see Sect. 4.2.2.

The Hill 1948 material model overestimates in this case the equi-biaxial stress and since M is low, the stress state at plane strain is incorrect. This then yields the poor agreement with experiments for Area B in this case. In Area A, the agreement with experiments is good, which is due to the fact that this strain state is more biaxial than the strain state in Area A.

The example also shows the major improvement of the simulation accuracy changing from Hill 1948 material model to BBC 2005 material model. Based on the results from Hill 1948, the part would be classified as not feasible with this material, but with both settings of BBC 2005 material model one problem area disappears. The recommendation therefore is to always use the BBC 2005 material model. If only tensile test data are available it would still be a major improvement of the simulation accuracy.

Finally, a comment on these results compared to the results from the stretch forming experiment of the same material in Sect. 4.2.2. In the present case we see that in Area B is the formability of the material increases going from the Hill 1948 to the BBC 2005 material models, while in the stretch forming experiment the formability of material was reduced going from Hill 1948 to the BBC 2005 material model. At first these results seems to be in contradiction to each other, but what they really shows is the complexity of material modeling. One cannot make a general statement that going from Hill 1948 to BBC 2005 material models would give a certain effect for all grades and for all strain states. But, it is also clear that the agreement between simulation and experimental results always would be improved going from Hill 1948 to BBC 2005 material models, which this example have shown.

4.3.2 Simulation of a Sill Reinforcement for Volvo C30

The second example is a Sill Reinforcement for Volvo C30 (Fig. 4.29) [7]. In this case has a 1.1 mm thick DP600 is used. In this example two different material models are compared, the Hill 1990 and the BBC 2005 material models and the purpose of the study was to evaluate the influence of material and process scatter on springback predictions. The used material data in the stochastic simulations are presented in Table 4.17. For the Hill 1990 material model only σ_0, r_0, r_{45} and r_{90} used as input while for BBC 2005 are all data in Table 4.17. used as input.

As well as this, the hardening curve, Young's modulus, Draw bead restraining forces, friction coefficient and blank centre were allowed to vary in the AutoForm-Sigma simulations (see Sect. 4.4), but these variations were the same for both material models. For more information about the set up and also the results, see [7].

The springback after forming was evaluated in twenty different points that corresponded to the measuring point in running production. The min, mean, max and standard deviations from the simulations were then compared with results from

Fig. 4.29 The Sill reinforcement for Volvo C30

Table 4.17 Material data for Sill reinforcement study

	σ_0 (MPa)	σ_{45} (MPa)	σ_{90} (MPa)	σ_b (MPa)	r_0	r_{45}	r_{90}	r_b
Min	331	339	345	361	0.53	0.70	0.92	0.80
Median	383	386	402	416	0.74	0.87	1.16	0.90
Max	430	417	439	451	0.95	1.14	1.40	1.00
Std. Dev.	18.0	14.2	12.1	16.4	0.07	0.09	0.08	0.03

Table 4.18 Root mean square errors for the springback predictions

	Hill 1990	BBC 2005
Median value	1.21 (mm)	0.91 (mm)
Std. dev.	0.12 (mm)	0.07 (mm)

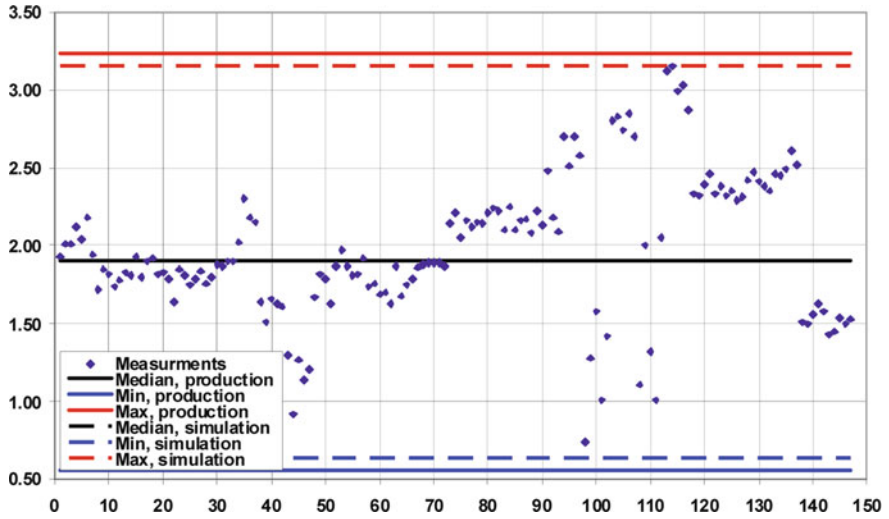

Fig. 4.30 Measured and predicted values obtained in one measuring point with BBC 2005 material model

production. Generally, the agreement between predicted and measured standard deviations was quite good, while the agreement between predicted and measured mean-values was poorer. Another interesting observation was that the BBC 2005 model has a better agreement with production measurements than the Hill 1990. This was determined by computing the root mean square error for the results from the two material models, see Table 4.18. In Fig. 4.30, all production measurements are presented together with predicted and measured min, median and maximum spring back values for the BBC 2005 material model for one of the measuring points. In this case the agreement is excellent.

4.4 Robust Design of Sheet Metal Forming Processes

Even with the extreme high level of today's simulations it still happens that in real life production scrap has been produced. On the one hand this is caused by the difference between reality and the simulation. On the other hand a simulation is only one simulation prescribing one specific set of properties and settings.

We all know that in reality variability and noise exist. The applied forces of the press are not as constant as we want them to be. The film of oil is not always as thick as we want it to be. And also the mechanical properties are not always as exact as we want them to be.

This uncertainty has been accommodated by introducing safety margins and worst case scenarios. Hence, this engineering practice has reduced the incorporation of the variability and noise into a deterministic problem. This approach however doesn't say anything about the variability of the result. It can result in much too conservative solutions which might be too expensive. On the other hand it doesn't even guarantee a reliable process.

So, in order to improve the prediction of the reliability of the production we have to incorporate the variability and noise and solve a stochastic problem instead of a deterministic one [8].

4.4.1 Variability of the Material Parameters

In this section we will consider the variability of the material properties incorporated by the parameters of the constitutive equations. Next we will have a closer look at the mechanical properties of a high strength steel, in this case HCT600X. The mechanical properties of the HCT600X according to DIN EN 10336 are listed in Table 4.19.

The norm data shows a relatively large tolerance range. 132 batches of material delivered according to the above mentioned specifications have been evaluated. Table 4.20 gives a summary of the mechanical properties $R_{p0.2}$ and R_m, and the thickness variation from the nominal thickness.

The average values of the mechanical properties perfectly fit with the above mentioned norm. But looking at the minimum and maximum values one can see that a

Table 4.19 Mechanical properties for HCT600X according to DIN EN 10336

Yield strength	Tensile strength	Elongation
$R_{p0.2}$	R_m min	A80 min
MPa	MPa	%
340–410	600	20

Table 4.20 Mechanical property and thickness variation for HCT600X

	$R_{p0.2}$ (MPa)	R_m (MPa)	Dt (mm)
Average	378	631	0.00
Min	330	518	–0.09
Max	430	697	0.07
Stand. dev.	20.4	29.7	0.03
No. of Samples	132	132	132

Table 4.21 Variation of the r_0, r_{45} and r_{90} values for HCT600X

	$r_{0°}$	$r_{45°}$	$r_{90°}$
Average	0.73	0.88	0.94
Min	0.50	0.72	0.07
Max	1.05	1.05	1.35
Stand. dev.	0.09	0.06	0.09
No. of Samples	122	122	122

large window of both the yield stress and tensile strength exits. It even turns out that some of the samples fall outside the norm prescriptions. The standard deviation of the $R_{p0.2}$ and R_m are both roughly 5% of the average value, meaning that 68% of the samples are varying from 358 to 398 for the $R_{p0.2}$ and from 601 to 661 for the R_m.

Although not in the norm, for simulation purpose later, we will have a look at the r-values. Table 4.21 gives a summary of the three r-values, r_0, r_{45} and r_{90}. Studying this data, one can see that also the variation of the r-values is relatively large. The standard deviation is roughly 10% of the average value. As an example we can have a look at the most extreme of the three *r*-values, the r_0. The average value is 0.73 and 68% of the samples have a value between 0.64 and 0.82.

In summary we can say that the properties of the HCT600X are not a constant set of properties. In general one can say that for every material grade mechanical properties vary. In order to incorporate this variation into a simulation model, we have to step into stochastic analysis.

4.4.2 AutoForm-Sigma

Today's simulations are mainly applied to evaluate the feasibility of a part and its forming process. The outcome is a virtual prototype saying that it is possible to produce the part. In fact one process point has been defined. However, when going into production a process window must be known to guarantee a stable production process. In order to achieve the latter condition, we are suggesting a stochastic analysis. Based on multiple simulations, the influence and sensitivity of various process parameters on the forming process can be identified. By combining the analysis with the statistical process control evaluation, the process capability (Cpk-values) can be defined. The result of the stochastic analysis is the identification of the process window and process capability before any tool has been manufactured. So, we have to solve the stochastic problem instead of the deterministic one.

Looking up the word *stochastic* in the dictionary one finds a description like: *being or having a random variable*. The mechanical properties as described in Sect. 4.4.1 clearly have a variability. So, if we want to incorporate this variability we have to enter the world of stochastics.

How should such an analysis look like? The stochastic analysis consists of multiple simulations. In the various simulations some parameters are varied. The

parameters which are varied are called the design variables. In our case the design variables are the mechanical properties like $R_{p0.2}$, R_m and the three r-values. The thickness variation can also be defined as a design variable.

The exact values of the design variables are chosen randomly but it can be defined that this random distribution represents the normal distribution. The combination or pairing of the various design variables is also chosen randomly. In this case we are making use of Latin Hypercube techniques. The set of simulations are all solved automatically generating several result files. The number of simulations strongly depends on the number of design variables. The total number of simulations can exceed 100.

It is relatively impossible and very time consuming to evaluate these simulations individually. How can we evaluate the set of stochastic simulations? For that reason, special result variables have been defined to ease the evaluation of multiple simulations at once. These result variables are based on statistic algorithms. Several of these result variables will be described below.

The variation of the result is described with the help of the Standard Inter Quantile Range (Standard IQR). This measure can be applied on random distributions and is equivalent to the standard deviation in case of a normal distribution. So, this result variable indicates how much the result will vary. In worst cases this result variation will yield in production failure.

The influence is a measure for the extent to which a parameter influences the result. The influence can vary from 0 to 1. A value of 0 means no influence at all so the result is absolutely independent of the parameter. A value of 1 means a strong influence so the result is completely dependent on the parameter.

The sensitivity is a measure of the capability of the parameter to control the result. Its value shows how much the result will change in case that the parameter will be changed.

Statistical process control is normally applied during production in order to validate the productivity and capability of the production process. Since we have the possibility to perform multiple simulations taking into account the real life variability it is only a small step to apply the statistical process control on the simulation results. By doing so, we can evaluate the success rate of the proposed production process in an early stage without manufacturing any of the tools.

For statistical process control, the process precision (also called process capability) Cpk has often been used. The process precision indicates the controllability of the process around the given specification limit. It indicates the probability of the result exceeding the specification limit because of the given variation of the input [9].

4.4.3 Robust Design: Case Studies

The methodology described in Sect. 4.4.2 is applied on two cases of automotive parts currently in production: a Front Side Member Inner and a Hood Inner. The application examples show how the stochastic analysis can be applied today in engineering practice.

4.4.3.1 Case 1: Front Side Member Inner

The first case presents the results from a project carried out by Volvo Car Corporation and AutoForm Engineering. The objective of this project was to study the influence of the scatter in mechanical properties on the sheet metal forming simulation results.

The project has studied the forming of the front side member inner (FSMI) made from a tailor welded blank (HCT600X and HCT260P) incorporated in the Volvo S40/V50 model. This part was chosen since it was known to have splitting problems in production that were not visible in the final forming simulation [10].

An effective way to visualize splitting is using the result variable failure. This variable is defined as the ratio between the major strain at a specific point and the major strain of the FLC at the same minor strain value. This implies that splits occur at a value of 1.0 or more since at that value the point reaches the FLC. Values below 1.0 indicate that the point is still below the FLC, i.e. a value of 0.8 indicates the point is 20% below the FLC. In engineering practice one works with values between 0.6 and 0.8 as limit introducing a 40–20% safety margin.

Figure 4.31 shows the failure values of the FSMI as obtained in the basic simulation. One can clearly distinguish that all failure values are below the 0.6 mark (red) being at the very safe side.

As mentioned before, we studied this part since it was known to have splitting problems in production that were not visible in the final forming simulation. The hypothesis was that these differences come from the scatter of the blank mechanical properties. To investigate this, a stochastic analysis has been performed based on the

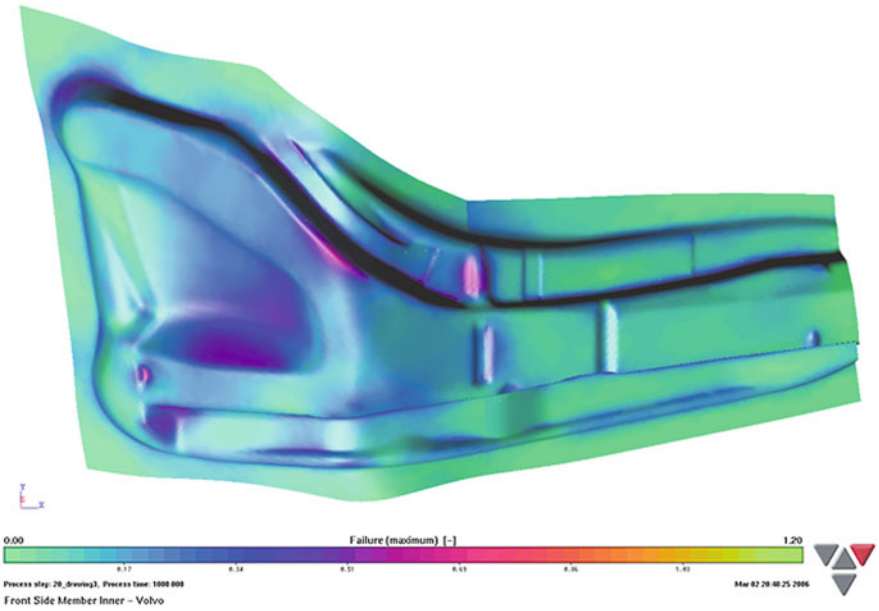

Fig. 4.31 Maximum failure results of the basic simulation

scatter values as indicated in Tables 4.20 and 4.21. The variation of the mechanical properties $R_{p0.2}$ and R_m has been introduced by manipulating the basic flow curve. The variations of the r-values are incorporated in the constitutive equation, in this case we used the Hill 1948 model. The thickness variation is simply introduced by varying the initial thickness.

For this stochastic analysis, 100 simulations have been performed automatically while varying the design variables, which are actually noise variables.

It is a relatively impossible and very time consuming task to evaluate these 100 simulations individually to check whether and how much of the simulations are critical. So, the special result variables will be used to ease the evaluation of the 100 simulations at once.

In order to evaluate the sensitive zones, the result variable Standard IQR of failure is used as shown in Fig. 4.32. The larger the value of the Standard IQR, the more variation of the failure values due to the variation of the input exists. So, in the yellow zones, the most important variation of the failure value is seen, meaning that in those regions the failure value is sensitive to the variation of the mechanical properties. In these sensitive zones the failure value can easily exceed critical values due to the variation of the input. Two sensitive zones can be distinguished as indicated with white circles in Fig. 4.32.

The easiest way to check whether a sensitive zone exceeds a critical value is to define a limit value and calculate the probability whether the result will exceed this value. In this case we define an Upper Specification Limit (USL) of 0.8 for the

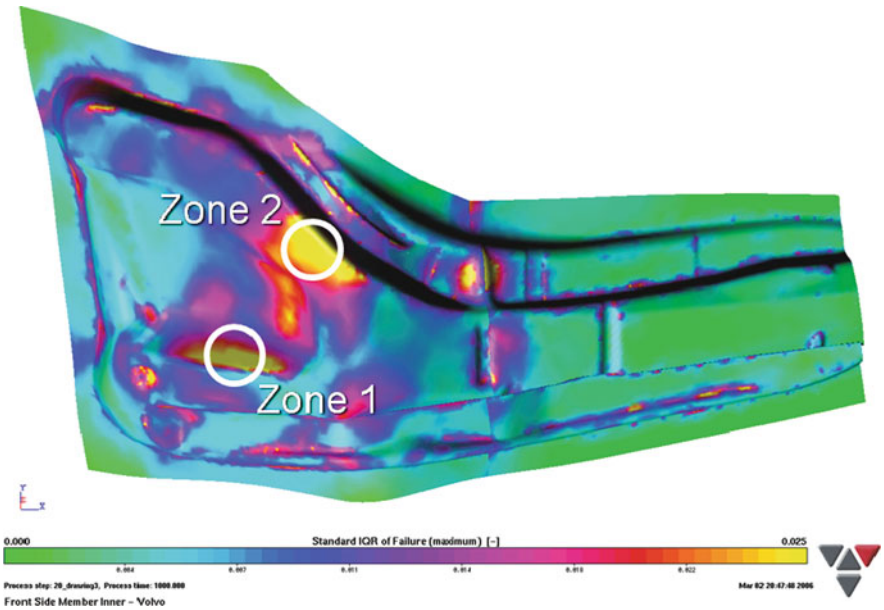

Fig. 4.32 Standard IQR of failure of the stochastic analysis to indicate the sensitive zones as indicated with the *white circles*

failure value and evaluate the process precision Cpk. The process precision is used very often in quality process control and is evaluated according to the colour scheme as given in Table 4.22. The traffic light color scheme directly expresses the process precision according to DIN 55319.

This process precision classification can directly be plotted on the part (Fig. 4.33). Most of the part is green, meaning that the process is reliable. A reliable process has an expected reject rate smaller than 0.004%.

But in zone 1 a red spot can be distinguished. This red spot indicates that the process is unacceptable resulting in more than 2.25% rejects. This spot indeed coincides with the spot which has been indicated as a critical area during production.

For a more detailed evaluation of the process precision, the histogram shows the frequency of how often a failure result has been obtained due to the variation of the input (Fig. 4.34). The vertical black line shows the defined specification limit of 0.80 maximum failure. It can be seen that in some cases the 0.80 mark is passed which indicates risk of failure. With help of the histogram one can more precisely analyze how reliable or unreliable the process is. In zone 1 three from the 100 simulations

Table 4.22 Colour scheme of process precision according to DIN 55319

Green	Reliable	No more than 0.004% of the results are outside the limits
Yellow	Control required	Between 0.004 and 0.14% of the results are outside the limits
Orange	Unreliable	Between 0.14 and 2.25% of the results are outside the limits
Red	Unacceptable	More than 2.25% of the results are outside the limits

Fig. 4.33 Process precision Cpk of failure plotted on the front side member inner

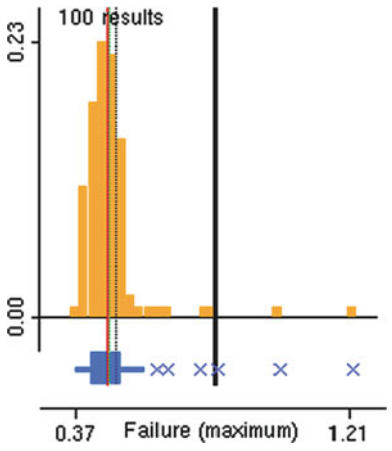

Fig. 4.34 Histogram for zone 1 showing the frequency of failure

result in a failure value higher than the USL of 0.8, which in quality process control measures means unacceptable.

The application example showed that realistic scatter of blank mechanical properties clearly influence the sheet metal forming simulation.

4.4.3.2 Case 2: Hood Inner

The second case shows a hood inner [11]. The basic parameters of the hood inner production have been listed in Table 4.23. The hood inner has been produced with uncoated material as well as zinc coated material. The material specification SPCD (Japanese norm) is equivalent with DC03 (European norm) and SPCD GA (Japanese norm) is equivalent with DX53D (European norm).

The optimized stamping process showed a feasible part in the simulation. The formability evaluation shows a 'green' result. The tolerated thinning has been defined on a demanding –0.20. Unfortunately, the production of the part didn't go as easily as the optimized simulation predicted. During a 10 weeks monitoring phase, splitting at two areas of the part have been observed resulting in unacceptable reject rates (Fig. 4.35).

During the monitoring phase the mechanical properties of all coils have been determined as well. An overview of the mean values and its extremes is listed

Table 4.23 Basic parameters of the hood inner production

Thickness	0.62 mm
Material	SPCD, SPCD GA
Coil width	1,439 mm
Coefficient of friction	0.15
Blank holder force	60 tons
Press type	Single action

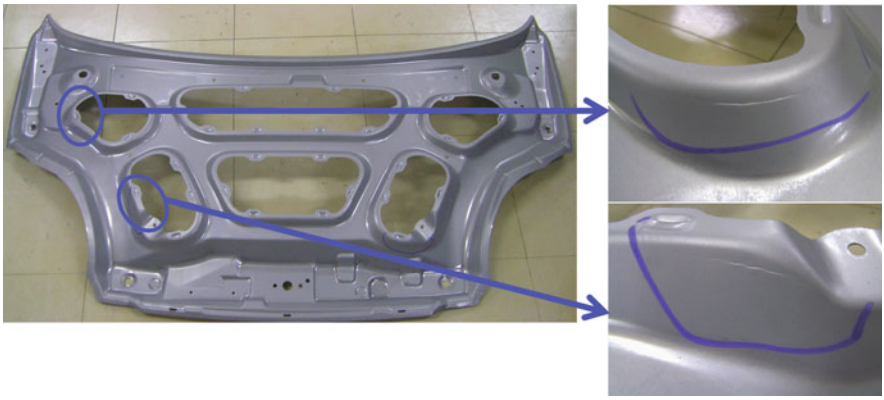

Fig. 4.35 Necking of the hood inner

in Table 4.24. We have to state that no difference in mechanical properties of the uncoated and zinc coated material has been found.

The surface structure of both materials (the uncoated and zinc coated variant) are different. Because of this, strip draw tests have been performed in order to determine the coefficient of friction. Since the amount of conservation oil also varies, strip draw tests with material as delivered and the oil wiped off have been performed. The results of the strip draw tests are summarized in Table 4.25. One can clearly see that the coefficient of friction for the zinc coated material is very sensitive to the lubricant condition.

The stochastic analysis has been performed in order to investigate the influence of the above mentioned parameter variations on the stamping result. In our case the noise variables are the mechanical properties like yield strength and tensile strength. The thickness variations as well as the variation of the coefficient of friction have been defined as noise variables too. The noise variable input is defined in

Table 4.24 Mechanical property variation

	Mean	Min	Max
Yield strength (MPa)	154	142	165
Tensile strength (MPa)	311	303	321
Thickness (mm)	0.620	0.615	0.629
r-value	1.89	1.76	2.06
n-value	0.232	0.224	0.237

Table 4.25 Coefficient of friction for different lubricant conditions for both materials

Lubricant condition	Uncoated	Zinc coated
Conservation oil	0.141	0.139
Wiped off	0.144	0.189

Table 4.26. A theoretical normal distribution has been assumed, which represents the real distribution very well [9].

The nominal simulation has been evaluated with respect to thinning. As can be seen in Fig. 4.36, several areas have thinning values close to the critical limit of –0.20, although none of them exceeds this critical limit. In order to evaluate the stochastic analysis of 100 simulations, the special result variables have been applied.

The easiest way to check whether a result might exceed a critical value is to define a limit value and calculate the probability whether the result will exceed this value. In this case we define a Lower Specification Limit (LSL) of –0.2 thinning and evaluate the process precision Cpk.

The process precision classification (Cpk) can be plotted directly on the part (Fig. 4.37). Most of the part is green, meaning that the process is reliable. But also

Table 4.26 Noise variable input

Noise variable	Median	Standard deviation	Min	Max
Yield strength (MPa)	154	3	142	165
Tensile strength (MPa)	311	3	303	321
Thickness (mm)	0.620	0.0023	0.615	0.629
Coefficient of friction	0.15	0.0067	0.13	0.18

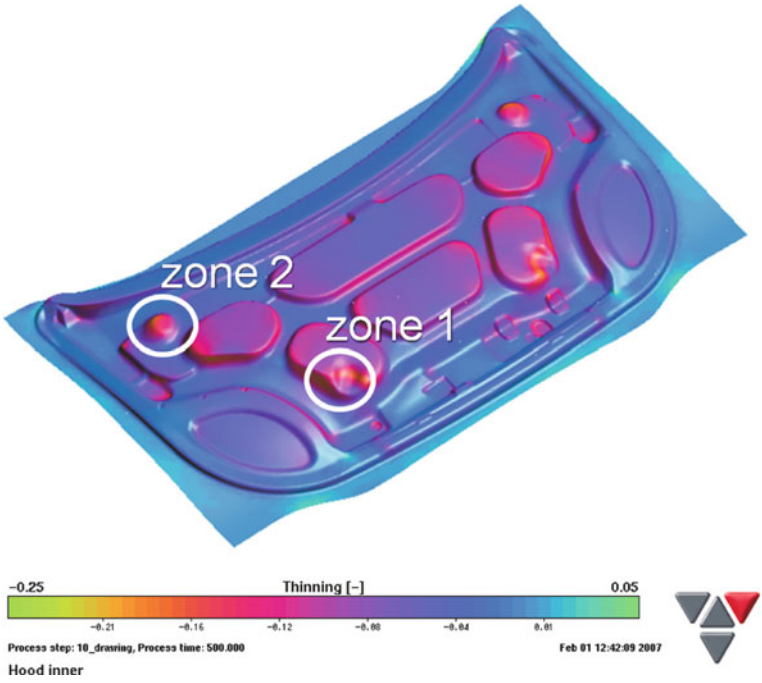

Fig. 4.36 Thinning distribution of the hood inner

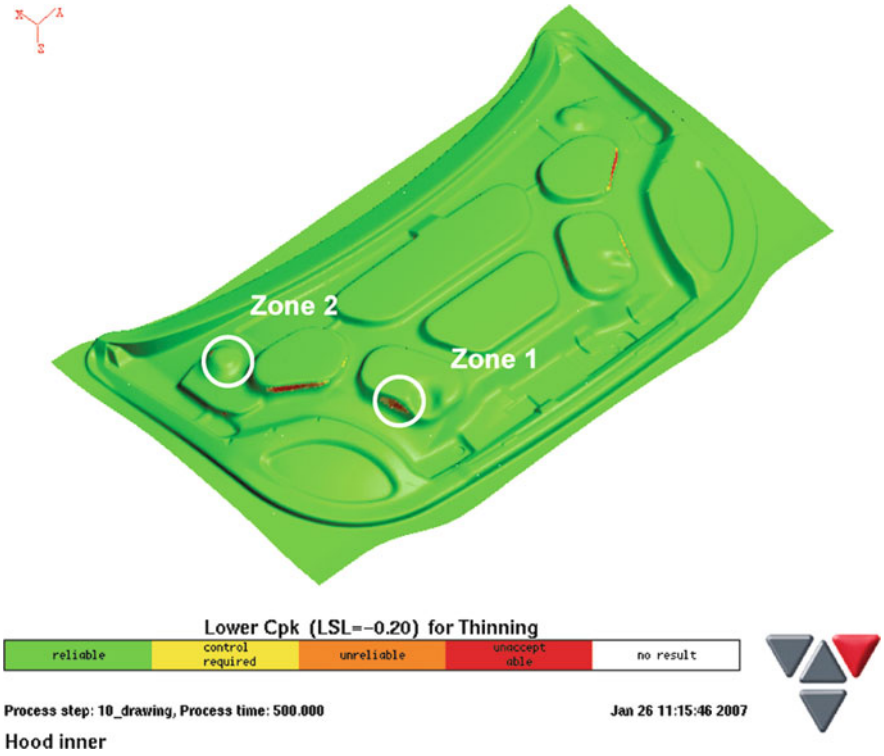

Fig. 4.37 Identification of unacceptable process precision

red spots can be distinguished. These red spots indicate that the process is unacceptable. These spots indeed coincide with the spots which have been indicated as a critical area during the monitoring phase.

The robustness analysis clearly indicates that production problems might occur. The analysis even managed to point exactly the areas where these problems would occur. Without incorporating the uncertainty of the property variations we would never have been able to judge the reliability or robustness of the production process.

For the purpose of this study we will focus on the result evaluation of two areas. These two areas are indicated in Fig. 4.36 as well as in Fig. 4.37. The first area (zone 1) shows a thinning value of –0.17 in the nominal simulation and is identified as having unacceptable process precision in the robustness analysis. The second area (zone 2) shows a thinning value of –0.18 in the nominal simulation and is identified as having reliable process precision in the robustness analysis.

The Pareto chart shows the influences of the considered noise variables sorted in decreasing order (Fig. 4.38). For zone 1, one can clearly see that the thinning is mainly influenced by the coefficient of friction (Lub). The other parameters hardly influence the thinning result. For zone 2, the coefficient of friction is again the dominant variable. But the yield strength still has a significant influence on the thinning result.

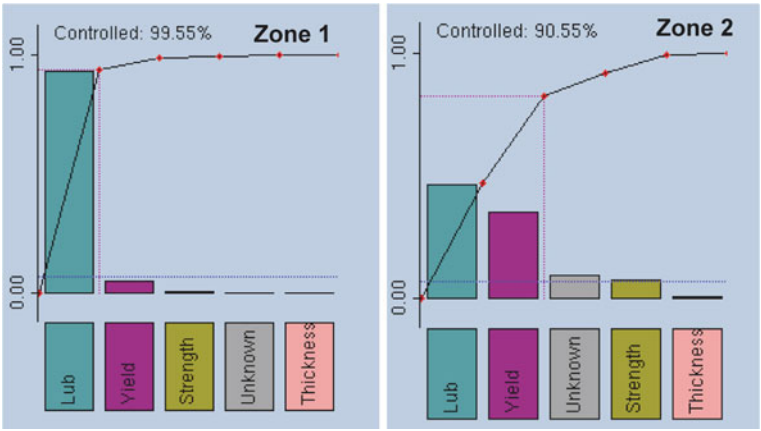

Fig. 4.38 Pareto chart for zone 1 and zone 2 showing the influence of the noise variables on the thinning

So, to control the result in zone 1 the coefficient of friction must be controlled. In zone 2 the coefficient of friction must be controlled as well as the yield strength. But before starting any action to control these parameters, the sensitivity of the thinning behavior to the variations must be evaluated.

So, for a more detailed analysis we will have a look at the relationship between the coefficient of friction and thinning. Figure 4.39 shows the scatter plot for zone 1 and zone 2. The scatter plot shows the raw result variable value and the selected noise variable value in an xy-scatter plot for all simulations. The x-axis represents the value for the coefficient of friction; the y-axis represents the resulting thinning.

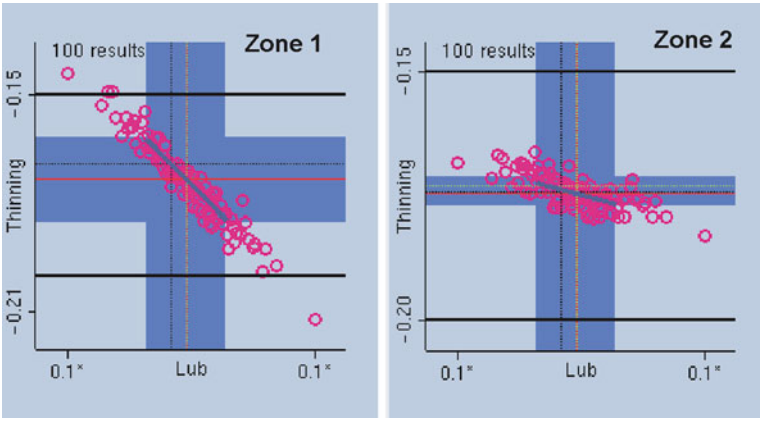

Fig. 4.39 Scatter plot for zone 1 and zone 2 showing the relationship between the thinning and the variation of the coefficient of friction

The critical limit of –0.20 thinning is indicated with help of the lower black horizontal line. The upper black horizontal line indicates a thinning value of –0.15 and has just been used for scaling purposes

The scatter plots of Fig. 4.37 clearly show that zone 1 is much more sensitive to the variation in friction than zone 2. So, the robustness analysis shows that zone 1 will cause more problems in production although the nominal simulation shows less thinning for zone 1 than for zone 2.

Since zone 2 is insensitive to the variations it is not needed to take any measures on the control of the yield strength. Since zone 1 is very sensitive for the variation of the coefficient of friction this parameter must be controlled carefully to achieve a robust production process.

This result coincides with experiences in the real production. The zinc coated material caused problems. Strip draw test gave that the coefficient of friction varies considerably depending on the oiling condition. The robustness analysis showed that the production reliability is strongly dependent on the value of the coefficient of friction.

So, in case of controlling the oiling condition of the zinc coated material the production reliability will increase.

4.4.4 Conclusion

The results of the two cases presented here unmask the common practice of evaluations with fixed safety margins as either non-effective and hence very dangerous or as extremely conservative and thus costly. The application of stochastic simulation methods reduces the need for wide safety margins while at the same time increasing the reliability of the process by incorporating uncertainty into the simulation itself.

4.5 The Springback Analysis

4.5.1 Introduction

When stamped sheet components are removed from the forming tools, the residual internal stresses will relax, and a new equilibrium state will be reached. As a result, the final shape of the drawn part will deviate from the shape imposed by the forming tool. This phenomenon is known as springback.

Springback is the major quality concern in the stamping field. The final shape of a part is determined by the springback deviation. If the shape deviation due to springback exceeds the given tolerance, it can create serious problems for the subsequent assembly operations. In recent years, the trends of applying high strength steel and aluminium to automobile components have widely emerged due

to their desirable low weight-to-strength ratio, which leads to better fuel efficiency. Consequently, springback deviations became more severe due to the higher yield strength-to-modulus ratio.

Modern finite element codes for sheet metal forming simulation have been shown to be able to produce excellent results regarding the formability prediction. The accurate simulation of springback, however, has still been proven difficult. Springback simulation is the last step of numerical simulation of sheet metal forming, consequently, any calculation errors resulting from previous simulation of forming processes will be accumulated and influence the springback analysis. Therefore, the accuracy of springback simulation is not only related to springback analysis itself, but also strongly dependent on the accuracy of forming processes.

There are many papers [12–16] published to investigate the numerical factors which influence the accuracy of springback simulation, however, most of the researchers have concentrated on the improvement of dynamic explicit FE codes. The static implicit FE codes with different strategies of contact, matrix solutions and element formulation etc., are not often discussed and no practical result is concluded.

In the present subchapter, the static implicit FE code AutoForm is considered, and the main factors which influence the accuracy of springback simulation, for instance, element formulation, time step, material model, drawbead model and other numerical parameters, are discussed. Optimized numerical parameters, so-called final validation settings, which aim at obtaining a robust and accurate springback result, are suggested. For verification and comparison, examples of Numisheet benchmarks are used and stable and accurate results are achieved.

4.5.2 Example Description

To simplify the investigation, a well known U-bending benchmark of Numisheet'93 is used during the optimization of numerical parameters [17]. Figure 4.40 illustrates the tool information and measurement method of the U-bending processes. The blank dimension is 0.81 mm × 35 mm × 350 mm, with a value of Young's modulus of 71 GPa, a Possion's ratio of 0.33, a density of 2.7×10^3 kg/m^3, a friction coefficient of 0.162 and the blank holder force of 2.45 kN. The blank material is Aluminium and its stress-strain relation is expressed as $\sigma = 570.4\,(0.01502 + \varepsilon_P)^{0.3469}$, the anisotropic coefficients are 0.71, 0.58, 0.70 at 0, 45 and 90° with respect to the rolling direction. Due to the symmetry, only the strip in one half is analyzed; therefore, the blank-holder force is taken as 1.225 kN. Moreover, the gap between die and punch is additionally extended to 3 mm instead of 1 mm only for the investigation of the influence of element size, time step and the integration scheme, which aims at eliminating the combined influence from other factors, e.g. contact treatment etc. For other factors' investigation, the real gap of 1 mm is used.

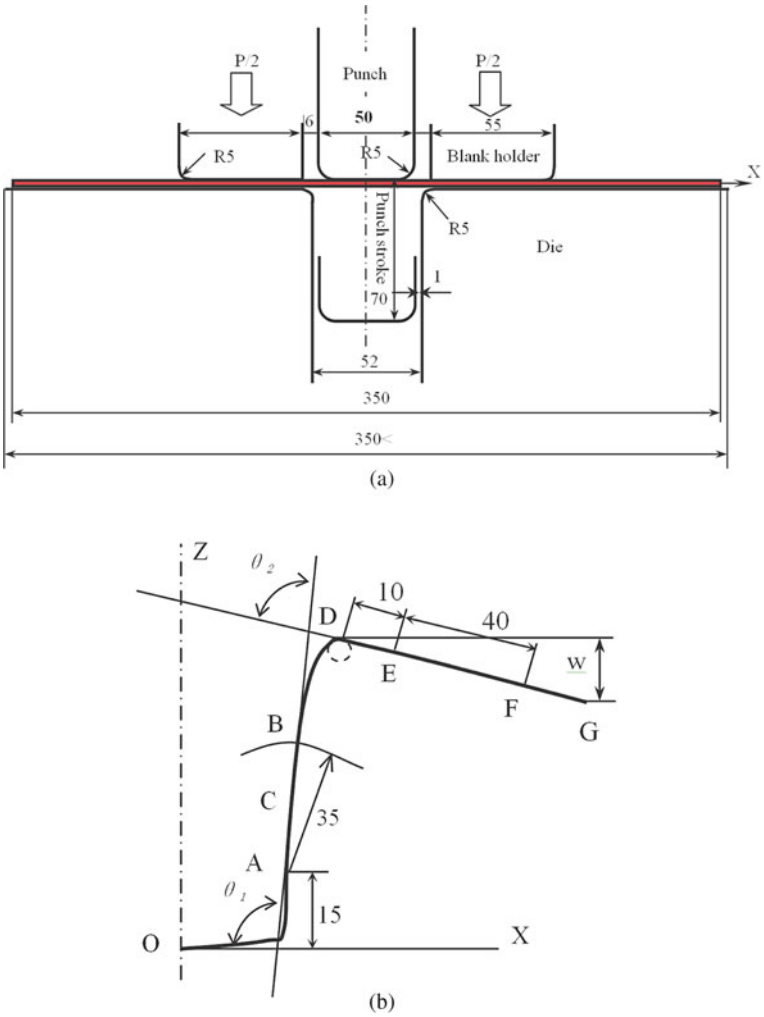

Fig. 4.40 Tool dimensions (a) and measurement method (b) of U-Bending benchmark of Numisheet'93

4.5.3 The Influences on the Accuracy of Springback Simulation

4.5.3.1 The Influence of the Element Formulation

The element formulation is the core technology in numerical simulation of sheet metal forming, which has significant influence on the simulation result, particularly on springback simulation. Two classes of elements are provided in AutoForm, bending enhanced membrane (BEM) and elastic-plastic shell (EPS), respectively. Both are based on a 3-node constant strain element formulation.

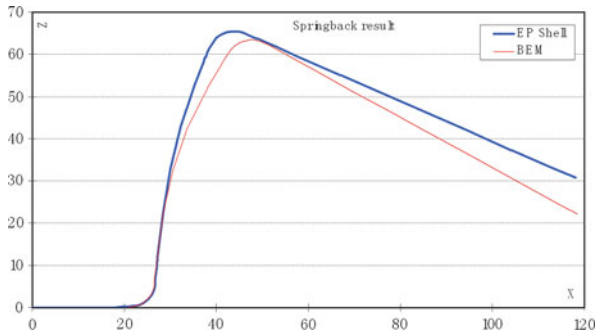

Fig. 4.41 Comparison of calculated springback between EPS and BEM

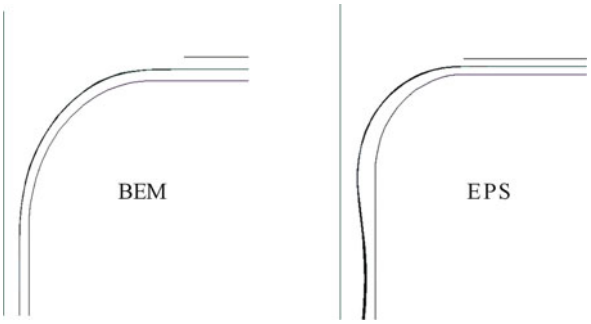

Fig. 4.42 Comparison of bending behavior between EPS and BEM

Bending enhanced membrane based on the scheme of uncoupled bending and stretching solution [18], is the simplest one, which is very effective and cheap for the numerical simulation of industrial parts, and has been verified with good accuracy on formability prediction [17, 19]. For springback analysis, however, BEM provides inadequate accuracy, especially in the area of bending/inverse bending, due to relative insufficient ability of description of bending effects.

Elastic-plastic shell element based on Mindlin-Reissner shell assumption is well accepted in numerical simulation of sheet metal forming, which has good accuracy in wrinkling prediction and springback analysis due to the better description of stress distribution. Figure 4.41 shows the comparison of springback simulations obtained by EPS and BEM. The reason why BEM has less accuracy as compared with EPS can be explained in Fig. 4.42, in which, EPS demonstrates a better ability of bending behavior description than BEM.

4.5.3.2 The Influence of the Element Size

Linear elements with 3 or 4 nodes are widely used in numerical simulation of sheet metal forming due to cheaper cost. Their accuracy has been well verified for the simulation in flat regions, in which the relative curvature (t/R) is smaller than 1/6.

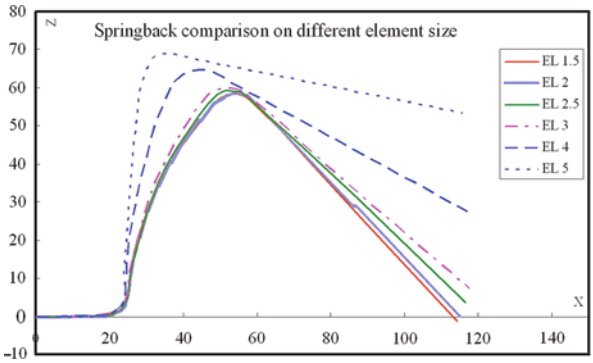

Fig. 4.43 The calculated springback varies with different element sizes

However, the calculated error cannot be neglected in small bending/inverse bending regions ($t/R > 1/6$ [20]) where the linear shape function is insufficient. To improve the accuracy of simulation in bending/inverse bending regions, a smaller element size is required from theoretical point view. Figure 4.43 shows the tendency of calculated springback varying with element size, which can verify that a smaller element size will result in improved accuracy of calculated springback. When the element size reaches 1/2∼1/3 of relative bending radii, the magnitude of calculated springback is starting to be robust and no further improvement is introduced any more.

It should be kept in mind that the further decrease of element size will not only notably increase the time consumption, but also increase the cost of contact treatment and matrix solution etc., which might inversely introduce additional error of springback simulation. As a result, 4 to 5 elements per radii are suggested for the purpose of both accuracy and robustness of springback simulation.

4.5.3.3 The Influence of the Integration Scheme and Integration Points

The integration scheme and the number of integration points through sheet thickness have been the key topics in springback simulation. The magnitude of springback depends on the bending moment which in turn depends on the stress distribution through sheet thickness. Most shell elements require numerical integration of stress and strain distribution through sheet thickness in order to obtain bending moments and tensile force, which will inevitably introduce numerical error in the simulation results.

There are three types of integration schemes commonly recommended in element formulation; which are, Gauss integration scheme, Gauss-Simpson combined integration scheme and Lobatto integration scheme. The Lobatto integration scheme is employed by the AutoForm element model due to its accurate description of numerical integration.

For the influence of the number of integration points through thickness (Nip), there are many articles published [12–15, 20, 21], however, different number of through thickness integration points (varying from 5 to 51) are specified, which implies that the number of integration points through thickness is still an open issue in springback simulation. In this subchapter, the influence of the number of integration points based on triangular element is investigated as well. Figure 4.44 shows how simulated springback varies with the number of integration points. It is no doubt that poor springback result will be obtained when the Nip is less than 3, however,

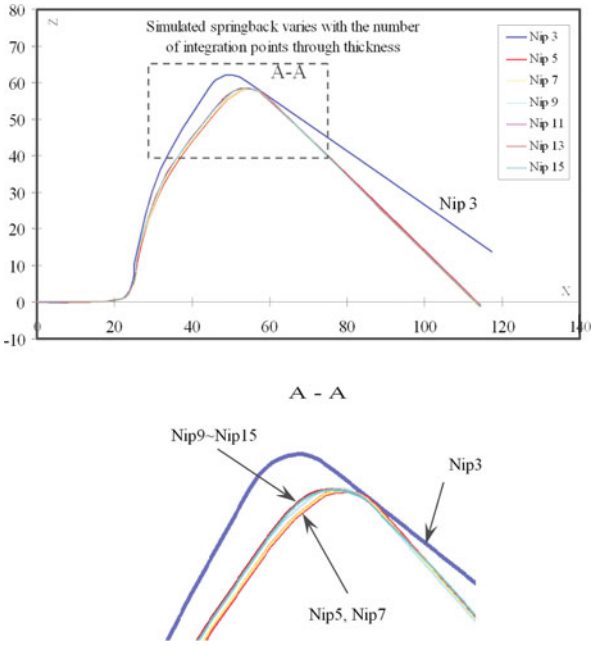

Fig. 4.44 The influence of the number of integration points through thickness

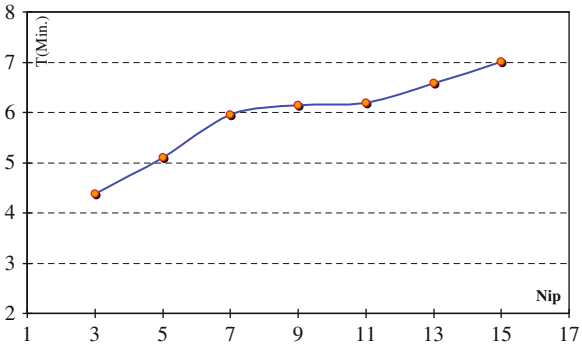

Fig. 4.45 Time consumption versus number of integration points

when the Nip is larger than 5, the simulated springback starts to be stable, and there is nearly no further improvement introduced after Nip is over 9.

Figure 4.45 shows how time consumption varies with the number of integration points through thickness. Larger Nip will result in more time consumption, when the Nip is over 13, the time consumption will notably increase, however, no further improvement of springback simulation is introduced (shown in Fig. 4.44). Considering complicated bending/inverse bending cases (e.g. drawbead), and the efficiency and accuracy, 11 Nip is recommended in AutoForm for springback analysis.

4.5.3.4 The Influence of the Time Step

Different from the concept in dynamic explicit FE software [12, 13, 15], the time step in the static implicit FE code, AutoForm, denotes the time interval to update the strain and stress information of elements, or the tool displacements. The time step can influence the description of strain and stress history (e.g. bending/inverse bending history) and the treatment of friction etc. It is no doubt that a smaller time step will result in more accurate simulation results, however, the time consumption will be increased as well. Figure 4.46 shows the simulation results using various time steps. The smaller time step will result in more stable springback. When the time step is less than 2.5 s (based on a tool velocity of 1 mm/s) or maximum tool displacement of 2.5 mm per increment, the magnitude of simulated springback is starting to concentrate in a narrow band and no further improvement is introduced. To track the bending/inverse bending history and the treatment of friction, the time step of 1.6 s (or 1.6 mm) per increment is suggested in this subchapter.

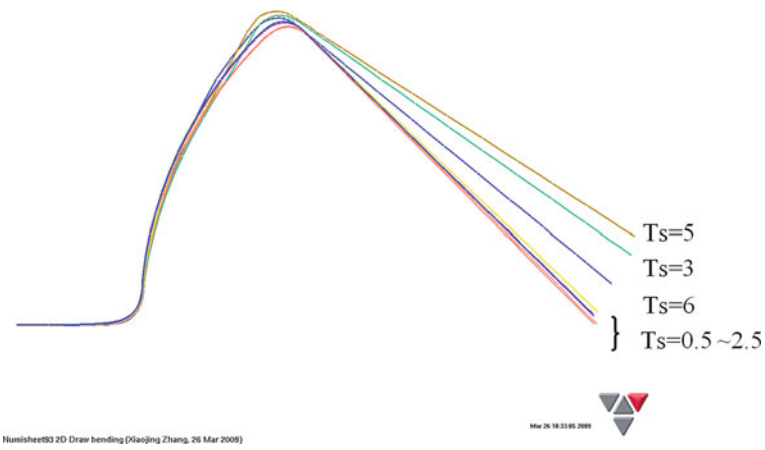

Fig. 4.46 The calculated springback varies with time step

4.5.3.5 The Influence of the Material Model

Material modeling has been another key topic in numerical simulation of sheet metal forming, where, the hardening model is widely thought to have an obvious influence on springback simulation. Figure 4.47a shows the comparison of calculated springback between isotropic hardening model and kinematic hardening model, while Fig. 4.47b shows the transient softening compression curve and the kinematic hardening parameters of Aluminum. With the kinematic hardening model introduced in Sect. 2.8, an obvious improvement of calculated springback is obtained in this benchmark.

However, it should be kept in mind that improvement of calculated springback with kinematic hardening model is not guaranteed. Some examples with negative influence have been found as well during the investigation. The reason can

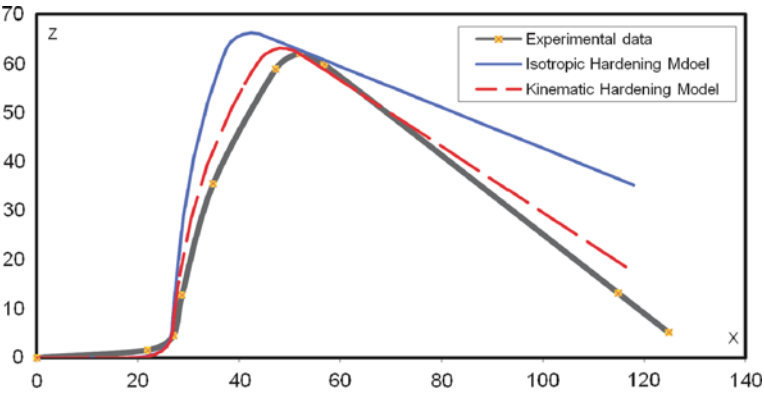

a)

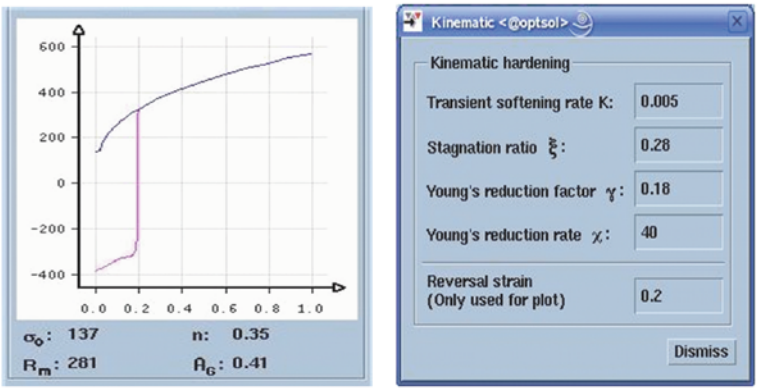

b)

Fig. 4.47 The comparison of calculated springback between kinematic hardening model and isotropic hardening model. (**a**) The comparison of calculated springback between isotropic and kinematic hardening model; (**b**) The kinematic hardening parameters

be explained as follows. There are two main factors in the kinematic hardening model which may influence the final springback result; these are the transient softening of the hardening curve and the reduction of Young's modulus. While the factor of Young's modulus reduction will cause larger springback deformation, on the other hand, the factor of transient softening of the unloading hardening curve will inversely result in smaller springback deviation. The final springback result is decided by the combined influence of these two factors. In reality, the measurement of kinematic hardening parameters is not so easy, in many cases, the error of measurement is so large that even springback simulation becomes worse.

For an accurate springback simulation, well-measured experimental data related to kinematic hardening parameters are required.

4.5.3.6 The Influence of the Drawbead Model

Drawbeads are widely used in stamping processes which aim at controlling the material flow and improving the formability. There are two types of drawbead models in numerical simulation, which are, namely, physical drawbead and equivalent drawbead model.

Physical drawbead model can simulate the real behavior of bending and inverse bending history. However, it requires about 2.5∼8 times more computation time than the equivalent drawbead model. Moreover, the radii of drawbeads are commonly so small that the application limit of shell theory is often exceeded, which will introduce great challenges in numerical simulation of sheet metal forming.

Due to the above-mentioned reasons, the equivalent drawbead model is widely used in numerical simulation, and it has been verified to provide good accuracy in formability prediction [22, 23]. Springback analysis, however, is still in discussion due to the neglection of bending and inverse bending history in the equivalent drawbead model.

To investigate the influence of drawbeads on springback behavior, the well-known S-Rail benchmark with drawbead provided in Numisheet 2008 [23] is used in this investigation. Figure 4.48 shows the comparison of springback result between a physical drawbead model and an equivalent drawbead model. Obvious differences in behavior of calculated springback are obtained after drawing (Fig. 4.48a), however, nearly the same springback is observed after trimming (Fig. 4.48b).

To analyse the reasons why the springback calculated with the physical bead and the equivalent bead is different after the processes of drawing and trimming, the history of material flow over the whole forming processes is tracked in Fig. 4.49, where, the highlighted curve on the blank surface denotes the bead impact lines. As shown in Fig. 4.49, the material which flows through the drawbead was finally cut after the trimming process, that means that the difference of bending and inverse bending path between physical drawbead and equivalent drawbead model was finally trimmed, and the stress and strain distribution of the final part is nearly identical, which gives the reason why the final springback is nearly the same.

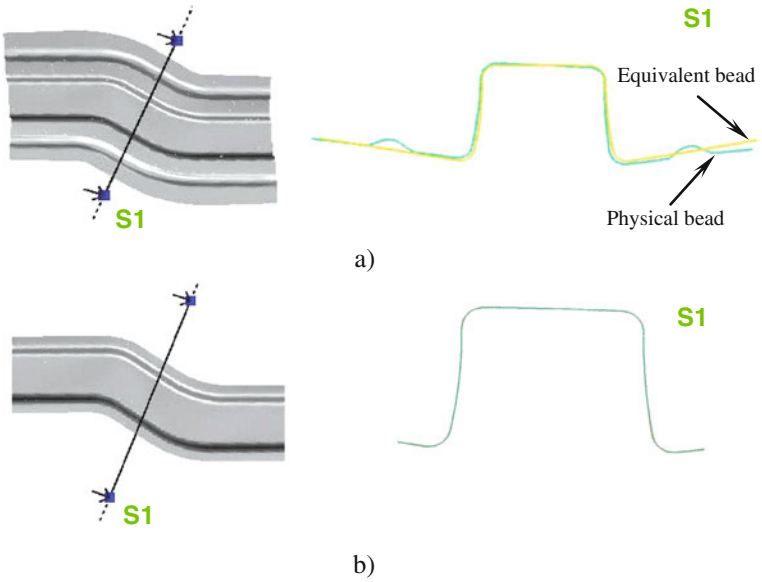

Fig. 4.48 The comparison on springback simulation between physical drawbead model and equivalent drawbead model. a) The springback comparison with/without physical drawbead; b) The springback comparison with/without physical drawbead(after trimming)

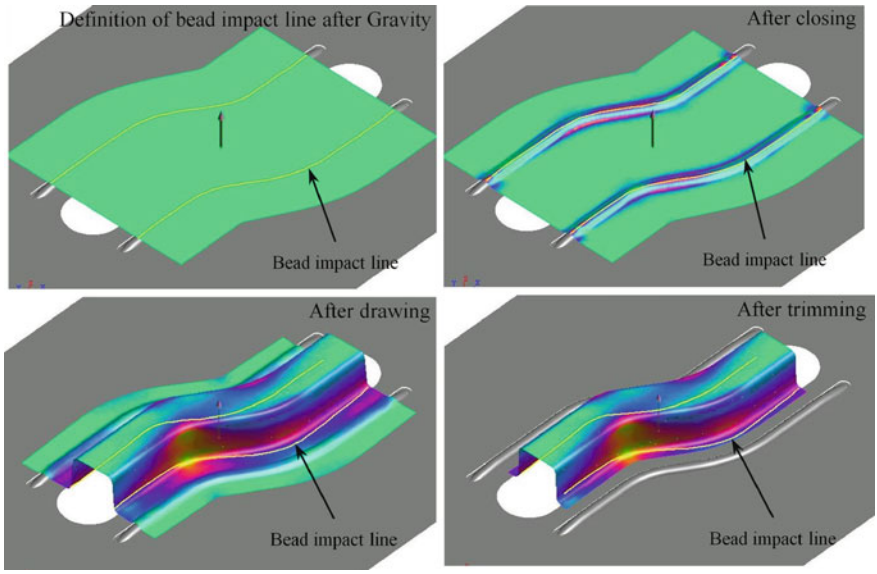

Fig. 4.49 Movement of a bead impact line during the forming process

For the purpose of time consumption, the equivalent drawbead model is commonly recommended, because it makes no sense to handle complicated geometric bead models if the equivalent drawbead can do the same. However, when the material passing a drawbead remains on the final part, the difference of bending/inverse bending history resulting from drawbead model cannot be neglected and the physical drawbead model is necessary.

4.5.4 The Optimized Numerical Parameters of Springback Simulation: Final Validation Settings

Based on the above-mentioned investigations, the optimized numerical parameters, which aim at obtaining a robust and accurate springback simulation, are suggested. Table 4.27 shows the optimized numerical parameters suggested in this subchapter, named as final validation settings.

With these settings, a robust and accurate springback simulation is expected to be obtained.

4.5.5 The Simulation of Numisheet 2005 Benchmark #1: Decklid Inner Panel

4.5.5.1 Description of the Benchmark

To check the behaviour and the accuracy of springback with the optimized numerical parameters described above, the Numisheet 2005 Benchmark #1, Springback prediction of decklid inner panel [22], which was provided by the GM Metal Fabricating Division, US Steel, and Troy Design Manufacturing, is used. The

Table 4.27 The optimized numerical parameters for springback simulation

Element formulation	Elastic-plastic shell
Radius penetration	0.22
Maximum element angle	15∼22.5
Initial element size	Min (2 $R_{\min}$, 20 mm)
Maximum refinement level	3
Maximum time step or maximum displacement	1.6∼2.2 mm
Tangential refinement	ON
The number of integration points through thickness (Nip)	11
Drawbead model	Equivalent bead: material passing bead is finally cut Physical bead: material passing bead remains on part

where, $R_{\min}$ denotes minimum bending radius.

process involves pre-bending of the sheet, forming, trimming and constrained springback. The objective of this study is to benchmark the springback prediction capability of various software and skills of users on a complex inner body panel.

Lower punch, binder and upper die are illustrated in Fig. 4.50. This tooling geometry has a symmetry plane at x=0. The process is a three-piece air draw. The punch is stationary. The upper die is a solid one-piece tool. The binder is supported by hydraulic cylinders, which provide the binder holding force. One metal thickness equalizer [22] is used to provide a constant binder gap. Therefore, no binder pressure is applied through the sheet during the drawing process.

Aluminum 6111 T4P is used in this subchapter with a value of Young's modulus 70.9 of GPa, a Possion's ratio of 0.3, a density of 2.7×10^3 kg/m^3, a friction coefficient of 0.09, and the blank thickness is 0.9 mm. The BBC 2005 model is used in this benchmark research which aims at an accurate description of the yield locus. Table 4.28 illustrates the material parameters of AL 6111-T4P.

Due to the fact that there is no experimental data available for the kinematic hardening model, the isotropic hardening model is still used in this benchmark research. The equivalent drawbead model is used in this benchmark due to the fact that the material passing drawbead is finally cut.

In the end, the optimized numerical parameters shown in Table 4.27, are used in this benchmark, which aims to verify whether a reasonable springback simulation can be obtained.

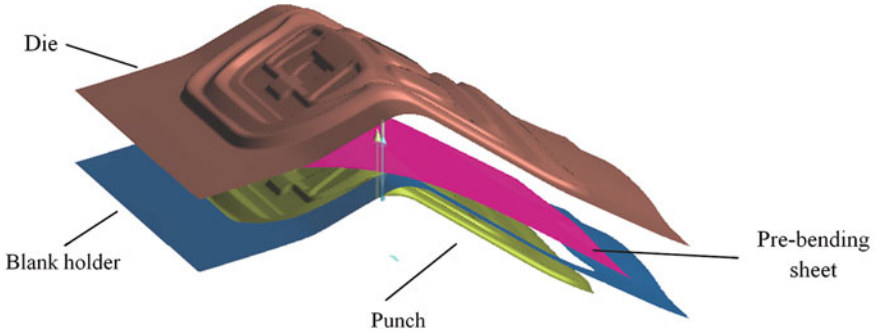

Fig. 4.50 The Benchmark #1 in Numisheet 2005

Table 4.28 Material parameters of AL 6111-T4P

Material	True stress–true plastic strain descriptions: $\sigma = C(\varepsilon_p - \varepsilon_0)^m$			r_0	σ_0 (MPa)	r_{45}	σ_{45} (MPa)	r_{90}	σ_{90} (MPa)	r_b	σ_b (MPa)	M
	ε_0	m	C (MPa)									
Al 6111 T4P	0.0044	0.268	558.6	0.616	127	0.646	132	0.778	136	0.58	128	8

4.5.5.2 The Result of Numerical Simulation

Figure 4.51 illustrates the simulation of the entire forming processes of this benchmark, including pre-bending of the sheet, gravity, closing, drawing, trimming, rigid body rotation in car position and constrained springback.

Figure 4.52 shows the simulation result of constrained springback based on the optimized numerical parameters. Figure 4.53 gives the comparison between simulation and experimental data at the pre-defined measuring points. The statistical

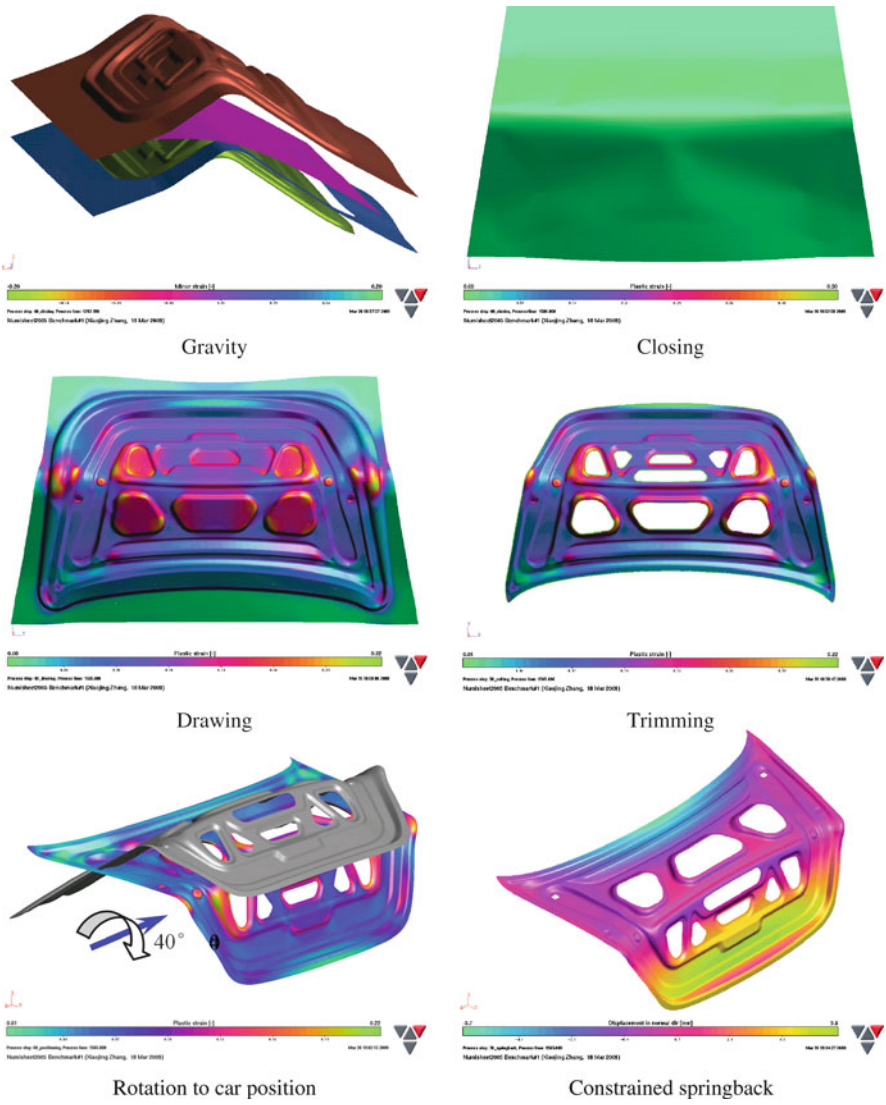

Fig. 4.51 The simulation of the entire forming processes of a decklid inner panel

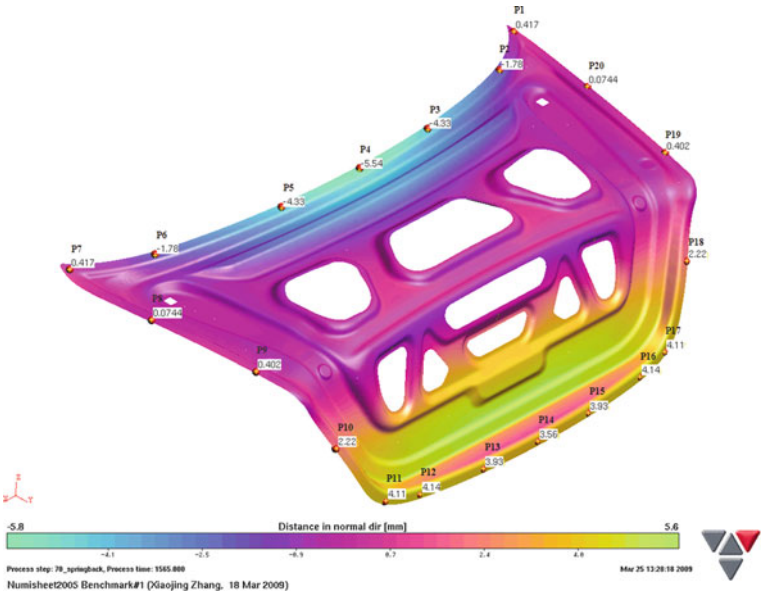

Fig. 4.52 The simulation result of constrained springback

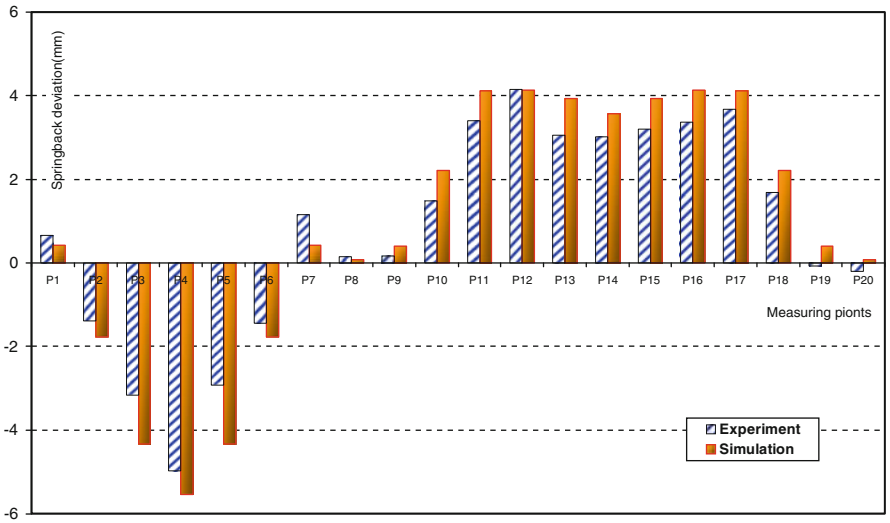

Fig. 4.53 The springback comparison between simulation and experiment

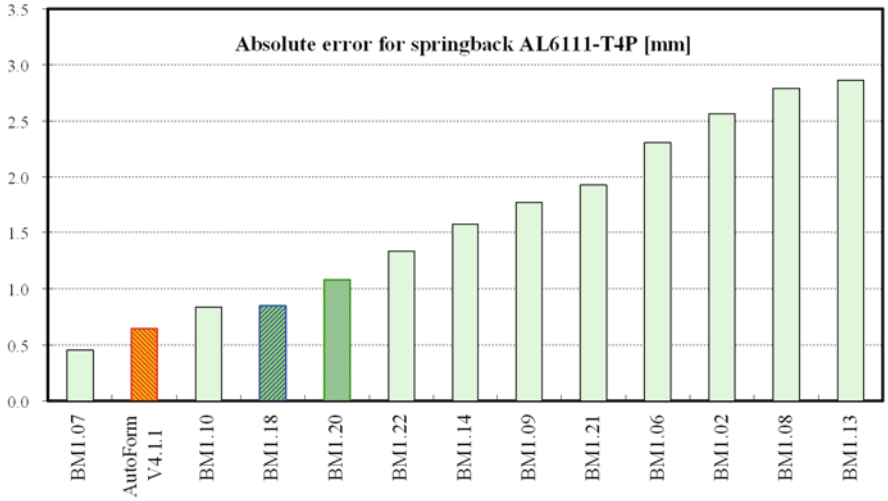

Fig. 4.54 The comparison on the statistical result of springback deviation between simulation and experiment

analysis shows that the standard deviation between the calculated springback and the experimental results is well-controlled under the value of 0.65 mm.

Figure 4.54 shows the comparison of the statistical result of absolute error for springback in normal direction, based on the published data of Numisheet 2005 [22], where, AutoForm V4.1.1 is the statistical result of calculated springback in this subchapter based on the final validation settings, BM1.18 is the published result of the author, and BM1.20 is the published result of the AutoForm user in Numisheet 2005 [22], both are based on AutoForm V4.0 and similar settings of the numerical parameters shown in Table 4.27.

All these results verify that a robust and accurate springback simulation can be guaranteed with so-called final validation settings.

4.5.6 Conclusion

The springback simulation is a well-known to be a sensitive process, which is not only influenced by springback computation itself, but also strongly depends on the accuracy of previous forming simulation. There are so many numerical parameters influencing the accuracy of springback calculation, that it is not easy to obtain a robust and accurate springback simulation.

In this subchapter, the influences on springback simulation are thoroughly investigated, and the optimized numerical parameters, so-called final validation settings, are provided. The verification of experiment has shown that the robust and accurate springback simulation can be guaranteed with these settings. With the robust and

accurate springback simulation, further developments, for instance, computer aided springback compensation etc. can be realized.

4.6 Computer Aided Springback Compensation

4.6.1 Introduction

Springback is an inevitable problem in the field of die face engineering. Although it is impossible to prevent the springback, it can be minimized by some techniques, for instance, reinforcing part by smaller radii or additional folding, raising the stretching deformation of the sheet etc. [24]. Even so, there are still many cases where the springback deviation exceeds the given tolerance. Where the minimized springback deviation is still so large that the subsequent assembly operation is seriously influenced, the additional geometric modification of the tool surface, the so-called springback compensation, has to be introduced in order to reduce the shape deviation between the drawn part and desired product. With the increasing usage of high strength steel and aluminum, springback deviation becomes more and more severe. Therefore, the geometric compensation of springback is generally necessary to be taken into account.

In the past, springback compensation was done manually by doing extensive measurements on prototype or even production tools, and altering tool geometry by hand, which is a time consuming and cost-prohibitive process. It was reported [24] that a single correction loop of springback compensation for a hood inner like part, takes about 5 weeks and costs about €70,000. If additional operations are involved, one extra-iteration may additionally take about 10 weeks and cost about €150,000. In many cases, numbers of iterations are needed during the compensation, which seriously increases the cost of tool development. With complex part shapes and new materials, it is difficult or even impossible, to rely on such kind of experience to estimate shape deviations and compensate the die surfaces. Therefore, how to control the cost of compensation and shorten the period of tool development becomes one of the key issues in current die manufacturing industry.

With the development of computer technologies and the finite element method, particularly with recent improvements of springback prediction, a new compensation method based on calculated springback has been developed. With the help of this method, the springback can be compensated easily and effectively and the cost of tool development can be significantly decreased. In this subchapter, the basic methodologies of springback compensation are presented, and the factors which influence the springback compensation, for instance, the accuracy of springback simulation, the robustness of springback responding to the variation of material and process parameters in manufacturing process, are discussed, and a guide line which aims at fulfilling a successful springback compensation is recommended. As a discussion subject, the example of Numisheet 2005 Benchmark #1 [22] is used again in this subchapter.

4.6.2 The Basic Methodologies of Computer-Aided Springback Compensation

There are two methodologies used to realize the geometric compensation of springback. They are the so-called spring-forward compensation and spring-back compensation. Both are based on an iterative procedure.

In the approach of spring-forward compensation, the stress tensor of the part, which is used to calculate springback, is multiplied with a negative factor, therefore, the shape after 'springback' simulation is already the subsequent compensated surface. This approach has been thought as an effective method. However, only few successful stories are reported, as compared with the approach of springback compensation. The reason can be explained as follows. The spring-forward approach is based on the assumption that the sign change of stress tensor correspondingly results in the response of spring forward deformation instead of spring backward, which is not 100% true in reality due to the complicated stress distribution in drawn part.

In the approach of springback compensation, the geometric compensation is based on the real calculated springback. Therefore, there is no artificial error introduced as compared with spring-forward approach. Figure 4.55 illustrates the basic work flow of computer-aided springback compensation [25]. First, the forming and springback simulation must be run based on the original CAD geometry and process parameters. After that, the shape deviation between the sprung part and the desired shape has to be analysed in order to determine whether the dimension of the drawn piece can meet the needs of the desired shape. If the shape deviation exceeds the

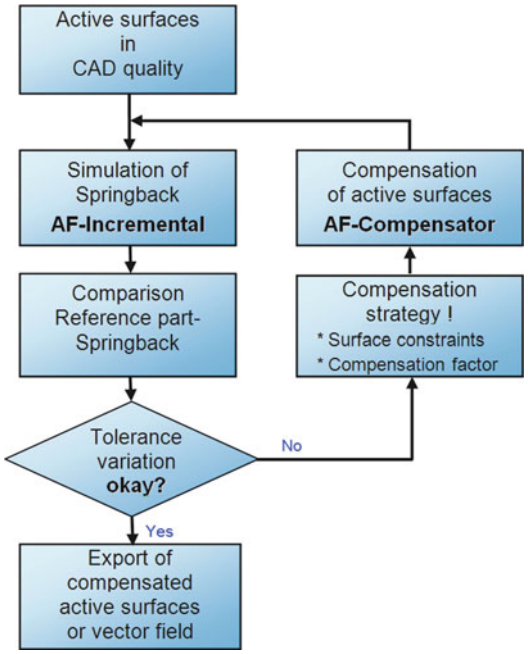

Fig. 4.55 The work flow of computer-aided springback compensation

given tolerance, the geometric compensation of springback based on pre-defined strategies of compensation and compensation factor, must be implemented, in order to decrease the shape deviation with respect to the desired shape. In the end, the drawing and springback processes have to be assessed again, because the springback might have been significantly changed due to the modified tool geometry. This procedure is repeated until the desired shape is obtained.

In this subchapter, the second approach of springback compensation is used due to the fact that it is closer to the compensation routine used in practice.

4.6.3 The Influences of the Quality of Computer Aided Springback Compensation

The quality of computer aided springback compensation (CASC) is critical for tool development. Unreliable compensated data or unstable springback behavior will significantly increase the cost of tool development, thereby influence the time schedule of car development. There are two main factors which will influence the quality of computer aided springback compensation, namely the robustness and accuracy of springback prediction, and the robustness of springback responding to the variation of material and process parameters.

4.6.3.1 The Robustness and Accuracy of Springback Calculation

The robust and accurate springback simulation is critical for computer-aided springback compensation. It is well-known that the springback simulation is sensitive to many numerical parameters, for instance, element formulation, element size, number of integration point through thickness, time step, material model etc. To ensure the reliable compensated data being introduced, the optimized numerical parameters, so-called final validation settings, are strongly required during the computer aided springback compensation. It has been well-verified by many examples [22, 23] that both accuracy and robustness of springback simulation can be guaranteed with such a kind of final validation settings.

4.6.3.2 The Robustness of Springback Responding to Variation of Material and Process Parameters

It is also well known that the springback can sensitively respond to the variation of the material properties and process parameters existing in the manufacturing process. Small relative variations of the parameters might result in significant changes of springback, in some cases, even the direction of springback, which introduces great challenges for springback compensation. Particularly with the increasing usage of high strength steel and aluminum, such problems become more serious. To ensure the quality of springback compensation, a robustness analysis is recommended before and after compensation. If the scatter of springback exceeds the allowed tolerance of springback compensation, the process parameters or tooling conception have to be optimized in order to obtain a repeatable result.

4.6.4 The Recommended Work Flow of Computer-Aided Springback Compensation

To obtain a successful springback compensation, a recommended work flow of computer-aided springback compensation [25] (shown in Fig. 4.56) is suggested as follows.

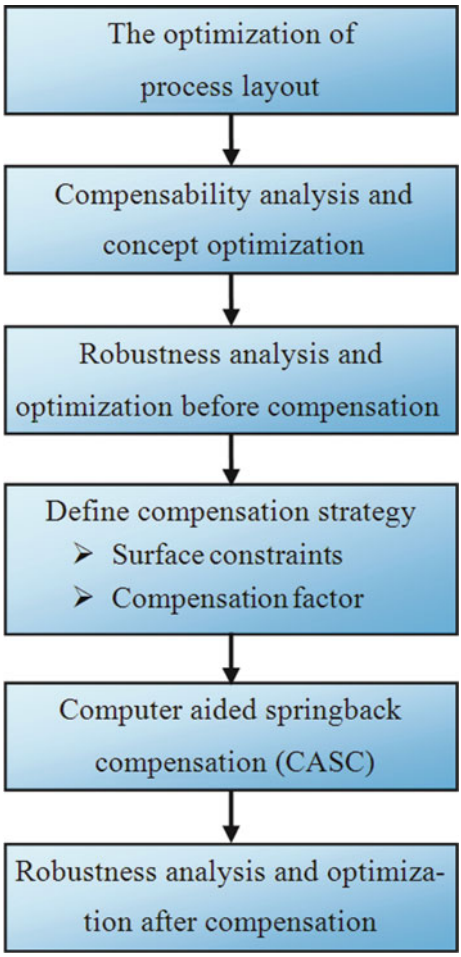

Fig. 4.56 The recommended work flow of CASC

4.6.4.1 The Optimization of Process Layout

When the first tooling conception is generated, the layout of deep drawing stage should be validated with respect to splits, wrinkles, thinning and potential skid/impact lines etc. which aims at obtaining a feasible process layout in the

first optimization. Moreover, the optimization of material usage based on nesting has to be considered as well, because any change of sheet outline later might cause a significant change of springback deviation, therefore, all efforts following might be irrevocably lost. It should be kept in mind as well that the springback compensation is only the last measure to reduce the shape deviation between the drawn part and desired product, due to the fact that it is a time consuming and cost-prohibitive process. Trying our best to reduce the springback in the stage of geometry and process improvement is strongly recommended before springback compensation.

4.6.4.2 Compensability Analysis and Optimization of Tooling Concept

After the optimization of process layout, the first survey of springback has to be done in order to clarify whether the springback can be compensated geometrically or whether the tooling concept needs to be modified. If not, additional optimization loops have to be introduced.

4.6.4.3 Robustness Analysis and Optimization Before Compensation

Based on the optimization of process layout and compensative analysis, the robustness of springback responding to the variation of manufacturing processes is recommended to be analyzed before compensation, because a successful compensation is closely connected to a robust forming process. It has been shown in practice that more dimensional deviation due to springback occurred despite the compensated tools, when a non-robust springback is introduced [25].

4.6.4.4 Computer Aided Springback Compensation

Based on a robust springback response, the geometric compensation can be introduced when springback deviation exceeds the given tolerance. Three different areas within the tool are required to be defined during the compensation. First, the area of the part which will be compensated directly based on the node vector of springback displacement and the compensation factor. Second, the area of binder surface which remains fixed in order to make sure that no wrinkles occur during the closing of tools. Third, a transition area corresponding to rest part of tool is used for generating the smooth transition surface between direct compensation and fixed region. With the definition of compensation areas, the computer aided springback compensation based on the above mentioned springback compensation approach (see Fig. 4.55) will be introduced and the compensated tool will be generated.

4.6.4.5 Robustness Analysis and Optimization After Compensation

Due to springback compensation, material flow might be changed, in turn, the springback behavior might become non-robust again if there is a great amount

of geometric change of tool surface. Therefore, the robustness analysis after the springback compensation is necessary in order to ensure that the final scheme of springback compensation is repeatable.

Based on the above guideline, the robust springback compensation can be guaranteed and the cost of tool development related to the springback compensation can be significantly decreased.

4.6.5 The Springback Compensation of Numisheet 2005 Benchmark #1

To demonstrate the application of the new method outlined above, the Numisheet 2005 Benchmark#1 Decklid inner panel [22] is used. The process parameters and material properties are described in the previous subchapter in detail.

4.6.5.1 The Feasibility Analysis of the Forming Processes and Springback

The numerical simulation of the entire processes of this benchmark has been presented in the previous subchapter. The verification of the experiment has well-testified that the accurate and robust simulation result can be obtained with the optimized so-called final validation parameters.

Based on the simulation, the deep drawing process has been analyzed and well-verified with respect to splits, wrinkles and thinning etc.. Therefore, the feasibility of the tooling conception and process parameters of this benchmark can be taken as guaranteed and the subsequent possibility of the geometric springback compensation can be discussed.

From the springback simulation shown in Figs. 4.52 and 4.53 in the previous Sect. 4.5, we can find that the maximum shape deviations between the sprung piece and the desired shape are –5.54 mm at the measuring point P4, and 4.14 mm at the measuring points P12 and P16, which exceeds the required tolerance. Therefore, the geometric compensation of the tool surface is necessary for this benchmark.

4.6.5.2 The Robustness Analysis of Springback Before Compensation

The stable springback responding to the variation of the manufacturing noise is critical for the successful springback compensation. Therefore, the robustness analysis of springback is necessary in order to guarantee that the dimension of the drawn part is repeatable for the stamping process. According to the process layout of this benchmark, the variation of the following parameters is considered:

- Sheet thickness
- Sheet position

- Friction coefficient
- Yield strength and tensile strength of the material at 0, 45 and 90° with respect to the rolling direction
- Drawbead restraining force resulting from friction and wear, etc.

With the help of AutoForm-Sigma, these parameters are automatically varied according to the defined variation range and the individual simulations are evaluated based on statistical methods.

Figure 4.57 shows the distribution of the standard IQR [26] which denotes the variation of springback along the normal direction (the meaning of standard IQR is similar to the standard deviation in statistics). From Fig. 4.57, we can see that the value of the standard IQR is well-controlled under 0.374. Thus one may consider that the springback is still robust.

Figure 4.58 shows the scatter of springback deviation in Zone 1 and Zone 2 (the positions of Zone 1 and Zone 2 are marked in Fig. 4.57), which approximately correspond to the largest negative and positive springback respectively. From Fig. 4.58, we can see that the springback along the normal direction varies between –5.44 and –6.76 mm in Zone 1, and between 3.45 and 4.69 mm in Zone 2. This fact proves that the springback directions of both zones are stable. Therefore, the quality of springback compensation can be guaranteed.

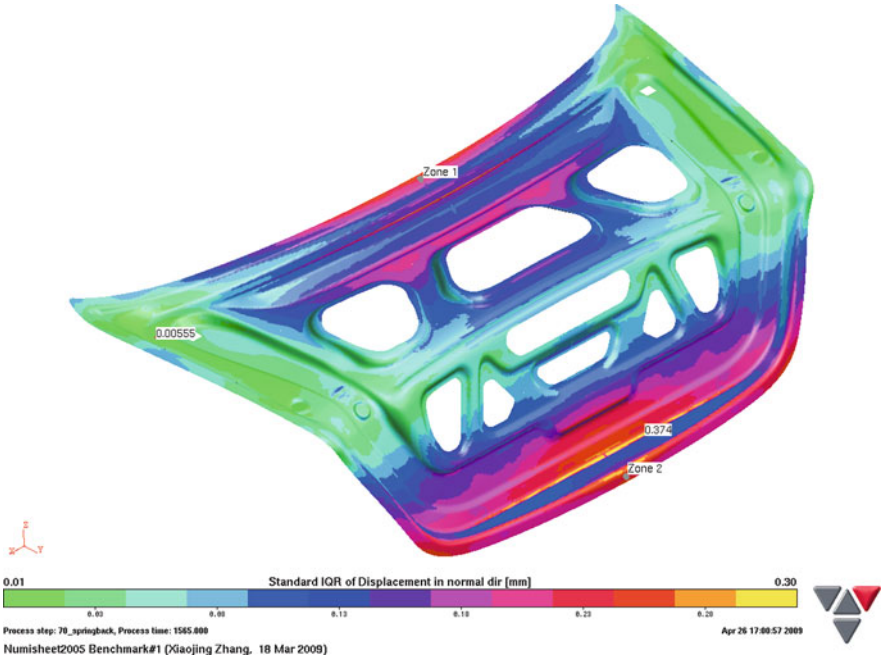

Fig. 4.57 The variation of springback along the normal direction

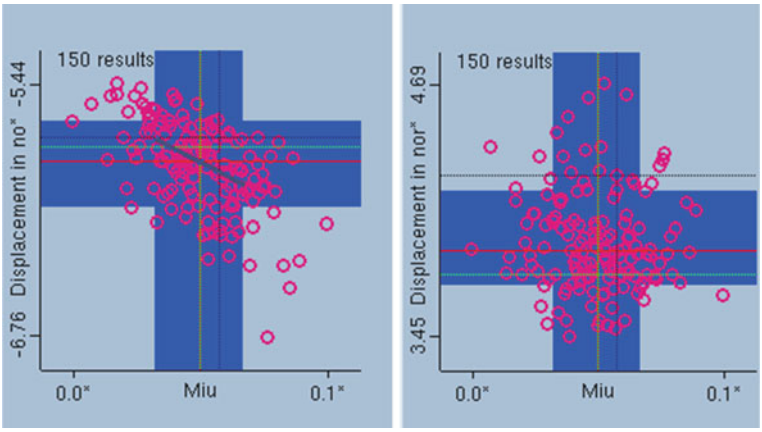

Fig. 4.58 The scatter of springback deviation of Zone 1 (*left*) and Zone 2 (*right*) before compensation (Miu: friction coefficient)

4.6.5.3 Computer-Aided Springback Compensation

Using the module AutoForm—Compensator, the compensation strategy of this benchmark is defined. In this compensation strategy, the tool geometry is subdivided into the areas of 'Fixed region', 'Direct compensation region', and 'Transition region', which are shown in Fig. 4.59. The binder surface is defined as fixed in order to make sure that no obvious change of the deformed shape will be introduced after closing.

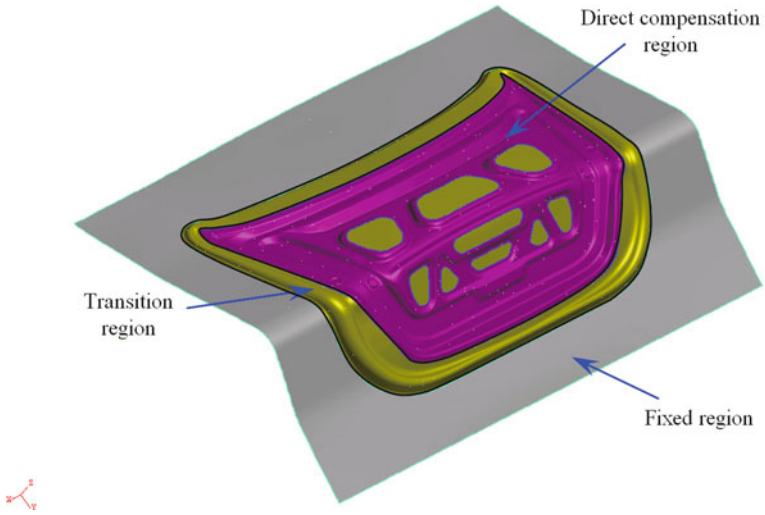

Fig. 4.59 The definition of springback compensation regions

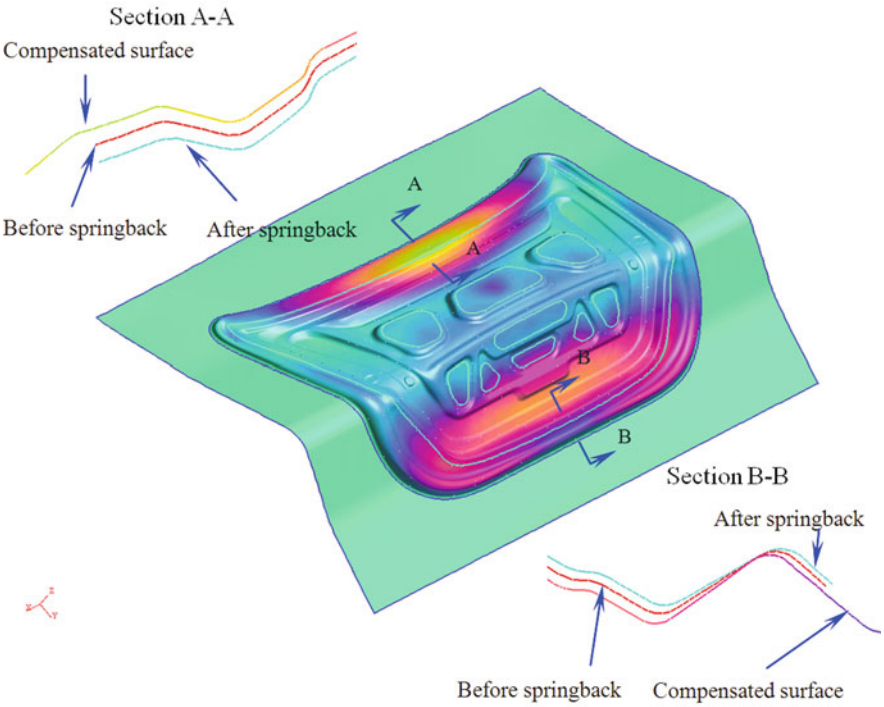

Fig. 4.60 The tool geometry after springback compensation

With the well-defined compensated regions, the springback compensation is automatically done by AutoForm—Compensator. Figure 4.60 shows the tool geometry after springback compensation, where, section A-A and section B-B are the comparison between the compensated surface and the part before and after springback.

After only two iteration loops of springback compensation, the geometric deviation with respect to desired shape is well controlled under the required tolerance of 0.2 mm. Figure 4.61 shows the geometric deviation between the sprung part and the desired shape, where, section A-A and section B-B in this figure are the comparison between the drawn part and the desired shape. Figure 4.62 shows a comparison of shape deviation before and after compensation at measuring points.

4.6.5.4 Robustness Analysis of Springback After Compensation

Due to the change in tool geometry, it cannot be assumed that the robust forming process before compensation is still robust after compensation. Therefore, a final robustness analysis based on the compensated tool surface is necessary to be

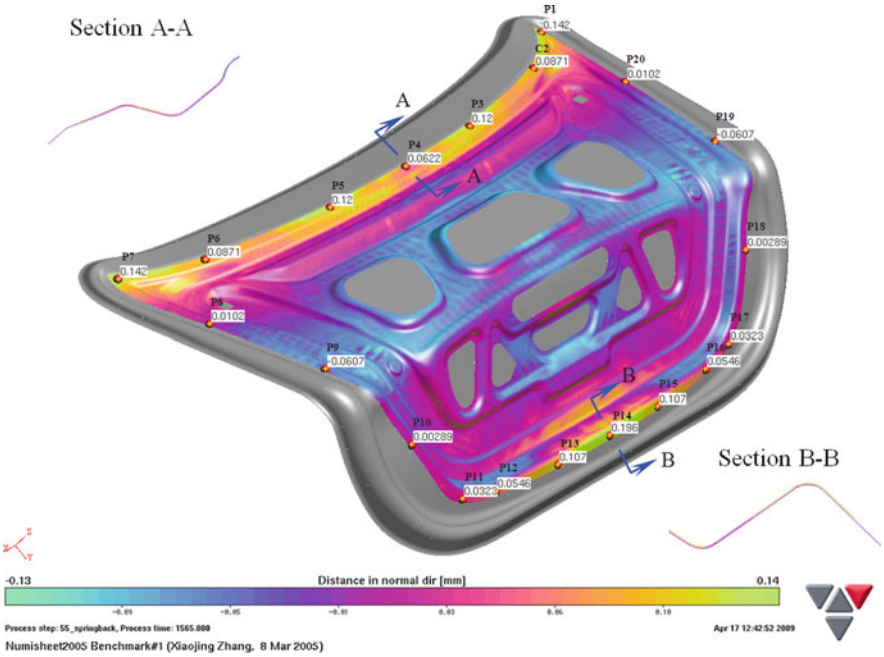

Fig. 4.61 The geometrical deviation between the sprung part and the desired shape after springback

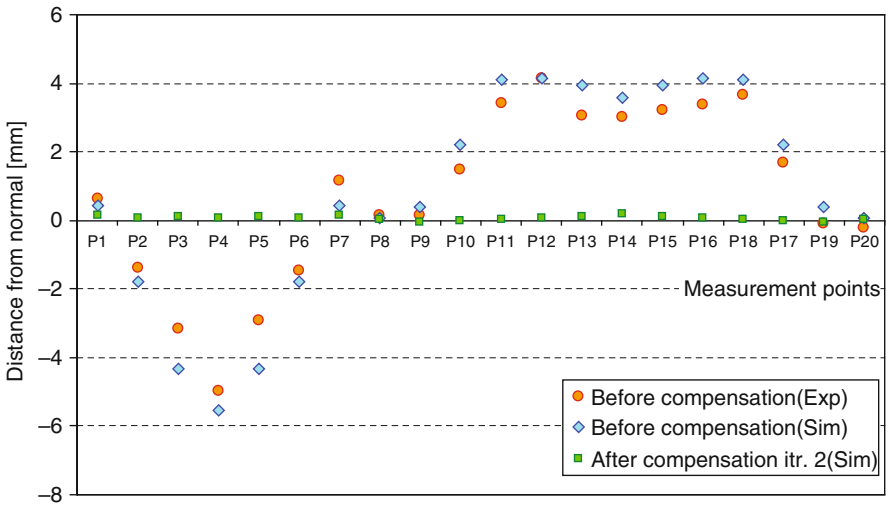

Fig. 4.62 Comparison of the shape deviations before and after compensation

checked again. The variation of the following parameters is considered during the robustness analysis:

- Sheet thickness
- Sheet position
- Friction coefficient
- Yield strength and tensile strength of the material at 0, 45 and 90° with respect to the rolling direction
- Drawbead restraining force resulting from friction and wear, etc.

Figure 4.63 shows the distribution of the standard IQR [26] which denotes the variation of distance from the desired shape along the normal direction. It can be seen that no values of standard IQR greater than 0.3 mm are identified. Therefore, the process after compensation can be considered as robust and the quality of this compensation scheme can be taken as guaranteed.

Figure 4.64 shows the Cp [26] assessment for the distance with repect to the desired shape along the normal direction. From Fig. 4.64 we can see that most areas of the drawn part belong to the reliable region (marked with the green colour), which denotes that the compensation is reliable and the compensated tool can be manufactured.

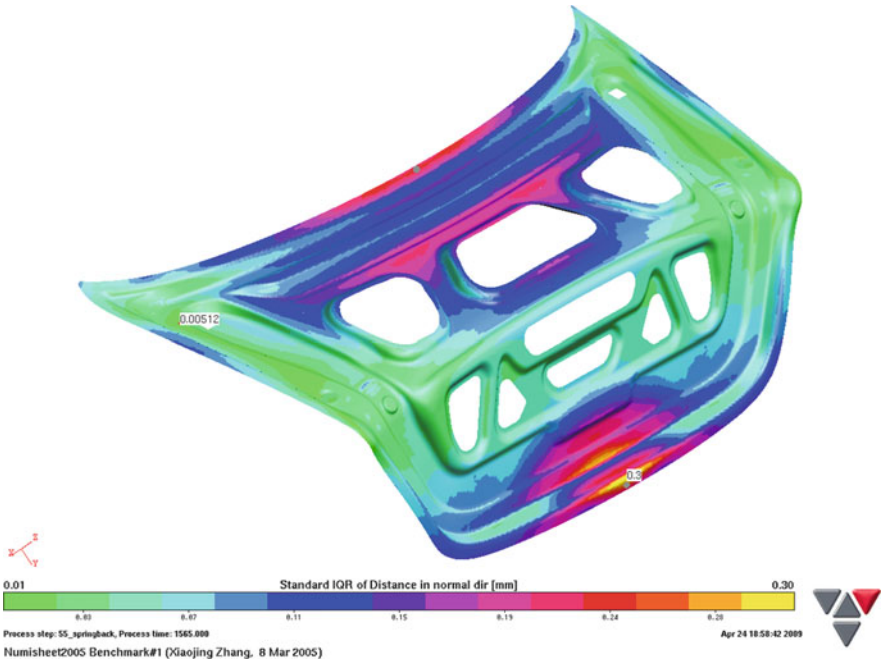

Fig. 4.63 Variation of the distance from the desired shape along the normal direction

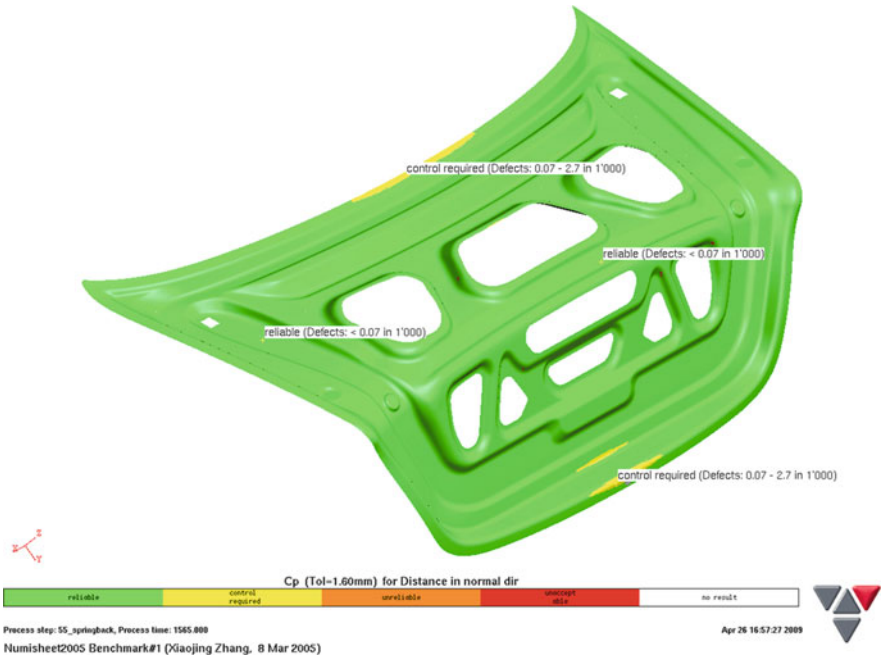

Fig. 4.64 The Cp assessment for distance from the desired shape along the normal direction

4.6.6 Conclusion

Springback compensation is a challenging and cost prohibitive process in current die manufacturing. With help of computer-aided springback compensation, this process can be easy and effective. To obtain a successful springback compensation, additional analysis and optimization have to be done before and after compensation.

- The robust and accurate calculated springback is critical for computer aided springback compensation. Therefore, the use of optimized numerical parameters, the so-called final validation settings, is strongly recommended in springback simulation in order to ensure the reliable compensated values.
- The repeatability of springback deviation in the real stamping process is the central premise to fulfill the springback compensation. Therefore, the robustness analysis and optimization before and after compensation is necessary in order to make sure that the springback compensation is reliable.
- In the end, a guideline for the sucessful computer aided springback compenstion is presented in this subchapter. Using this guideline, a robust compensation scheme can be guaranteed and the cost of tool development can be significantly decreased.

Acknowledgements Finally, I would like to thank all my colleagues, especially Thomas Schoenbach, who were involved in the preparation of this subchapter.

References

1. Kleiner M et al. (2002) Material parameters for sheet metal forming simulations by means of optimization algorithms. Final Report of the European Project 7210-PR-244, Research Fund for Coal and Steel (RFCS)
2. AutoForm 4.1 Software Manual. (2007) AutoForm Engineering GmbH, Zurich
3. Sigvant M, Mattiasson K, Vegter H, Thilderkvist P (2009) A viscous pressure bulge test for the determination of plastic hardening curve and equibiaxial material data. International Journal of Material Forming, 2:235–242
4. Hosford WF (1996) On the crystallographic basis of yield criteria. Texture and Microstructures 26–27:479–493
5. Mattiasson K, Sigvant M (2004) Material characterization and modeling for industrial sheet forming simulations. In: Ghosh S, Lee JK, Castro JC (eds) Proceedings of the NUMIFORM 2004, AIP, New York, NY, 875–880
6. Forming of new metallic materials. Brite Euram Project, 1996–1999.
7. Sigvant M, Mattiasson K, Skogsgårdh A (2007) Industrial experiences of stochastic simulations of sheet metal forming In: Hora P (ed) Proceedings of the Application Stochastics and Optimization Methods, Zürich, 23–31
8. Bonte MHA et al. (2006) Optimizing towards robust metal forming processes. In: Juster N, Rosochowski A (eds) Proceedings of the International Conference on Material Forming ESAFORM 2006, Glasgow, 47–51
9. Dietrich E, Schulze A (2005) Statistische Verfahren zur Maschinen- und Prozessqualifikation, Hanser Verlag, Munchen
10. Carleer B (2006) Applicability of stochastical methods in the control of the scatter influence of constitutive parameters. Proceedings of the FLC Conference, March 15th–16th 2006, Zürich
11. Lee CH (2006) Application of AutoForm Sigma on a hood inner. Proceedings of the 5th Press Forming Symposium, Korean Society of Technology for Plasticity, Jeju Island, June 2006
12. Xu WL, Ma CH, Li CH, Feng WJ (2004) Sensitive factors in springback simulation for sheet metal forming. Journal of Materials Processing Technology 151:217–222
13. Valente F, Li XP, Messina A (1997) Springback prediction for stamping tools compensation by numerical simulation. Centro Ricerche Fiat, Torino
14. Chung WJ, Cho JW, Belytschko T (1996) A study on dynamic effects of dynamic explicit FEM in sheet metal forming analysis. In: Lee JK Kinzel JL, Wagoner RH (eds) Proceedings of the NUMISHEET'96 Conference, Columbus, OH, 414–426
15. Lin Z, Liu G (2000) Study on the effects of numerical parameters on the precision of springback prediction. Proceedings of the 6th International LS_DYNA User's Conference, Session 13C, Dearbon, MI
16. Huang M, Gerdeen JC (1994) Springback of doubly curved developable sheet metal surface – An overview. SAE Technical Paper No. 940938, 718–731
17. Makinouchi A, Nakamachi E, Onate E, Wagoner RH (eds) (1993) Proceeding of the 2nd International Conference and Workshop on Numerical Simulation of 3D Sheet Metal Forming Processes, Isehara
18. Kubli W, Anderheggen E, Reissner J (1991) Nonlinear solver with uncoupled bending and stretching deformation for simulating thin sheet metal forming. Proceedings of the 1st International Conference and Workshop on Numerical Simulation of 3D Sheet Metal Forming Processes, VDI, Dusseldorf, 325–343
19. Yang DY, Hug H, Oh SI, Kim YH (eds) (2002) Proceedings of the 5th International Conference and Workshop on Numerical Simulation of 3D Sheet Metal Forming Processes-Verification of Simulation with Experiment, Jeju Island

20. Li K, Wagoner RH (1998) Simulation of springback. In: Huetink J, Baaijens FPT (eds) Simulation of Materials Processing: Theory, Methods and Applications. Proceedings of the 6th International Conference on NUMIFORM 1998, Enschede, 21–31
21. Wagoner RH, Li M (2005) Advances in springback. In: Smith LM, Pourboghrat F, Yoon JW, Stoughton TB (eds) Proceedings of the 6th International Conference and Workshop on Numerical Simulation of 3D Sheet Metal Forming Processes-Verification of Simulation with Experiment, Numisheet 2005, Detroit, 209–214
22. Smith LM, Pourboghrat F, Yoon JW, Stoughton TB (eds) Proceedings of the 6th International Conference and Workshop on Numerical Simulation of 3D Sheet Metal Forming Processes-Verification of Simulation with Experiment, Numisheet 2005, Detroit
23. Hora P (ed) (2008) Proceedings of the 7th International Conference and WorkShop on Numerical Simulation of 3D Sheet Metal Forming Processes-Verification of Simulation with Experiment, Numisheet 2008, Interlaken
24. Roll K, Lemke T, Wiegand K (2005) Possibilities and strategies for simulation and compensation for springback. In: Smith LM, Pourboghrat F, Yoon JW, Stoughton TB (eds) Proceedings of the 6th International Conference and Workshop on Numerical Simulation of 3D Sheet Metal Forming Processes-Verification of Simulation with Experiment, Numisheet 2005, 295–302
25. Schoenbach T, Bauer T (2008) New method to calculate and compensate springback. In: Hora P (ed) (2008) Proceedings of the 7th International Conference and Workshop on Numerical Simulation of 3D Sheet Metal Forming Processes-Verification of Simulation with Experiment, Numisheet 2008, Interlaken, 515–520
26. AutoForm Release Notes 4.0 (2005) AutoForm Engineering. GmbH, Zurich

Index

D. Banabic, *Sheet Metal Forming Processes*, DOI 10.1007/978-3-540-88113-1,